

Design and synthesis of organic small molecules with high triplet energy for blue light emission

By

Nikhil Sahotra



UNIVERSITY OF
BIRMINGHAM

A thesis submitted to

The University of Birmingham

For a degree of

DOCTOR OF PHILOSOPHY

School of Chemistry

College of Engineering and Physical Sciences

University of Birmingham

September 2017

UNIVERSITY OF
BIRMINGHAM

University of Birmingham Research Archive

e-theses repository

This unpublished thesis/dissertation is copyright of the author and/or third parties. The intellectual property rights of the author or third parties in respect of this work are as defined by The Copyright Designs and Patents Act 1988 or as modified by any successor legislation.

Any use made of information contained in this thesis/dissertation must be in accordance with that legislation and must be properly acknowledged. Further distribution or reproduction in any format is prohibited without the permission of the copyright holder.

Abstract

For the past two decades, organic light emitting diodes (OLEDs) have been the subject of intense research in the realm of display and lighting applications. Recently, thermally activated delayed fluorescence (TADF) has shown great potential in further advancing OLED technology. In order to achieve TADF, synthesis of acceptor and donor compounds has been undertaken to achieve exciplex formation. Little is currently known about exciplex formation and emission, so systematic structural variations have been performed on MCP and DPBI (Figure 1) in order to gain fundamental knowledge.

Compound analyses were performed in both the solid and solution state. In the case of MCP derivatives, demonstration of their ability to act as an acceptor is possible, alongside an appropriate choice of donor molecule. Reducing the extent of conjugation in derivatives of DPBI, did not result in an increase in triplet energy. Consequently, to eliminate possible conformers, steric blocking was introduced in an attempt to increase the triplet energy. In the case of the ME-DPBI derivative it was shown possible to formulate a device showing 2.5% external quantum efficiency while emitting at ≈ 450 nm which is a true blue colour.

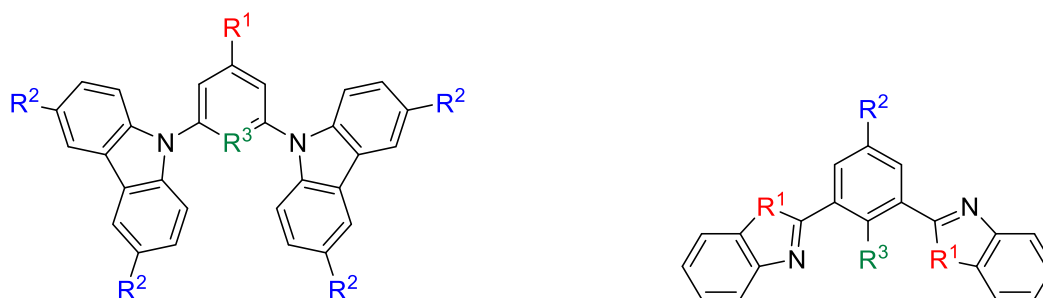


Figure 1: Left: Molecular structure of **MCP** derivative Left (R¹: H, CF₃, OMe, Carbazole; R²: H ^tBu; R³: C, N). Right:

Molecular structure of **DPBI** derivatives (R¹: O, S, N-Ph and R²: H, Ph, ^tBu-Ph, Pyrimidine; R³: H, Me).

Acknowledgements

Firstly, I would like to thank all the academics who have assisted me in the past and present. All throughout my academic studies I have had great help and I would like to take this opportunity to applaud all the academic staff for their hard work.

I am very grateful to the analytical department for their assistance and support. I would like to thank Dr. Chi Tsang in particular. I would like to take this opportunity to express my gratitude to the EPSRC, School of Chemistry at University of Birmingham and to Samsung for their financial support.

I would like to thank all the members of the Baranoff group. A special thanks is extended to Prof. Yafie Wang for his support both in the laboratory as well as in spending time to review and correct this thesis.

I would like to thank all of my family for their love and support over the years. Their encouragement throughout the years has been invaluable. Lastly, I would like to show my special appreciation for my now fiancée Dr. Catherine Barton, who I met at the start of the PhD. This time would have definitely been a lot more difficult if it wasn't for her. She too has assisted me in correcting this thesis and has helped to push me at times when I was struggling. One form of encouragement included a short motivational poem she created to keep my spirits up.

Chemistry can be fun...
But after A-levels I was done.
Nik, however, he was looney...
Decided to carry on at uni.
Etienne he's trying to please...
By making blue O-L-E-Ds.
A few things on the way exploded...
His white glasses even eroded!
That's why you need safety specks...
Yannouck WILL be doing checks.
All his columns have been run...
His time in labs is almost done.
In Preston recently he's been...
Away from his Edinburgh machine.
Very soon he's going back...
For B-ham he will need to pack.
Then there'll be graphs to make...
He'll find it hard to stay awake!
To do a thesis now, he's got-ta...
So he can be like me, a doctor.

By

Dr. Catherine Barton



List of abbreviations

γ	Charge Balance Factor
η_{fl}	Fluorescence Efficiency
η_{fr}	Singlet Formation Ratio
η_{out}	Light Out Coupling Efficiency
ΔE_{ST}	Energy Gap between Singlet and Triplet
λ_{max}	Emission Max
$[\text{PdCl}(\pi\text{-allyl})]_2$	allylpalladium (II) chloride dimer
A	Acceptor
A_{max}	Absorption Max
Ar	Aryl
B3LYP	Becke three parameters hybrid functional with Lee-Yang-Perdew correlation function
B_i	Incident Beam
Br-DPBI	2,2'-(5-bromo-1,3-phenylene)bis(1-phenyl-1H-benzo[d]imidazole)
B_t	Transmitted Beam
cBRIDP	di- <i>tert</i> -butyl (2, 2-diphenyl-1-methyl-1-cyclopropyl) phosphine
cd	Candela
CLB	Chlorobenzene
CT	Charge Transfer

D	Donor
DBO	1,3-bis(benzo[d]oxazol-2-yl)benzene
DBT	1,3-bis(benzo[d]thiazol-2-yl)benzene
DCM	Dichloromethane
DFT	Density Functional Theory
DMAc	Dimethylacetamide
DMF	Dimethylformamide
DMSO	Dimethylsulphoxide
DPBI	1,3-bis(1-phenyl-1H-benzo[d]imidazol-2-yl)benzene
DPPF	1,1'-ferrocenediyl-bis(diphenylphosphine)
e-	Electron
E _g	Band Gap
EL	Electroluminescence
E _T	Triplet Energy
ETL	Electron Transfer Layer
Eq.	Equivalent
EQE	External Quantum Efficiency
H-L Gap	HOMO-LUMO Gap
HOMO	Highest Occupied Molecular Orbital
HTL	Hole Transport Layer
ICT	Intermolecular Charge Transfer
ISC	Inter-system crossing
IQE	Internal Quantum Efficiency

L	Ligand
LED	Light Emitting Diode
LEDs	Light Emitting Diodes
Lm/W	Lumens per Watt
LUMO	Lowest Un-occupied Molecular Orbital
MCP	1,3-Di(9H-carbazol-9-yl)benzene
ME-DPBI	2,2'-(2-methyl-1,3-phenylene)bis(1-phenyl-1H-benzo[d]imidazole)
ME-MCP	9,9'-(5-methyl-1,3-phenylene)bis(9H-carbazole)
ME-T-MCP	9,9'-(5-methyl-1,3-phenylene)bis(3,6-di-tert-butyl-9H-carbazole)
MeMgCl	Methylmagnesium Chloride
OLED	Organic Light Emitting Diode
OLEDs	Organic Light Emitting Diodes
OME-MCP	9,9'-(5-methoxy-1,3-phenylene)bis(9H-carbazole)
OME-T-MCP	9,9'-(5-methoxy-1,3-phenylene)bis(3,6-di-tert-butyl-9H-carbazole)
PH-DPBI	3,5-bis(1-phenyl-1H-benzo[d]imidazol-2-yl)-1,1'-biphenyl
PHT-DPBI	2,2'-(4'-(tert-butyl)-[1,1'-biphenyl]-3,5-diyl)bis(1-phenyl-1H-benzo[d]imidazole)
PL	Photoluminescence
POLED	Phosphorescent Organic Light Emitting Diode
PY-DPBI	2,2'-(5-(pyrimidin-5-yl)-1,3-phenylene)bis(1-phenyl-1H-benzo[d]imidazole)
PY-MCP	2,6-di(9H-carbazol-9-yl)pyridine
PY-T-MCP	2,6-bis(3,6-di-tert-butyl-9H-carbazol-9-yl)pyridine

RISC	Reverse Intersystem Crossing
S ₀	Ground State
S ₁	Singlet/ Singlet State
S	Scattering
SM-OLED	Small Molecule Organic Light Emitting Diodes
SN _{Ar}	Nucleophilic aromatic substitution
Std	Standard Purity
Std II	High Purity Sample
T-MCP	1,3-Bis(3,6-di-tert-butyl-9H-carbazol-9-yl)benzene
T ₁	Triplet/ Triplet state
T	Temperature
TADF	Thermally Activated Delayed Fluorescence
T-MCP	1,3-bis(3,6-di-tert-butyl-9H-carbazol-9-yl)benzene
TD-DFT	Time-Dependent Density Functional Theory
THF	Tetrahydrofuran
TOL	Toluene
TPBI	2,2',2''-(1,3,5-Benzinetriyl)-tris(1-phenyl-1-H-benzimidazole)
TTA	Triplet Triple Annihilation
TTF	Triplet Triple Fusion
Wt%	Weight Percent
Xphos	2-Dicyclohexylphosphino-2',4',6'-triisopropylbiphenyl

Table of Contents

1	Introduction	1
1.1	Organic Light Emitting Diodes.....	2
1.1.1	History summarized	3
1.1.2	Electroluminescence of Fluorescent OLEDs	5
1.1.3	Efficiency of Organics	8
1.2	Harvesting Triplet and Singlet via Molecular Design	9
1.2.1	Phosphorescent Materials	10
1.2.2	Issues with Blue Phosphorescence	12
1.3	Harvesting Triplet and Singlet via Photo-physical Processes.....	12
1.3.1	Triplet-Triplet Annihilation.....	13
1.3.2	Thermally Activated Delayed Fluorescence	14
1.4	Achieving TADF using Exciplex Systems	19
1.5	Thesis Motivation and Scope.....	24
1.6	References	25
2	Synthesis and Analysis of 1,3-Di(9<i>H</i>-carbazol-9-yl)benzene Derivatives	31
2.1	Introduction	32
2.2	Results and Discussion.....	32
2.2.1	Synthesis of 1,3-Di(9 <i>H</i> -carbazol-9-yl)benzene Derivatives via Ullmann Reaction....	35
2.2.2	Synthesis of 1,3-Di(9 <i>H</i> -carbazol-9-yl)benzene Derivatives via Buchwald-Hartwig Reaction	39

2.2.3 Synthesis of 1,3-Di(9 <i>H</i> -carbazole-9-yl)pyridine derivatives	50
2.3 Theoretical Studies of MCP and T-MCP Derivatives	52
2.4 In solution Photophysical Analysis of 1,3-Di(9 <i>H</i> -carbazol-9-yl)benzene Derivatives	57
2.5 Solid State Photophysical Analysis of 1,3-Di(9 <i>H</i> -carbazol-9-yl)benzene Derivatives	67
2.6 Conclusion	70
2.7 References	71
3 Synthesis and Analysis of 1,3-Bis(1-phenyl-1<i>H</i>-benzo[D]imidazol-2-yl)-benzene Derivatives.....	75
3.1 Introduction	76
3.2 Results and Discussion.....	77
3.2.1 Synthesis of First Generation DPBI Derivatives	78
3.2.2 Synthesis of Second Generation DPBI Derivatives	81
3.2.3 Synthesis of Third Generation DPBI Derivative	82
3.3 Computational Analysis of DPBI Derivatives	83
3.4 In solution Photophysical Analysis of DPBI Derivatives	89
3.5 Solid State Photophysical Analysis of DPBI Derivatives	98
3.6 Conclusion	109
3.7 References	110
4 Conclusion and Future Work.....	112
5 Experimental	114
5.1 Synthesis of MCP Derivatives via Ullmann Reaction.....	116

5.2	Synthesis of MCP derivatives via the Buchwald-Hartwig Reaction	118
5.3	Synthesis of MCP Derivatives via Method 3	125
5.4	Synthesis of First Generation DPBI Derivatives.....	127
5.5	Synthesis of Second Generation DPBI Derivatives	129
5.6	Synthesis of Third Generation DPBI Derivatives	134
5.7	References	136
6	Appendix i	138
6.1	Analytical Data of MCP Derivatives via Ullmann Reaction	139
6.2	Analytical Data of MCP derivatives via the Buchwald-Hartwig Reaction.....	145
6.3	Analytical Data of MCP Derivatives via Method 3.....	162
6.4	Analytical Data of First Generation DPBI Derivatives.....	167
6.5	Analytical Data of Second Generation DPBI Derivatives	172
6.6	Analytical Data of Third Generation DPBI Derivatives	185
7	Appendix ii.....	189
7.1	Photophysical Analysis of Second Generation DPBI.....	190
7.2	Fluorescence Lifetime Measurements in DCM.....	190
7.3	Fluorescence Lifetime Measurements in THF	192
7.4	Fluorescence Lifetime Measurements in Toluene.....	194
7.5	Fluorescence Lifetime Measurements in Chlorobenzene.....	197
7.6	Solid state Analysis of Devices Formulated using DPBI.....	199
7.7	Solid state Analysis of Devices Formulated using ME-DPBI	205

1 INTRODUCTION

1.1 Organic Light Emitting Diodes

The invention of the incandescent light bulb, by Thomas A. Edison in 1880, revolutionised domestic light.¹ This inefficient but low-cost lighting could not be replaced for over 100 years. The power efficiency reaches ≈ 14.8 Lm/W, while the rest of the energy is emitted as heat.² Moreover, the operational lifetime is limited to approximately 1000 hours. Since this time, advances in lighting technology led to the discovery of the fluorescent lamp. Although the efficiency and lifetime were improved, the light produced is of lower colour quality and the bulb itself contains mercury, which is harmful to the environment.

Research into alternative lighting sources resulted in the discovery of organic materials with conducting properties in the 1950s.³ Shortly after, electroluminescence (EL) from organic material was observed.⁴ Furthermore, conductive polymers were discovered and developed, resulting in a Nobel prize in 2000 for Alan J. Heeger, Alan G. MacDiarmid and Hideki Shirakawa.⁵ Fourteen years later, another Nobel prize in physics was awarded to Isamu Akasaki, Hiroshi Amano and Shuji Nakamura for the invention of efficient blue light emitting diode (LED).⁶ This invention enabled the production of white light emitting diodes (LEDs), which are much more efficient (≈ 100 Lm/W) in comparison to their predecessors, i.e. incandescent light bulbs and the fluorescent lamp.

Another attractive source of next generation displays and solid-state lighting are the organic light emitting diodes (OLEDs). A significant proportion of high-end smartphone and television displays are based on organic light emitting diode (OLED) technology today. OLED technology for signage and lighting has reached the market in the past year which has been a great leap forward. This technological advance is being driven by large electronic companies such as Samsung and LG, who are both currently utilising OLED displays in their flagship models, for

example Samsung Galaxy S8 and LG G6. OLEDs offer unique features, such as the possibility to produce flexible and transparent devices. Furthermore, they have the potential to achieve exceptional colour rendering as well as increased device lifetime. Advantages of OLEDs in comparison to the predecessor LEDs also include minimised thickness, improved resolution, brightness, contrast and a wider viewing angle (Figure 1.1).⁷



*Figure 1.1: Figure to show the comparison between **OLED** and **LED** television.*⁸

This chapter will give an introduction to the basic principles of OLED technology. The reader will be updated on the current interests within this field of research and the materials used. Emphasis will be given to topics which are applicable to the work described later in the thesis. This chapter will conclude with an overview of limitations in the field of OLED technology and pathways to overcome these challenges, with the aim of achieving further developments and establishing the full potential of OLED applications.

1.1.1 History Summarised

The early history of OLEDs dates back to the 1950s. The original proof of electroluminescence was provided by A. Bernanose in 1955, using an acridine derivative (Figure 1.2).⁴ This was followed by advances in 1962 which showed EL from 10 - 20 μ m thick crystals of anthracene

(Figure 1.2). However, in order to obtain this EL, high voltages amounting to greater than 400 Volts (V) were required.⁹ Unfortunately these high voltages are impractical for most applications; hence, the research wasn't able to have a significant impact until the anthracene crystals were revisited in 1982.



Figure 1.2: Molecular structure of acridine and anthracene.

Developments in the production of thin solid films via vacuum deposition enabled anthracene electroluminescence to be achieved at lower voltages ranging from 30 V to 100 V.¹⁰ Using vacuum deposition Vincett *et al.* were able to achieve $\approx 0.6\mu\text{m}$ films of anthracene through which a steady current could be passed. Although most of the initial focus was based on small organics, R. H. Partidge successfully demonstrated EL from polymer material in 1983.¹¹

The vital breakthrough in the field occurred a few years later in 1987 when C. W. Tang and S. A. VanSlyke, developed the first two-layer diode based organic EL device, an OLED device as we know it today. The device itself operated below 10 V and with a power efficiency of 1%.¹² This ignited further exploration into the field of OLEDs and improvements were subsequently reported at a steady pace. Collected efforts of chemists and physicists have since facilitated the production of tailored materials with higher luminescence and efficient device architecture.

The first report of a white OLED device was made by J. Kido *et al.* in 1995, who used a combination of red, green and blue emitting organics to produce white.¹³ A major increase in efficiency was later achieved by M. A. Baldo *et al.* in 1988 which originated from the use of phosphorescent metal complexes. Despite these advances, the performance of blue light

emitting devices remains limited. The power efficiencies of green and red OLEDs are far superior to that of blue. This phenomenon will be elaborated further in this thesis.

1.1.2 Electroluminescence of Fluorescent OLEDs

Conducting organic materials must contain an aromatic substituent in their molecular structure. The conjugated substituent enables the π -orbital overlap leading to delocalisation of the π -electrons, hence facilitating conduction. The energy levels of such aromatic compounds show a gap between the highest occupied molecular orbital (HOMO) and lowest unoccupied molecular orbital (LUMO), Figure 1.3. The energy difference between the HOMO and the LUMO is known as the band gap, E_g . An electron (e^-) in the HOMO can be excited, for example by absorption of a photon, to the LUMO, leaving behind a hole in the HOMO. Both holes and electrons are able to migrate onto neighbouring molecules, giving rise to an electrical current if an external voltage is applied.

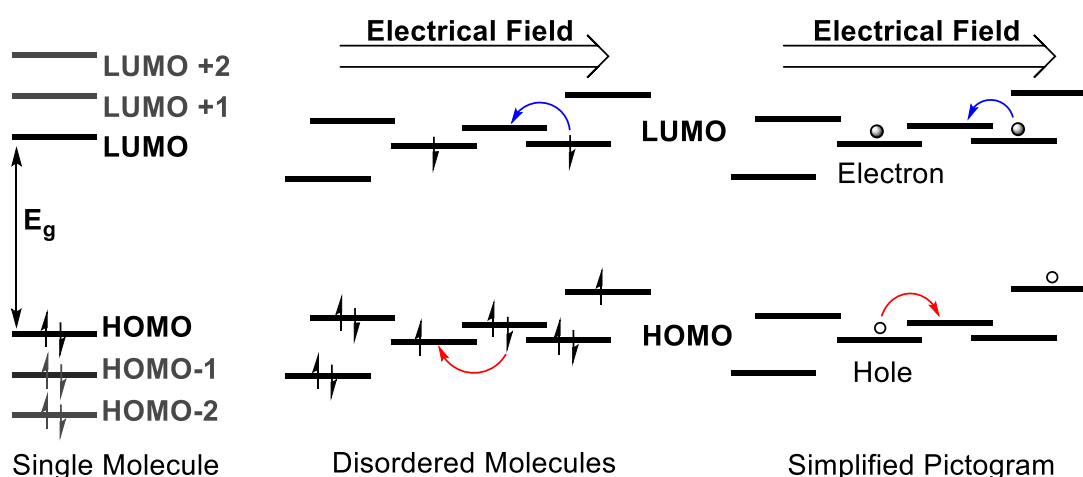


Figure 1.3: Figure to show electron/ hole migration on application of an electric field. Left: The energy levels correspond to different orbitals of a single molecule. Each arrow represents an electron with its spin up or down. The band gap (E_g) is the difference between the HOMO and LUMO. Middle: shows the charge transport through the disordered material. The arrows indicate the migration of an electron. Electrons move in the opposite direction to the electrical field. Right: a simplified pictogram where the charge transport is illustrated in terms of electron and hole.

Molecules typically reside in the ground state, where electrons of opposite spins reside as a pair, Figure 1.3. Electrons can be electronically excited on application of electrical current, which results in direct injection of electron/hole into the LUMO/HOMO. The electrons and holes migrate from molecule to molecule, until they both end up on the same molecule. This electron-hole pair is known as an exciton. The process itself is referred to as recombination. Depending on the combination of the spin, two types of excitons can be formed, singlet excitons or triplet excitons (opposite spin/identical spin). Singlet excitons, once formed, can relax. These excitons can decay via emitting a photon, in a process known as fluorescence, Figure 1.4. The Pauli Exclusion Principle forbids two electrons with identical spins to be situated close to each other, due to repulsion. Hence, triplet excitons will generally not give rise to a photon of light.

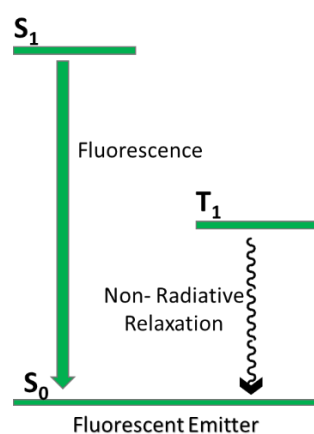


Figure 1.4: Jablonski diagram to show the fluorescence process for organic fluorescent emitters. The wavy line represents non-radiative decay, the solid line represents the radiative fluorescent process. S_0 is ground state, S_1 is singlet state, T_1 is triplet state.

The device structure of OLEDs is based on the pioneering work of Tang and Van Slyke.¹² Since this time the fundamental design of OLEDs has remained the same, with the exception of the addition of few extra layers in some cases. OLED devices in their most basic form consist of single or multiple-layers of organic material sandwiched between two electrodes, Figure 1.5.

Upon application of an electrical field, electrons are injected from the metal cathode into the LUMO of the electron transport layer (ETL). Holes are injected from the anode into the HOMO of the hole transport layer (HTL). The electrons and holes migrate through their respective transport layers until they are delivered to the emitting layer. Electrons and holes accumulate in the emitting layer, where recombination takes place, leading to photon production. In order to assist the accumulation of electrons and holes in the emissive layer, some devices utilise additional layers of materials with electron or hole blocking properties. These are effectively employed to achieve multiple spectra of light, used to obtain white emission. The device architecture shown in Figure 1.5 can be extended to include multiple emissive layers (i.e. red, green and blue). Exciton blocking layers are employed, if necessary to confine excitons to their respective recombination layer.

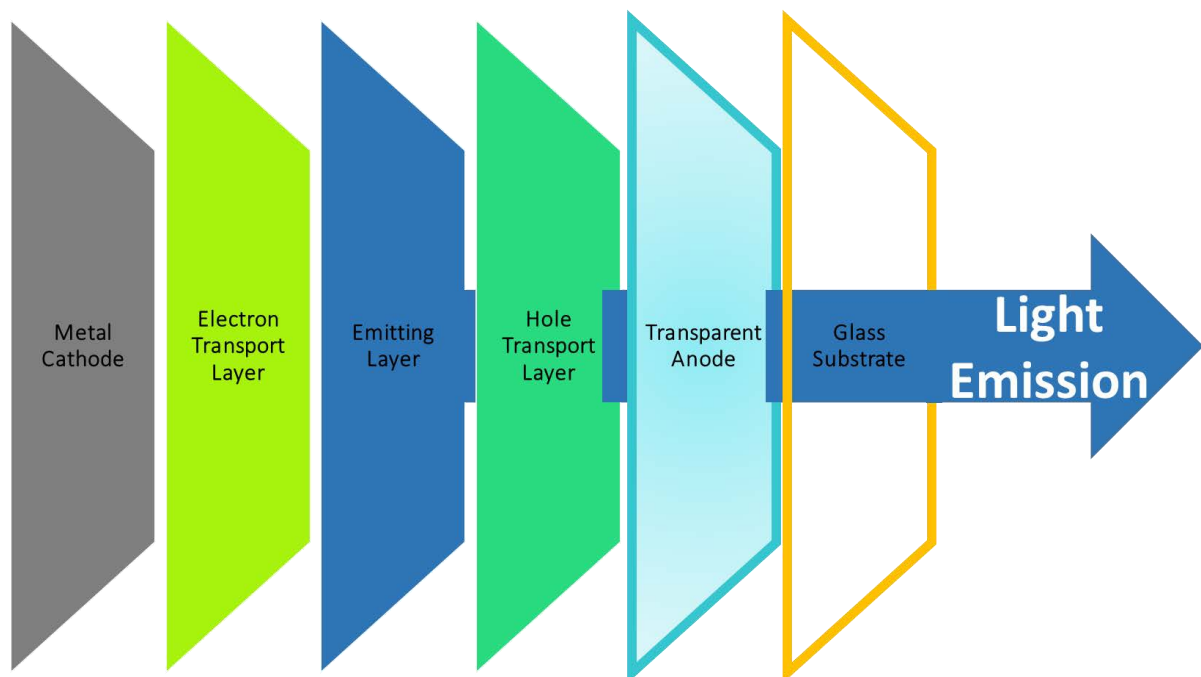


Figure 1.5: Schematic of an OLED device.

1.1.3 Efficiency of Organics

One of the reasons why OLEDs are well established in the display market and not the general lighting market is the so called efficient 'roll-off'. This refers to a reduction in efficiency with increasing brightness or current density. Figure 1.6 illustrates the effect that an increase in current density has on external quantum efficiency.

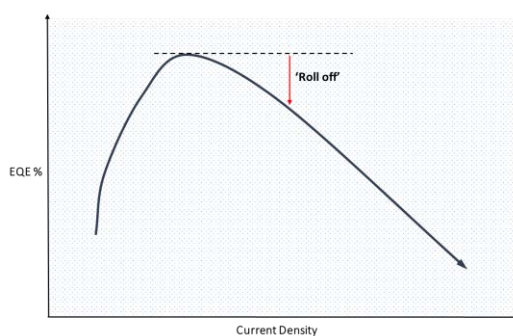


Figure 1.6: Figure to show the rough correlation between increase in current density and external quantum efficiency (EQE%). The EQE peaks at approximately 30% and the current density starts at 1 to 500 mA/cm².

Typical brightness of mobile phone displays is around 100-400 cd m⁻² at which these devices have a reasonable lifetime.¹⁴ However, general lighting requires brightness levels in the range of 1000 – 10,000 cd m⁻².^{15,16} The increased current required to generate this brightness has a negative impact on efficiency as well as causing increased electrical stress, ultimately resulting in a reduction in device lifetime. In efficient fluorescent and phosphorescent OLED devices higher currents cannot be reached, often due to material degradation.

In organics the process of electrical excitation statistically results in formation of 25% singlet (S₁) and 75% triplet (T₁) excitons. This fundamentally limits the internal quantum efficiency (IQE) and external quantum efficiency (EQE).¹⁷ Thus, utilising S₁ and T₁ can increase the EQE significantly. External quantum efficiency is dependent on four factors, which are exemplified in the equation below:

$$EQE = \eta_{out} \cdot \eta_{fl} \cdot \gamma \cdot \eta_{fr}$$

η_{out} : Light out coupling efficiency

η_{fl} : Fluorescence efficiency

γ : Charge Balance factor

η_{fr} : Singlet formation ratio

Light out coupling efficiency is generally considered to be 20%.¹⁸ Fluorescence efficiency is aimed to be 1. Charge balance factor can also be assumed to be 1 if the HOMO level, the LUMO level of organic layers and the work-function of electrodes are adjusted accordingly. If there is charge imbalance (where either hole or electron dominates) then EL will have poor efficiency. Theoretical singlet formation ratio is 25%, which consequently limits the EQE to 5% for organic emitters ($EQE \approx 0.2 \cdot 1 \cdot 1 \cdot 0.25 = 0.05$). Thus, it is clear that one could increase quantum efficiency four-fold through harvesting triplet excitons. This has been achieved successfully using heavy metal complexes as emissive dopants.

1.2 Harvesting Triplet and Singlet via Molecular Design

Organic and inorganic compounds have been used in the application of OLEDs. Organic compounds have been fundamentally limited in terms of internal quantum efficiency. Hence, we briefly look into inorganic materials and their current standing. As aforementioned, we are able to achieve 100% IQE using heavy metal complexes, which emit light via the phosphorescent emission pathway. Despite the enormous advances in the design and synthesis, further improvements are still required: for instance, efficiency and stability.

1.2.1 Phosphorescent Materials

Since the inventive work of Baldo *et al.*, illustrating the ability of phosphorescent materials to enhance efficiency of OLED devices, considerable scientific research has provided numerous new materials for electro-phosphorescent devices.¹⁹ Compared to fluorescence, phosphorescence (Figure 1.7) has a longer emission lifetime.²⁰ The spin forbidden nature of intersystem crossing between S_1 to T_1 becomes favourable via an interaction known as spin orbit coupling. The magnitude of spin orbit coupling increases with atomic number. While the group eight metals have been investigated, the group six metals have been particularly successful in this domain. These include iridium,²¹ osmium²² and platinum¹⁹. Complexes based on these metals have metal-to-ligand charge transfer characteristics.²³

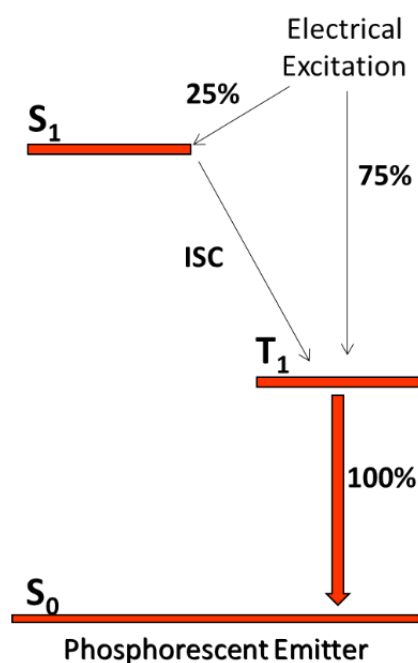


Figure 1.7: Jablonski diagram to show the phosphorescence process. The solid line represents the radiative phosphorescence process. S_0 is ground state, S_1 is singlet state, T_1 is triplet state and ISC is intersystem crossing.

One of the superior candidates for phosphorescent devices are the cyclometalated iridium (III) complexes, because of their relative short phosphorescence lifetime and colour tunability via ligand modification. However, it has been observed that blue-emitting heavy metal complexes

are often unstable. An example of the instability is Flrpic (Figure 1.8), which is considered to be an excellent dopant for blue phosphorescent-OLED (POLED). However, Flrpic has the tendency to degrade during vacuum deposition and device operation.²⁴

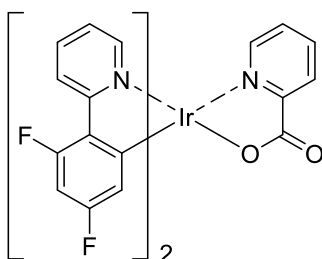


Figure 1.8: Molecular structure of Flrpic.

Generally, the phosphorescent emitter is dispersed in a suitable host material to obtain high photoluminescence. This enhances the efficiency by eliminating the possibility of reverse energy transfer and non-radiative decay from triplet to ground state, Figure 1.9.²⁵ The host material needs to have a higher triplet energy than the triplet energy of the phosphorescent emitter. The development of such a host-dopant system with sufficient efficiency has remained an on-going challenge, mainly due to stability issues.

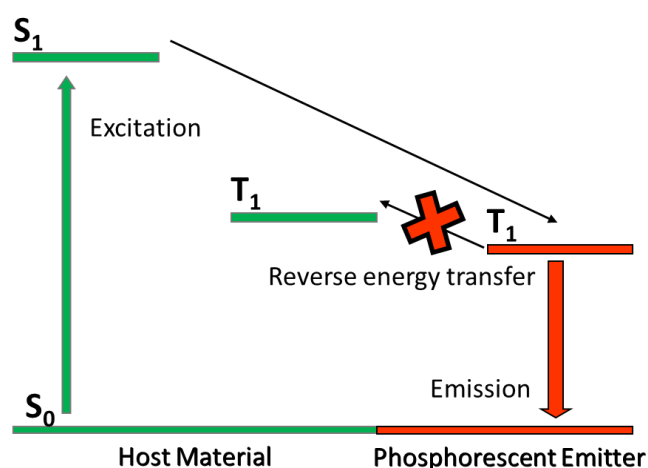


Figure 1.9: The reverse energy transfer process from phosphorescent emitter to host material. The absorption is represented by the green line; the non-radiative process is represented by black lines and the radiative process is represented by the bold orange line.

1.2.2 Issues with Blue Phosphorescence

The red and green emitting phosphorescent devices are well established and optimised.^{26,27} However, the design and fabrication of a blue counterpart remains challenging.²⁸ There are three major issues with current blue phosphorescent emitters: 1) The chromaticity of the blue phosphor is not a true blue colour.²⁹ 2) The emission efficiency of red and green phosphor is far greater than that of blue. 3) The lifetime stability of blue phosphor ($\geq 20,000$ hours) is shorter than that of red and green phosphor ($\geq 100,000$).³⁰ These three issues are mainly due to:

- Fluorine: Fluorine-substituted materials have been widely used to blue shift the emission of the metal complexes. However, due to strong acceptor characteristics, de-fluorination occurs during device fabrication and during device operation.²⁴
- Metal-centred state: Metal-centres can become thermally accessible under operating conditions, due to high energy of the blue exciton.³¹ The bond between metal ion and the ligand are able to break, resulting in non-radiative quenching of the emissive state and chemical degradation of the emitter through reaction with oxygen, water or host.
- Host: The high energy of the blue exciton demands hosts with high triplet energy, to confine the excitons within the emissive layer.³² Designing such hosts requires a decrease in conjugation, resulting in lower electron transport properties. This subsequently impacts upon the efficiency of the device.

1.3 Harvesting Triplet and Singlet via Photo-physical Processes

Among the primary RGB colours, deep blue light (450nm) is essential to achieve good colour rendering in white OLEDs for lighting application. Until now, we have discussed fluorescence

and phosphorescence and the limitations of both have been explained. As a result of these, other processes that can harvest triplet and singlet states are explored.

We explore the possibility of up-conversion of excitons, which is a process that can convert triplet photons with low energy to a singlet exciton of higher energy. For example, the production of singlet via triplet-triplet annihilation, also named triplet-triplet fusion. Another process of great interest is thermally activated delayed fluorescence (TADF), where organic emitters are able to undergo reverse intersystem crossing (i.e. from triplet to singlet).

1.3.1 Triplet-Triplet Annihilation

The phenomenon of triplet-triplet annihilation (TTA) was first observed in 1962 by Parker and Hatchard in a solution of anthracene.³³ High exciton densities give rise to a probability of two triplet excitons meeting each other, subsequently resulting in fusion upon interaction ($T_1 + T_1 \rightarrow S_0 + S_1$). This leads to a non-radiative recombination for at least one.³⁴ There are nine theoretical outcomes of triplet exciton annihilation,^{35,36} the resulting excited singlet gives rise to delayed fluorescence. Kondakov *et al.* illustrated an efficient fluorescent OLED device employing TTA.³⁷ A number of theories have been explored to determine the factor by which TTA can increase the efficiency. Conversely, scientists have concluded, the maximum theoretical internal quantum efficiency is 62.5%. This is much lower than the 100% internal quantum efficiency of phosphorescent emitters.³⁸

1.3.2 Thermally Activated Delayed Fluorescence

An alternative way of harvesting the triplet excitons in metal free emitters is through thermally activated delayed fluorescence, also known as E-type delayed fluorescence. Figure 1.10 displays the differences between the fluorescence, phosphorescence and TADF emission pathways. TADF emitters decay first via the usual fluorescence route, while some singlet excitons undergo intersystem crossing ($S_1 \rightarrow T_1$). These triplet excitons are able to undergo reverse intersystem crossing (RISC), upon thermal activation, leading to delayed fluorescence. Indeed, this is a cyclic process from $S_1 \rightarrow T_1$ and vice-versa, however, due to the decay lifetime of fluorescence ($S_1 \rightarrow S_0$) being shorter than phosphorescence ($T_1 \rightarrow S_0$), most triplet excitons will decay via the singlet pathway.

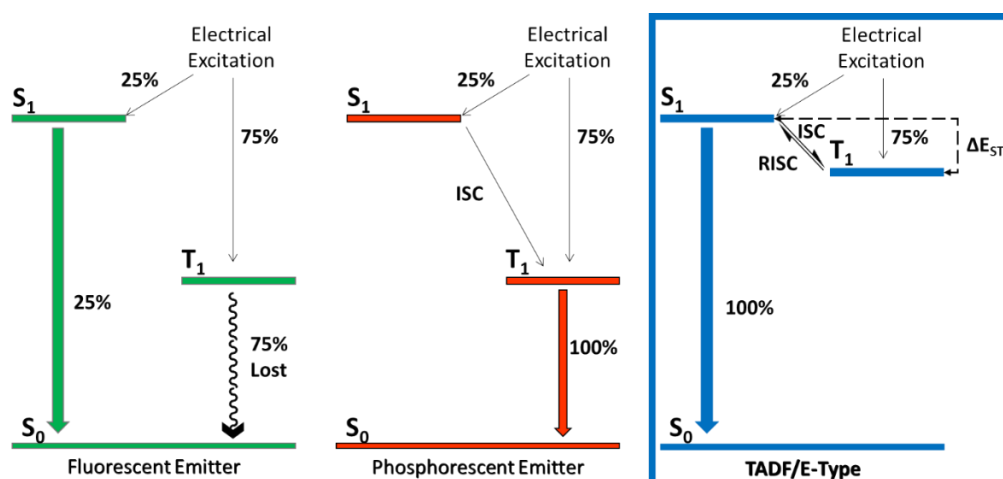


Figure 1.10: Comparison of emission mechanisms between fluorescence, phosphorescence and TADF emitters. Wavy lines represent non-radiative decay, solid coloured lines represent radiative processes, S_0 is ground state, S_1 is singlet state, T_1 is triplet state, ISC is intersystem crossing, RISC is reverse intersystem crossing and ΔE_{ST} is the energy gap between S_1 and T_1 .

E-type delayed fluorescence was first observed in 1929 by Perrin.³⁹ Although the principles of TADF were described in the correct way, Perrin believed this was a way in which phosphorescence occurs, because he assumed that triplet state to ground state transition was strictly forbidden. Lewis and Kasha identified that the triplet states were being thermally

activated and up-converted to singlet states, in 1944.⁴⁰ Studies based upon phosphine supported diatomic copper-diamond core complex ($\{\text{Cu}(\text{PNP-}t\text{-Bu})\}_2$, Figure 1.11) by Deaton *et al.* suggested that reverse intersystem crossing can be encouraged using compounds with a low energy gap between singlet and triplet.⁴¹ Using the copper-diamond core complex Deaton *et al.* were able to report a green device capable of yielding an EQE of 16.1%,⁴¹ close to that obtained with POLED. Endo *et al.* reported a device using tin-porphyrin ($\text{SnF}_2\text{-OEP}$, Figure 1.11) which was temperature dependent, i.e. at 400 Kelvin (K) the reverse intersystem crossing was enhanced.⁴² Since then, attempts have been made to achieve high external quantum efficiency using metal-free compounds.

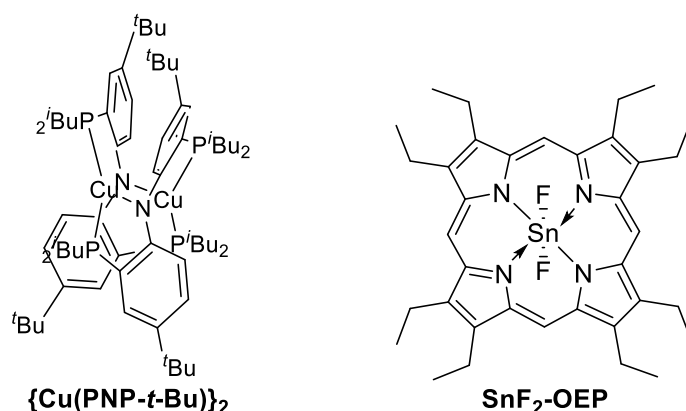


Figure 1.11: Molecular structure of $\{\text{Cu}(\text{PNP-}t\text{-Bu})\}_2$ and structure of $\text{SnF}_2\text{-OEP}$.

Following on from their earlier success, Endo *et al.* reported an organic blue/green device using 12,12'-(6-([1,1'-biphenyl]-4-yl)-1,3,5-triazine-2,4-diyl)bis(11-phenyl-11,12-dihydroindolo[2,3-a]carbazole) (**PIC-TRZ**) and 1,3-di(9H-carbazol-9-yl)benzene (**MCP**) (Figure 1.12). Utilising **PIC-TRZ** and **MCP** Endo *et al.* demonstrate an EQE of 5.3%.⁴³ Although the efficiency was not exceptional, this did demonstrate that efficiencies of stable metal-free organic compounds could be improved via TADF. The efficiency of TADF is determined by the energy gap between the singlet and triplet (ΔE_{ST}), where a smaller ΔE_{ST} encourages the rate of reverse intersystem crossing. This can be achieved using intramolecular charge transfer (CT) emitters, thus, the

increased efficiency of **PIC-TRZ**. In CT emitters the highest occupied molecular orbital (HOMO) and the lowest unoccupied molecular orbital (LUMO) can be spatially separated, hence, reducing electron-electron repulsion. This separation of HOMO and LUMO can be achieved by molecular design containing a donor moiety and an acceptor moiety.

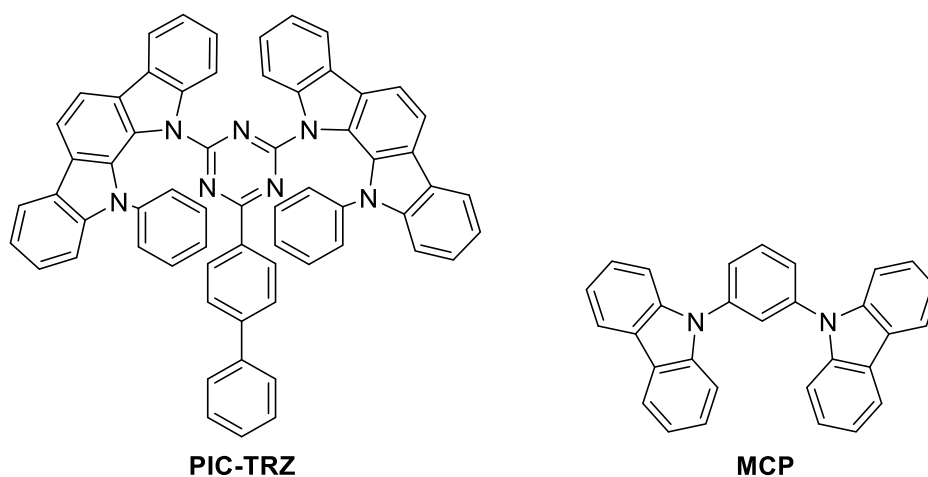


Figure 1.12: Molecular structure of **PIC-TRZ** and **MCP**.

Since the charge transfer principle worked well in **PIC-TRZ**, several new metal-free organic compounds have been reported recently as efficient TADF emitters, such as 1,2,3,5-tetrakis(carbazole-9-yl)-4,6-di-cyanobenzene (**4CzIPN**, Figure 1.13). **4CzIPN**, presented by Adachi and co-workers, exhibits an internal quantum efficiency of almost 100% and an external quantum efficiency of 19% for green OLED device.⁴⁴

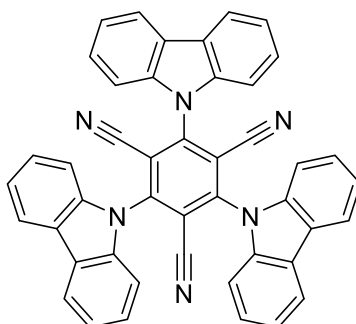


Figure 1.13: Molecular structure of **4CzIPN**.

Another way to achieve the spatial separation of donor (D) and acceptor (A) moieties is by introducing a twist within the molecular design (Figure 1.14). The twist forces the D and A moieties to be in different planes. This can be achieved using a linkage that connects both parts.

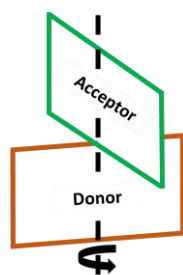


Figure 1.14: Depicted principle of twisting donor and acceptor moieties.

Employing the principle of twist, Nakagawa *et al.* were able to demonstrate a small ΔE_{ST} using a spirofluorene derivative, **Spiro-CN** (Figure 1.15).⁴⁵ This emitter successfully separates the HOMO and LUMO, resulting in an EQE of 4.4%. This is much lower than the EQE of **4CzIPN** which equates to 19%.

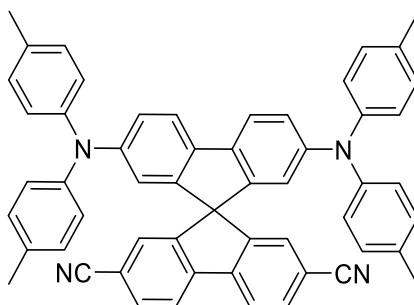


Figure 1.15: Molecular structure of 2',7'-bis(di-p-tolylamino)-9,9'-spirobi[fluorene]-2,7-dicarbonitrile (**Spiro-CN**).⁴⁵

Further research in the field has resulted in the discovery of 10,10'-(sulfonylbis(4,1-phenylene))bis(9,9-dimethyl-9,10-dihydroacridine) (**DMAC-DPS**, Figure 1.16) as a donor, reported by Zhang *et al.* The blue device formulated using **DMAC-DPS** demonstrated an efficiency of 19.5%,⁴⁶ which is an improvement on previously reported efficiency. However, the combination of **DMAC-DPS** and **DPEPO** host (Figure 1.16) in the device structure leads to

stability issues. Of merit, however, is the fact that, this research does prove that using organic emitters, 100% internal quantum efficiency can be achieved, via innovative molecular design.

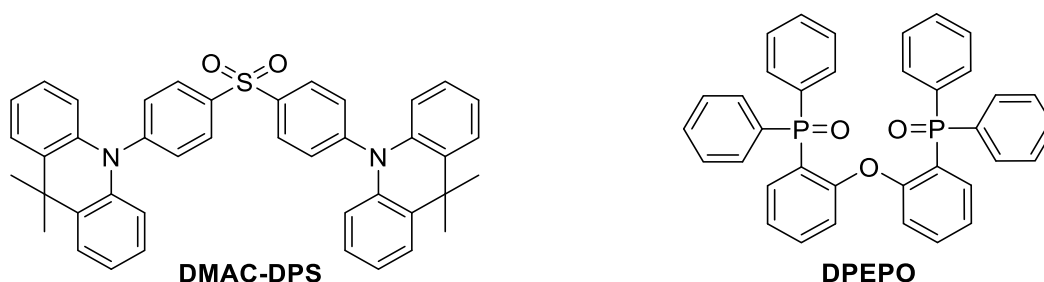


Figure 1.16: Molecular structure of **DMAC-DPS** and **DPEPO**.

In 2015 Kaji *et al.* reported an exceptional, purely organic electroluminescent device achieving 30% external quantum efficiency.⁴⁷ This device consists of 9-(4-(4,6-diphenyl-1,3,5-triazin-2-yl)phenyl)-N³,N³,N⁶,N⁶-tetraphenyl-9H-carbazole-3,6-diamine (**DACT-II**), Figure 1.17, which contains diphenylamino-carbazole as an electron donating unit and triphenyltriazine as an electron accepting unit. The authors claim the efficiency could be even further increased by optimising the device, in specific, the out coupling efficiency. The success of this device is due to a small energy gap between singlet and triplet, which is lower than the thermal energy at room temperature.⁴⁷ This leads to effective reverse intersystem crossing.

In principle, RISC can be accelerated via heating the device, resulting in high electroluminescence efficiency, as demonstrated by Kaji *et al.*⁴⁷ TADF emitting systems are therefore generating significant interest in the field, as they have eliminated the need for metal-complexes to achieve 100% internal quantum efficiency.

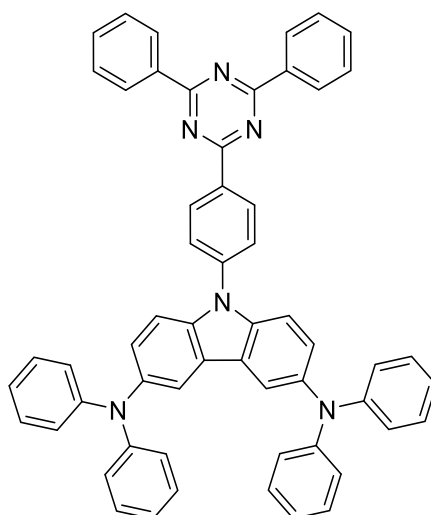


Figure 1.17: Molecular structure of **DACT-II**.

1.4 Achieving TADF using Exciplex Systems

In chemically identical organic solids which do not aggregate in the ground state, bimolecular excited states are possible due to resonance interaction of an excited molecule with a neighbouring non-excited molecule. They are known as excimers.⁴⁸ In bimolecular solids (chemically different), especially for electron donor and electron acceptor mixtures, the formation of bimolecular excited states by electron transfer from donor to acceptor is highly facilitated. This is known as exciplex,⁴⁹ Figure 1.18. An exciplex can be defined as an intermolecular charge transfer (ICT) state formed between bimolecular excited states. The bimolecular excited states can be generated in both photoluminescence and electroluminescence. This phenomenon can be observed by the comparison of emission spectra of individual donor and acceptor, where narrow and structured spectra switch to broader red-shifted spectra, Figure 1.19.

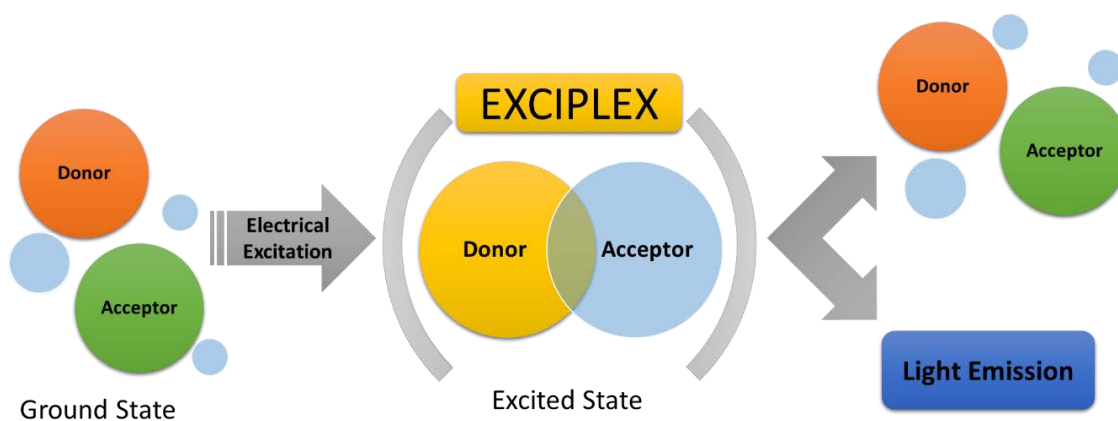


Figure 1.18: Figure to depict an exciplex between donor and acceptor molecules, forming a bi-molecular excited state, followed by relaxation of *D/A* to ground state and light emission.

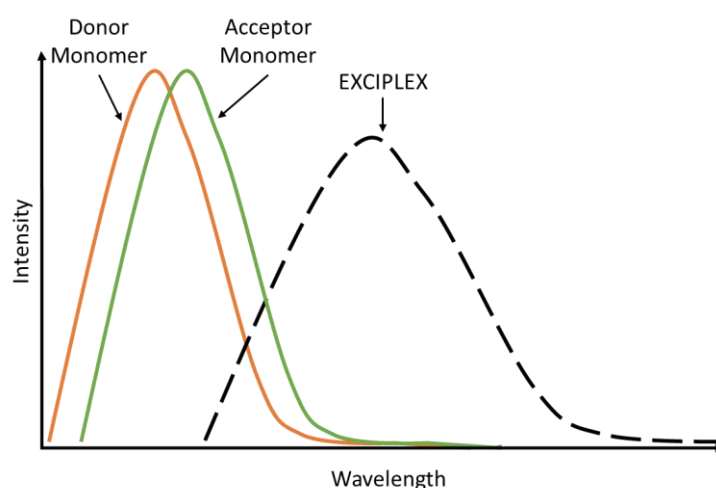


Figure 1.19: Figure to show the differences between monomer emission and exciplex emission.

Exciplex emissions were first reported in the early days of OLED research, however, at that time they were considered as a drawback.⁴⁸ This earlier work focused on exciplexes formed unintentionally at the interface between the electron/hole transport layer and emitting layer. As such, they were considered to be responsible for a reduction in device performance.

The first report of an interfacial exciplex was published in 1998 by Itano *et al.*,⁵⁰ followed by a blended exciplex device by Cocchi *et al.*⁵¹ The device by Cocchi *et al.* was inefficient as the emitter molecules (**m-MTDATA** and **PBD**, Figure 1.20) were immersed in a polycarbonate matrix, leading to low photoluminescence quantum yield (17%). In 2003, Palilis *et al.* were the first to obtain a true blue (476nm) exciplex device with a reasonable photoluminescence

quantum yield of 62%. Employing **PPSPP** (Figure 1.20) and **NPB** (Figure 1.21), they demonstrated an external quantum efficiency of 3.4%.⁵²

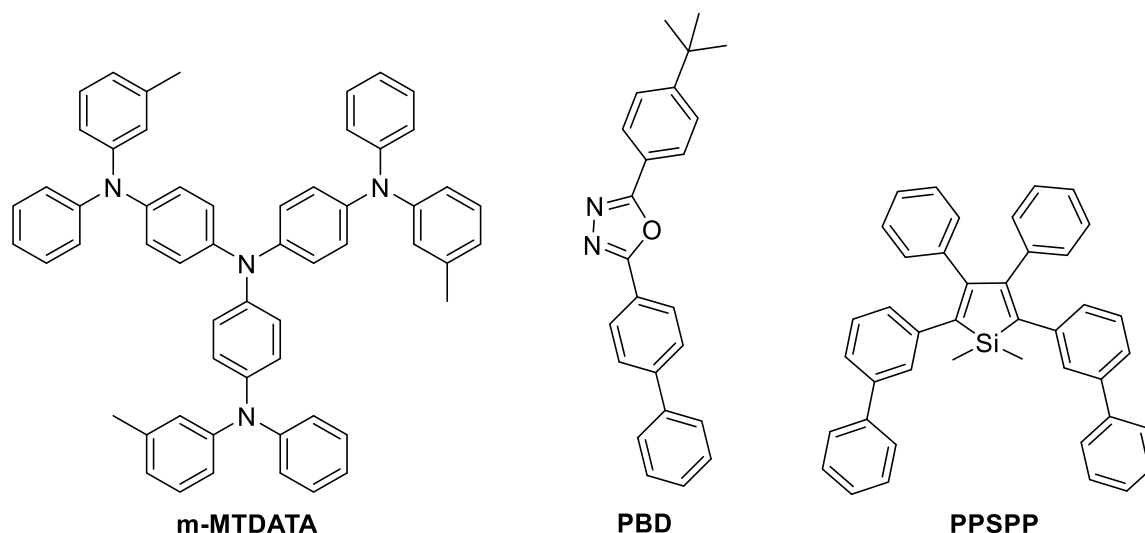


Figure 1.20: Molecular structure of **m-MTDATA**, **PBD** and **PPSPP**.

TADF emission was thought to be an inefficient process as most materials require significant energy for electron exchange (i.e. triplet to singlet). Cocchi *et al.* were the first to discuss the possibility of exciplex systems requiring small exchange energies. However, their system consisted of **TPD: BCP** (Figure 1.21) in a polycarbonate matrix, which had a large singlet-triplet energy gap of 0.4eV.⁵³ In 2008, Frederichs and Staerk were the first to demonstrate experimentally, the claim that some exciplex systems could exhibit small electron exchange energies (0.1eV).⁵⁴ They were also able to illustrate thermally assisted reverse intersystem crossing from an exciplex triplet state to singlet state using the same exciplex system of N,N-diethylaniline (**DEA**) and 1,4-dicyanobenzene (**DCNB**), Figure 1.21.

The first intentional exciplex based device giving rise to thermally activated delayed fluorescence was pioneered by Goushi *et al.*, in 2012.⁵⁵ The exciplex system utilised donor compound **m-MTDATA** (Figure 1.20) and **3TPYMB** (Figure 1.21) as an acceptor compound. The 50:50 blend of these compounds afforded them an OLED device with an EQE of up to 5.4%. Of

interest is the fact that the device has an extremely simple architecture, consisting of only three organic layers; **m-MTDATA** (HTL), **m-MTDATA: 3TPYMB** emitting layer and **3TPYMB** (ETL).⁵⁵ This simplified device architecture led to low working voltages ($\approx 2.5\text{V}$), thus improved power efficiency. The reason for this phenomenon is the ability to inject electron and hole directly into the exciplex, which was first demonstrated by Morteani *et al.*⁵⁶ Another explanation is the minimal voltage drop through the layers, for the electron and hole to meet at the emitting layer. Following this success, Goushi and Adachi reported a green exciplex device with simple architecture using **m-MTDATA** (Figure 1.20) and **PPT** (Figure 1.21), resulting in EQE of up to 10%.⁵⁷

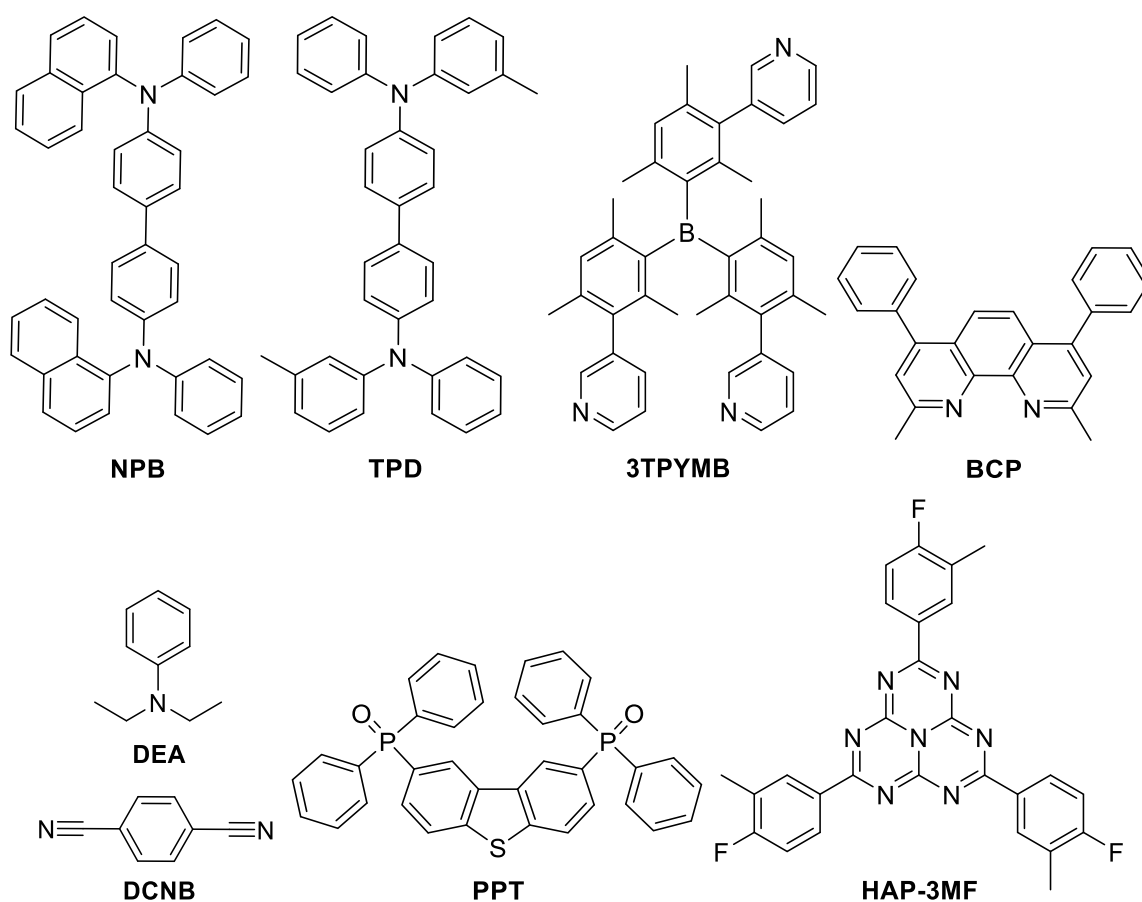


Figure 1.21: Figure to show structures of **NPB**, **TPD**, **3TPYMB**, **BCP**, **DEA**, **DCNB**, **PPT** and **HAP-3MF**.

Two years on from Goushi and Adachi's work, limited improvements were made, despite the progress in reverse intersystem crossing efficiency. Li *et al.* reported an exciplex device with an

EQE of 11.3%, using **MCP** (Figure 1.11) and **HAP-3MF** (Figure 1.21). This is much below the theoretical EQE of 12.1 – 18.1%, calculated by the group, taking into account the TADF mechanism. Due to the limited number of advances in the field Liu *et al.* explored three exciplex based systems, one of which utilised **TAPC:DPTPCz** (Figure 1.22), and resulted in an EQE of 15.4%. This is the highest performing exciplex based device reported.

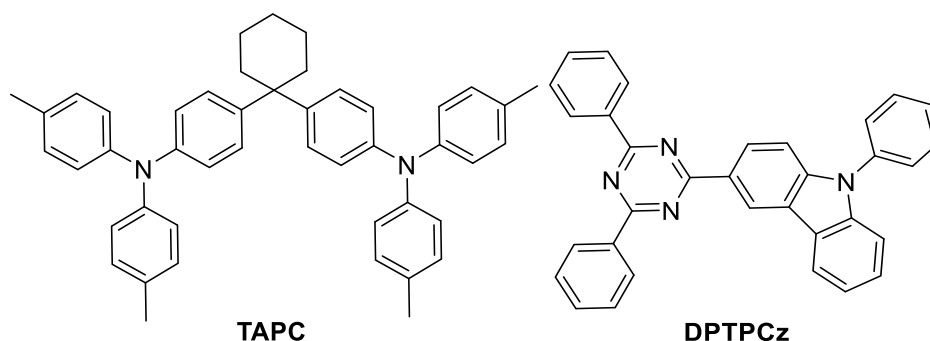


Figure 1.22: Molecular structure of **TAPC** and **DPTPCz**.

The lack of complete understanding in formation of exciplexes recently motivated Santos, Dias and Monkman to investigate exciplex systems which are able to emit via the TADF pathway.⁵⁸ In this research paper they report and compare a set of 17 exciplex systems emitting via the TADF mechanism, in order to identify key characteristics required to design exciplex emitters. In the study they compare HOMO, LUMO, the difference between the HOMO of **D** and **A** molecules, the difference between the LUMO of **D** and **A**, singlet, triplet and ΔE_{ST} . Their study illustrated no evidence of any correlation for the H-H or L-L values and exciplex formation, however, they conclude that these values might influence the rate of charge transfer. Analysing the ΔE_{ST} values, the study shows that they are able to estimate which pair of molecules are likely to yield TADF emission. They conclude that small values for ΔE_{ST} are preferable for efficient exciplex emitters, as this prevents highly populated triplet states giving rise to emission quenching via TTA. However, this is not an essential criterion to achieve TADF. One example for this phenomenon is the comparison of device performance reported by Chen *et*

al., who compared **m-MTDATA:TPBI** (Figure 1.23) and **m-MTDATA:BCP** (Figure 1.21).⁵⁹ The device using **m-MTDATA:TPBI** shows a better performance when compared to **m-MTDATA:BCP**. The reason for this improved performance is associated with a large exciplex bandgap (which is the energy difference between the LUMO of **D** and the HOMO of **A**) and it is also possible to correlate this performance difference in terms of ΔE_{ST} . The smaller ΔE_{ST} leads to favourable TADF and subsequently enhanced performance in comparison to **m-MTDATA:BCP**.

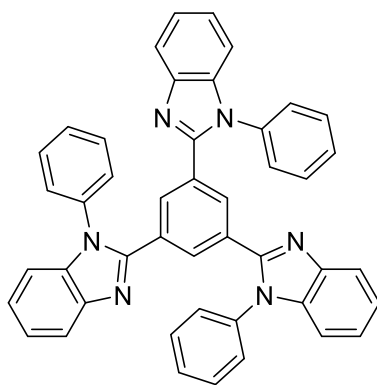


Figure 1.23: Molecular structure of **TPBI**.

1.5 Thesis Motivation and Scope

Despite the on-going research into blue phosphorescent materials, the design of highly efficient true blue emitter remains a challenge. Even if phosphorescent materials achieve authentic blue colour, their long term efficiency and stability is still questionable. Thus, the use of purely organic compounds emitting at 450 nm (true blue), solves the stability issues. Subsequently, our objective is to synthesise stable metal-free fluorescent emitters.

As outlined previously, very little is understood about exciplex systems. Most of the improvements made are based upon a trial and error, which is a time consuming process. Although attempts to understand exciplex system formation have been made, unfortunately, there remains very limited knowledge in this field. As materials for exciplex systems are limited,

the task of material synthesis has been undertaken. In this thesis we aim to introduce systematic structural variation and to further the knowledge regarding exciplex formation and emission.

The overall ambition of this thesis is to synthesise materials for blue exciplex devices emitting via thermally activated delayed fluorescence. In order to successfully design materials, the following parameters were taken into consideration:

- I. The donor must possess high hole mobility.
- II. The acceptor must possess high electron mobility.
- III. The triplet energies of donor and acceptor need to be high, to eliminate TTA.

1.6 References

- 1 T. A. Edison, *Pat. US223898 A*, 1880, 1–14.
- 2 R. V. Steele, *Nat. Photon.*, 2007, **1**, 25.
- 3 H. Akamatu, H. Inokuchi and Y. Matsunaga, *Nature*, 1954, **173**, 168.
- 4 A. Bernanose, *Br. J. Appl. Phys.*, 1955, **6**, S54.
- 5 Nobel Prize in Chemistry 2000,
http://www.nobelprize.org/nobel_prizes/chemistry/laureates/2000/, Accessed on 02/11/2016.
- 6 Nobel Prize in Physics 2014,
http://www.nobelprize.org/nobel_prizes/physics/laureates/2014/, Accessed on 03/11/2016.

- 7 K. Hong and J.-L. Lee, *Electron. Mater. Lett.*, 2011, **7**, 77.
- 8 4k.com, <http://4k.com/tv/lg-e6-signature-oled-4k-hdr-ultra-hd-tv-review-oled65e6p-oled55e6p/>, Accessed on 06/11/2016.
- 9 M. Pope, H. P. Kallmann and P. Magnante, *J. Chem. Phys.*, 1963, **38**, 2042.
- 10 P. S. Vincett, W. A. Barlow, R. A. Hann and G. G. Roberts, *Thin Solid Films*, 1982, **94**, 171.
- 11 R. H. Partridge, *Polymer (Guildf.)*, 1983, **24**, 748.
- 12 C. W. Tang and S. A. VanSlyke, *Appl. Phys. Lett.*, 1987, **51**, 913.
- 13 J. Kido, M. Kimura and K. Nagai, *Science*, 1995, **267**, 1332.
- 14 G. He, S. Murano, A. Werner and S. I. D. Member, *J. Soc. Inf. Disp.*, 2009, **2008**, 159.
- 15 M. C. Gather, A. Köhnen and K. Meerholz, *Adv. Mater.*, 2011, **23**, 233.
- 16 C. Murawski, K. Leo and M. C. Gather, *Adv. Mater.*, 2013, **25**, 6801.
- 17 T. V Pho, P. Zalar, A. Garcia, T.-Q. Nguyen and F. Wudl, *Chem. Commun.*, 2010, **46**, 8210.
- 18 H. Yersin, A. F. Rausch, R. Czerwieniec, T. Hofbeck and T. Fischer, *Coord. Chem. Rev.*, 2011, **255**, 2622.
- 19 M. A. Baldo, D. F. O'Brien, Y. You, A. Shoustikov, S. Sibley, M. E. Thompson and S. R. Forrest, *Nature*, 1998, **395**, 151.
- 20 F. De Angelis, S. Fantacci, N. Evans, C. Klein, S. M. Zakeeruddin, J.-E. Moser, K. Kalyanasundaram, H. J. Bolink, M. Grätzel and M. K. Nazeeruddin, *Inorg. Chem.*, 2007,

- 46**, 5989.
- 21 Y. You and S. Y. Park, *Dalt. Trans.*, 2009, **9226**, 1267.
 - 22 J. K. Yu, Y. H. Hu, Y. M. Cheng, P. T. Chou, S. M. Peng, G. H. Lee, A. J. Carty, Y. L. Tung, S. W. Lee, Y. Chi and C. S. Liu, *Chem. - A Eur. J.*, 2004, **10**, 6255.
 - 23 R. C. Evans, P. Douglas and C. J. Winscom, *Coord. Chem. Rev.*, 2006, **250**, 2093.
 - 24 V. Sivasubramaniam, F. Brodkorb, S. Hanning, H. P. Loeb, V. van Elsbergen, H. Boerner, U. Scherf and M. Kreyenschmidt, *J. Fluor. Chem.*, 2009, **130**, 640.
 - 25 S. O. Jeon and J. Y. Lee, *J. Mater. Chem.*, 2012, **22**, 4233.
 - 26 W.-Y. Wong and C.-L. Ho, *J. Mater. Chem.*, 2009, **19**, 4457.
 - 27 P.-T. Chou and Y. Chi, *Chemistry*, 2007, **13**, 380.
 - 28 G. Zhou, W.-Y. Wong and X. Yang, *Chem. Asian J.*, 2011, **6**, 1706.
 - 29 L. Xiao, Z. Chen, B. Qu, J. Luo, S. Kong, Q. Gong and J. Kido, *Adv. Mater.*, 2011, **23**, 926.
 - 30 Y. Chi and P.-T. Chou, *Chem. Soc. Rev.*, 2010, **39**, 638.
 - 31 Y.-S. Yeh, Y.-M. Cheng, P.-T. Chou, G.-H. Lee, C.-H. Yang, Y. Chi, C.-F. Shu and C.-H. Wang, *Chemphyschem*, 2006, **7**, 2294.
 - 32 S. Haneder, E. Da Como, J. Feldmann, J. M. Lupton, C. Lennartz, P. Erk, E. Fuchs, O. Molt, I. Münster, C. Schildknecht and G. Wagenblast, *Adv. Mater.*, 2008, **20**, 3325.
 - 33 C. A. Parker and C. G. Hatchard, *Proc. Chem. Soc. London*, 1962, 386.
 - 34 A. Köhler and H. Bässler, *Mater. Sci. Eng. R Reports*, 2009, **66**, 71.
 - 35 J. Jortner, S. I. Choi, J. L. Katz and S. A. Rice, *Phys. Rev. Lett.*, 1963, **11**, 323.

- 36 R. E. Merrifield, *Pure Appl. Chem.*, 1971, **27**, 481.
- 37 D. Y. Kondakov, T. D. Pawlik, T. K. Hatwar and J. P. Spindler, *J. Appl. Phys.*, 2009, **106**, 124510.
- 38 S. M. King, M. Cass, M. Pintani, C. Coward, F. B. Dias, A. P. Monkman and M. Roberts, *J. Appl. Phys.*, 2011, **109**, 74502.
- 39 F. Perrin, *Ann. Phys. (N. Y.)*, 1929, **12**, 169.
- 40 G. N. Lewis and M. Kasha, 1944, **66**, 2100.
- 41 J. C. Deaton, S. C. Switalski, D. Y. Kondakov, R. H. Young, T. D. Pawlik, D. J. Giesen, S. B. Harkins, A. J. M. Miller, S. F. Mickenberg and J. C. Peters, *J. Am. Chem. Soc.*, 2010, **2**, 9499.
- 42 A. Endo, M. Ogasawara, A. Takahashi, D. Yokoyama, Y. Kato and C. Adachi, *Adv. Mater.*, 2009, **21**, 4802.
- 43 A. Endo, K. Sato, K. Yoshimura, T. Kai, A. Kawada, H. Miyazaki and C. Adachi, *Appl. Phys. Lett.*, 2011, **98**, 83302.
- 44 H. Uoyama, K. Goushi, K. Shizu, H. Nomura and C. Adachi, *Nature*, 2012, **492**, 234.
- 45 T. Nakagawa, S.-Y. Ku, K.-T. Wong, C. Adachi, C. W. Tang, S. A. VanSlyke, S. Reineke, F. Lindner, G. Schwartz, N. Seidler, K. Walzer, B. Lussem, K. Leo, C. Adachi, M. A. Baldo, M. E. Thompson, S. R. Forrest, D. F. O'Brien, M. A. Baldo, M. E. Thompson, S. R. Forrest, C. T. Brown, D. J. Kondakov, D. Kondakov, T. D. Pawlik, T. K. Hatwer, J. P. Spindler, A. Endo, M. Ogasawara, A. Takahashi, D. Yokoyama, Y. Kato, C. Adachi, M. N. Berberan-Santos, J. M. M. Garcia, J. C. Deaton, S. C. Switalski, D. Y. Kondakov, R. H. Young, T. D.

- Pawlik, D. J. Giesen, S. B. Harkins, A. J. M. Miller, S. F. Mickenberg, J. C. Peters, R. Czerwienic, J. Yu, H. Yersin, T.-C. Chao, Y.-T. Lin, C.-Y. Yang, T. S. Hung, H.-C. Chou, C.-C. Wu, K.-T. Wong, Y. Wu, J. Li, Y. Fu, Z. Bo, C.-L. Chiang, M.-F. Wu, D.-C. Dai, Y.-S. Wen, J.-K. Wang, J. Luo, Y. Zhou, Z.-Q. Niu, Q.-F. Zhou, Y. Ma, J. Pei, Y. T. Lee, C.-L. Chiang, C.-T. Chen, W.-Y. Hung, T.-C. Tsai, S.-Y. Ku, L.-C. Chi, K.-T. Wong, Z. Jiang, H. Yao, Z. Zhang, C. Yang, Z. Liu, Y. Tao, J. Qin, D. Ma, Y.-Y. Lyu, J. Kwak, W. S. Jeon, Y. Byun, H. S. Lee, D. Kim, C. Lee, K. Char, A. Endo, K. Sato, K. Yoshimura, T. Kai, A. Kawada, H. Miyazaki, C. Adachi, C. Ganzorig, M. Fujihira, L. Zhang, S. Hu, J. Chen, Z. Chen, H. Wu, J. Peng, Y. Cao, H. Wu, G. Zhou, J. Zou, C.-L. Ho, W.-Y. Wong, W. Yang, J. Peng and Y. Cao, *Chem. Commun.*, 2012, **48**, 9580.
- 46 Q. Zhang, B. Li, S. Huang, H. Nomura, H. Tanaka and C. Adachi, *Nat. Photonics*, 2014, **8**, 326.
- 47 H. Kaji, H. Suzuki, T. Fukushima, K. Shizu, K. Suzuki, S. Kubo, T. Komino, H. Oiwa, F. Suzuki, A. Wakamiya, Y. Murata and C. Adachi, *Nat. Commun.*, 2015, **6**, 8476.
- 48 S. A. Jenekhe and J. A. Osaheni, *Science*, 1994, **265**, 765.
- 49 J. Kalinowski, *Mater. Sci. Pol.*, 2009, **27**.
- 50 K. Itano, H. Ogawa and Y. Shirota, *Appl. Phys. Lett.*, 1998, **72**, 636.
- 51 M. Cocchi, D. Virgili, G. Giro, V. Fattori, P. Di Marco, J. Kalinowski and Y. Shirota, *Appl. Phys. Lett.*, 2002, **80**, 2401.
- 52 L. C. Palilis, a. J. Mäkinen, M. Uchida and Z. H. Kafafi, *Appl. Phys. Lett.*, 2003, **82**, 2209.
- 53 M. Cocchi, D. Virgili, C. Sabatini and J. Kalinowski, *Chem. Phys. Lett.*, 2006, **421**, 351.

- 54 B. Frederichs and H. Staerk, *Chem. Phys. Lett.*, 2008, **460**, 116.
- 55 K. Goushi, K. Yoshida, K. Sato and C. Adachi, *Nat. Photonics*, 2012, **6**, 253.
- 56 A. C. Morteani, A. S. Dhoot, J.-S. Kim, C. Silva, N. C. Greenham, C. Murphy, E. Moons, S. Ciná, J. H. Burroughes and R. H. Friend, *Adv. Mater.*, 2003, **15**, 1708.
- 57 K. Goushi and C. Adachi, *Appl. Phys. Lett.*, 2012, **101**, 23306.
- 58 P. L. Dos Santos, F. B. Dias and A. P. Monkman, *J. Phys. Chem. C*, 2016, **120**, 18259.
- 59 P. Chen, Q. Peng, L. Yao, N. Gao and F. Li, *Appl. Phys. Lett.*, 2013, **102**.

2 SYNTHESIS AND ANALYSIS OF 1, 3-DI (9*H*- CARBAZOL-9-YL) BENZENE DERIVATIVES

2.1 Introduction

Carbazole derivatives have been widely used in small molecule,¹ polymer² and phosphorescent³ OLED devices. Carbazole is a heterocyclic aromatic compound consisting of a central five-membered ring fused with benzene on either side (Figure 2.1). Carbazole derivatives have been used in the emitting layer of an OLED devices because they are thermally stable and have the ability to emit blue light via photoluminescence and electroluminescence.⁴ However, carbazole derivatives are much more widely known for their use in the hole-transport layer, utilising their high charge mobility. An example of this is 1,3-di(9H-carbazol-9-yl)benzene (**MCP**, Figure 24), which is utilised as a blue host material in phosphorescent OLEDs. **MCP** exhibits a high triplet energy of 2.9 eV and good hole mobility,⁵ which is an essential starting point for the purpose of this thesis.

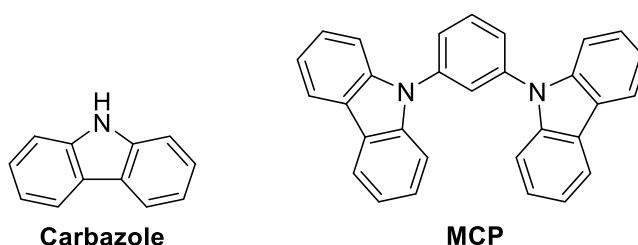


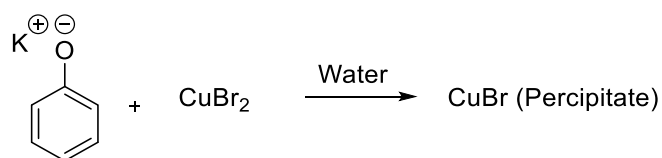
Figure 2.1: Molecular structure of carbazole and **MCP**.

The hypothesis is that by structural variation we will be able to achieve control over exciplex formation and emission. To achieve this, the structure of **MCP** will be systematically modified. The aim will be to retain the *meta*-substitution on the central phenyl ring, as this is essential to obtain high triplet energy. We aim to fine tune the HOMO/LUMO of **MCP** which will be altered through substitution on the central phenyl. The central phenyl ring will be substituted with both electron withdrawing and electron donating functional groups. Subsequently, photo-

physical analysis of **MCP** derivatives will be performed. The aim of the research is to study the effect that different substituents, have on emission and exciplex formation.

2.2 Results and Discussion

N-(Hetero)arylazoles have been conventionally synthesised via the Ullmann reaction.⁶ Typical Ullmann reaction conditions involve the use of copper compounds as catalysts along with base and a polar solvent.⁷ Fritz Ullmann discovered copper compounds were able to catalyse the formation of bi-aryl compounds through coupling of two aryl halides in 1901.⁶ After a couple of years the same methodology was applied by F. Ullmann to synthesise *N*-aryl amines in 1903.⁸ Since this early discovery scientists were unsure which copper species was responsible for catalysis. Thus, many different copper sources (Cu(0), Cu(I) and Cu(II)) were explored. These studies concluded that both copper salts and copper oxides performed particularly well in the process of arylation.⁹ Subsequently, this suggested a common copper species may be formed during the reaction from different sources. In 1964, Weingarten suggested Cu(I) could be the common species, as Cu(I) seemed to yield higher reaction rates.¹⁰ It was later demonstrated by Weingarten that Cu(II) could be reduced to Cu(I), Scheme 2.1.



Scheme 2.1: Scheme to show the reduction of Cu (II) to Cu (I) as demonstrated by Weingarten.

Despite the early impressive examples and further advances in copper mediated chemistry, the Ullmann reaction remains limited and requires harsh reaction conditions, i.e. high temperature, strong base, long reaction time and stoichiometric amounts of copper catalyst.

This complicates the reaction work up and product purification. The reaction also remains restricted to substrates with high reactivity such as aryl bromides/iodides and requires high boiling solvents. Furthermore, copper mediated coupling reactions are still considered unpredictable.⁷

An alternative to the Ullmann reaction was developed in the 1990s by Buchwald¹¹ and Hartwig¹², now known as the Buchwald-Hartwig cross coupling. The palladium mediated reaction was a major breakthrough in formation of C-N cross coupling. Typical Buchwald-Hartwig reaction conditions involve the use of aryl halides, palladium catalyst, phosphine ligand, base and a fairly non-polar solvent can be utilised. Aryl bromides are most frequently used as substrates for the coupling of primary and secondary amines,¹³ however, reactions are able to proceed reasonably well with aryl chlorides. Unlike Ullmann method, the Buchwald-Hartwig cross coupling is able to utilise substrates with both electron-donating and electron-withdrawing characteristics.¹³ Although palladium is more expensive and more toxic than copper, the catalyst loading (0.1-5 mol%) is significantly lower the reaction times are reduced. Overall the Buchwald-Hartwig reaction provides significant advantages over the Ullmann reaction, including milder reaction conditions and the ability to use a wider range of substrates.

In this chapter 1,3-di(9*H*-carbazole-9-yl)benzene derivatives will be synthesised and characterised. First, substitution at position five of the central benzene ring is performed, as shown in Figure 2.2 (**R**¹). Both the Ullman conditions and Buchwald-Hartwig reaction conditions were utilised to achieve the target compounds. Subsequently, we substitute the hydrogen at position five and ten on the carbazole moiety of **MCP**, Figure 2.2 (**R**₁).

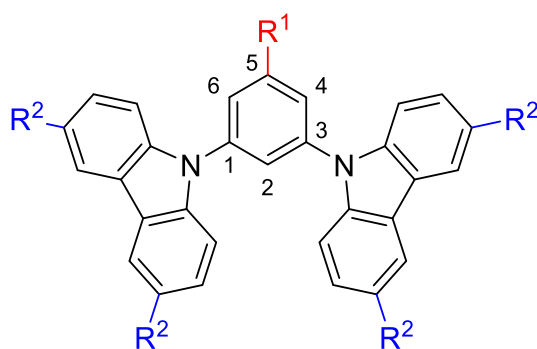


Figure 2.2: The structural variation of 1,3-di(9*H*-carbazole-9-yl)benzene.

2.2.1 Synthesis of 1,3-Di(9*H*-carbazole-9-yl)benzene derivatives via the Ullmann Reaction

Researching the reaction conditions to synthesise **MCP** from SciFinder only six experimental procedures were found, two of which utilise Buchwald-Hartwig conditions. The most reported method to synthesise **MCP** is using Ullmann reaction conditions.^{14, 15, 16} From the four reported reaction conditions, three were very similar using 1,3-dibromobenzene, 1,4,7,10,13,16-hexaoxacyclooctadecane (18-crown-6), copper iodide (CuI), potassium carbonate (K₂CO₃) and polar high boiling solvent, achieving a yield of $\leq 55\%$. The other reported reaction condition utilised copper sulphate (CuSO₄) as the catalyst. As discussed previously, copper (I) is required to catalyse the reaction, thus, this reaction condition was neglected due to the use of copper (II). With the aim of reducing reaction time and enhancing yield, the base was changed from potassium carbonate to potassium *tert*-butoxide (KO^{*t*}Bu). However, this change did not have the desired effect as the reaction did not proceed as expected and all starting materials were retrieved, Table 2.1, Entry 1.

In search for an efficient synthetic route to **MCP**, other Ullmann reaction conditions were considered. Due to the limited number of synthetic procedures available for **MCP**, we adapted

the synthetic route available for mono-**MCP**. The reported reaction conditions for mono-**MCP** utilised dimethylformamide (DMF), K₂CO₃ and CuI, Table 2.1 Entry 2. Even after small adaptations, the reaction conditions yielded a favoured formation of the mono-**MCP**.

Subsequently, the reaction conditions were further optimised to enhance the yield for bis-**MCP**. As illustrated in Table 2.1, an attempt was made to optimise the reaction conditions to afford **MCP**, Entries 2 & 3, with some success. DMF was then replaced with dimethylacetamide (DMAc) to access higher reaction temperature. Accordingly, the catalyst loading and base quantity were increased, resulting in Bis-**MCP** with a yield of 63% (Table 2.1, Entry 4).

Table 2.1: Synthetic route to **MCP**. All reactions were performed under argon atmosphere for 24 hours. Yields obtained after purification. ^a Starting materials fully recovered.

Reaction scheme: 1,3-dibromobenzene (1 eq.) + carbazole (2.2 eq.) $\xrightarrow[\text{Base, T, 24H}]{\text{Catalyst, Solvent}}$ Mono-**MCP** + Bis-**MCP**

Entry	Catalyst	Solvent	Base	T(°C)	Yield (%) Mono/Bis
1	Dibenzo-18-crown-6 (0.2eq.)/ CuI (4eq.)	DMF	KO ^t Bu (8eq.)	155	0/0 ^a
2	CuI (2.3 eq.)	DMF	K ₂ CO ₃ (3 eq.)	155	58/7
3	CuI (2.3 eq.)	DMF	K ₂ CO ₃ (6 eq.)	155	50/14
4	CuI (2.8 eq.)	DMAc	K ₂ CO ₃ (7 eq.)	165	11/63
Method 1					

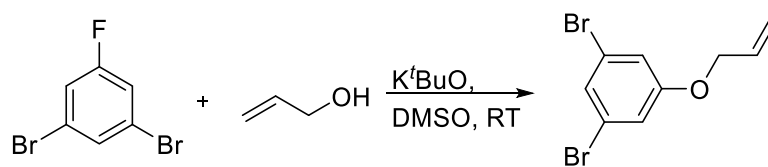
The reaction conditions of **Method 1** were applied to different starting substrates to afford **MCP** derivative, Table 2.2. We were able to synthesise 9, 9'-(5-methyl-1,3-phenylene)bis(9H-carbazole)(**ME-MCP**, **2**), Table 2.2, Entry 2. While attempting to synthesise fluorine-**MCP** using 1, 3-dibromo-5-fluorobenzene, we surprisingly synthesised 1, 3, 5-tri(9H-carbazol-9-yl)benzene (**TCP**, **3**), Table 2.2, Entry 3.

Table 2.2: **MCP** derivative synthesis via **Method 1**. Reactions performed under argon atmosphere using aryl halide (1 eq.), carbazole (2.2 eq.), CuI (2.8 eq.) and K₂CO₃ (7 eq.) in DMAc refluxed at 165°C. Yields were calculated after purification.

R: H, Me, Carbazole

Entry	Starting Substrate	Code Name	Structure	Yield (%)
1		MCP (1)		63
2		ME-MCP (2)		59
3		TCP (3)		20

Usually fluorine is considered to be un-reactive under Ullmann conditions. However, in this case, the aromatic ring is activated by the two bromines. Inspecting this phenomenon in the literature resulted in one comparable example where the aromatic ring is activated by two bromine atoms (Scheme 2.2).¹⁷ Fluorine is the most electronegative element and the carbon-fluorine is the strongest bond in organic chemistry (bond dissociation energy C-H: 98.8 kcal mol⁻¹ and C-F: 105.4 kcal mol⁻¹).¹⁸ Thus, the cleavage of C-F bonds usually requires harsh reaction conditions.¹⁹ However, in this case the aromatic ring is activated leading to the C-N cross coupling.



Scheme 1.2: Example to show the activation of fluorine.

The scope of **Method 1** was then put to the test by substituting 1,3-dibromobenzene with 1,3-dichlorobenzene. However, the reaction did not progress and all the starting materials were retrieved. 1,3-dibromobenzene was also substituted with 3,5-dibromoanisole and 3,5-dichlorobenzotrifluoride which yielded no product.

In summary, **MCP** synthesis via the Ullmann reaction requires the use of large amounts of CuI catalyst in the presence of a large quantity of base and a polar high boiling solvent. In addition to this, the reaction also suffers from long reaction times, taking over 24 hours to achieve reasonable yield. All of these issues combined lead to further problems in reaction work-up and compound purification. In spite of harsh reaction conditions, the reaction still remains limited to aryl-bromide/iodide. Inspecting the mechanism of the reaction (Figure 2.3), key issues can be identified. Firstly, copper is able undergo four oxidation states 0-3+, but only utilises 1+/2+ oxidation states. Regenerating the copper catalyst through reductive elimination may bear bromine rather than the initial iodide. This may eventually lead to deactivation of the copper catalyst altogether, thus resulting in poor yields.

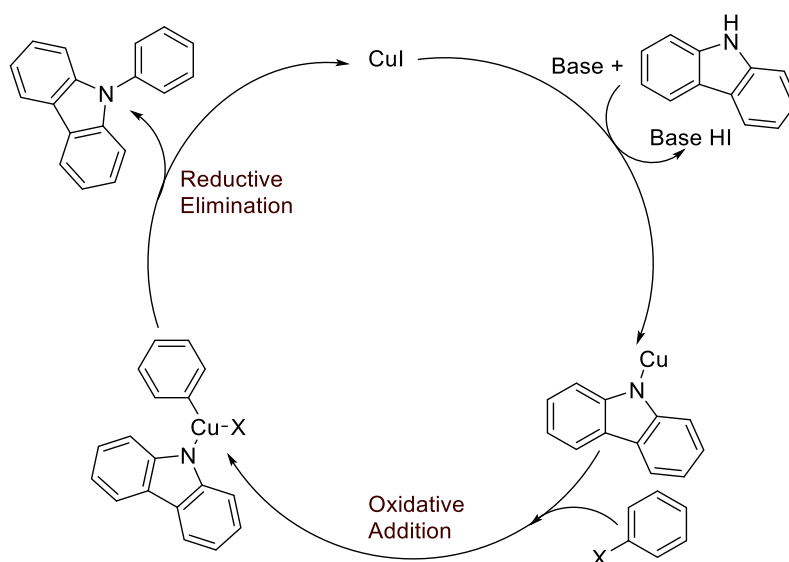


Figure 2.3: Mechanism of Ullmann reaction.

2.2.2 Synthesis of 1, 3-Di(9*H*-carbazole-9-yl)benzene derivatives via the Buchwald-Hartwig Reaction

The Pd-catalysed Buchwald-Hartwig cross coupling of amines and aryl halides to form C-N bonds was a major breakthrough in the preparation of aromatic amines. This process has been highly applicable in numerous industries such as pharmaceuticals, natural products and organic materials. Thus, the development process has been increasing exponentially. The continuous improvements in ligands and catalysts has led to reliable reaction protocols.²⁰ Three families of phosphine ligands have emerged. Typically, these ligands bear an alkyl group, aryl group or both. Despite the fact that monodentate phosphine ligands can be used, bidentate ligands are more widely utilised. One of the common examples of chelating phosphine is BINAP (Figure 2.4) used in *N*-arylation. Additional bidentate ligands such as DPPF (Figure 2.4) and DTBPF (Figure 2.4) are also often used as supporting ligands.^{13,21} Another class of commonly employed ligands are the biaryldialkylphosphines or arylphosphinepyrrole ligands,^{22,23} such as BippyPhos (Figure 2.4), which have been used in Pd-catalysed C-N cross coupling.²⁰

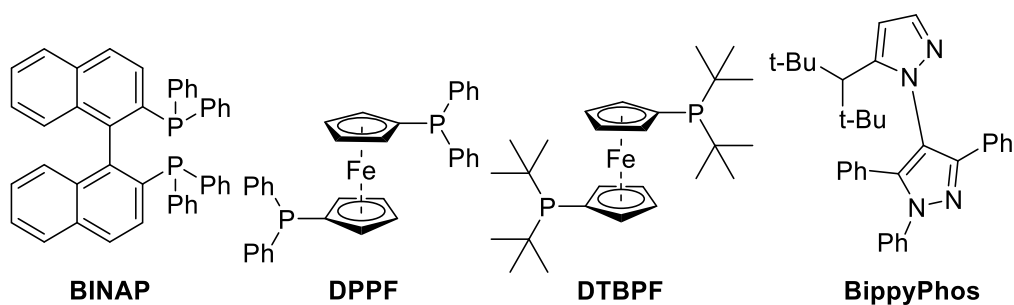


Figure 2.4: Molecular structure of BINAP, DPPF, DTBPF and BippyPhos.

Another area of substantial progress was the development of a pre-catalyst for the quick generation of an active catalyst in the reaction mixture.²⁴ A variety of π -allyl palladium complexes,²⁵ palladacycles²⁶ and pyridine-containing palladium complexes²⁷ rapidly activate under the commonly used reaction conditions to release active catalytic species (Figure 2.5). In comparison to the traditional process involving the separate addition of ligand and palladium precursor, pre-catalysts simplify the reaction setup and, in some cases, allow lower catalyst loading and lower temperatures to be employed. These air stable compounds form the active catalyst upon exposure to base. Since the discovery of pre-catalysts, steady improvements have been made.²⁸ Until now, base-activated pre-catalysts have accomplished the greatest success in the application of C-N cross coupling.

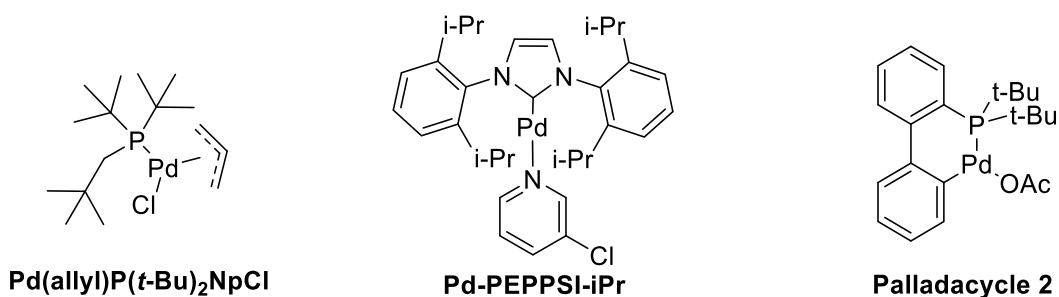


Figure 2.5: Examples of pre-catalysts.

In the search for a synthetic method to obtain **MCP** derivatives using aryl chlorides, we applied a couple of well-established catalytic systems. The use of dialkylbiarylphosphines based ligand, 2-dicyclohexylphosphino-2',4',6'-triisopropylbiphenyl (**XPhos**) with palladium acetate

(Pd(OAc)₂), Figure 2.6, resulted in trace amounts of desired product. The XPhos/Pd(OAc)₂ system has been widely reported in the literature with exceptional yields, in particular for coupling primary alkylamines/arylamines, and has also been reported to be utilised in the coupling of secondary aryl amines. Varieties of dialkylbiarylphosphines (“Phos”) ligands have been widely reported to catalyse the C-N cross coupling, one of the most studied being XPhos. These “Phos” ligands have the core diphenyl in common as illustrated in Figure 2.6. Indeed there are many more “Phos” ligands with much more complicated structural variations. However, we were unable to identify the exact cause of poor catalytic activity. We assume it could be due to steric hindrance as the cyclohexane attached to phosphine could be preventing carbazole from accessing the catalytic active site.

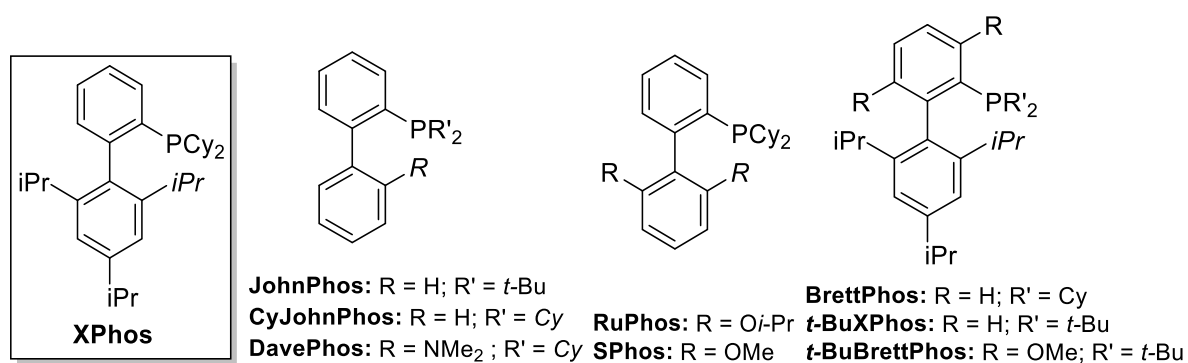


Figure 2.6: Structure of XPhos and examples of dialkylbiarylphosphines “Phos” ligands.

In pursuit of a catalytic system to synthesise **MCP**, we investigated the possibility of using much more advanced pre-catalysts. A range of palladium complexes with *N*-heterocyclic carbene ligands have been developed for cross coupling.^{29,30} One of the catalysts which emerged to be highly active, functional group tolerant and widely applicable is Pd-PEPPSI-IPr (Figure 2.7).³¹ In 2008, Organ *et. al.* demonstrated Pd-PEPPSI-IPr was highly effective at room temperature, coupling primary and secondary amines with aryl/alkyl chlorides.³² Commonly reported reaction conditions were employed to afford **MCP** via C-N cross coupling using aryl chloride (1 eq.), Pd-PEPPSI-IPr catalyst (3 mol%), potassium *tert*-butoxide (2.1eq.) and dimethoxy

ethane.³³ Despite the fact that this catalytic system is reported to perform carbon-nitrogen coupling using secondary aryl amines, the reaction did not proceed as anticipated.

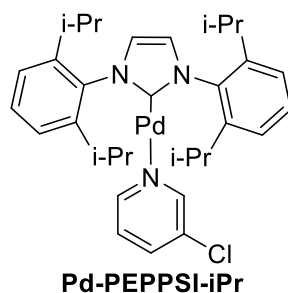


Figure 2.7: Molecular structure of Pd-PEPPSI-IPr.

Exploring the literature further, it seems that carbazole coupling with aryl halides has attracted special attention in previous years and many research groups have found it challenging to achieve reasonable yield for bis-coupling. In 1998, Hartwig's group reported the coupling reaction between carbazole and 4-cyanophenylbromide using palladium acetate along with 1,1'-ferrocenediyl-bis(diphenylphosphine) (DPPF). Watanabe *et al.* reported the synthetic procedure for coupling carbazole with bromobenzene using palladium acetate with tri-*tert*-butylphosphine. They achieved good yields using potassium carbonate and rubidium carbonate, whereas under the same reaction conditions cesium carbonate and sodium *tert*-butoxide performed poorly.

In 2008, Suzuki *et al.* published "A new hybrid Phosphine ligand for Palladium-catalysed amination of aryl halides". They specifically researched into catalysing secondary amines coupling with carbon. They described that previously successful phosphine ligands consisted of two main structural characteristics: 1) ligands having aryl groups in a fixed position by using an appropriate spacer, for example Xphos; and 2) ligands bearing *tert*-alkyl substituents, such as tri-*tert*-butylphosphine.³⁴ Thus, they designed a ligand incorporating both of these characteristics, leading to di-*tert*-butyl (2,2-diphenyl-1-methyl-1-cyclopropyl) phosphine

(cBRIDP) production. Figure 2.8 illustrates the molecular structure of cBRIDP. The ligand consists of methylcyclopropane and two *tert*-butyl moieties directly bound to phosphorus. Using cBRIDP and allylpalladium (II) chloride dimer ($[\text{PdCl}(\pi\text{-allyl})]_2$, Figure 2.8) they were able to demonstrate the enhanced efficiency of this catalytic system even with low catalyst loading of 0.1 mol%, when compared to other systems.

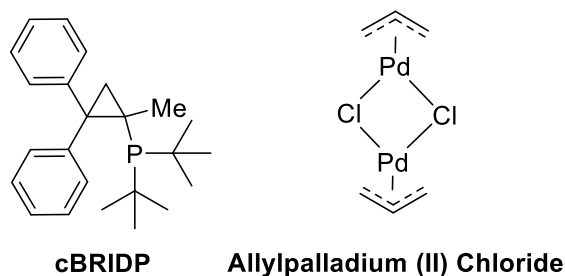
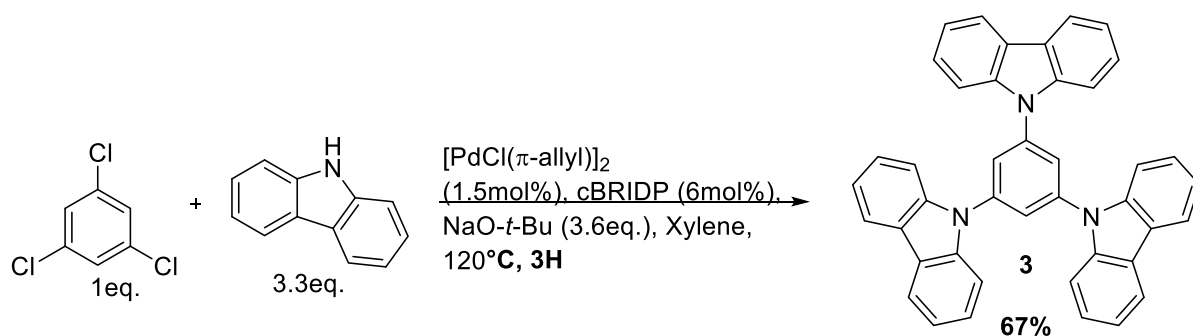


Figure 2.8: Molecular structure of cBRIDP and $[\text{PdCl}(\pi\text{-allyl})]_2$.

Most importantly, the reaction was applicable with aryl chlorides, even when aryl chlorides consisted of electron donating groups such as methoxy. Carbazole coupling was also reported in this paper, where they successfully coupled bromo/chlorobenzene to afford *N*-phenylcarbazole in excess of 90% isolated yield. One of the key aspects of this research was the synthesis of **TCP** using 1,3,5-trichlorobenzene via the synthetic procedure in Scheme 2.3, affording an isolated yield of 67%.



Scheme 2.3: Synthetic procedure to synthesise 1,3,5-tri(9H-carbazol-9-yl)benzene.

Following the success of cBRIDP, Kobayashi's research group published another paper in 2011, providing an in depth study of the application of "BRIDP" ligands.³⁵ This paper specifically

highlighted the ability of the $[\text{PdCl}(\pi\text{-allyl})]_2/\text{cBRIDP}$ (Pd/cBRIDP) catalytic system to be versatile as well as efficient. This system was not only efficient in Buchwald-Hartwig amination but also had exceptional catalytic activity for Suzuki-Miyaura coupling, Sonogashira coupling and α -arylation of ketones. In the same year, Kobayashi *et al.* also filed a patent (WO2013/032035 A1) consisting of similar synthetic procedures based on cBRIDP. However, there was one major difference in the synthetic route; rather than using sodium *tert*-butoxide, methymagnesium chloride (MeMgCl) was used as the base. This resulted in improvement of catalytic activity by up to 500 times in some cases.

Owing to the versatility and efficiency of the $\text{cBRIDP}/[\text{PdCl}(\pi\text{-allyl})]_2$ system, we chose to further explore and adapt the procedures published in the literature to afford **MCP** with electron donating and electron deficient substituents. **Method 2** was formulated for the synthesis of **MCP (1)**, 9,9'-(5-(trifluoromethyl)-1,3-phenylene)bis(9H-carbazole) (**CF3-MCP, 4**) and 9,9'-(5-methoxy-1,3-phenylene)bis(9H-carbazole) (**OME-MCP, 5**) (Table 2.3). Firstly, we altered the catalyst loading by increasing it from 0.1 mol% ($[\text{PdCl}(\pi\text{-allyl})]_2$) and 0.4 mol% (cBRIDP) ten-fold.

The original solvent system was retained which is xylene/THF, even though the reaction does work just as well using toluene/THF. An increased reaction time of 4 hours enabled us to obtain the bis-substituted **MCP** rather than the non-favoured mono-substituted **MCP** (9-phenyl-9H-carbazole). However, it is worth noting that regardless of a longer reaction time, 9-phenyl-9H-carbazole is always present upon "reaction completion". This can make purification of the final compounds difficult, with one of the most important factor in the field of electronics being the purity of compounds. As such, percentage yields were compromised in order to obtain pure

samples. Multi-step purification techniques such as column chromatography, recrystallisation and preparative thin layer chromatography were employed to produce pure samples.

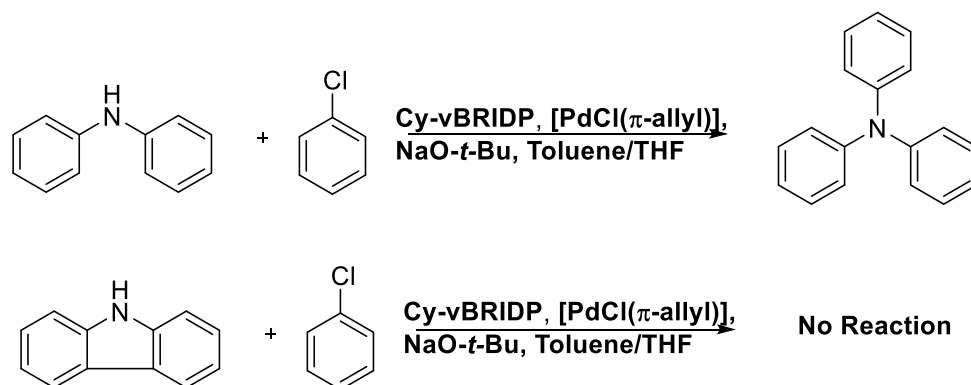
Table 2.3: The synthesis of **MCP** derivative via **Method 2**. Reactions performed under argon atmosphere using aryl halide derivatives (1 eq.), carbazole (2.2 eq.), MeMgCl (2.2 eq.), cBRIDP (5 mol%) and $[\text{PdCl}(\pi\text{-allyl})]_2$ (1 mol%) in xylene/THF at 80°C. ^a Reaction time of 6 hours. Yields were calculated after purification.

$\text{R: H, CF}_3, \text{OMe}$
 THF, MeMgCl, cBRIDP, 4H
 Carbazole, Xylene, $[\text{PdCl}(\pi\text{-allyl})]_2$

Entry	Starting Substrate	Code Name	Structure	Yield (%)
1		MCP(1)		85
2		CF3-MCP(4)		71
3		OME-MCP(5)		50 ^a

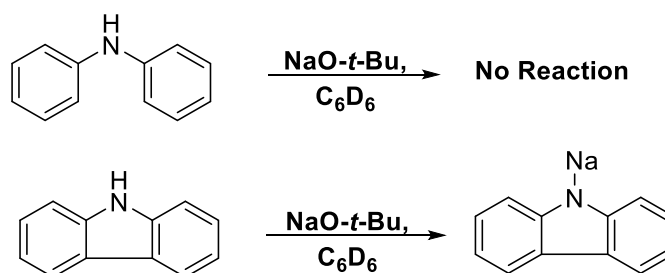
Despite the success of the synthetic procedure, we explored the unique behaviour of carbazole in the Buchwald-Hartwig reaction. In 2015, Nakayama *et al.* reported a simple comparative reaction test of diphenylamine/carbazole with chlorobenzene.³⁶ The test was performed with the use of sodium *tert*-butoxide (NaO-*t*-Bu) as a base in the presence of $[\text{PdCl}(\pi\text{-allyl})]_2$ / Cy-vBRIDP. In the case of diphenylamine the reaction reached completion in 2 hours (Scheme 2.4). Conversely, when carbazole was used under the same conditions, no reaction was observed.

We also faced similar challenges when using reaction conditions that have been shown to be effective for diphenylamine (XPhos/PEPPSI-IPr). Translating these methods to carbazole reactions did not yield the same results.



Scheme 2.4: Buchwald-Hartwig cross coupling between chlorobenzene and diphenylamine/carbazole. Reactions were performed at 100°C for 2 hours.

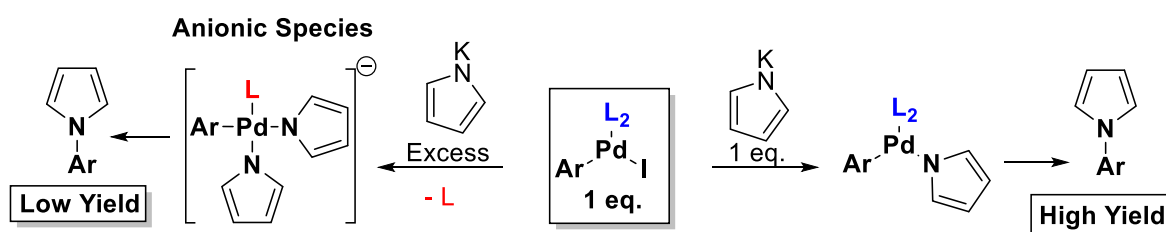
To investigate the cause of this difference in behaviour of carbazole, an NMR study was performed. Carbazole and diphenylamine were treated with sodium tert-butoxide in D_6 -benzene at 80°C and analysed by 1H NMR.³⁶ In the case of carbazole, the peak for the proton on nitrogen atom disappeared. This in turn meant that carbazole was acidic enough to react with the base to form a carbazole-sodium salt (Scheme 2.5). These results also indicated that the carbazole-sodium salt could be involved in a *transmetalation* process with arylpalladium(II) halide when reactions are performed with sodium tert-butoxide. The implications of this are discussed below.



Scheme 2.5: Scheme to illustrate the results of 1H NMR study.

According to research by Mann *et al.*, the arylpalladium(II) halide can be transformed into an anionic bis(*N*-azole)arylpalladate(II) complex, which renders it less reactive towards reductive elimination when compared to a neutral mono(*N*-azole)arylpalladium(II) complex. This occurs via the process of *transmetalation*. Two experiments were reported with two different palladium complexes, using DPPF and PPh₃ ligands, to prove this hypothesis. Scheme 2.6 (centre to left) illustrates the reaction of a palladium complex with excess potassium pyrrolyl salt. This forms an anionic complex by displacing one of the palladium-phosphine linkage.³⁷ The formation of this anionic complex leads to reduced favourability to reductive elimination, thus, lower yields. In contrast, when using stoichiometric control of one equivalent, the formation of ionic species is minimised, leading to higher yields (Scheme 2.6, centre to right). Hence, in the coupling reaction of carbazole using sodium *tert*-butoxide, the Pd catalyst would be deactivated by generation of similar anionic species.³⁶

Substituting the base to MeMgCl can suppress the bis-*transmetalation* process. The nucleophilicity of the group two metals is estimated to be weaker than that of group one metals due to the higher electronegativity (Mg \approx 1.31; K \approx 0.82; Na \approx 0.93). Therefore, this leads to formation of soft nucleophile *N*-carbazolymagnesium chloride which is able to react smoothly in the presence of the monodentate cBRIDP/allylic palladium chloride catalyst.



Scheme 2.6: Scheme to illustrate the reductive elimination chemistry of an *N*-Azole-Palladium complex.

Following the success of **Method 2**, we applied similar reaction conditions for the synthesis of 1,3-bis(3,6-di-*tert*-butyl-9H-carbazol-9-yl)benzene derivatives (**T-MCP**, Figure 2.9). 3,6-di-*tert*-butyl-9H-carbazole was employed to couple aryl chlorides to afford corresponding **T-MCP** derivatives. Even though we did find success with **Method 2** previously, we adapted the method further to be utilised with 3,6-di-*tert*-butyl-9H-carbazole. Firstly, we were able to make the reaction concentrated by using minimal solvent, thanks to better solubility of 3,6-di-*tert*-butyl-9H-carbazole. Secondly, the solvent of the reaction was altered from xylene to toluene due to easy accessibility of anhydrous toluene. These changes led to shortened reaction times to reach reaction completion with much better yields (69-92%) when compared with **MCP** derivatives (50-85%). Table 2.4 shows the reaction scheme used for the synthesis of **T-MCP** derivatives and their corresponding yields after purification.

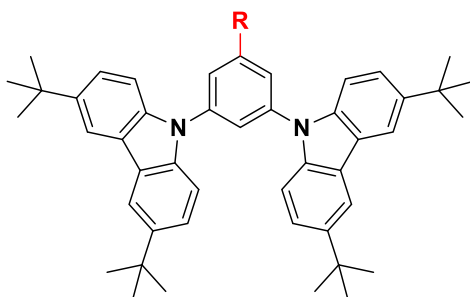
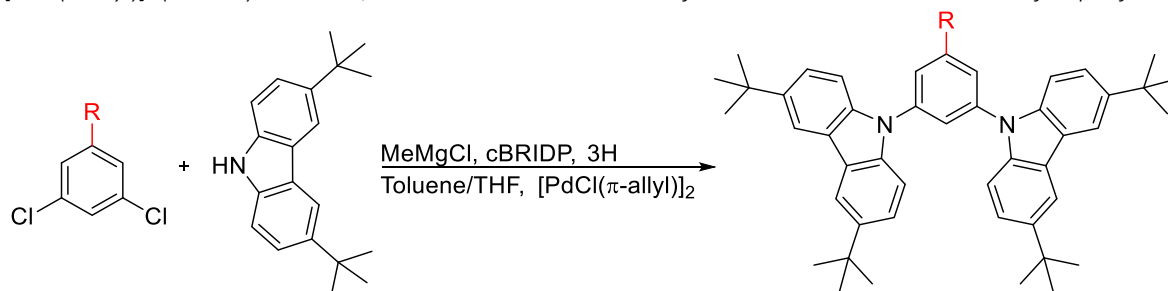


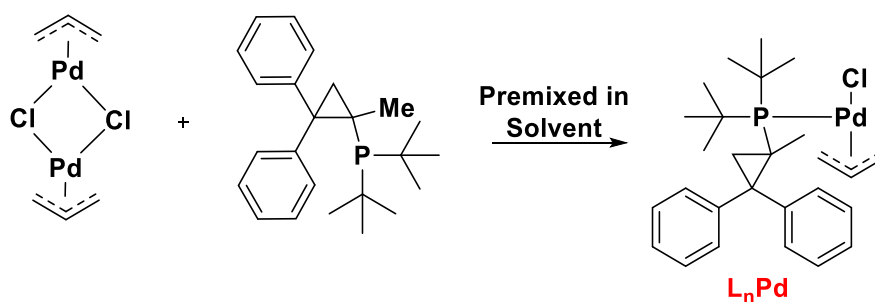
Figure 2.9: Molecular structure of 1,3-bis(3,6-di-*tert*-butyl-9H-carbazol-9-yl)benzene (**T-MCP**), where R is an hydrogen atom.

Table 2.4: The synthesis of **T-MCP** derivative synthesis via altered **Method 2**. Reactions performed under argon atmosphere using aryl halide derivatives (1 eq.), carbazole (2.2 eq.), MeMgCl (2.2 eq.), cBRIDP (5 mol%) and [PdCl(π -allyl)]₂ (1 mol%) in toluene/THF at 80°C. ^a Reaction time of 5 hours. Yields were calculated after purification.



Entry	R	Code Name	Yield (%)
1	H	T-MCP(6)	87
2	CH ₃	ME-T-MCP(7)	79
3	CF ₃	CF3-T-MCP(8)	77
4	OMe	OME-T-MCP(9)	69 ^a

The catalytic cycle of the cross coupling reaction between carbazole and aryl halides is depicted in Figure 2.10. First, oxidative addition of arylhalide to L_nPd (Scheme 2.7) leads to an arylpalladium (II) chloride complex (**1**). Second, the desired *transmetalation* process of the carbazole magnesium chloride salt to complex **1** results in a neutral mono (*N*-carbazole) arylpalladium (II) complex (**2**). The excess carbazole magnesium chloride salt would react with complex **2** through the second *transmetalation* process to give an anionic bis (*N*-carbazole) arylpalladium (II) complex (**3**) as a plausible inactive species. The role of the Grignard reagent (MeMgCl) is to decrease the nucleophilicity of the carbazole salt and limits the second *transmetalation*. Finally, *N*-arylcabazole is generated via reductive elimination of L_nPd (0) species from complex **2**. However, the reductive elimination from complex **2** is known to be the limiting step. Therefore, higher temperatures and careful selection of ligand, such as **cBRIDP**, aid the acceleration of the reductive elimination process while promoting the desired *transmetalation*.



Scheme 2.7: Scheme to show the formation of active catalyst L_nPd .

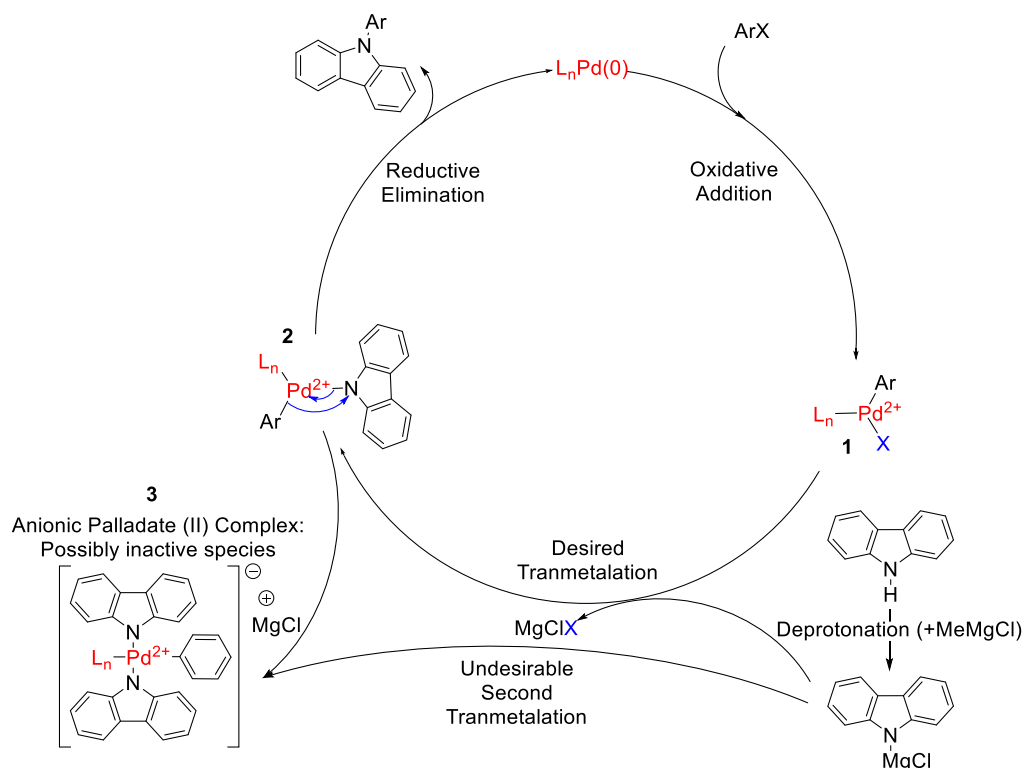
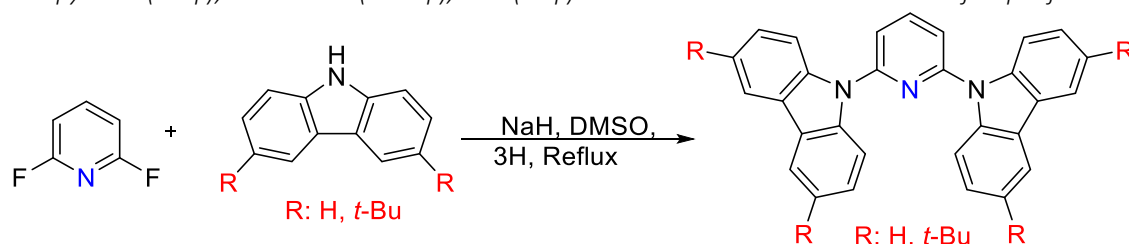
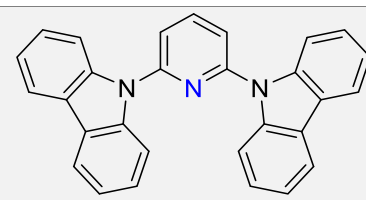
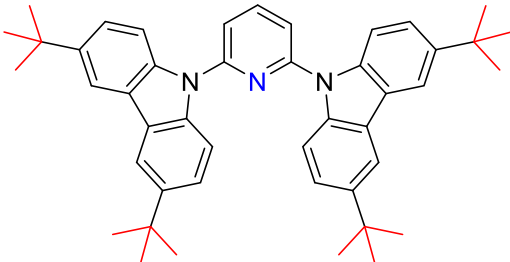


Figure 2.10: Mechanism of Buchwald-Hartwig reaction.

2.2.3 Synthesis of 1,3-Di(9H-carbazole-9-yl)pyridine derivatives

A further two **MCP** derivatives were synthesised, the central benzene ring being replaced by pyridine ring. This yielded 2,6-di(9H-carbazol-9-yl)pyridine (**PY-MCP, 10**) and 2,6-bis(3,6-di-tert-butyl-9H-carbazol-9-yl)pyridine (**PY-T-MCP, 11**) via nucleophilic aromatic substitution, **Method 3** (Table 2.5). Aromatic pyridines substituted at the *ortho* position are known to be very reactive via the SN_{Ar} mechanism, due to the negative charge which is effectively delocalised at the nitrogen (Figure 2.11).

Table 2.5: The synthesis of **MCP** derivatives via **Method 3**. Reactions performed under argon atmosphere using 2,6-Difluoropyridine (1 eq.), *R*-carbazole (2.2 eq.), NaH (3eq.) and DMSO. Yields were calculated after purification.

			
Entry	Code Name	Structure	Yield (%)
1	Py-MCP (10)		54
2	Py-T-MCP(11)		66

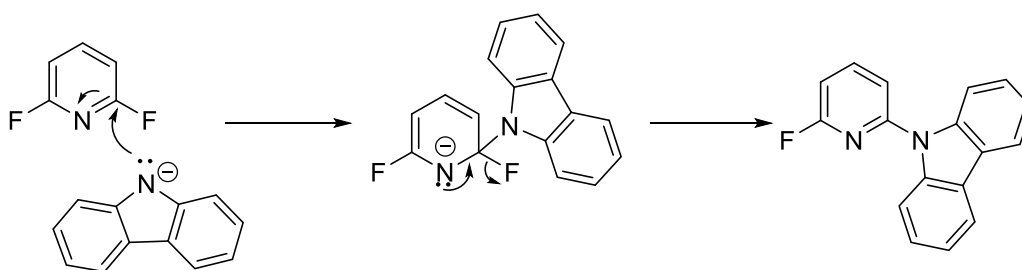


Figure 2.11: S_NAr mechanism for the formation of **PY-MCP** derivatives.

2.3 Theoretical Studies of MCP and T-MCP Derivatives

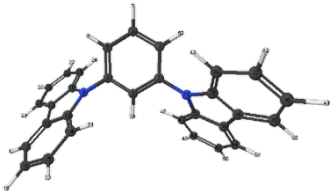
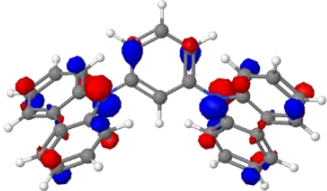
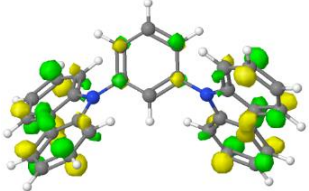
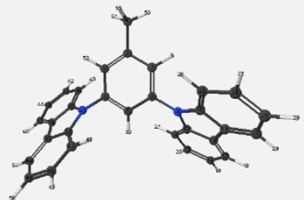
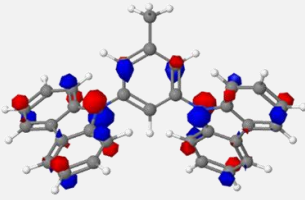
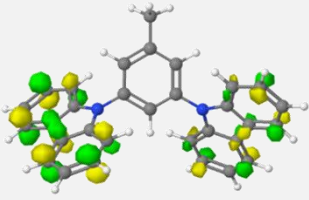

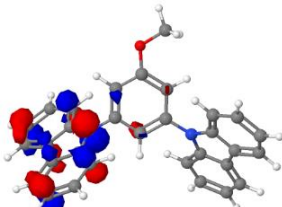
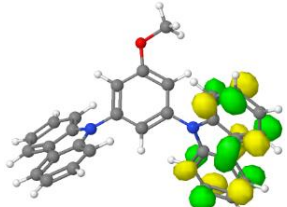
Computational analysis was performed in partnership with Marcus Taylor at the University of Birmingham, School of Chemistry. The HOMO-LUMO energies and minimum energy conformations of the molecules were explored using a Gaussian program package 09.³⁸ The geometric and electronic properties of **MCP** and **T-MCP** derivatives were analysed. The geometries were optimised using B3LYP (Becke three parameters hybrid functional with Lee-Yang-Perdew correlation function) with the 6-31G (d) basis set.³⁹ Electronic properties of the minimised structures were then analysed using DFT (Density Functional Theory) and TD-DFT (Time-Dependent Density Functional Theory) to obtain the HOMO, LUMO and singlet energies. All the results of these computational analyses are presented in Table 2.6. All calculations were carried out in the gas phase and on a single molecule.

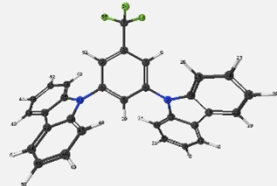
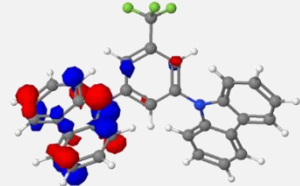
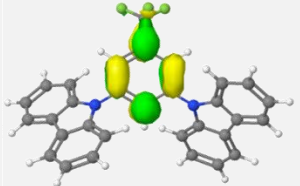
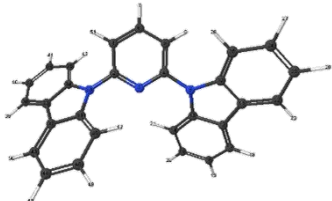
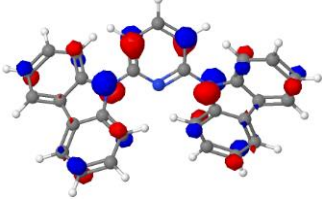
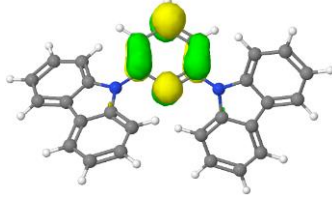
The HOMO of all **MCP** derivatives predominantly consists of carbazole orbitals. Hence, these compounds have similar HOMO levels. The DFT calculations suggest not much of a change in HOMO energy in comparison to **MCP** (-5.45 eV). However, **CF3-MCP** has a significantly lower HOMO energy level of -5.62 eV. When studying the LUMO, the calculations show **MCP**, **ME-MCP** and **OME-MCP** LUMO mainly consists of carbazole orbitals. Thus, the LUMO value is very similar for these compounds at around -0.7 eV. In the case of **CF3-MCP** and **PY-MCP** the LUMO electron density lies on the central aromatic moiety. This phenomenon results in lowering of the LUMO value to around -1 eV. Comparing the calculated HOMO-LUMO gap, we can observe a similar trend. **MCP**, **ME-MCP** and **OME-MCP** have a very similar gap of 4.7eV whereas the **CF3-MCP** and **PY-MCP** HOMO-LUMO gap is decreased. This could be advantageous depending on the partner molecule used to form an exciplex.

The **T-MCP** series follows a similar trend to **MCP** derivatives in terms of HOMO and LUMO electron density. However, **ME-T-MCP's** LUMO electron density lies on the central phenyl. This does not have a significant impact on the HOMO/LUMO/HOMO-LUMO gap values. In general, **T-MCP** derivatives have higher HOMO and LUMO values than **MCP** derivatives. With regards to the HOMO-LUMO gap, **T-MCP** derivatives have a generally lower HOMO-LUMO gap. The calculated singlet values for the **T-MCP** derivatives are lower than those of **MCP** derivatives, thus, we expect the emission spectra to be red shifted.

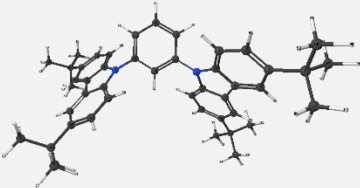
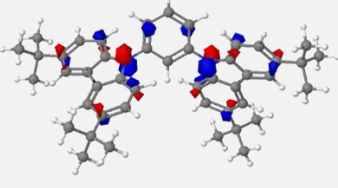
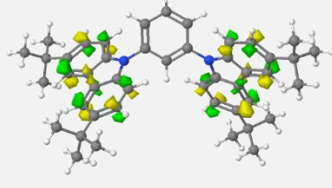
These theoretical studies suggest that changes in the chemical structure of **MCP's** have some effect on molecular electronics. In some cases these changes are small, however, when we introduce functional groups with acceptor characteristics on the central phenyl, DFT predicts considerable change. Introduction of a donor moiety on the central phenyl ring does not have a significant impact of the HOMO/LUMO values.

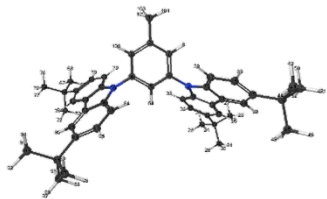
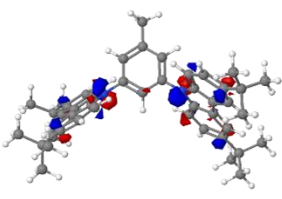
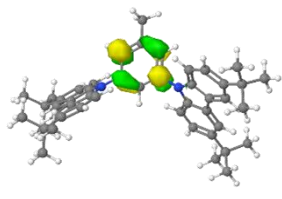
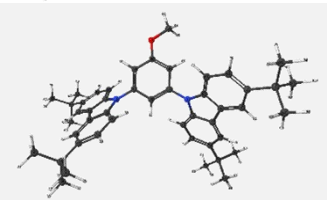
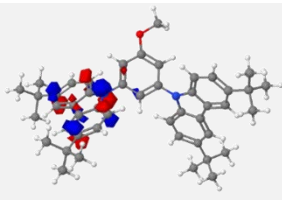
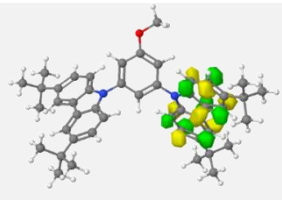
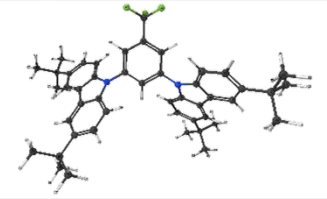
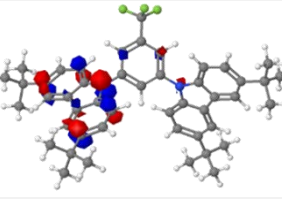
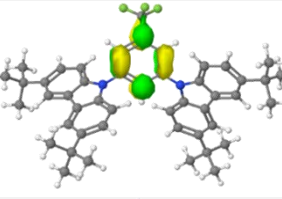
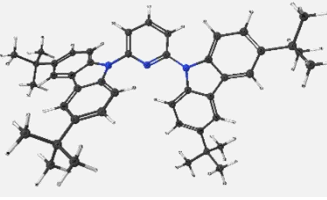
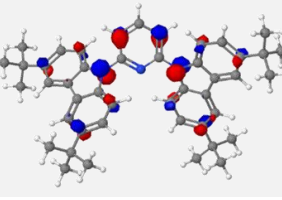
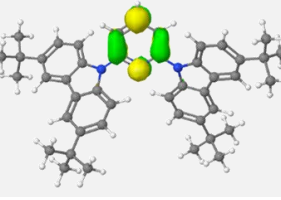
Table 2.6: Visual representation of optimised geometry, HOMO surface, calculated HOMO value in electron volts (eV), LUMO surface, calculated LUMO value in eV, calculated HOMO-LUMO (H-L) gap and calculated Singlet value in eV of **MCP** and **T-MCP** series from density functional theory (DFT) calculations.

<i>MCP Derivatives</i>						
	Geometry Optimised Structure	HOMO	HOMO (eV)	LUMO	LUMO (eV)	H-L Gap (eV)
<i>H</i>			-5.45		-0.75	4.70
<i>ME</i>			-5.42		-0.72	4.70
<i>OME</i>			-5.40		-0.75	4.65

<i>CF3</i>			-5.62		-1.25	4.37	3.59
<i>PY</i>			-5.43		-1.07	4.37	3.62

T-MCP Derivatives

	Geometry Optimised Structure	HOMO	HOMO (eV)	LUMO	LUMO (eV)	H-L Gap (eV)	Singlet (eV)
<i>H</i>			-5.22		-0.68	4.54	3.75

ME			-5.18		-0.62	4.56	3.71
OME			-5.40		-0.68	4.50	3.74
CF3			-5.38		-1.13	4.25	3.47
PY			-5.21		-0.93	4.28	3.54

2.4 In solution Photo-physical Analysis of 1,3-Di(9*H*-carbazol-9-yl)benzene

Derivatives

Photophysics involves the interaction between light and matter, resulting in net physical change. When a beam of light interacts with matter, several processes can take place, as shown in Figure 2.12. The intensity of the incident beam (B_i) is reduced to transmitted beam (B_t) through scattering, luminescence and absorption.

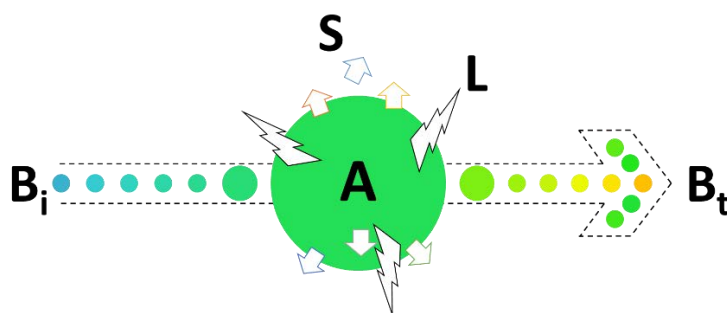


Figure 2.12: Photo-physical processes of light interacting with matter. B_i is the incident beam of light; A is absorption; S is scattering of light; L is luminescence and B_t is the rest of the transmitted beam of light.

The absorbed light becomes the excitation energy for the sample. In order of increasing energy requirement, molecules have translational, rotational, vibrational and electronic excited states (approx. 700 nm – 200 nm). An electronic transition facilitates a molecule from ground state to one of its excited states or *vice versa*. The upward transition from ground state (S_0) to excited state requires absorption of light and the downward transition leads to emission of light (radiative deactivation), Figure 2.13.

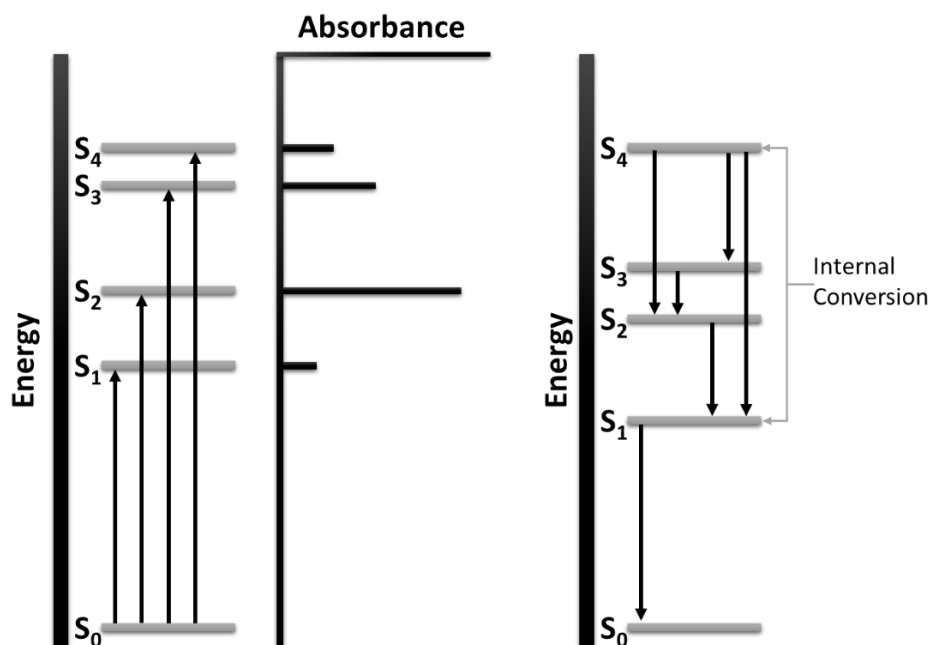


Figure 2.13: Jablonski diagram of photo-physical transitions.

In solution, photo-physical studies of **MCP** derivatives were carried out in four different solvents. These included two polar solvents, DCM and THF, and two comparatively non-polar solvents, chlorobenzene (CLB) and toluene (TOL). First, we analyse the absorption spectra of these compounds. The absorption dependence on concentration of **MCP** and **T-MCP** derivatives was measured. As an example, **MCP** and **T-MCP** absorbance in DCM at low concentrations is illustrated in Figure 2.14.

In the case of **MCP** absorbance spectra, the sharp peak at 294 nm could be attributed to the $n-\pi^*$ transition (carbazole moiety),⁴⁰ the peak at 327 could be attributed to $S_0 \rightarrow S_2$ transition and the peak at 340 nm could be attributed to $S_0 \rightarrow S_1$ transition. The absorbance dependence on concentration at 327 nm and 340 nm was found to be linear. In the case of **T-MCP**, the sharp peak observed at 297 nm could be attributed to the $n-\pi^*$ transition (carbazole moiety),⁴⁰ the peak at 331 nm could be attributed to $S_0 \rightarrow S_2$ transition and the peak at 345 nm could be attributed to $S_0 \rightarrow S_1$ transition. The absorbance dependence on concentration at 331 nm and 345 nm was once again found to be linear.

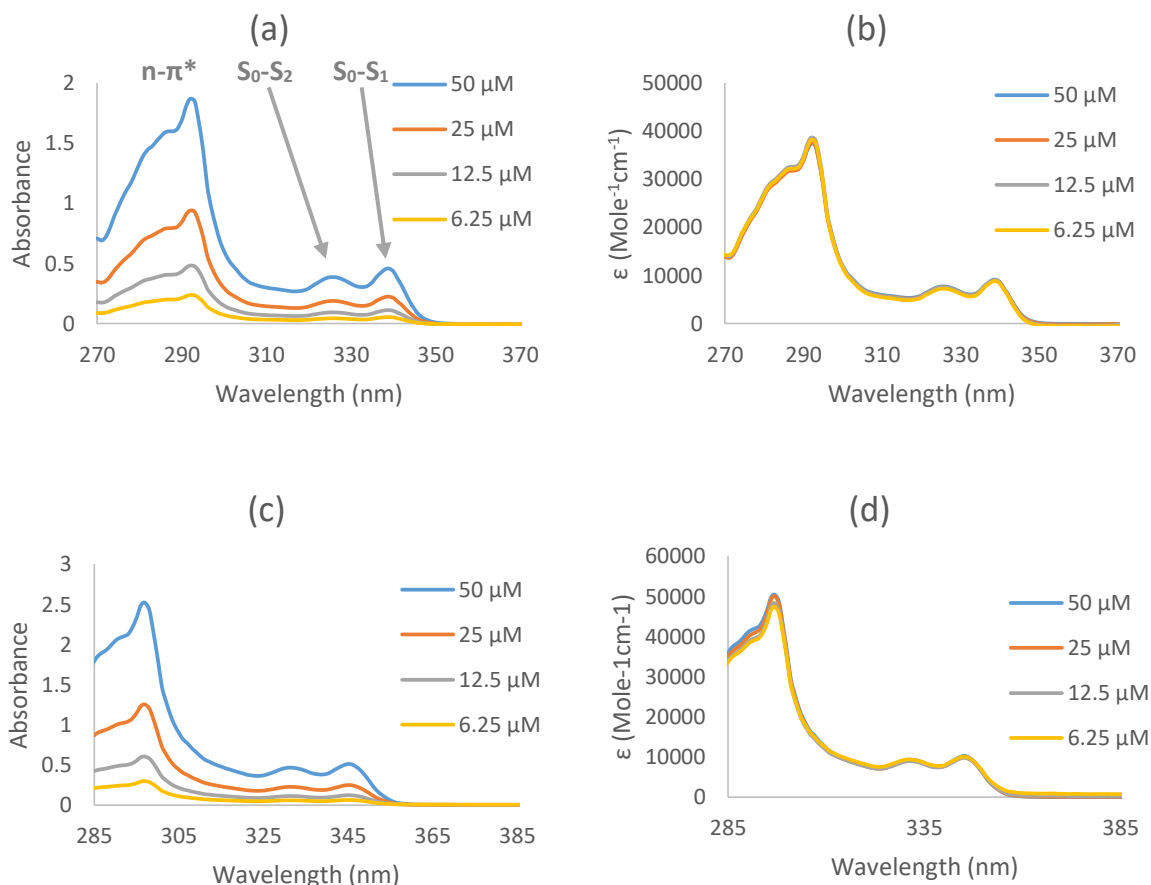


Figure 2.14: (a) Absorption spectra of **MCP** in **DCM** at low concentrations. (b) Plot of the calculated epsilon values against wavelength for **MCP** in **DCM**. (c) Absorption spectra of **T-MCP** in **DCM** at low concentrations. (d) Plot of the calculated epsilon values against wavelength for **T-MCP** in **DCM**.

Following the concentration dependency of absorption, the effect of solvent was investigated. The solvent used appears to have minimal effect on absorption. Figure 2.15 shows the absorption spectra of **ME-MCP** and **ME-T-MCP** in different solvents as an example. The effect of solvents seems minimal across the series.

Figure 2.16 shows the absorption of all **MCP** derivatives in CLB, DCM, THF and TOL. All of the **MCP** derivatives display a sharp peak at 293 nm which could be attributed to the $n-\pi^*$ transition (carbazole moiety). **MCP** and **ME-MCP** absorption spectra are identical. However, there are some noticeable differences in **OME-MCP**, **PY-MCP** and **CF₃-MCP** spectra which show a blue-shifted $S_0 \rightarrow S_2$ and $S_0 \rightarrow S_1$ transition. In the case of **PY-MCP**, a greater absorbance for $S_0 \rightarrow S_2$

and $S_0 \rightarrow S_1$ transition in comparison to other derivatives. It can be observed that the absorbance of the compounds in different solvents is comparable. Excitation studies were performed which confirm the findings of the absorption studies.

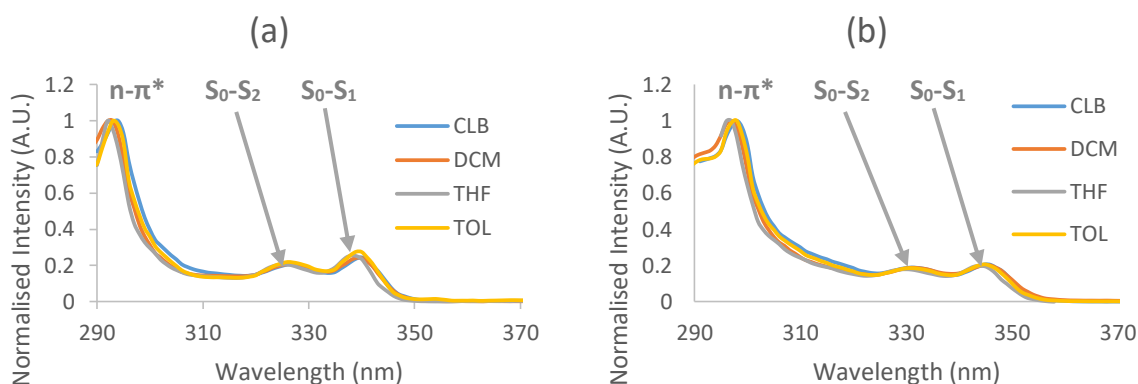


Figure 2.15: Comparison of absorption spectra of **ME-MCP** (a) and **ME-T-MCP** (b) in chlorobenzene, dichloromethane, tetrahydrofuran and toluene.

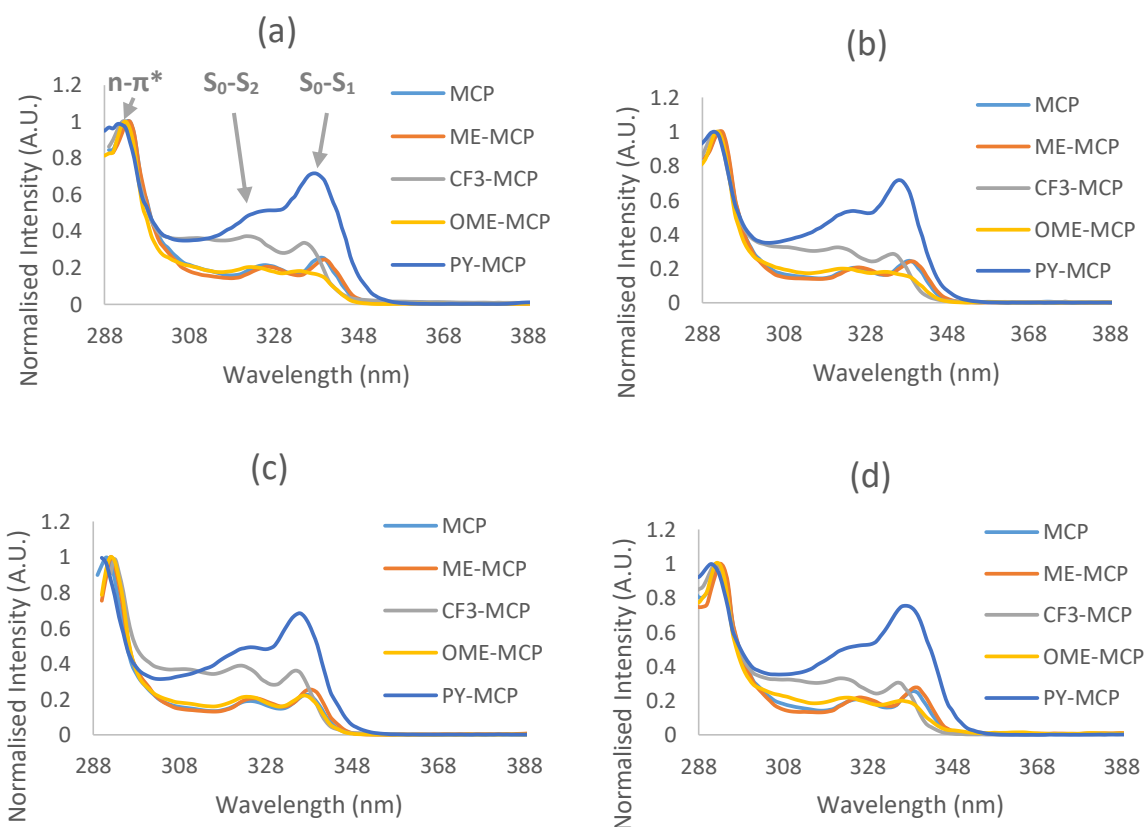


Figure 2.16: Absorption spectra of **MCP** derivatives. (a) Absorption spectra in chlorobenzene. (b) Absorption spectra in dichloromethane. (c) Absorption spectra in tetrahydrofuran. (d) Absorption spectra in toluene.

Figure 2.17 shows the absorption spectra of all **T-MCP** derivatives in CLB, DCM, THF and TOL. All of the **T-MCP** derivatives display a sharp peak at 297 nm which could be attributed to the $n-\pi^*$ transition (carbazole moiety). **T-MCP**, **ME-T-MCP** and **OME-T-MCP** absorption spectra are very similar. However, there are some noticeable differences in spectra of **CF3-T-MCP** which show a blue-shifted $S_0 \rightarrow S_2$ and $S_0 \rightarrow S_1$ transition. In the case of **PY-T-MCP** we also observe a greater absorbance for $S_0 \rightarrow S_2$ and $S_0 \rightarrow S_1$ transition in comparison to other derivatives. It is interesting to note blue-shift is not observed for **OME-T-MCP** in comparison to the shift observed for **OME-MCP**. Comparing the **MCP** and **T-MCP** derivatives we observe a red shift for **T-MCP** derivatives which correlates with the computational studies. Excitation studies were performed which confirm the findings in the absorption studies.

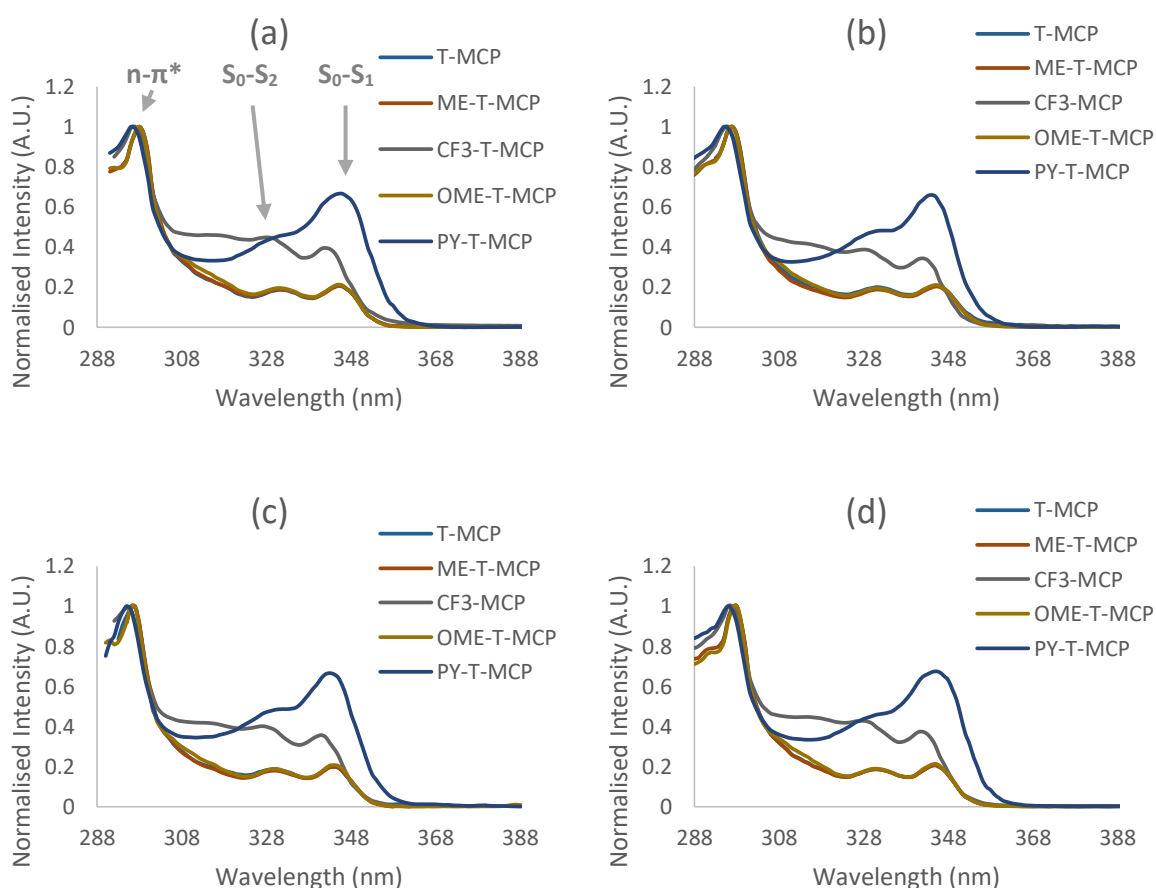


Figure 2.17: Absorption spectra of **T-MCP** derivatives. (a) Absorption spectra in chlorobenzene. (b) Absorption spectra in dichloromethane. (c) Absorption spectra in tetrahydrofuran. (d) Absorption spectra in toluene.

Using the absorption spectra, the transitional energy of S_0 to S_1 was calculated. Table 2.7 shows the calculated energy of $S_0 \rightarrow S_1$ transition in electron volts (eV) in all four solvents. The literature value of for the $S_0 \rightarrow S_1$ transition for **MCP** is 3.7eV,⁴¹ thus we can conclude that these calculations are accurate to ± 0.3 eV. We can observe that changing the substituent has a subtle effect on these energies. The biggest increase in energy is demonstrated with the $-\text{CF}_3$ substituent in comparison to base **MCP**. There is an overall decrease in energy for **T-MCP** in comparison to **MCP**.

Table 2.7: The $S_0 \rightarrow S_1$ transitional energy for **MCP** and **T-MCP** derivatives in chlorobenzene, dichloromethane, tetrahydrofuran and toluene.

	<i>CLB</i>	<i>DCM</i>	<i>THF</i>	<i>TOL</i>
	(eV)	(eV)	(eV)	(eV)
MCP	3.67	3.67	3.69	3.67
ME-MCP	3.66	3.67	3.68	3.67
OME-MCP	3.66	3.67	3.69	3.70
CF₃-MCP	3.71	3.71	3.71	3.71
PY-MCP	3.69	3.70	3.70	3.69
T-MCP	3.60	3.60	3.61	3.60
ME-T-MCP	3.60	3.60	3.61	3.60
OME-T-MCP	3.60	3.60	3.61	3.60
CF₃-T-MCP	3.64	3.63	3.64	3.64
PY-T-MCP	3.60	3.61	3.62	3.60

Following on from absorption studies, emission dependence on concentration was investigated. As an example, **MCP** and **T-MCP** emission spectra in toluene at low concentration

are illustrated in Figure 2.18. Across the board we notice emission quenching for all compounds. The 50 μM solutions show sharp concentration quenching, which could be due to aggregation. However, we do not observe a red shift, which usually indicates aggregation. Apart from high concentration quenching, the data correlates well when normalised, an example of which is shown below.

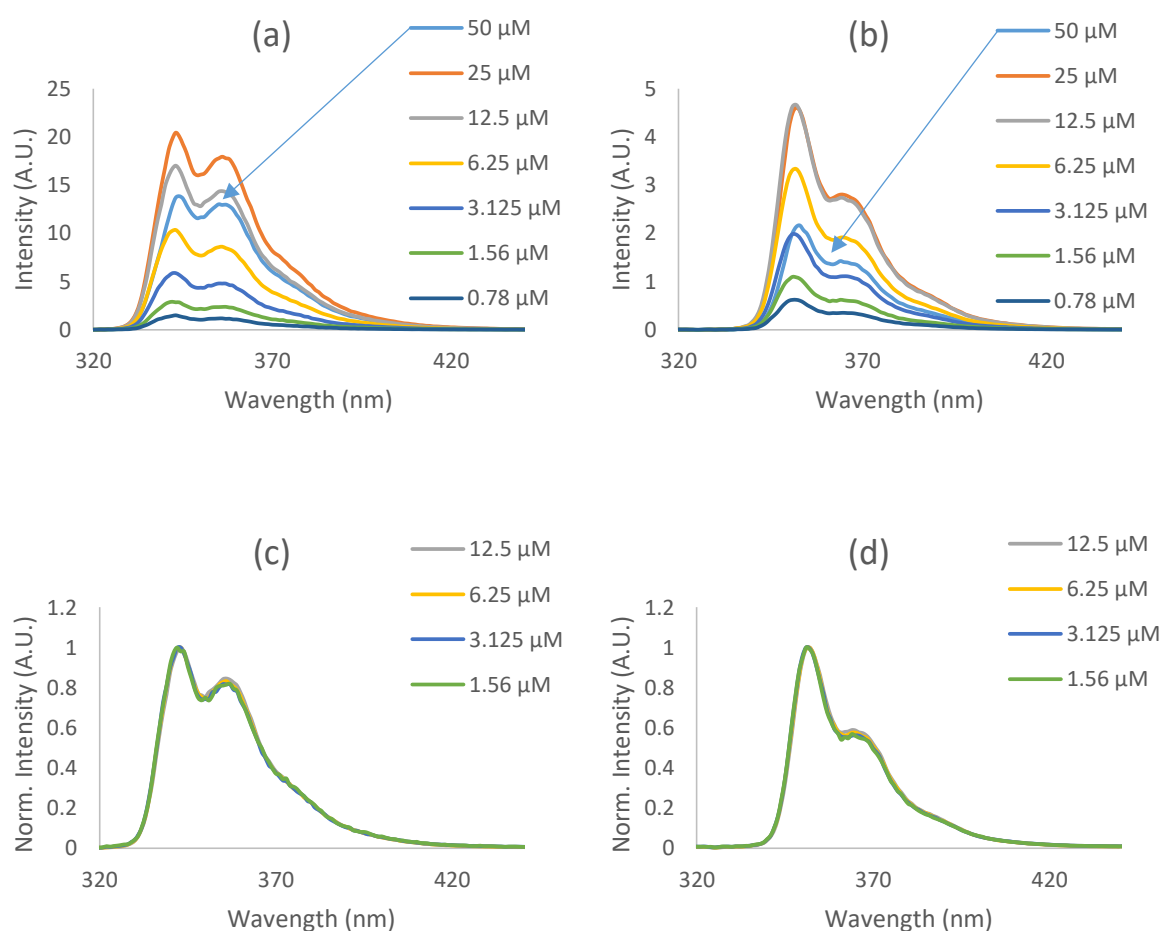


Figure 2.18: (a) Emission spectra of **MCP** in toluene at low concentrations. (b) Emission spectra of **T-MCP** in toluene at low concentrations. (c) Normalised emission spectra of **MCP** in toluene. (d) Normalised emission spectra of **T-MCP** in toluene.

Figure 2.19 shows the comparison of **MCP** derivatives. The λ_{PL} of **MCP** is 343 nm. The λ_{PL} can be blue shifted by adding a trifluoromethyl substituent, whereas the emission spectra is red shifted when the central benzene ring is replaced by a pyridine ring. It is interesting to note that the methoxy functional group does not have a significant impact on the singlet energy. In

contrast, for **T-MCP** derivatives we observe the same singlet energy levels for **T-MCP**, **ME-MCP** and **OME-MCP**. However, the **CF₃-T-MCP** does not follow the same trend as **CF₃-MCP**. The emission spectrum of **CF₃-T-MCP** is red shifted when compared to **T-MCP**. Comparing **MCP** and **T-MCP** derivatives, we can observe a red shift in all cases. Figure 2.19 illustrates the comparison between **MCP** /**T-MCP** and **CF₃-MCP** /**CF₃-T-MCP**. In the case of **CF₃-T-MCP** we observe a significant change in the shape of emission spectra.

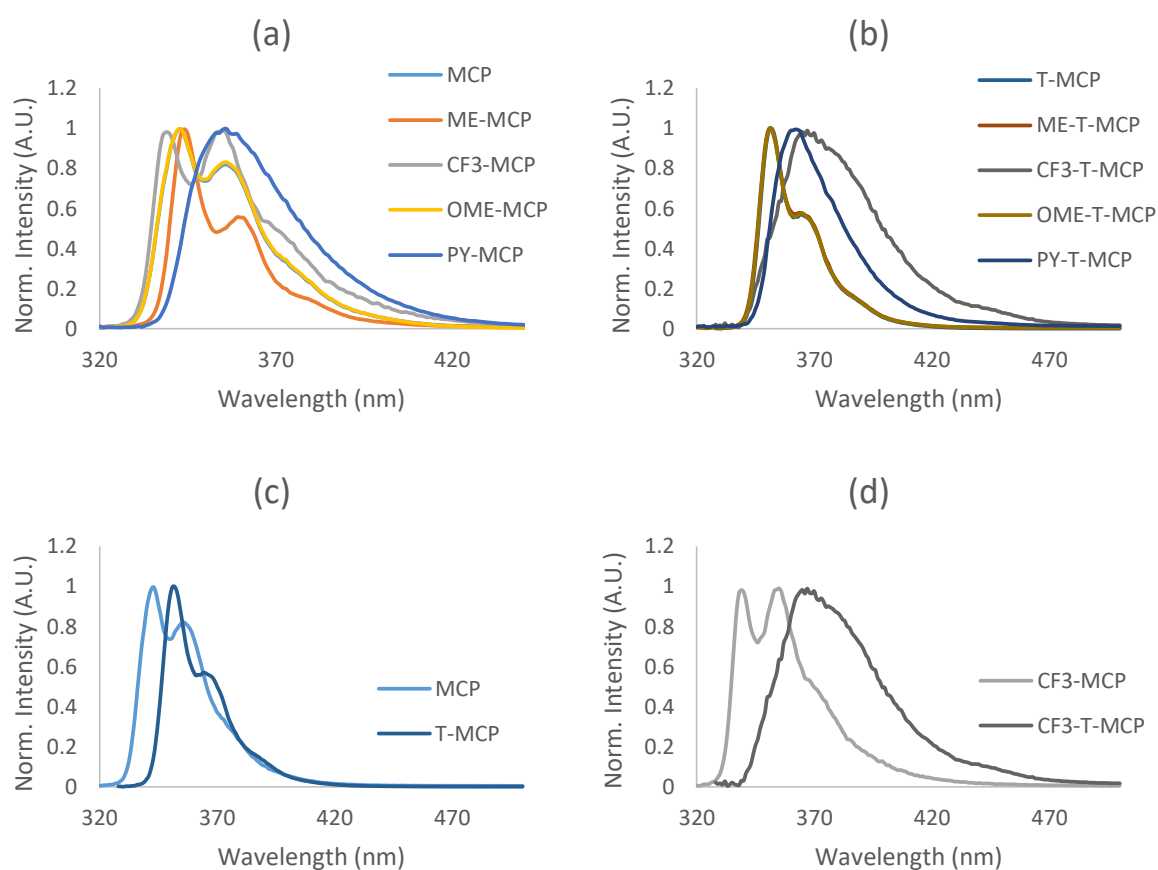


Figure 2.19: (a) Emission spectra of **MCP** derivatives in toluene. (b) Emission spectra of **T-MCP** derivatives in toluene. (c) Comparison of emission spectra of **MCP** and **T-MCP** in toluene. (d) Comparison of emission spectra of **CF₃-MCP** and **CF₃-T-MCP** in toluene.

Fluorescence lifetimes of the **MCP** series was measured and the samples were excited using a laser emitting at 290 nm. Data was collected until the photon count reached 10,000 in each case. The lifetime decay data is summarised in Table 2.8, complete data is attached in appendix

ii, along with the fits. We anticipate the decay life to be fairly short for all the **MCP** series as they are small organics. Thus, it is no surprise that the fluorescence decay lifetime is less than 10 ns. It is interesting to note that the fluorescence lifetime is reduced considerably when the central benzene ring is replaced with a pyridine ring. Another molecule of interest is **CF3-T-MCP** which has a significantly shorter lifetime when compared to **MCP** and **CF3-MCP**.

Table 2.8: Fluorescence lifetime decay measurements of **MCP** series in nanosecond (ns).

	DCM (ns)	TOL (ns)	THF (ns)	CLB (ns)
MCP	5.08	5.73	6.13	5.61
ME-MCP	5.01	5.78	6.14	5.83
OME-MCP	5.76	6.48	6.98	6.25
CF3-MCP	6.15	7.11	6.56	6.86
PY-MCP	2.17	1.61	1.90	1.78
T-MCP	5.03	5.66	5.93	5.61
ME-T-MCP	5.10	5.59	5.92	5.64
OME-T-MCP	5.08	5.73	6.15	5.69
CF3-T-MCP	4.45	2.32	4.05	3.31
PY-T-MCP	3.05	1.78	2.22	2.15

Table 2.9 summarises the results from in solution photophysical analysis and also has computation values for comparison. From the table we can conclude the computational values are much higher than those found experimentally. Even though these value do not agree, one can argue the computation analysis gives a reasonable idea as to how the molecules could behave in the solid state.

Table 2.9: Summary of in solution photophysical studies with computational analyses. The S_0 - S_1 was calculated from the λ_{abs} value rather than the λ_{PL} . All the values are in electron volts unless stated otherwise. The values in brackets under the S_0 - S_1 column are calculated values. E_g is the HOMO-LUMO gap and τ is fluorescence lifetime decay in nanoseconds.

	Absorption	S_0 - S_1	Fluorescence	Cal.	Cal.	E_g	τ (ns)
	λ_{abs} (nm)	(eV)	λ_{PL} (nm)	HOMO	LUMO	(eV)	
MCP	292, 326, 339	3.67 (3.88)	343, 359	-5.452	-0.750	4.703	5.64
ME-MCP	293, 326, 339	3.67 (3.87)	344, 359	-5.419	-0.724	4.695	5.69
OME-MCP	292, 323, 335	3.68 (3.86)	343, 356	-5.400	-0.746	4.654	6.37
CF3-MCP	292, 309, 322, 335	3.71 (3.59)	339, 355	-5.625	-1.253	4.371	6.67
PY-MCP	291, 325, 337	3.69 (3.63)	356	-5.434	-1.066	4.368	1.87
T-MCP	298, 331, 345	3.61 (3.75)	352, 364	-5.223	-0.681	4.543	5.56
ME-T-MCP	298, 331, 345	3.61 (3.72)	351, 364	-5.182	-0.621	4.561	5.56
OME-T-MCP	298, 331, 345	3.61 (3.74)	351, 365	-5.179	-0.679	4.500	5.66
CF3-T-MCP	296, 315, 328, 342	3.64 (3.47)	365	-5.381	-1.129	4.252	3.53
PY-T-MCP	296, 331, 345	3.61 (3.54)	362	-5.212	-0.933	4.279	2.30

2.5 Solid State Photo-physical Analysis of 1,3-Di(9*H*-carbazol-9-yl)benzene Derivatives

Solid state photo-physical studies of **MCP** derivatives were carried out by Christopher Coward who was working under Prof. Andrew P. Monkman in the Physics Department of Durham University. They have developed a solution process of drop cast film which was utilised in these studies. The usual method of forming thin films for analysis is via vacuum deposition, which can be time consuming. The solution process takes equimolar solutions of donor (**D**) and acceptor (**A**), which are then deposited onto a substrate by a drop casting technique, resulting in thin film of a **D/A** blend (Figure 2.20).

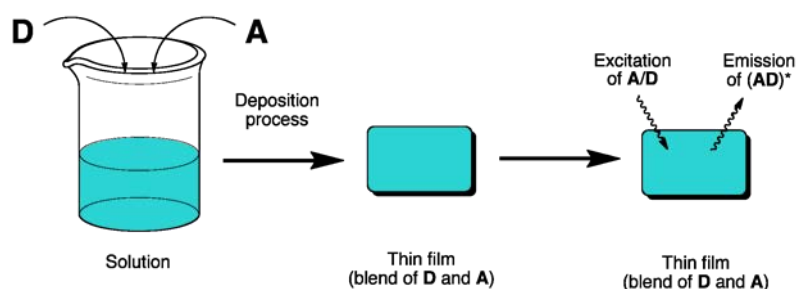


Figure 2.20: Process of drop casting to achieve thin films for photo-physical analysis.

Purity is a highly important factor when assessing the photo-physical properties of organic materials for use in optoelectronic devices, as a small amount of impurities could have a significant impact on their behaviour. As a result, two standards of purified samples were prepared, standard one (Std) was purified using recrystallisation and column chromatography. Whilst standard two (Std II) samples were further purified via preparative TLC.

Initially, exciplex formation experiments were performed using **OXD-7/MCP** derivatives. From the spectra of the mixed drop cast films (Figure 2.21), it is clear that no exciplex formation occurs. It should be noted that the purity has no major impact on the spectra.

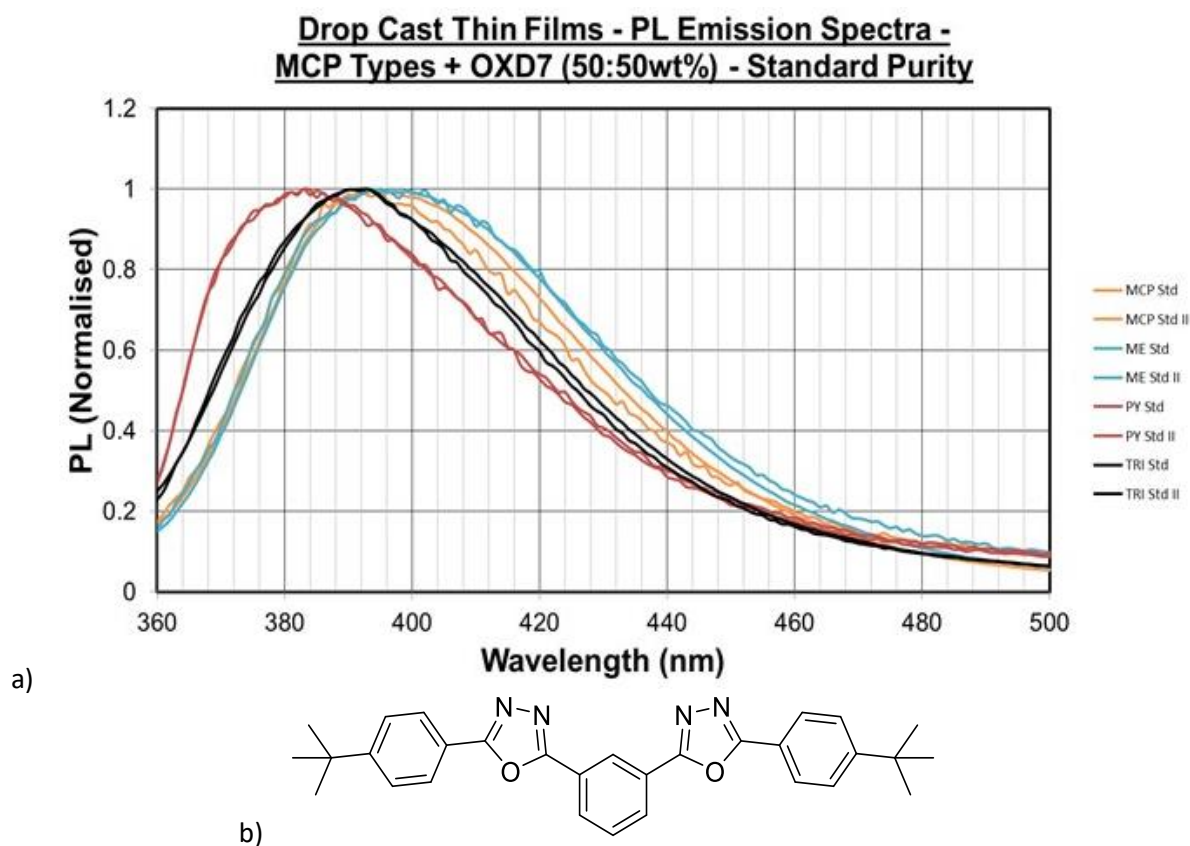


Figure 2.21: a) Fluorescence of drop cast films of **MCPs** and **OXD-7** (50:50 wt%) with standard purity (Std) and high purity samples (std II). b) Molecular structure of **OXD-7**.

Following on from the unsuccessful attempts of exciplex formation with **OXD-7**, **MCP** derivatives were used as the acceptor molecule and mixed with donor molecule (**MTDATA**, Figure 2.22). The photoluminescence data of **MTDATA** film was found in literature, the λ_{max} is 425 nm and emission of aggregated **MTDATA** is situated at 500 nm.⁴² The new blends of **MCP/MTDATA** illustrate exciplex formation, but some show mixed exciplex emission with aggregated **MTDATA** emission, peaking at ≈ 490 nm. The difference in purity can be compared, as shown in Figure 2.22. The extra pure samples illustrate minimised aggregated **MTDATA** emission peaks at ≈ 490 nm.

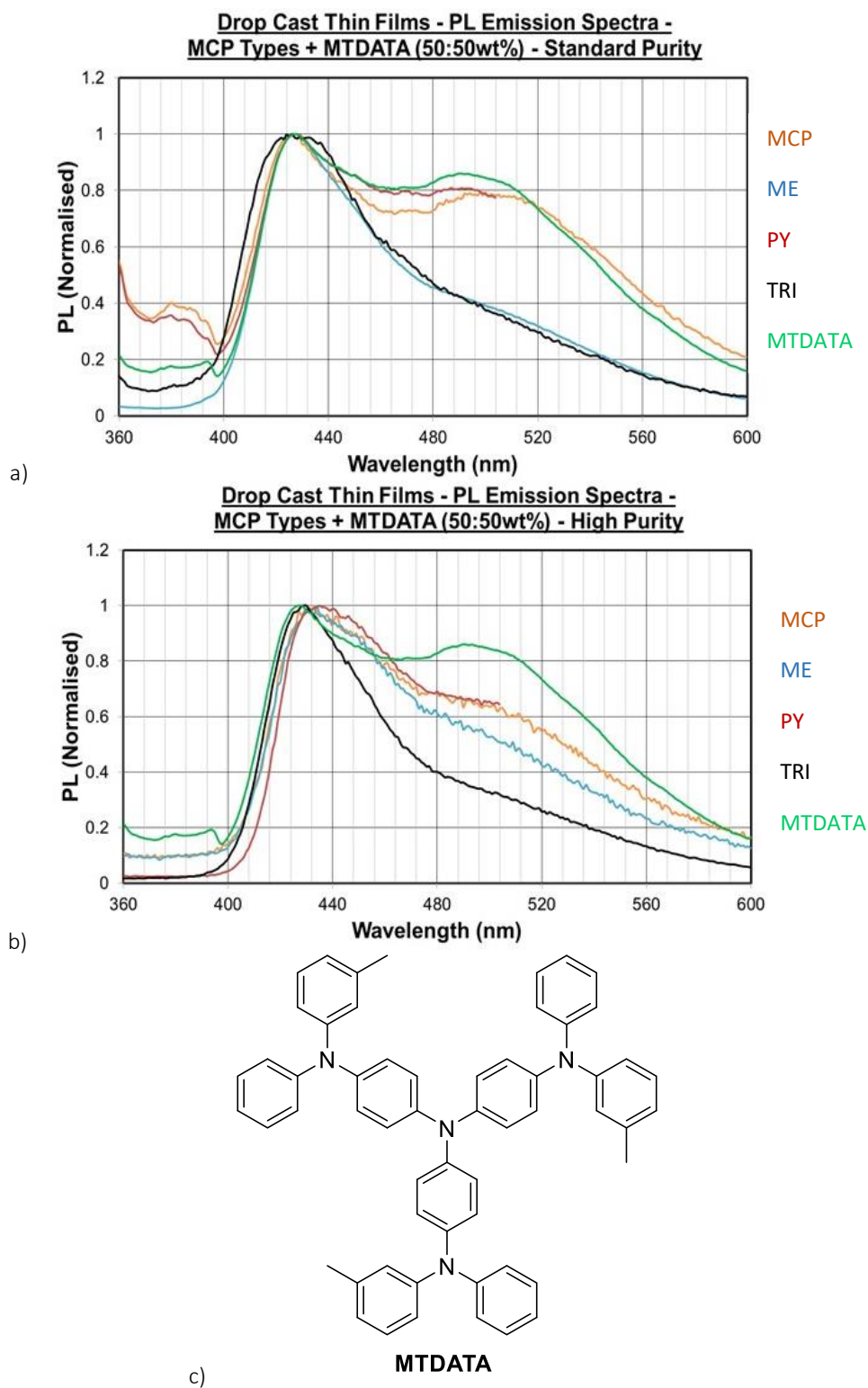


Figure 2.22: a) Fluorescence of drop cast films of **MCPs** and **MTDATA** (50:50 wt%). b) Fluorescence of drop cast films of **MCPs** and **MTDATA** (50:50 wt%) with high purity samples. c) Molecular structure of **MTDATA**.

From the spectra, it can be concluded that the different substituents on **MCP** have minimal effect on the spectral position of the exciplex, given they all form an exciplex peaking at 430

nm. However, it is interesting to note that these analogues have the ability to work as electron donor or acceptor with the corresponding correct choice of partner molecule.

2.6 Conclusion

In short, both the Ullmann and Buchwald-Hartwig reactions have been adapted for carbon-nitrogen cross coupling between aryl bromide/chloride and carbazole. All the synthesised **MCP** and **T-MCP** derivatives were purified and characterised. We were able to synthesise **MCP** and **T-MCP** derivatives with electron donor as well as electron acceptor moieties on the central phenyl. Computational analysis via DFT calculations was performed for all **MCP** and **T-MCP** derivatives. From the computational analysis we can observe that we have successfully tuned the HOMO and LUMO of **MCP** derivatives. This tuning could be vital in the process of choosing a pairing molecule for exciplex formation.

In solution, photophysical characterisation was performed for all **MCP** and **T-MCP** derivatives. Absorption, excitation and emission data were obtained. From the absorption data we were able to determine the peaks for the carbazole moiety and the energy of ground to singlet state. From the emission data we were able to conclude that different substituents on the central phenyl of **MCP** derivatives have minimal effect on the spectral position. The emission spectra of the **T-MCP** derivatives are red shifted when compared with **MCP** derivatives.

Solid state studies of some **MCP** derivatives have been performed. We observe a red shift in the emission spectra of the thin films in comparison to the in solution studies. The emission spectra of thin films with greater purity do not show a significant difference in spectra. **MCP** as donor and **OXD-7** as acceptor do not form an exciplex. However, we can confirm that all the tested compounds do form an exciplex with **m-MTDATA**. It is interesting to note that **MCP**

derivatives are able to work as either donor or acceptor molecules with the corresponding correct choice of partner molecule.

2.6 References

- 1 A. Endo, K. Sato, K. Yoshimura, T. Kai, A. Kawada, H. Miyazaki and C. Adachi, *Appl. Phys. Lett.*, 2011, **98**, 83302.
- 2 A. Van Dijken, J. J. A. M. Bastiaansen, N. M. M. Kikken, B. M. W. Langeveld, C. Rothe, A. Monkman, I. Bach, P. Stössel and K. Brunner, *J. Am. Chem. Soc.*, 2004, **126**, 7718.
- 3 Y. K. Kim, S. J. Lee, J. H. Seo, J. H. Seo, G. Y. Kim and Y. Y. Jin, *J. Nanosci. Nanotechnol.*, 2009, **9**, 7044.
- 4 X. Ren, J. Li, R. J. Holmes, P. I. Djurovich, S. R. Forrest and M. E. Thompson, *Chem. Mater.*, 2004, **16**, 4743.
- 5 J. Lee, N. Chopra, S.-H. Eom, Y. Zheng, J. Xue, F. So and J. Shi, *Appl. Phys. Lett.*, 2008, **93**, 123306.
- 6 F. Ullmann and J. Bielecki, *Berichte der Dtsch. Chem. Gesellschaft*, 1901, **34**, 2174.
- 7 C. Sambigiagio, S. P. Marsden, A. J. Blacker and P. C. McGowan, *Chem. Soc. Rev.*, 2014, **43**, 3525.
- 8 F. Ullmann, *Berichte der Dtsch. Chem. Gesellschaft*, 1903, **36**, 2382.
- 9 J. Lindley, *Tetrahedron*, 1984, **40**, 1433.
- 10 H. Weingarten, *J. Org. Chem.*, 1964, **29**, 3624.
- 11 A. S. Guram, R. A. Rennels and S. L. Buchwald, *Angew. Chemi. Int. Ed.*, 1995, **34**, 1348.

- 12 J. Louie and J. F. Hartwig, *Tetrahedron Lett.*, 1995, **36**, 3609.
- 13 J. P. Wolfe and S. L. Buchwald, *J. Org. Chem.*, 2000, **65**, 1144.
- 14 C. Xu, J. Zhao, M. Wang, Z. Wang, C. Cui, Y. Kong and X. Zhang, *Electrochim. Acta*, 2012, **75**, 28.
- 15 T. Y. H. Lee, Q. Wang, J. U. Wallace and S. H. Chen, *J. Mater. Chem.*, 2012, **22**, 23175.
- 16 W. Han, H. Son, K. Wee, K. Min, S. Kwon, I. Suh, S. Choi, D. H. Jung and S. O. Kang, *J. Phys. Chem. C*, 2009, **98**, 19686.
- 17 H. Rueeger, R. Lueoend, R. Machauer, S. J. Veenstra, L. H. Jacobson, M. Staufenbiel, S. Desrayaud, J. M. Rondeau, H. Möbitz and U. Neumann, *Bioorganic Med. Chem. Lett.*, 2013, **23**, 5300.
- 18 D. O'Hagan, *Chem. Soc. Rev.*, 2008, **37**, 308.
- 19 T. A. Unzner and T. Magauer, *Tetrahedron Lett.*, 2015, **56**, 877.
- 20 P. Ruiz-Castillo and S. L. Buchwald, *Chem. Rev.*, 2016, **116**, 12564.
- 21 F. Rataboul, A. Zapf, R. Jackstell, S. Harkal, T. Riermeier, A. Monsees, U. Dingerdissen and M. Beller, *Chem. Eur. J.*, 2004, **10**, 2983.
- 22 X. Huang, K. W. Anderson, D. Zim, L. Jiang, A. Klapars and S. L. Buchwald, *J. Am. Chem. Soc.*, 2003, **125**, 6653.
- 23 D. W. Old, M. C. Harris and S. L. Buchwald, *Org. Lett.*, 2000, **2**, 1403.
- 24 P. G. Gildner and T. J. Colacot, *Organometallics*, 2015, **34**, 5497.
- 25 C. C. C. J. Seechurn, S. L. Parisel and T. J. Colacot, *J. Org. Chem.*, 2011, **76**, 7918.

- 26 D. Zim and S. L. Buchwald, *Org. Lett.*, 2003, **5**, 2413.
- 27 C. Valente, M. Pompeo, M. Sayah and M. G. Organ, *Org. Pro. Res. Dev.*, 2014, **18**, 180.
- 28 N. C. Bruno, N. Niljianskul and S. L. Buchwald, *J. Org. Chem.*, 2014, **79**, 4161.
- 29 W. a Herrmann, *Angew. Chem. Int. Ed.*, 2002, **41**, 1290.
- 30 E. A. B. Kantchev, C. J. O'Brien and M. G. Organ, *Angew. Chem. Int. Ed.*, 2007, **46**, 2768.
- 31 C. J. O'Brien, E. A. B. Kantchev, C. Valente, N. Hadei, G. A. Chass, A. Lough, A. C. Hopkinson and M. G. Organ, *Chem. Eur. J.*, 2006, **12**, 4743.
- 32 M. G. Organ, M. Abdel-Hadi, S. Avola, I. Dubovyk, N. Hadei, E. A. B. Kantchev, C. J. O'Brien, M. Sayah and C. Valente, *Chem. Eur. J.*, 2008, **14**, 2443.
- 33 K. H. Hoi, J. A. Coggan and M. G. Organ, *Chem. Eur. J.*, 2013, **19**, 843.
- 34 K. Suzuki, Y. Hori and T. Kobayashi, *Adv. Synth. Catal.*, 2008, **350**, 652.
- 35 K. Suzuki, Y. Hori, Y. Nakayama and T. Kobayashi, *J. Synth. Org. Chem. Jpn.*, 2011, **69**, 1231.
- 36 Y. Nakayama, N. Yokoyama, H. Nara, T. Kobayashi and M. Fujiwhara, *Adv. Synth. Catal.*, 2015, **357**, 2322.
- 37 G. Mann, J. F. Hartwig, M. S. Driver and C. Fernández-Rivas, *J. Am. Chem. Soc.*, 1998, **120**, 827.
- 38 Gaussian 09, M. J. Frisch, G. W. Trucks, H. B. Schlegel, G. E. Scuseria, M. A. Robb, J. R. Cheeseman, G. Scalmani, V. Barone, G. A. Petersson, H. Nakatsuji, X. Li, M. Caricato, A. Marenich, J. Bloino, B. G. Janesko, R. Gomperts, B. Mennucci, H. P. Hratchian, J. V. Ortiz, A. F. Izmaylov, J. L. Sonnenberg, D. Williams-Young, F. Ding, F. Lipparini, F. Egidi,

- J. Goings, B. Peng, A. Petrone, T. Henderson, D. Ranasinghe, V. G. Zakrzewski, J. Gao, N. Rega, G. Zheng, W. Liang, M. Hada, M. Ehara, K. Toyota, R. Fukuda, J. Hasegawa, M. Ishida, T. Nakajima, Y. Honda, O. Kitao, H. Nakai, T. Vreven, K. Throssell, J. A. Montgomery, Jr., J. E. Peralta, F. Ogliaro, M. Bearpark, J. J. Heyd, E. Brothers, K. N. Kudin, V. N. Staroverov, T. Keith, R. Kobayashi, J. Normand, K. Raghavachari, A. Rendell, J. C. Burant, S. S. Iyengar, J. Tomasi, M. Cossi, J. M. Millam, M. Klene, C. Adamo, R. Cammi, J. W. Ochterski, R. L. Martin, K. Morokuma, O. Farkas, J. B. Foresman and D. J. Fox, *Gaussian Inc., Wallingford CT*, 2016.
- 39 P. J. Stephens, F. J. Devlin, C. F. Chabalowski and M. J. Frisch, *J. Phys. Chem.*, 1994, **98**, 11623.
- 40 Q. Zhang, J. Chen, Y. Cheng, L. Wang and D. Ma, *J. Mater. Chem.*, 2004, **14**, 895.
- 41 J. Wu, Y. Kan, Y. Wu and Z. Su, *J. Phys. Chem. C*, 2013, **117**, 8420.
- 42 D. Graves, V. Jankus, F. B. Dias and A. Monkman, *Adv. Funct. Mater.*, 2014, **24**, 2343.

3 SYNTHESIS AND ANALYSIS OF 1, 3-BIS(1-PHENYL-1H-BENZO[D]DIMIDAZOL-2-YL-BENZENE DERIVATIVES

3.1 Introduction

Benzimidazole derivatives have proven to be very effective in improving the charge injection and electron transport of OLED devices.¹ For instance, **TPBI** (Figure 3.1) is commonly used in the electron transport layer and as a host material for phosphorescent OLED devices. **TPBI** has the ability to provide good electron mobility and a large HOMO-LUMO energy gap to confine excitons in the emissive layer; in addition to a triplet energy of 2.7eV.²

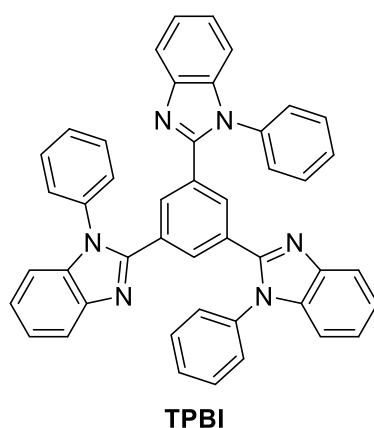


Figure 3.1: Molecular structure of **TPBI**.

TPBI is also known for its electron accepting ability. In this chapter we aim to retain the acceptor characteristic whilst increasing the triplet energy (E_T). Systematic structural variations will be performed in an attempt to increase E_T . Figure 3.2 illustrates the design strategy to remove a benzimidazole moiety with the aim of increasing the triplet energy. This strategic move was based upon a very well known literature example of **TCP** ($E_T = 2.82$ eV)³ and **MCP** ($E_T = 2.9$ eV)⁴, where removing one of the carbazole moieties results in a higher triplet energy (Figure 3.2). Utilising this knowledge, we hope to achieve higher triplet energy by removing one of the benzimidazole moieties to form bis-benzimidazole. The hetero atom of the benzimidazole moiety will be altered, followed by variation on the central phenyl. Photophysical

studies of these **TPBI** derivatives will be performed to conclude the effect of any variations made.

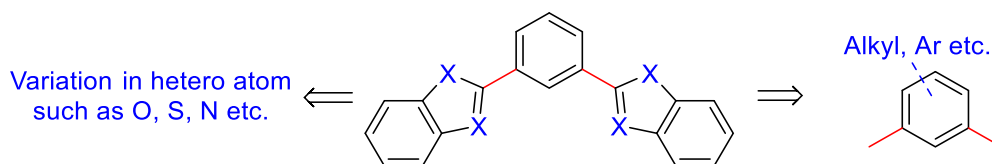


Figure 3.2: Systematic structural variation based on **DPBI**.

3.2 Results and Discussion

Benzimidazoles are bicyclic heterocycles, consisting of an imidazole ring fused with benzene, Figure 3.3. The synthetic procedures and properties of benzimidazole derivatives have been studied for more than one hundred years.

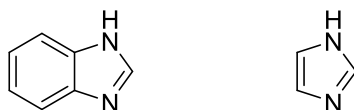


Figure 3.3: Molecular structure of benzimidazole (left) and imidazole (right).

The first benzimidazole (2,5-dimethylbenzimidazole) was prepared in 1872 by Hobrecker via the reduction of 2-nitro-4-methylacetanilide.⁵ Shortly after, 2,5-dimethylbenzimidazole was synthesised via the reaction of 3,4-diaminotoluene with acetic acid by Landenburg (Figure 3.4).⁶

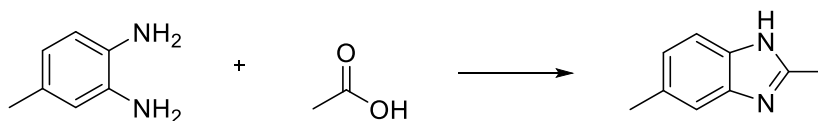


Figure 3.4: Synthesis of 2,5-dimethylbenzimidazole.

Benzimidazoles possess an extraordinary degree of stability; they are resistant to hot acids as well as alkalis.⁷ Oxidation and reduction of benzimidazole is challenging, and must be performed under harsh reaction conditions.⁸ Benzimidazoles are generally synthesised from *ortho*-phenyldiamines. *Ortho*-phenyldiamines are able to react with carboxylic acids, anhydrides, esters, acid chlorides etc. to yield the corresponding benzimidazole (Figure 3.5).⁹

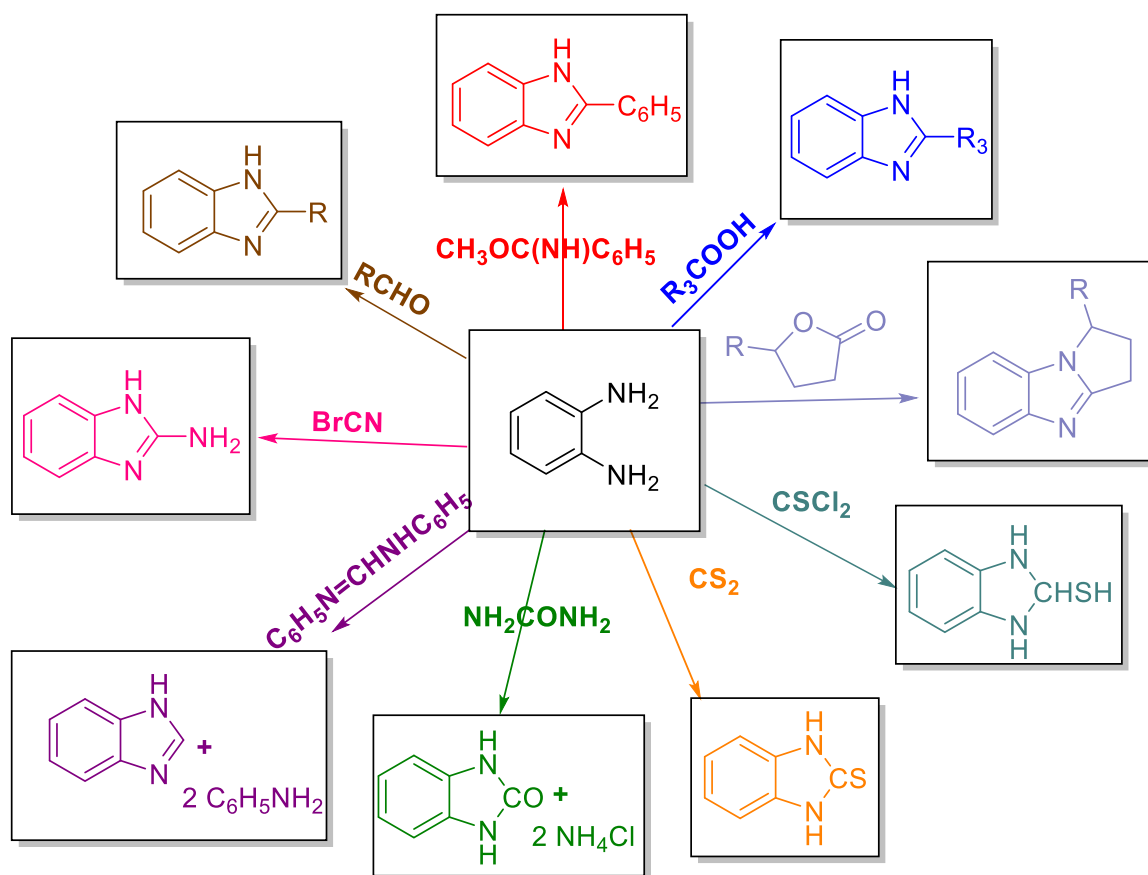


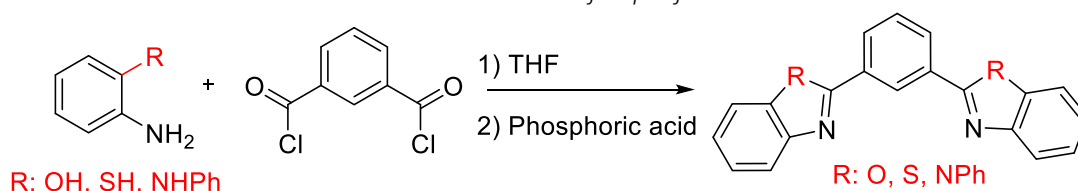
Figure 3.5: Formation of benzimidazoles using *ortho*-phenyldiamine.

3.2.1 Synthesis of First Generation DPBI Derivatives

A literature search on Scifinder for reaction scheme to synthesis **TPBI** resulted in ten procedures, nine of which are patented. This seemed strange, considering **TPBI**'s structure search results in 2733 results. The reported reaction conditions commonly utilised *ortho*-

phenyldiamine and aryl acid chloride derivatives to obtain **TPBI**.¹⁰ Typically acid chloride reacts with the amine to form the intermediate amide compound which then cyclises in the second step using an acid such as phosphoric acid. Thus, we employed Isophthaloyl chloride along with *ortho*-substituted aniline derivatives in order to afford target compounds. Compounds **DBT**, **DBO** and **DPBI** were achieved using **Method 4**, Table 3.1.

Table 3.1: Synthesis of **DPBI** derivatives via **Method 4**. Reactions performed using: Step 1) isophthaloyl dichloride (1eq.), *ortho*-aniline derivative (2.2eq.) and THF; Step 2) *o*-phosphoric acid. ^a Reaction under argon atmosphere. Yields were calculated after purification.

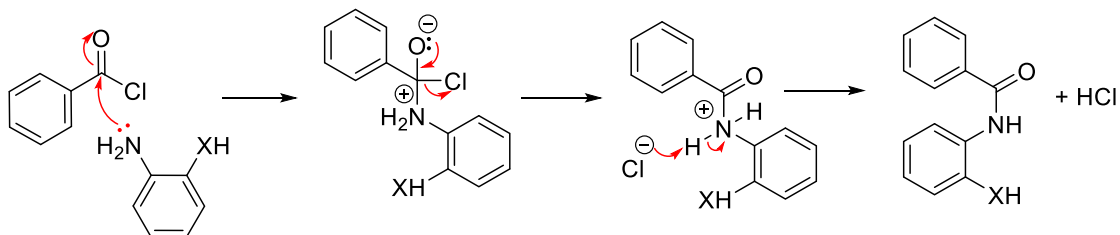


Entry	Code Name	Structure	Yield (%)
1	DBT (12)		46 ^a
2	DBO (13)		47
3	DPBI (14)		57

The **DPBI** derivatives were achieved using a two-step process, Table 3.1. Figure 3.6 illustrates the mechanism by which these hetero-x-azoles are formed. Firstly, nucleophilic addition/elimination takes place in presence of THF to afford the amide intermediate. The amide intermediate is then cyclised in the presence of *ortho*-phosphoric acid, affording the hetero-X-azole moiety, Figure 3.6. This reaction itself can be temperamental and **Method 4** doesn't always work as anticipated. This is mainly due to *ortho*-phosphoric acid being very

hydroscopic. We suspect this is due to the change in concentration of the *ortho*-phosphoric acid.

Step 1



Step 2

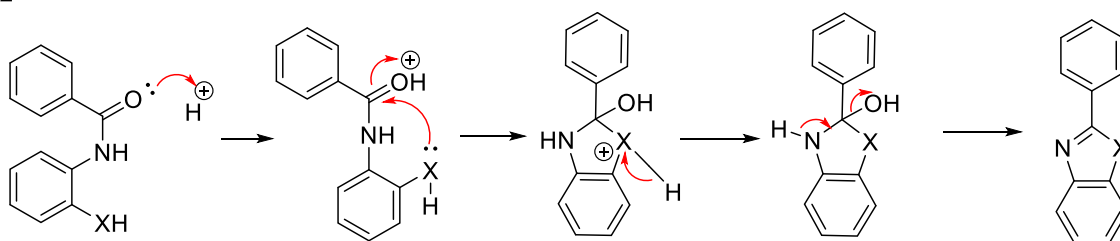


Figure 3.6: Step 1) Nucleophilic addition/elimination mechanism of amide intermediate; Step 2) Intramolecular nucleophilic substitution mechanism of hetero-X-azole formation.

There was an initial issue encountered with **DPBI** concerning its solubility and possible aggregation in the solid state. To understand this behaviour we analysed the X-ray crystal structure to investigate any source of π - π stacking within the molecule, in particularly focussing on the *N*-phenyl moiety (Figure 3.7a). We were unsuccessful in determining the source of possible π - π stacking in **DPBI** from the crystal structure. Figure 3.7b shows further investigation into crystal packing which shows the three molecules are well spaced out, thus eliminating any stacking. Figure 3.7c shows the two **DPBI** molecules within close vicinity, thus the spacing/stacking has been investigated further in Figure 3.7 d & e. Even though these molecules do appear to be in close proximity, there is no sign of π - π stacking as the phenyl rings do not align.

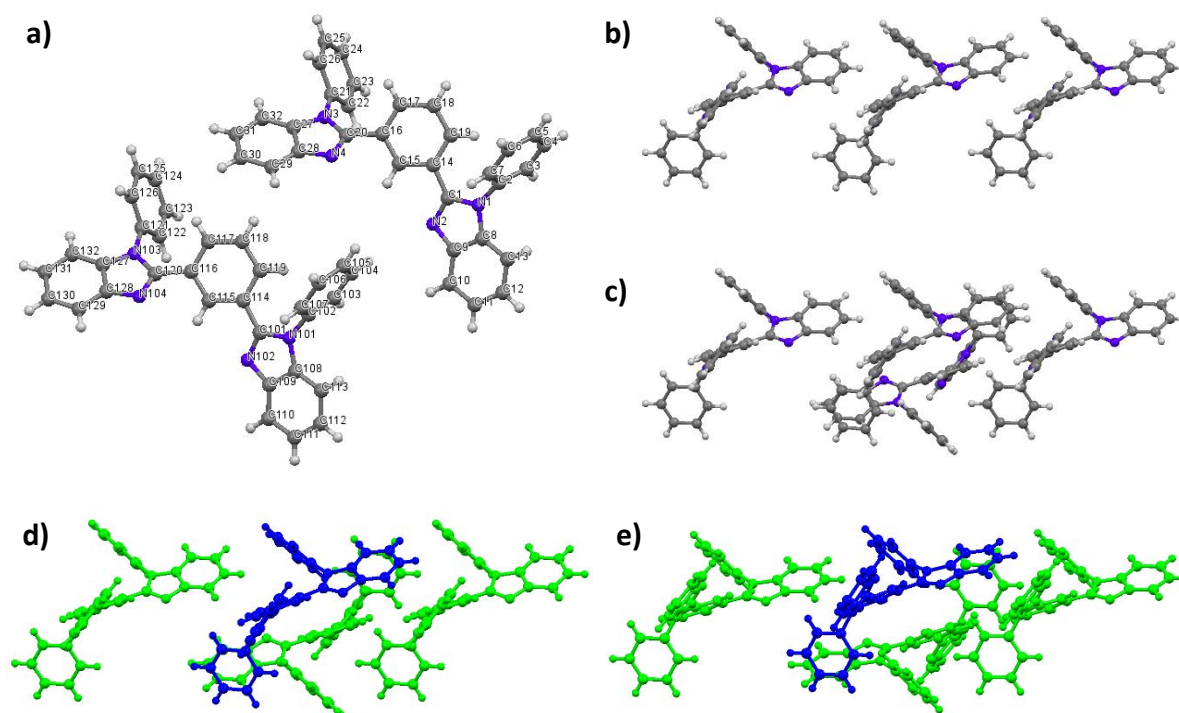


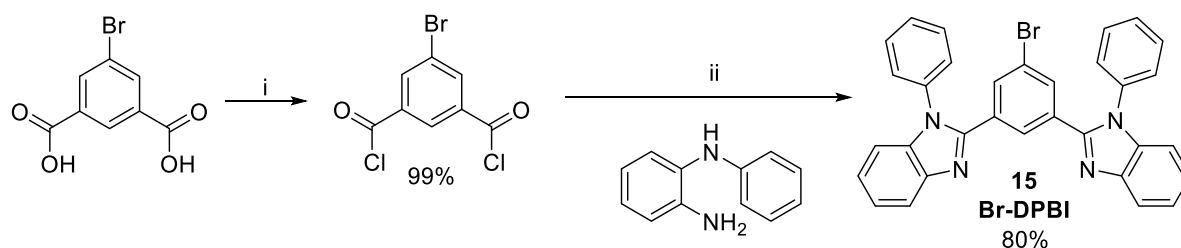
Figure 3.7: X-ray single crystal structure of **DPBI**.

3.2.2 Synthesis of Second Generation DPBI Derivatives

The aim of second generation **DPBI** derivatives was to improve solubility of **DPBI**. Benzimidazole characteristics were retained in the process to maintain the desired characteristics. Thus, **DPBI** derivatives were synthesised with variations on the central benzene ring. This design feature was thought to increase solubility of **DPBI** while having minimal effect of molecular electronics. Firstly, 2,2'-(5-bromo-1,3-phenylene)bis(1-phenyl-1H-benzo[d]imidazole) (**Br-DPBI**) was synthesised, Scheme 3.1. 5-bromoisophthalic acid was refluxed in thionyl chloride to form 5-bromoisophthaloyl dichloride. This was reacted further with *N*-phenyl-*o*-phenylenediamine to form **Br-DPBI** (80%) via **Method 4**.

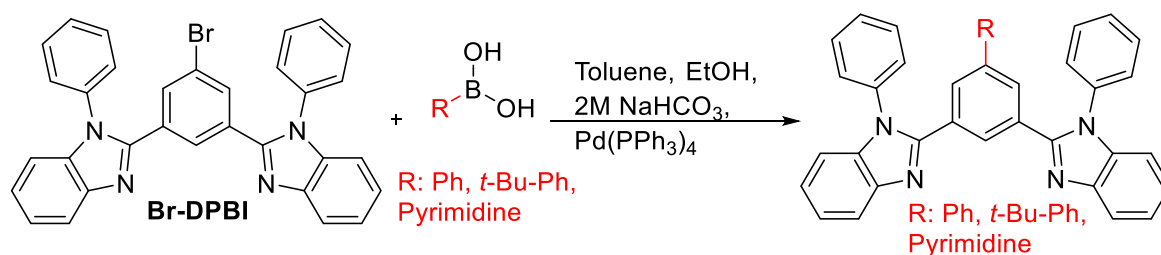
Aryl boronic acids were then employed to react with **Br-DPBI** via the Suzuki coupling reaction. We were able to synthesise **PH-DPBI**, **PH-T-DPBI** and **PY-DPBI** in reasonable yields using **Method**

5, see Table 3.2. Yet again the purification procedure was maximised to obtain the purest compound, rather than favouring a higher yield. Compounds were purified using a combination of recrystallisation and column chromatography in toluene.



Scheme 3.1: Synthesis of **Br-DPBI**. i) SOCl_2 (6eq.), reflux 3H; ii) **Method 4**: Step 1) Isophthalaldehyde (1eq.), ortho-aniline derivative (2.2eq.) and THF; Step 2) o-phosphoric acid.

Table 3.2: **DPBI** derivative synthesis via **Method 5**. Reactions performed using **Br-DPBI** (1 eq.), R-boronic acid (1.1 eq.), and $\text{Pd}(\text{PPh}_3)_4$ (2 mol%) under argon atmosphere. Yields were calculated after purification.



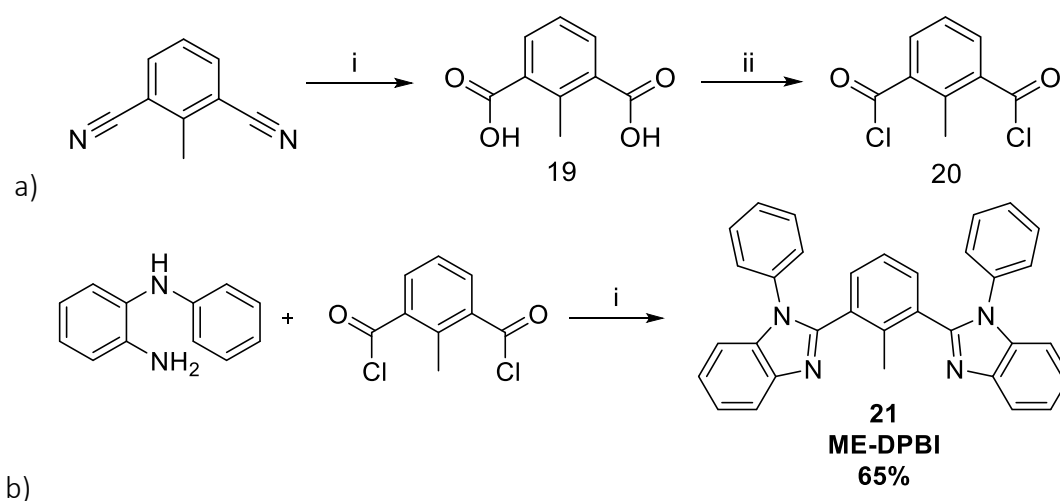
Entry	Code Name	R	Yield
1	PH-DPBI (16)		48
2	PHT-DPBI (17)		52
3	PY-DPBI (18)		27

3.2.3 Synthesis of Third Generation DPBI Derivative

Third generation **DPBI** was aimed to eliminate aggregation in the solid state. Introduction of a methyl group at position two of the central phenyl was hypothesised to possibly eradicate aggregation. Adding a methyl group would sterically block any possible π - π interactions

between the two *N*-phenyl rings of **DPBI** in the central position. This steric block should further decrease conjugation and, thus, lead to a higher triplet energy.

ME-DPBI (Scheme 3.2) was synthesised in a four step reaction procedure. Due to unavailability of the desired starting material, 2-methylisophthaloyl dichloride, 2, 6-dicyanotoluene was hydrolysed to form 2-methylisophthalic acid (Scheme 3.2). 2-methylisophthalic acid was reacted with SOCl_2 , resulting in the formation of 2-methylisophthaloyl dichloride via nucleophilic substitution. Subsequently, 2-methylisophthaloyl dichloride was reacted with *N*-phenyl-*o*-phenylenediamine via **Method 4**, affording **ME-DPBI** (65%) via a nucleophilic addition/elimination mechanism followed by intramolecular nucleophilic substitution.



Scheme 3.2: a) Synthesis of starting material for 2,2'-(2-methyl-1,3-phenylene)bis(1-phenyl-1*H*-benzo[*d*]imidazole)(**ME-DPBI**). i) Ethylene glycol and 14*M* NaOH refluxed at 180°C for 12 hours. Yield: 99% ii) SOCl_2 (excess) refluxed at 75°C for 4 hours. b) Synthesis of **ME-DPBI** via **Method 4**. i) Reactions performed using: 1) 2-Methylisophthaloyl dichloride (1 eq.), *ortho*-substituted aniline derivative (2.2 eq) and THF, 2) *ortho*-phosphoric acid. Yields were calculated after purification.

3.3 Computational Analysis of DPBI Derivatives

Computational analysis was performed in partnership with Marcus Taylor at the University of Birmingham, School of Chemistry. The HOMO-LUMO energies and minimum energy

conformations of the molecules were explored using a Gaussian program package 09.¹¹ The geometric and electronic properties of **TPBI** derivatives were analysed. The structures were optimised using B3LYP (Becke three parameters hybrid functional with Lee-Yang-Perdew correlation function) with the 6-31G (d) basis set.¹² Electronic properties of the minimised structures were then analysed using DFT (Density Functional Theory) and TD-DFT (Time-Dependent Density Functional Theory) to obtain the HOMO, LUMO and singlet energies. All calculations were performed in the gas phase and on a single molecule.

Table 3.3 presents the results from the computational analysis. Firstly, **TPBI** computational analysis was performed. Gaussian predicts the HOMO to be mostly situated on the benzimidazole moiety and the LUMO to be mostly situated on the central phenyl of **TPBI**. Using same parameters as **TPBI**, calculations for **DPBI** were performed. We can observe the HOMO surface is still predominantly situated on the benzimidazole moiety. The calculated HOMO value for both these compounds is -5.65 eV. The LUMO surface portrays similar features, but the LUMO value is marginally higher for **DPBI**. This results in a slightly higher HOMO-LUMO energy gap for **DPBI**, with a resultant figure of 4.44 eV.

The major difference in energies between these compounds is their calculated singlet and triplet energies. In the case of **TPBI**, singlet energy is 3.78 eV (328 nm) while the singlet energy of **DPBI** is calculated to be 3.92 eV (316 nm). As anticipated, we do observe a significant increase in triplet energy from 2.71 eV to 3.30 eV. The calculated triplet energy of **TPBI** does correlate well with the experimental measurements of 2.7 eV, as mentioned previously. In regard to the singlet-triplet gap, we notice a decrease in gap for **DPBI** which could be advantageous for TADF. Thus, we can conclude that we have successfully designed a

compound with higher energy, which should result in a blue shift for **DPBI** in comparison to the emission of **TPBI** and have a higher triplet energy than the parent **TPBI**.

Substituting the *N*-phenyl moiety of **DPBI** with a sulfur or oxygen atom results in opposite effects. The HOMO and LUMO orbitals are very similar for both of these compounds. The HOMO consists of orbitals right across the compounds whereas the LUMO majorly consists of orbitals on the central phenyl. The HOMO energy for both of these compounds is lower than that of **DPBI**. There is a significant decrease in LUMO energies for both **DBT** and **DBO**. This results in a lower HOMO-LUMO gap. It is interesting to note that DFT analysis predicts a slight red shift in the spectra of **DBT** and a blue shift in the case of **DBO**. In both cases, the triplet energies of these compounds are calculated to be higher than that of **TPBI**. However, the electronics of these compounds are significantly different to **TPBI**.

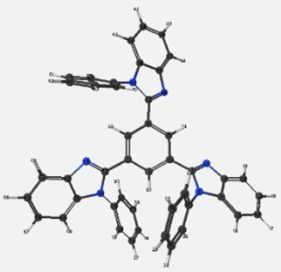
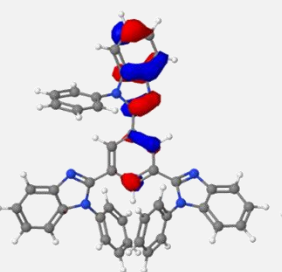
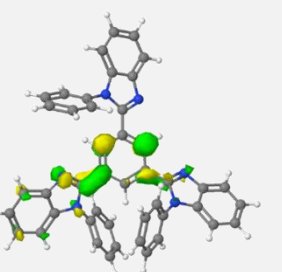
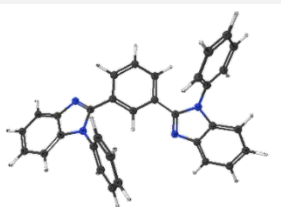
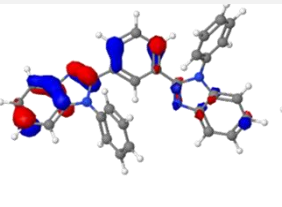
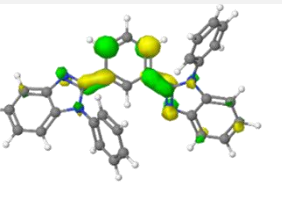
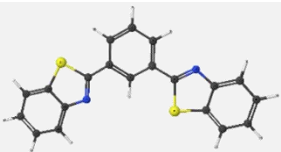
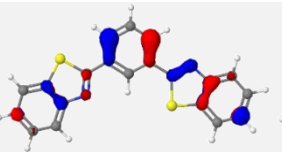
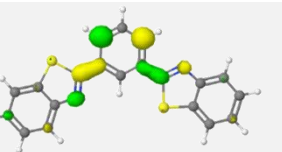
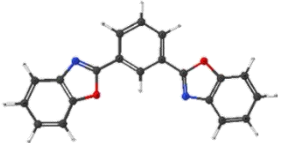
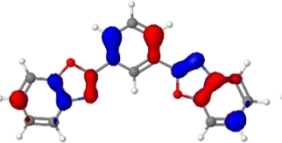
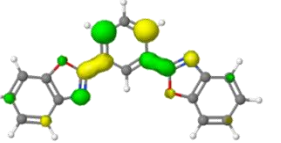
The DFT calculations for second generation **DPBI** derivatives suggest an insignificant change in the HOMO/LUMO values. The only change in these values is observed for **PY-DPBI**, where the HOMO/LUMO values are of lower energy while maintaining the HOMO/LUMO gap. The singlet energy for **PY-DPBI** is also lower, which should result in a red shift in the emission spectra. When focusing on the triplet energies, we observe exactly the same triplet energy for **DPBI**, **PH-DPBI** and **PHT-DPBI**. However, in the case of **PY-DPBI**, the triplet energy is slightly lower. From these calculations we can conclude that we have successfully added substituents to basic **DPBI** to increase solubility without significantly affecting the photophysics. In short, the DFT calculations for **ME-DPBI** look very promising. First, we compare the geometry optimised molecular structures of **TPBI**, **DPBI** and **ME-DPBI**. In the case of **TPBI**, the *N*-phenyl substituent, in essence, is able to overlap which could be a source of increased π - π conjugation, whereas in **DPBI** and **ME-DPBI** this phenomenon is not observed. This overlap between the *N*-phenyl

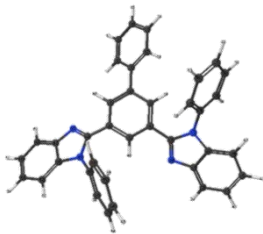
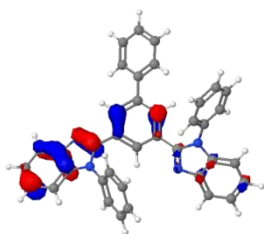
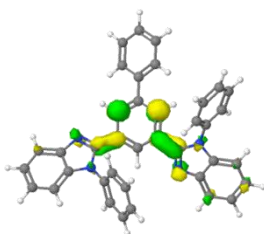
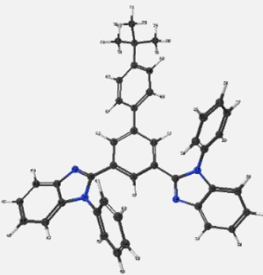
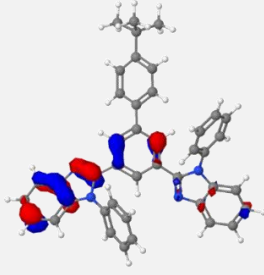
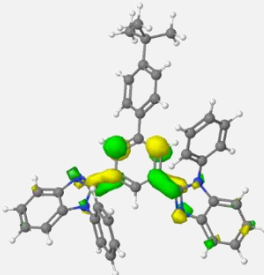
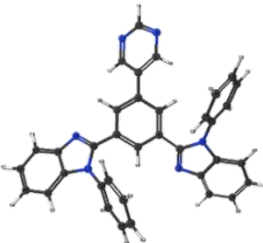
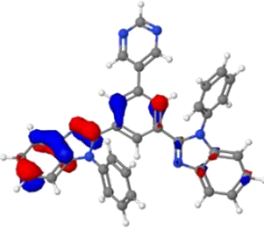
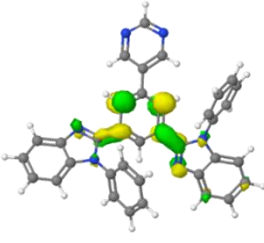
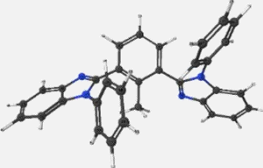
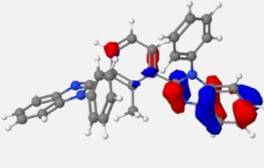
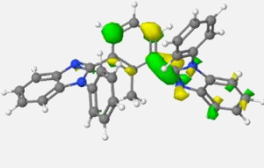
may be the source of aggregation in the solid state. The HOMO maps for these compounds are very similar to each other. Like **TPBI**, the HOMO mainly consists of the benzimidazole orbitals. However, the HOMO value is significantly decreased from ≈ -5.7 eV to ≈ -5.9 eV.

The LUMO of **ME-DPBI** mainly consists of orbitals on the central phenyl, like **TPBI** and **DPBI**. Even then, the LUMO value is slightly higher from ≈ -1.2 eV to ≈ -1.0 eV. A reduction in HOMO energy and increase in LUMO energy results in a higher HOMO/LUMO energy gap of ≈ 4.9 eV in comparison to a gap of ≈ 4.4 eV for **TPBI** and **DPBI**. Comparing the calculated singlet energies we can observe a trend. The singlet energy of **TPBI** (3.78 eV) is the lowest, followed by **DPBI** with singlet energy of 3.92 eV and **ME-DPBI** with the highest singlet energy of 4.23 eV.

Comparing the calculated triplet energies of these compounds we observe that they follow a similar trend to their singlet energies. In the case of **ME-DPBI** the computational studies predict an even further increase in triplet energy from **DPBI**. These studies predict an increase in triplet energy by 0.9 eV when compared to **TPBI**. The singlet/ triplet gap of **ME-DPBI** is the same as that of **DPBI**. From these computational analyses of **ME-DPBI** we can conclude that we have been able to solve the issue of aggregation in the solid state whilst further increasing the triplet energy.

Table 3.3: Visual presentation of geometry optimised molecular structure, HOMO surface, HOMO value, LUMO surface, LUMO, HOMO-LUMO gap and singlet value of **TPBI** and **DPBI** series from density functional theory (DFT) calculations. All values in electron volts (eV)

	Geometry Optimised Structure	HOMO	LUMO	Cal. HOMO	Cal. LUMO	E_g	E_s	E_T	ΔE_{ST}
TPBI				-5.65	-1.25	4.40	3.78	2.71	1.07
DPBI				-5.65	-1.21	4.44	3.92	3.30	0.62
DBT				-6.06	-1.84	4.22	3.84	3.02	0.82
DBO				-6.04	-1.73	4.31	3.94	3.11	0.83

<i>PH-DPBI</i>				-5.66	-1.24	4.43	3.90	3.30	0.60
<i>PHT-DPBI</i>				-5.64	-1.21	4.44	3.89	3.30	0.59
<i>PY-DPBI</i>				-5.82	-1.45	4.37	3.83	3.26	0.57
<i>ME-DPBI</i>				-5.87	-1.02	4.85	4.23	3.61	0.62

3.4 In solution Photophysical Analysis of DPBI Derivatives

In solution photophysical studies of **DPBI** derivatives were carried out in two polar solvents DCM and THF, and two comparatively non-polar solvents CLB and TOL. The absorption dependence on concentration of **DPBI** derivatives was measured. **DPBI** absorbance in DCM at low concentrations is shown in Figure 3.8. There seems to be high solvent interactions with **DPBI** derivatives causing noticeable shifts. Also, due to the absorbance of the compounds being within close proximity of solvent absorbance, the calculated epsilon values do not always correlate well. In solution studies performed at Durham University by C. Corward show similar λ_{abs} values to those achieved by our studies, Figure 3.8d.

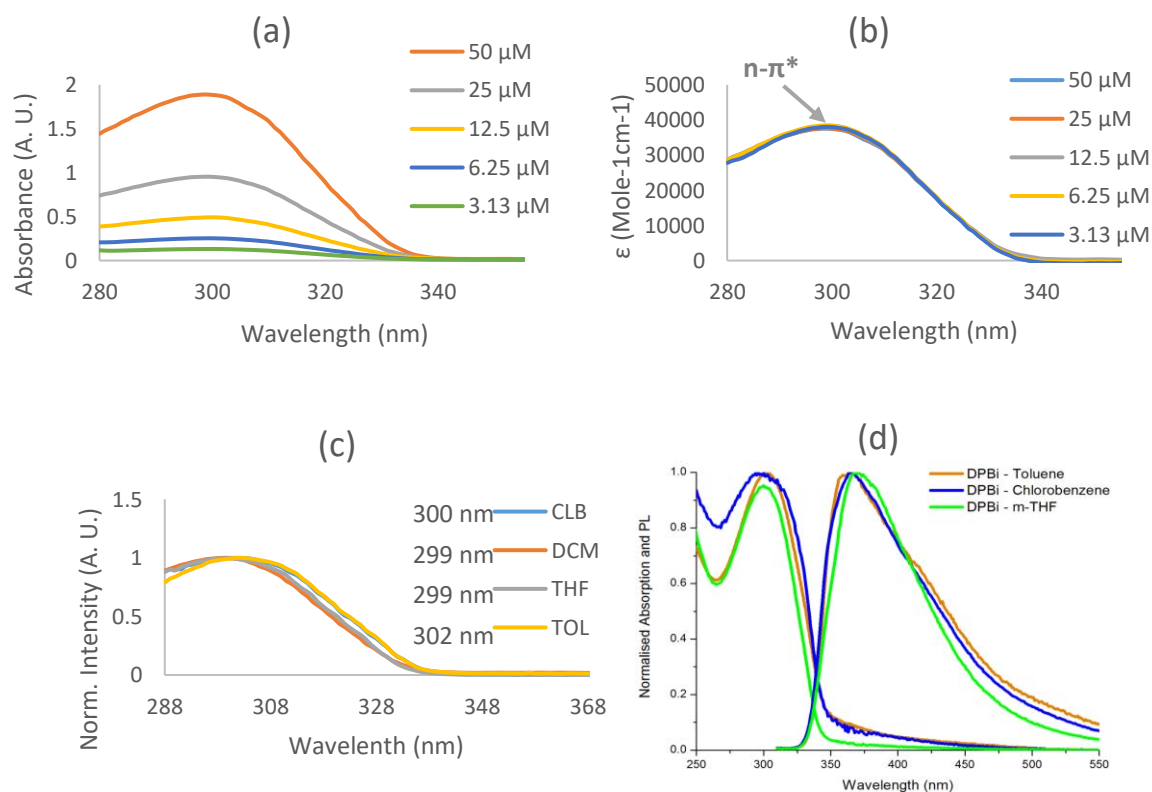


Figure 3.8: (a) Absorption spectra of **DPBI** in DCM. (b) Plot of the calculated epsilon values against wavelength for **DPBI** in DCM. (c) Norm. absorption spectra of **DPBI** in CLB, DCM, THF and TOL. (d) Absorptions and photoluminescence of **DPBI** measured at Durham University.

Figure 3.8 shows the absorption comparison between the first generation **TPBI** derivatives in CLB, DCM, THF and TOL. These studies show a red shift when the *N*-phenyl is substituted with sulfur or oxygen. The graphs also show slight solvent effect, which causes minor shifts in A_{max} values. Overall, the absorption spectra are quite featureless. Thus, we are unable to determine the $S_0 \rightarrow S_1$ transition with any certainty. However, we can assign the peak around 300 nm to be an $n\text{-}\pi^*$ transition, which is observed in all compounds.

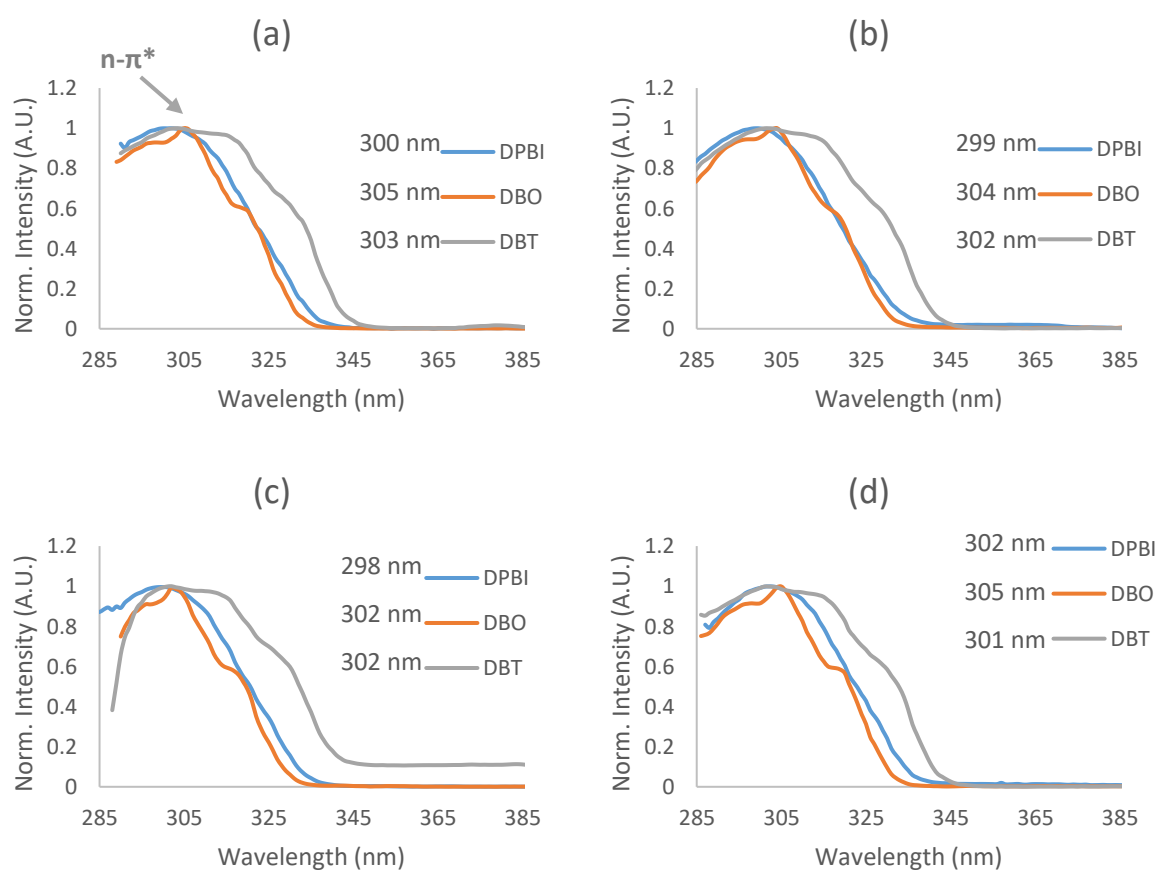


Figure 3.9: (a) Absorption spectra of **TPBI** derivatives in CLB at low concentrations. (b) Absorption spectra of **TPBI** derivatives in DCM at low concentrations. (c) Absorption spectra of **TPBI** derivatives in THF at low concentrations. (d) Absorption spectra of **TPBI** derivatives in TOL at low concentrations. (The values on the spectra are the A_{max} for each compound)

Following the measurements of first generation derivatives, we analysed the absorption spectra for second generation **DPBI** derivatives. Concentration dependency was investigated which showed no surprising measurements. In comparison to **DPBI**, we do observe a slight red

shift for the second generation **DPBI** derivatives. Similar to the data for the first generation, the absorption spectra for the second generation is also quite featureless. This limits our ability to determine $S_0 \rightarrow S_1$ transition with any certainty. All the second generation derivatives also show $n-\pi^*$ transition around 300 nm.

When looking at solvent effect, we observe minimal solvent effect for **PH-DPBI** and **PY-DPBI**, Figure 3.10. However, the λ_{abs} of **PHT-DPBI** varies from 290 to 303 nm. We believe the λ_{abs} of **PHT-DPBI** should be similar to that of **PH-DPBI** (≈ 302 nm). Analyses of the second generation **DPBI** derivatives were also performed at Durham University which peaked at ≈ 300 -310 nm, evidence of which is provided in appendix ii.

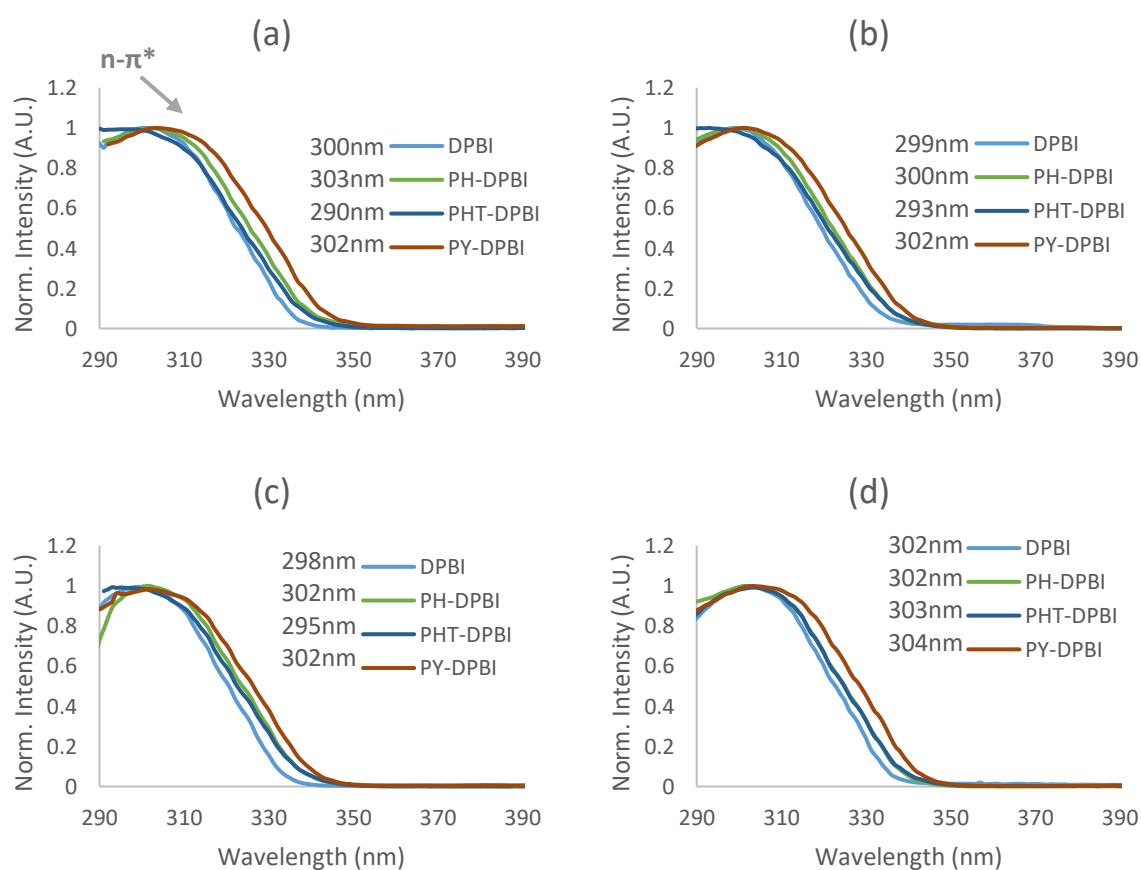


Figure 3.10: (a) Absorption spectra of **DPBI** derivatives in CLB. (b) Absorption spectra of **DPBI** derivatives in DCM. (c) Absorption spectra of **DPBI** derivatives in THF. (d) Absorption spectra of **DPBI** derivatives in TOL. (The values on the spectra are the λ_{abs} for each compound.)

The absorbance of **ME-DPBI** was analysed. However, the results were not reliable. This was mainly due to high solvent interactions and due to the absorbance of **ME-DPBI** being within close proximity to the solvent absorbance. As such, the absorbance and excitation spectra are not in agreement with each other.

When considering epsilon calculations, the absorption data in DCM illustrated some correlation in the highly concentrated solutions, Figure 3.11. In comparison to **DPBI**, we can say for certain that there is a blue shift of the λ_{abs} for **ME-DPBI**. An example is illustrated in Figure 3.10 to show the comparison between absorption spectra of **DPBI** and **ME-DPBI** in DCM. We observe this blue shift in all of the solvents.

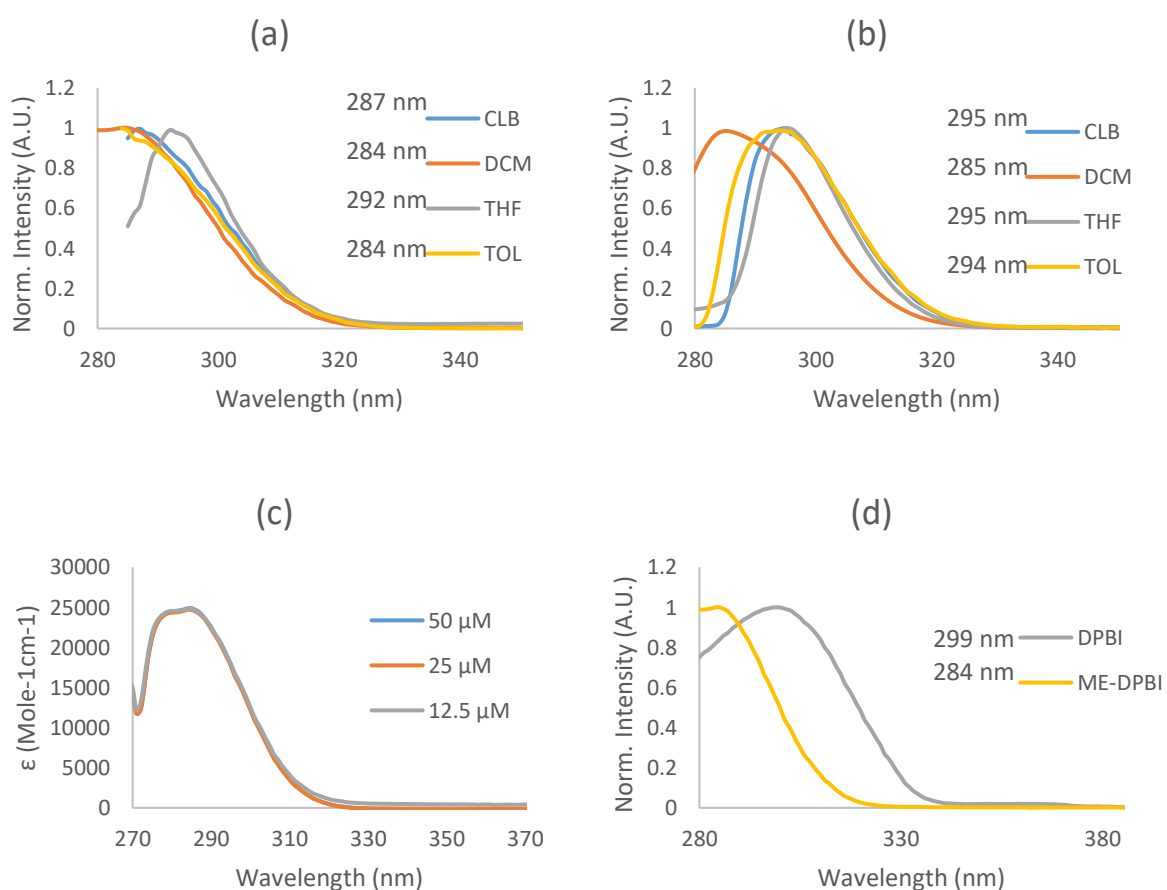


Figure 3.11: (a) Absorption of **ME-DPBI** derivatives in CLB, DCM, THF and TOL. (b) Excitation spectra of **ME-DPBI** derivatives in CLB, DCM, THF and TOL. (c) Plot of the calculated epsilon values against wavelength for **ME-DPBI** in DCM. (d) Comparison of absorption spectra of **DPBI** and **ME-DPBI** in DCM. (The values on the spectra are the λ_{abs} for each compound.)

Table 3.4 summarises the findings from the in solution absorption spectra analyses. Table 3.4 shows the absorption maximum for each compound in all four solvents. The absorption max represents the $n-\pi^*$ transition. Normally we are able to identify the $S_0 \rightarrow S_1$ transition. However, due to the spectra being so featureless we are unable to identify this transition with any certainty. **TPBI** has an absorption max value of 303 nm (4.09 eV) in DCM.¹³ Comparing the **DPBI** derivatives with **TPBI**, the only significant differences are in the values for **PH-T-DPBI** (4.19 eV) and **ME-DPBI** (4.32 eV). Therefore, we can conclude that the first generation of **TPBI** derivatives did not have a significant impact on the absorption spectra.

Table 3.4: Table to summarise the findings of the absorption studies of **DPBI** derivatives in chlorobenzene, dichloromethane, tetrahydrofuran and toluene. The table shows the λ_{max} for each compound which corresponds to the $n-\pi^*$ transition.

	<i>CLB</i>	<i>DCM</i>	<i>THF</i>	<i>TOL</i>	<i>Average</i>
	(nm)	(nm)	(nm)	(nm)	(nm)
DPBI	300	299	298	302	300 (4.13 eV)
DBT	303	302	302	301	302 (4.11 eV)
DBO	305	304	302	305	304 (4.08 eV)
PH-DPBI	303	300	302	302	302 (4.11 eV)
PH-T-DPBI	290	293	295	304	296 (4.19 eV)
PY-DPBI	302	302	302	303	302 (4.11 eV)
ME-DPBI	287	284	292	284	287 (4.32 eV)

In solution emission analyses were performed on **DPBI** derivatives. First, we investigated the emission dependence on concentration. Figure 3.12 shows the emission spectra of **DPBI** and **ME-DPBI** in DCM at low concentrations. From the spectra it is interesting to note that in DCM we observe concentration quenching for the 50 μ M solution of **DPBI**, but we do not observe

this phenomenon for the 50 μM solution of **ME-DPBI**. Concentration quenching is observed across the **DPBI** with the exception of **ME-DPBI**, which could be a sign of the potential aggregation issue being solved. Apart from high concentration quenching, the data correlates well across the series when normalised.

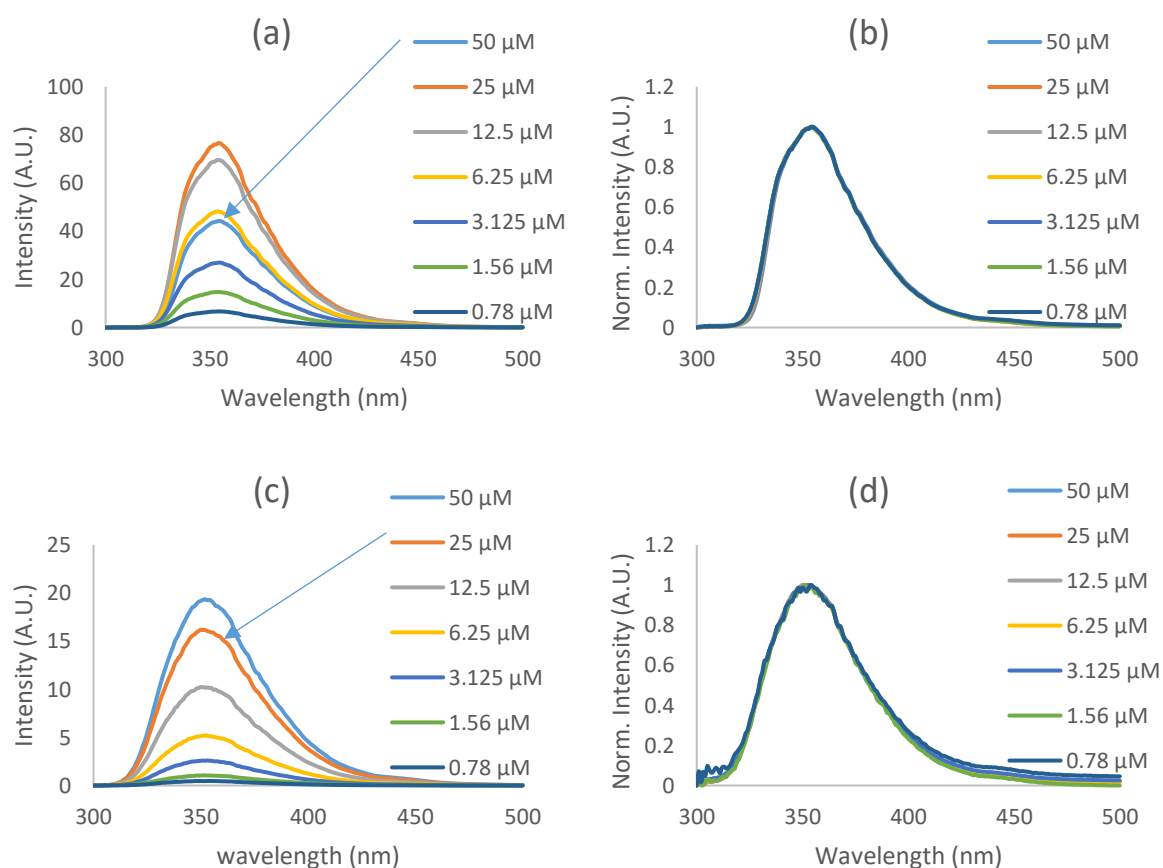


Figure 3.12: (a) Emission spectra of **DPBI** in DCM at low concentrations. (b) Normalised emission spectra of **DPBI** in DCM. (c) Emission spectra of **ME-DPBI** in DCM at low concentrations. (d) Normalised emission spectra of **ME-DPBI** in DCM.

The solvent effect on the emission spectra is compared in Figure 3.13. The normalised emission spectra for all **DPBI** derivatives in all four solvents are displayed. At a glance it appears that the emission spectra are red shifted in THF. However, upon closer inspection, we can observe that the spectra widen. Although THF has a broadening effect on emission spectra, the λ_{PL} of all compounds remains the same or within very close proximity to the λ_{PL} in other solvents. When

considering to the emission spectra of **DPBI** derivatives in CLB, DCM and TOL, the data sets are in agreement with, or within close proximity to each other. Thus, we can conclude that there is minimal solvent effect on emission for these compounds.

Next the effect of structural variation on emission relative to **DPBI** as the base compound was analysed. We observe an approx. 8 nm red shift when the *N*-phenyl of **DPBI** is substituted with sulfur (**DBT**). We also observe the emission spectra for **DBT** being irregular. This is due to the emission capability of the compound. All the parameters for the emission were kept the same throughout the series in order for the comparison to be accurate.

Substituting the *N*-phenyl of **DPBI** with an oxygen atom results in an approx. 5 nm blue shifted emission profile. When studying the second generation **DPBI** derivatives, we only observe a red shift for the **PY-DPBI**. On the whole this is a positive result, as we have managed to successfully alter the **DPBI** solubility without having a significant impact on the emission in the case of **PH-DPBI** and **PH-T-DPBI**.

Concerning the third generation **DPBI**, **ME-DPBI** emission is red shifted in THF which is due to solvent effect. However, if we compare the emission spectra in other solvents we observe an identical λ_{PL} to **DPBI**. In conclusion, we have successfully managed to perform some structural variation without having a significant impact on the emission capabilities of these compounds. As such, we still expect them to emit in the region of deep blue.

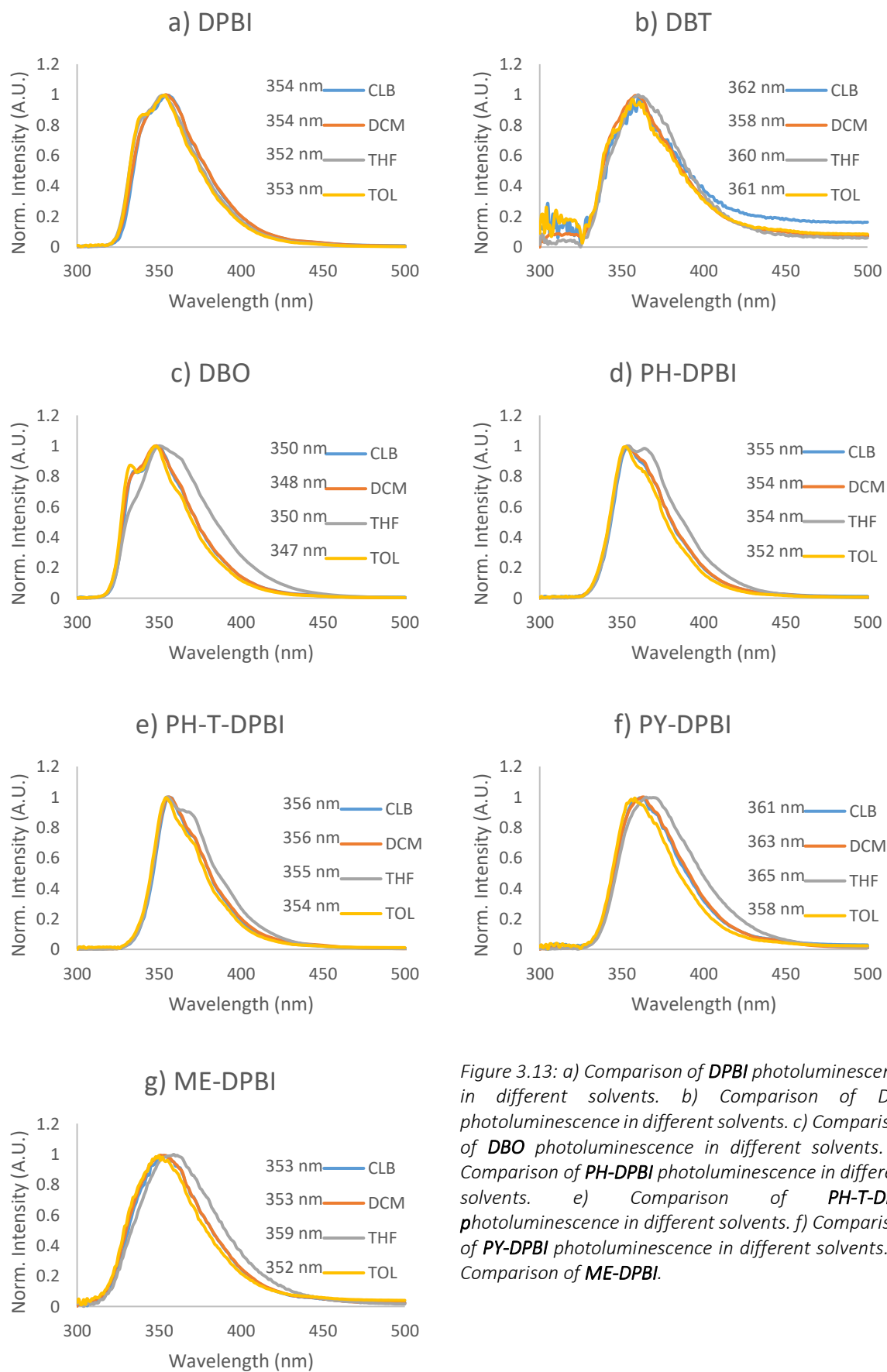


Figure 3.13: a) Comparison of **DPBI** photoluminescence in different solvents. b) Comparison of **DBT** photoluminescence in different solvents. c) Comparison of **DBO** photoluminescence in different solvents. d) Comparison of **PH-DPBI** photoluminescence in different solvents. e) Comparison of **PH-T-DPBI** photoluminescence in different solvents. f) Comparison of **PY-DPBI** photoluminescence in different solvents. g) Comparison of **ME-DPBI**.

Fluorescence lifetimes of the **DPBI** series were measured and the samples were excited using a 290 nm laser. As discussed previously, fluorescence lifetime decay data was collected until the photon count reached 10,000. The lifetime decay data is summarised in Table 3.5 and complete data is attached in appendix ii along with the fits. Although we do anticipate the decay lifetime to be short, we observe the decay to be almost instantaneous for all TPBI series.

Table 3.5: Lifetime decay measurements of **DPBI** series in nanoseconds (ns). The fit (χ^2) values are available in appendix ii.

	<i>DCM (ns)</i>	<i>TOL (ns)</i>	<i>THF (ns)</i>	<i>CLB (ns)</i>
<i>DBT</i>	2.08	1.83	2.56	1.72
<i>DBO</i>	2.24	2.21	2.67	2.02
<i>DBPI</i>	1.47	1.36	1.61	1.39
<i>PH-DPBI</i>	3.14	3.42	3.92	3.18
<i>PHT-DPBI</i>	3.90	4.04	4.56	3.88
<i>PY-DPBI</i>	2.61	1.68	1.98	2.38
<i>ME-DPBI</i>	1.54	1.95	1.51	1.42

3.5 Solid State Photophysical Analysis of TPBI Derivatives

Solid state photophysical studies of MCP derivatives were carried out by Christopher Coward and Prof. Andrew P. Monkman in the Physics Department of Durham University. Initially, measurements of **DPBI** (NXS-23-U) drop cast films were made from either toluene or chlorobenzene, which resulted in broad, featureless emission spectra which peaked at ≈ 375 nm, see Figure 3.14. These spectra are rather different to dilute solution spectra. These thin films were also analysed to obtain phosphorescence spectra which gave poor data, such that they were unable to determine the triplet energy of **DPBI** with any certainty. Due to the dimerization/aggregation in the solid state of **DPBI**, measurements were made in “solid solution”. Here, **DPBI** is dissolved at low concentration into an inert host matrix, Zeonex (a branched polyolefin used in the manufacture of compact discs etc.). In this way, it was possible to spatially separate **DPBI** molecules and obtain isolated **DPBI** molecule in the solid state.

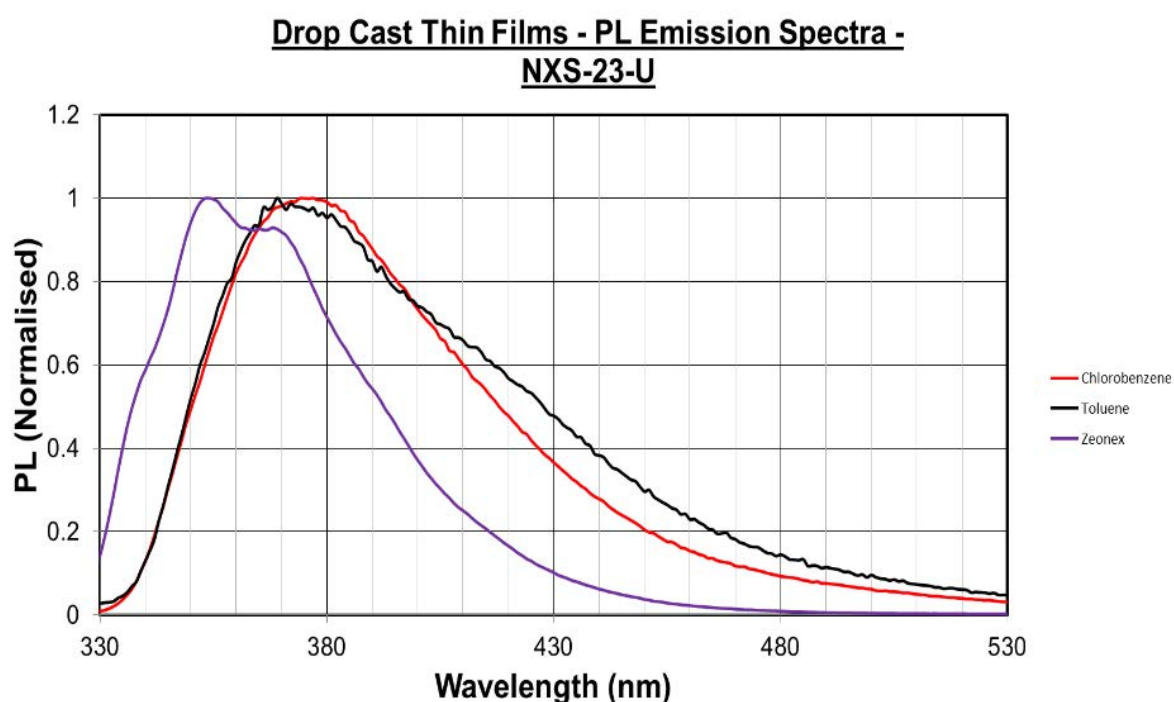


Figure 3.14: Fluorescence of **DPBI** from films drop casted from chlorobenzene (red), toluene (black) and Zeonex (purple).

The **DPBI**/Zeonex matrix film was analysed. Figure 3.15 shows the absorption, fluorescence and phosphorescence spectra of this film. To measure phosphorescence spectra, the sample was excited at 337 nm using a nitrogen laser (the most UV laser available). The excitation resulted in phosphorescent spectra, shown in Figure 3.15, indicating a triplet energy which was calculated to be 3.43 eV (361 nm). This is a significantly higher triplet energy than anticipated from computational analysis (3.30 eV). Encouragingly, this triplet energy is much higher than that of the parent **TPBI** molecule (2.73 eV).

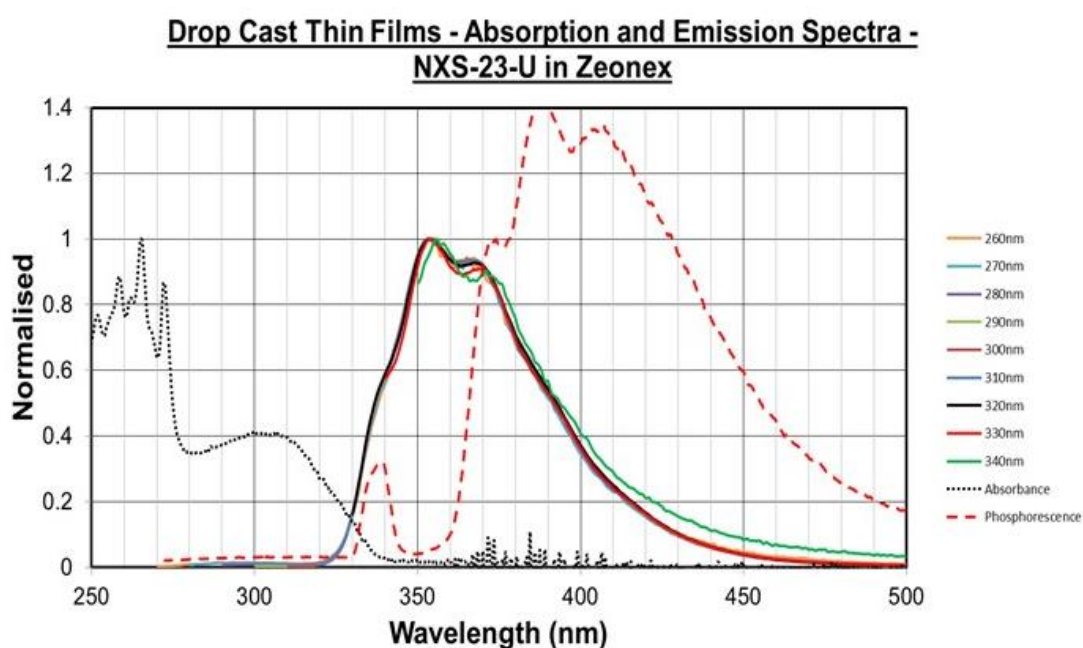


Figure 3.15: Absorption, emission and phosphorescence (obtained at 15K) spectra of **DPBI** in Zeonex. The sample was excited at different wavelengths to obtain the photoluminescence profile, the excitation wavelengths are depicted above. The peak at 337 on the phosphorescence profile is due to excitation.

Owing to the very high triplet energy of **DPBI**, Samsung research and development department requested a sample for testing. Samsung HQ measured the triplet energy level of **DPBI** using a frozen Me-THF (≈ 137 K) set-up, Figure 3.16. The studies at Durham were performed using Zeonex at ≈ 15 K. The value obtained by Samsung HQ was 2.71 eV, which is much lower than the 3.43 eV measurement in Zeonex. Both these measurements are reproducible and have been confirmed. Surprisingly, this is exactly the same triplet energy as that of **TPBI**.

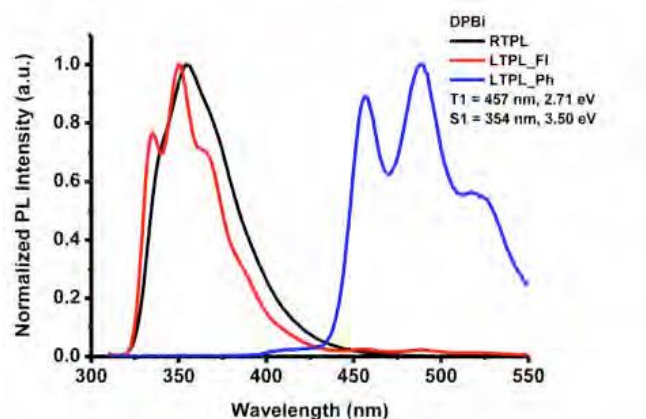


Figure 3.16: Normalized photoluminescence emission spectra of **DPBI** measured by Samsung; fluorescence at room temperature (black), fluorescence at low temperature (red), and phosphorescence at 137K in Me-THF (blue).

Looking at the current literature we found **MPBI** (Figure 3.17) to have a triplet energy of 3.17 eV.¹⁴ **DPBI** and **TPBI** have the same triplet energy of 2.7 eV whilst the triplet energy of **MPBI** is higher. This indicates an emitting state existing in both **DPBI** and **TPBI** but not **MPBI**. Furthermore, as **DPBI** is expected to have a higher triplet energy than **TPBI**, the emitting states must originate from some form of supramolecular interactions. Subsequently, our hypothesis is that there are two conformers possible in both **DPBI** and **TPBI**, Figure 3.17.

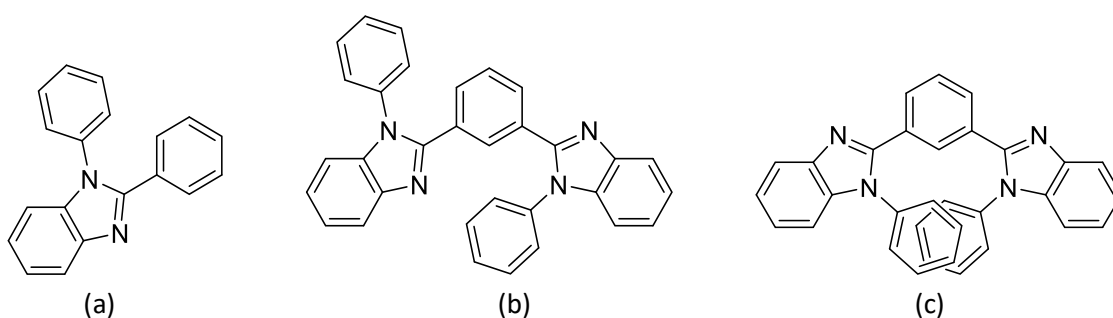


Figure 3.17: Figure to show molecular structure of **MPBI** (a), trans conformation of **DPBI** (b) and cis conformation of **DPBI** (c).

The cis conformations lead to dimer-like states of lower triplet energy ($E_{T(\text{trans conf.})} > E_{T(\text{cis conf.})}$), as the composition effectively increases conjugation. This cis confirmation may well be the most stable form of the molecule and we believe this is the geometry present in both solution and solid state. In this case, the cis conformation molecular emission would be red shifted by the

π - π overlap of the phenyl rings. However, this then implies that the measurements are of the red shifted energies of the closed form.

As the same geometry confirmation is possible with **TPBI**, this explains why the triplet energies are the same. However, in **MPBI**, such intramolecular confirmation is not possible, hence, the higher triplet energy. Our hypothesis is further reinforced via computational analysis.

Gaussian predicts the optimised geometry for **TPBI** to have the *N*-phenyl moieties within close proximity of each other, Figure 3.18. Indeed, such conformations will be dependent on the environment, with some favouring the closed geometry while others favour the open geometry. There remains a possibly of a range of compositions. In an attempt to block the intramolecular stacking by steric hindrance, **ME-DPBI** was designed and synthesised.

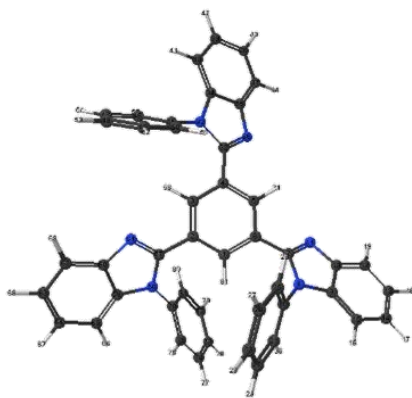


Figure 3.18: Geometry optimised molecular structure of **TPBI**.

Encouraged by the high triplet energy of **DPBI** before the measurements by Samsung, exciplex formation with **DPBI** as an acceptor was investigated. This requires the use of wide band gap donor compounds. A selected few donor materials were chosen for exciplex investigation. First, the emission profiles of potential donor compounds were analysed, Figure 3.19. Using **DPBI** as an acceptor compound, thin films were produced in Zeonex with partner donor

compounds. Figure 3.19 shows clear exciplex emission for four pairings with **DPBI**. Two of these pairings were investigated further below.

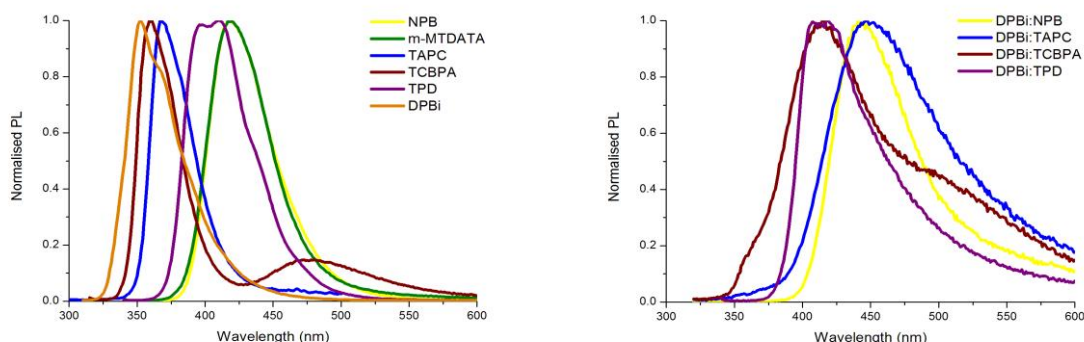


Figure 3.19: a) Photoluminescence of potential donor/Zeonex films (left). b) Exciplex emission between **DPBI** and donor compounds (right).

TAPC was one of the prime candidates for blue emission with a triplet energy of 2.85 eV, Figure 3.20.¹⁵ Figure 3.21 shows the analysis of a drop cast film consisting of a mixture of **DPBI:TAPC** (1:1wt%) which yields a clear exciplex emission. The spectral position of the exciplex emission is very promising for a blue emitter, spanning 390-500 nm, and peaking at 435 nm. However, the overlap between the emission and phosphorescence spectra, Figure 3.20b, suggests the emission at ≈ 435 nm actually corresponds to the π - π^* triplet. This leads to charge transfer state quenching by a lower lying triplet excited state. This, would lead to a moderately efficient device, enhanced through triplet fusion rather than TADF.

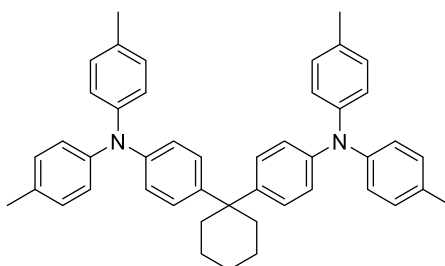


Figure 3.20: Molecular structure of **TAPC**.

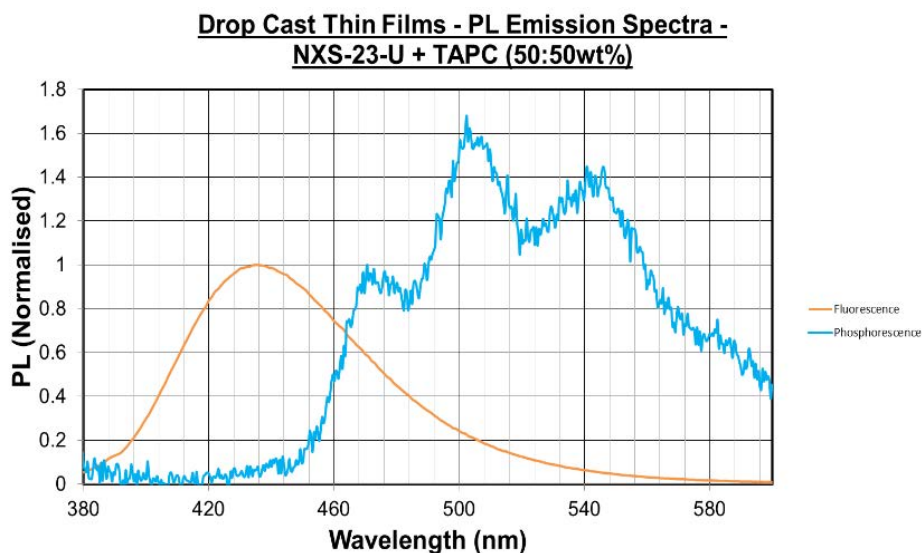


Figure 3.21: Exciplex emission from thin film of **DPBI:TAPC** and long lifetime emission to illustrate that the **TAPC** triplet state is quenching the exciplex.

As seen previously, substituting **TAPC** with **NPB** (Figure 3.22) also results in exciplex emission. Figure 3.23 shows the emission of pure compound thin films and how they compare to the exciplex emission. Interestingly, in comparison to **TPBI:TAPC** exciplex emission the **DPBI:NPB** thin films yield an exciplex centred at 444 nm with better colour purity. This makes it ideal for blue OLEDs. In summary, **DPBI** does have the capability to form an exciplex with the correct choice of donor material. Even though the experimental analysis shows no real increase in the triplet energy of **DPBI**, we are able to obtain devices with better colour purity when compared to **TPBI**.

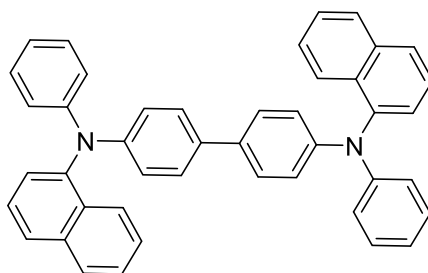


Figure 3.22: Molecular structure of **NPB**.

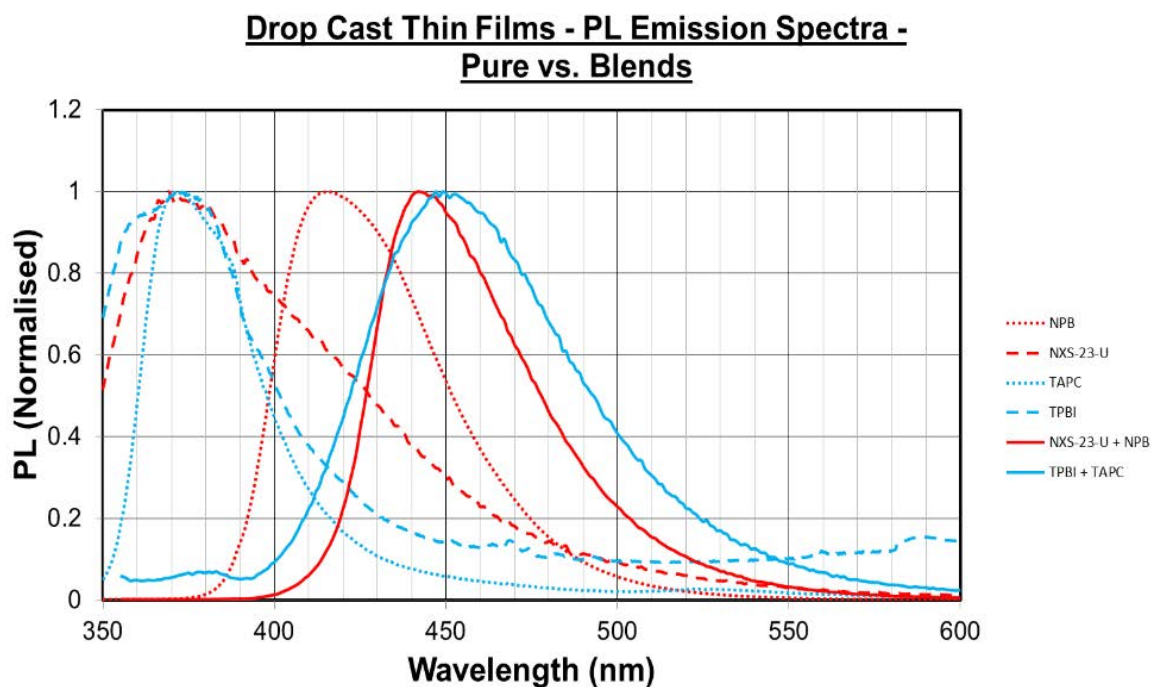


Figure 3.23: a) Molecular structure of **NPB**. b) Spectral compendium of **TPBI** and **DPBI** with donor compound to form exciplex.

Following the success of exciplex formation using **DPBI** under photoluminescence, OLED devices were formulated and their electroluminescence performance was measured. Many different device configurations were tried in order to optimise the charge transport balance within the device to achieve a high efficiency blue exciplex device. Table 3.6 shows six attempts at an efficient blue device. Current voltage for some of these devices can be viewed in appendix ii. In short, blue emitting devices were produced with a peak EQE of 1.70% using **DPBI**. We have been able to achieve a higher EQE of 6% using **DPBI**, but unfortunately it emits in the green region.

Table 3.6: Table to show exciplex devices using **DPBI** and their peak EQE. The values in bracket represent the layer thickness in nanometres.

	Emitting Layer	Device Structure	EQE (%)
1	DPBI:NPB (40)	ITO/TAPC(40)/DPBI:NPB/TPBI(20)/BCP(20)/LiF(1)/Al(70)	1.20
2	DPBI:NPB (30)	ITO/NPB(30)/DPBI:NPB/TPBI(60)/LiF(1)/Al(70)	1.60
3	DPBI:NPB (30)	ITO/NPB(30)/TAPC(10)/DPBI:NPB/TPBI(60)/LiF (1)/Al (70)	1.55
4	DPBI:TAPC (40)	ITO/NPB(40)/DPBI:TAPC/TPBI(20)/BCP(20)/LiF (1)/Al (70)	1.70
5	DPBI:TAPC (30)	ITO/NPB(30)/TAPC(10)/DPBI:TAPC/TPBI(60)/LiF(1)/Al(80)	0.60
6	DPBI:TAPC (30)	ITO/NPB(30)/TAPC(10)/DPBI:TAPC/TPBI(60)/BCP(20)/LiF(1)/Al(80)	6.00

Photophysical data for second generation **DPBI** were side-lined. From second generation **DPBI**, we presume the triplet energies to be similar to **DPBI**. We presume that the solubility of these compounds would be slightly better. However, we cannot assume this would translate well in terms of vacuum evaporation to formulate solid process thin films.

Some solid state studies have been performed for **ME-DPBI**, including device fabrication. Firstly, we compare the photophysical properties of a solution processed thin film of **ME-DPBI**, Figure 3.24. Solution processed thin films result in exactly the same absorptions and emissions when formulated from TOL, CLB or THF. A second thin film was produced in solid solution Zeonex which is compared with film produced from Toluene, Figure 3.24. As illustrated in the graph, we observe a blue shift in emission of **ME-DPBI** for thin films in Zeonex. This could be due to the fact that, in Zeonex the molecules are spatially separated resulting in no intermolecular interactions.

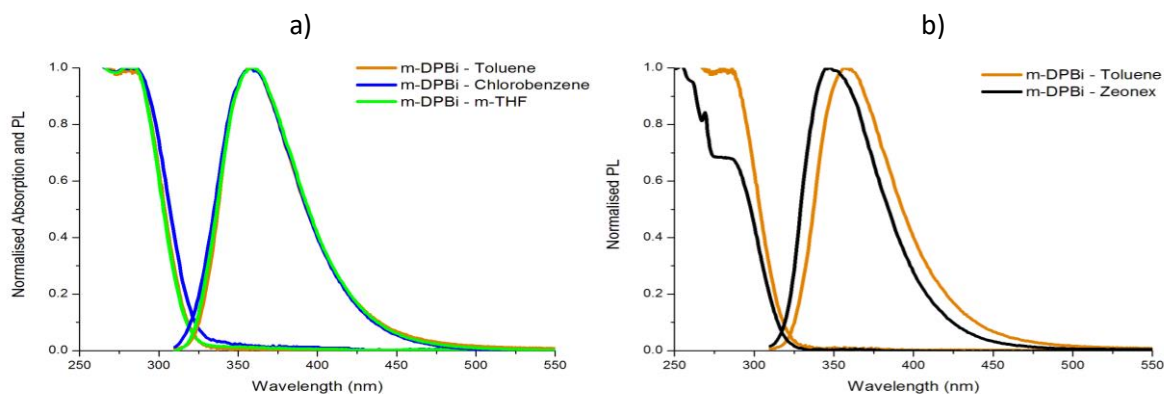


Figure 3.24: a) Absorption and photoluminescence of solution processed thin films of **ME-DPBI**. b) Absorption and photoluminescence comparison of **ME-DPBI** in solid solution Zeonex and toluene processed thin film.

Further photophysical analysis of **ME-DPBI** was performed at low temperature. Fluorescence and phosphorescence for **ME-DPBI** was measured from the solution process as well as using the Zeonex thin films. Figure 3.25 shows the result from the measurements at 80 K. As observed on the graphs, the solution processed thin films produce relatively featureless data. On the other hand, analysis in Zeonex is somewhat better but not exceptional. Thus, from the data we are not able to measure the triplet energy of **ME-DPBI** with any degree of certainty.

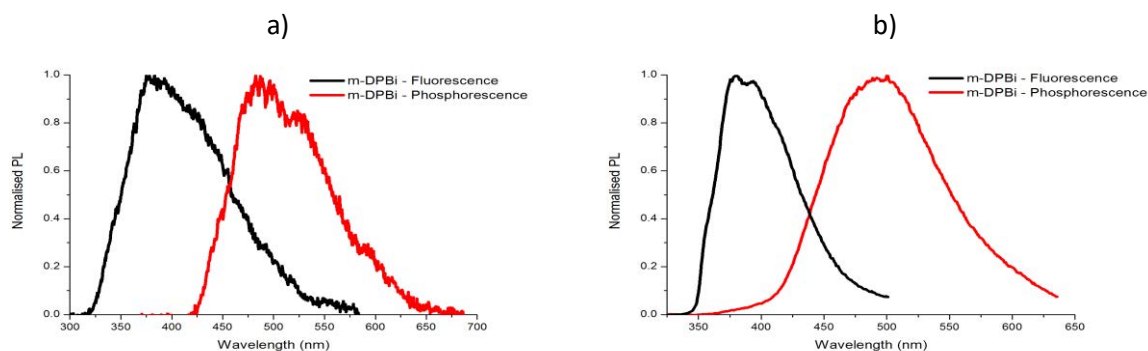


Figure 3.25: a) Fluorescence and phosphorescence measurements (80 K) of solution processed **ME-DPBI** film. b) Fluorescence and phosphorescence measurements (80 K) of Zeonex/**ME-DPBI** film.

It was suspected that the blue shift in Zeonex would be observed for all compounds, even for potential donors. Thus, for a fair comparison/understanding of potential exciplex behaviour, absorption and photoluminescence data were measured in Zeonex. Figure 3.26 illustrates the high energies of **ME-DPBI**, in both absorption and emission, which are promising. As can be

seen, **ME-DPBI** is able to form an exciplex with four donor compounds. As in the case of **DPBI**, **NPB** and **TAPC** pairing with **ME-DPBI** was further investigated.

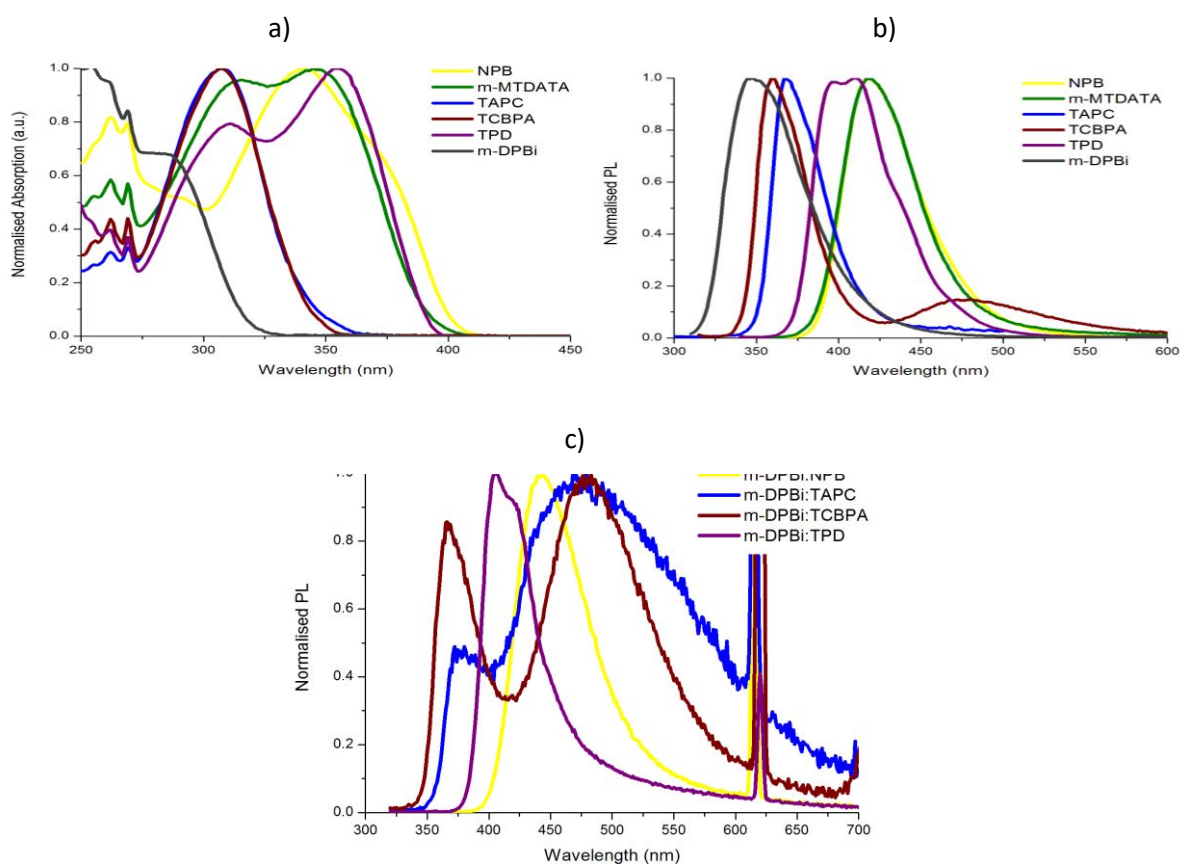


Figure 3.26: a) Donor absorption comparison with **ME-DPBI** in Zeonex. b) Donor emission comparison with **ME-DPBI** in Zeonex. c) Exciplex photoluminescence of **ME-DPBI**/donor.

Table 3.7 shows the device architecture using **ME-DPBI** and their measured peak performances. Like **DPBI**, similar combinations of device configurations were tried in order to optimise the charge transport balance within the device and achieve an efficient blue exciplex device. Seven comparable device configurations were produced. Current voltage graphs for these devices are attached in appendix ii. In the case of exciplex emission with pairing donor compound **NPB**, we notice a slight improved performance for **ME-DPBI**. However, exciplex emission with **TAPC** generally performed better using **DPBI** as the acceptor compound. Previously we reported a device with 6% EQE, using **DPBI** to produce a green emitting device.

Using the same architecture, we were able to achieve a 2.5% EQE using **ME-DPBI**. Most importantly, this device emits blue, peaking at 475 nm. This is illustrated in Figure 3.25.

Table 3.7: Table to show exciplex devices using **ME-DPBI** and their peak EQE. The values in bracket represent the layer thickness in nanometres.

	Emitting Layer	Device Structure	EQE
			(%)
1	ME-DPBI:NPB (40)	ITO/TAPC(40)/ME-DPBI:NPB/TPBI(20)/BCP(20)/LiF(1)/Al(70)	1.7
2	ME-DPBI:NPB (30)	ITO/NPB(30)/TAPC(10)/ME-DPBI:NPB/TPBI(60)/LiF(1)/Al(70)	1.55
3	ME-DPBI:NPB (30)	ITO/NPB(30)/ME-DPBI:NPB/TPBI(60)/LiF(1)/Al(70)	1.6
4	ME-DPBI:TAPC (40)	ITO/NPB(40)/ME-DPBI:TAPC/TPBI(20)/BCP(20)/LiF(1)/Al(70)	2.5
5	ME-DPBI:TAPC (40)	ITO/NPB(40)/ME-DPBI:TAPC/TPBI(20)/LiF(1)/Al(80)	0.6
6	ME-DPBI:TAPC (30)	ITO/NPB(30)/TAPC(10)/ME-DPBI:TAPC/TPBI(60)/BCP(20)/LiF(1)/Al(80)	0.6
7	ME-DPBI:TAPC (30)	ITO/NPB(30)/TAPC(10)/ME-DPBI:TAPC/TPBI(60)/LiF(1)/Al(80)	0.7

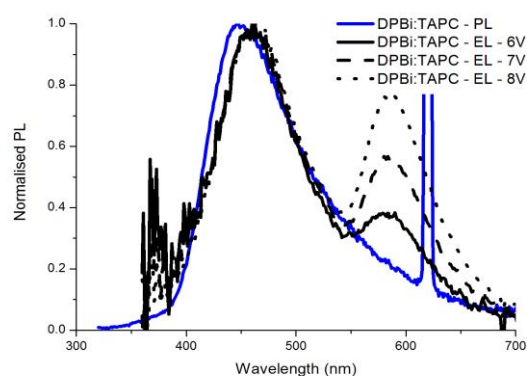


Figure 3.25: Comparison of PL and electroluminescence for device 4 from Table 3.7.

In summary, solid state photophysical studies have been performed for the new compounds of greater interest. Due to the high energies exhibited by these compounds, lead to difficulties in performing accurate measurements. The solid solution Zeonex provides a method to accurately measure the energies of monomers of these molecules. The highest external

quantum efficiency achieved is 6% for a green OLED device using **DPBI**. The highest external quantum efficiency achieved for a blue OLED device is 2.5% using **ME-DPBI**.

3.6 Conclusion

In summary, we have synthesised a series of dibenzazole-phenyl (O, S and *N*-Ph) and **DPBI** derivatives. The first aim for the molecular design was the increase in triplet energy. We assumed a reduction in conjugation should increase the triplet energy of the **TPBI** derivatives. There were initial problems in accurately measuring the triplet energy of **DPBI** owing to its propensity to dimerize/aggregate in the solid state. As a result, to solve the issue of solubility and the aggregation of **DPBI** derivatives, second and third generations of **DPBI** compounds were synthesised. In the case of **DPBI**, an increase in triplet energy was unfortunately unsuccessful, however, we remain hopeful in the application of **ME-DPBI**.

The phosphorescence measurements by Samsung proved that the triplet energy of **DPBI** is 2.7 eV which is the same as that of **TPBI**, as the same conformation is possible in both **DPBI** and **TPBI**. We assume the lower triplet energy is due to the *cis* conformation. Third generation **ME-DPBI** has been synthesised to eliminate the formation of this closed conformation, which should give a higher triplet energy than those of **TPBI** and **DPBI**.

Solid state photophysical analysis proved the capabilities of **DPBI** and **ME-DPBI** to form an exciplex. The exciplex formation depends on the proper choice of partner molecule. A blue OLED device with an EQE of 2.5% has been achieved using **ME-DPBI**. Additionally but unintentionally, we have also been able to formulate a green emitting OLED device with an EQE of 6%.

3.6 References

- 1 K. Tandy, M. Ullah, P. L. Burn, P. Meredith and E. B. Namdas, *Org. Elec.*, 2013, **14**, 2953.
- 2 S. Lee, J. Koo, G. Hyung, D. Lim, D. Lee, K. Lee, S. Yoon, W. Kim and Y. Kim, *Nanoscale Res. Lett.*, 2012, **7**, 23.
- 3 Y.-H. Chung, L. Sheng, X. Xing, L. Zheng, M. Bian, Z. Chen, L. Xiao and Q. Gong, *J. Mater. Chem.*, 2015, **3**, 1794.
- 4 J. S. Swensen, E. Polikarpov, A. Von Ruden, L. Wang, L. S. Sapochak and A. B. Padmaperuma, *Adv. Funct. Mater.*, 2011, **21**, 3250.
- 5 F. Hobrecker, *Eur. J. Inorg. Chem.*, 1872, **5**, 920.
- 6 A. Ladenburg, *Ber.*, 1875, **8**, 677.
- 7 F. M. Wang, S. A. Pradanawati, N. H. Yeh, S. C. Chang, Y. T. Yang, S. H. Huang, P. L. Lin, J. F. Lee, H. S. Sheu, M. L. Lu, C. K. Chang, A. Ramar and C. H. Su, *Chem. Mater.*, 2017, **29**, 5537.
- 8 H. Sharghi, S. Mohammad and H. Tabaei, *J. Heterocycl. Chem.*, 2008, **45**, 1293.
- 9 J. B. wright, *Chem. Rev.*, 1951, **48**, 397.
- 10 W. Forsythe and D. C. Morton, *US0172570*, 2013, 1.
- 11 Gaussian 09, M. J. Frisch, G. W. Trucks, H. B. Schlegel, G. E. Scuseria, M. A. Robb, J. R. Cheeseman, G. Scalmani, V. Barone, G. A. Petersson, H. Nakatsuji, X. Li, M. Caricato, A. Marenich, J. Bloino, B. G. Janesko, R. Gomperts, B. Mennucci, H. P. Hratchian, J. V. Ortiz, A. F. Izmaylov, J. L. Sonnenberg, D. Williams-Young, F. Ding, F. Lipparini, F. Egidi, J. Goings, B. Peng, A. Petrone, T. Henderson, D. Ranasinghe, V. G. Zakrzewski, J. Gao, N. Rega, G. Zheng, W. Liang, M. Hada, M. Ehara, K. Toyota, R. Fukuda, J. Hasegawa, M. Ishida, T. Nakajima, Y. Honda, O. Kitao, H. Nakai, T. Vreven, K. Throssell, J. A. Montgomery, Jr., J. E. Peralta, F. Ogliaro, M.

- Bearpark, J. J. Heyd, E. Brothers, K. N. Kudin, V. N. Staroverov, T. Keith, R. Kobayashi, J. Normand, K. Raghavachari, A. Rendell, J. C. Burant, S. S. Iyengar, J. Tomasi, M. Cossi, J. M. Millam, M. Klene, C. Adamo, R. Cammi, J. W. Ochterski, R. L. Martin, K. Morokuma, O. Farkas, J. B. Foresman and D. J. Fox, *Gaussian Inc., Wallingford CT*, 2016.
- 12 P. J. Stephens, F. J. Devlin, C. F. Chabalowski and M. J. Frisch, *J. Phys. Chem.*, 1994, **98**, 11623.
- 13 S. Takizawa, V. A. Montes and P. Anzenbacher, *Chem. Mater.*, 2009, **21**, 2452.
- 14 J. J. Huang, M. K. Leung, T. L. Chiu, Y. T. Chuang, P. T. Chou and Y. H. Hung, *Org. Lett.*, 2014, **16**, 5398.
- 15 K. Sato, K. Shizu, K. Yoshimura, A. Kawada, H. Miyazaki and C. Adachi, *Phys. Rev. Lett.*, 2013, **110**, 247401.

4 Conclusion and Future Work

This thesis successfully demonstrates both the MCP series and DPBI derivatives have the ability to form an exciplex. The aim of this thesis was to synthesise a blue metal-free fluorescent organic emitter, which has been achieved. Computational analyses were performed on all compounds.

From the computational analyses and in solution photophysical analyses of **MCP** series, we have established that the chemical modification on the central benzene ring has minimal effect on the HOMO/LUMO values. This work illustrates that change in HOMO/LUMO of **MCP** can be achieved when modifications are performed at the carbazole itself. Hence, the future work would entail chemical modification on the carbazole moiety. This thesis also illustrates that **MCPs** have the ability to work as acceptors. This affords the potential possibility that tuning the acceptor properties in future could be beneficial.

The design feature to reduce the conjugation to formulate **DPBI**, in order to increase triplet energy was unsuccessful. This thesis attempts to explore some of the potential reasons why the increase in triplet energy did not proceed as expected. Based on the hypothesis of conformer formation, chemical modification to the structure of **DPBI** was performed, resulting in **ME-DPBI**.

From the solid state data provided in the thesis it can be concluded that **DPBI** is able to form a device emitting with better colour purity when compared with the parent molecule **TPBI**. Devices formulated using **DPBI** have a peak external quantum efficiency of 1.7% for a blue exciplex device and 6% for a green device. The highest external quantum efficiency achieved in this thesis for a blue exciplex device is 2.5% using **ME-DPBI**. As both **DPBI** and **ME-DPBI** have the potential to show exciplex emission with other donor compounds, this should be further investigated via solid state analysis.

5 Experimental

General information and materials

All starting materials used were obtained from commercially available sources and used as received. Besides Carbazole, which was recrystallized in methanol before use, to remove the yellow impurities. Solvents and acids were generally purchased from Fisher. Tetrahydrofuran, toluene and dichloromethane were dried by a solvent purification system Pure Solv-MD Solvent instrument from Innovative Technology before use. Flash column chromatography was performed using 230-400 mesh Silica gel (60, 0.040-0.063mm).

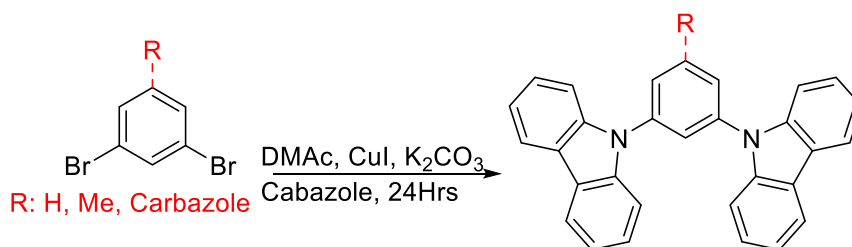
Computational measurements: Computational analysis was performed in partnership with Marcus Taylor at the University of Birmingham, School of Chemistry. The HOMO-LUMO energies and minimum energy conformations of the molecules were explored using a Gaussian program package 09.¹ The geometric and electronic properties of all compounds were analysed. The structures were optimised using B3LYP (Becke three parameters hybrid functional with Lee-Yang-Perdew correlation function) with the 6-31G (d) basis set.² Electronic properties of the minimised structures were then analysed using DFT (Density Functional Theory) and TD-DFT (Time-Dependent Density Functional Theory) to obtain the HOMO, LUMO and singlet energies. All calculations were performed in the gas phase and on a single molecule.

Physical measurements: the equipment used to record NMR spectra were Bruker AVIII 300 for ¹H and ¹⁹F NMR and Bruker AVIII 400 for ¹³C NMR. Chemical shifts (δ) are expressed in parts per million (ppm) and referenced to CDCl₃ residual peak ($\delta_{\text{H}} \approx 7.26$ ppm and $\delta_{\text{C}} \approx 77.16$ ppm) or DMSO-d₆ residual peak ($\delta_{\text{H}} \approx 7.26$ ppm and $\delta_{\text{C}} \approx 77.16$ ppm). NMR peaks and coupling constants were processed on MestReNova. All the high resolution mass spectroscopy (HRMS) were obtained using either; Waters Synapt-G2; Waters Micromass LCT; Waters Micromass MALDI micro MX with electron spray ionisation (ESI) or laser desorption ionisation (LDI). IR

spectra were recorded on Perkin Elmer Spectrum 100 FT-IR spectrometer. The elemental analysis was performed using CE instruments EA 1110 CHNS elemental analyser.

All the in solution photophysical studies were analysed at University of Birmingham, School of Chemistry. The absorption spectra were obtained using Varian Cary 50 UV-Visible spectrophotometer. All the excitation and emission data were obtained using Edinburgh Instruments FLS920 Time Resolved spectrometer.

5.1 Synthesis of MCP Derivatives via Ullmann Reaction

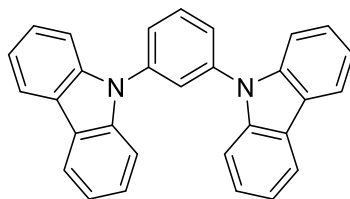


Scheme 4.1: MCP synthesis via the Ullmann reaction.

Note: All reactions performed at 0.5g scale (Aryl Halide).

Carbazole (2.4 eq.) and K₂CO₃ (7 eq.) in DMAc (15 mL) were charged into the 50 mL two neck round bottom flask equipped with Teflon-coated magnetic stirring bar, condenser and a gas inlet. Argon gas was bubbled through this mixture for 15 minutes and CuI (2.8 eq.) was then added to the reaction mixture. The flask was then sealed with septum and evacuated/filled with argon (3 cycles). Aryl halide (1 eq.) was then added to the reaction mixture through the septum using a syringe. The resulting mixture was stirred and refluxed at 165 °C for 24 hours. After cooling, the reaction mixture was poured into water (50 mL), then extracted with DCM (3 x 20 mL). The organic layer was dried using magnesium sulphate and rotary evaporated. The

crude brown liquid was purified using column chromatography using Hexane: Ethyl Acetate (9:1) followed by recrystallisation using MeOH, yielding corresponding **MCP**.



1

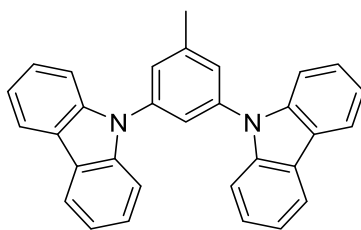
MCP

1,3-di(9*H*-carbazol-9-yl)benzene

Chemical Formula: $C_{30}H_{20}N_2$

Exact Mass: 408.16

MCP (1) Yield: 0.53g (63%).; **Appearance:** white solid.; 1H NMR (300 MHz, $CDCl_3$): δ_H = 8.09 (d, J = 7.6 Hz, 4H, Carb CH), 7.78 (m, 2H, Ph-CH), 7.64 (dd, J = 7.5, 2.0 Hz, 2H, Ph), 7.48 (d, J = 8.2 Hz, 4H, Carb CH), 7.38 (td, J = 7.2, 1.2 Hz, 4H, Ph CH) and 7.25 (td, J = 7.2, 1.2 Hz, 4H, Ph CH).; ^{13}C NMR (400 MHz, $CDCl_3$): δ_C = 140.6, 139.3, 131.2, 126.1, 125.8, 125.3, 123.6, 120.4, 120.3 and 109.7.; **MS (TOF ES⁺)** calculated for $C_{30}H_{20}N_2^+$ $[M+H]^+$ 409.16; found 409.2. As this is a known compound the analysis was compared to literature analysis, and was found to be in agreement.³



2

ME-MCP

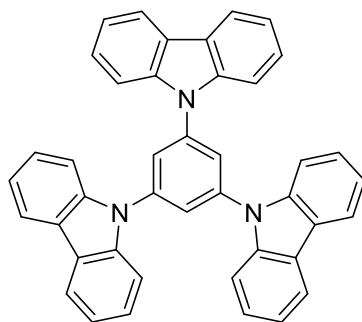
9,9'-(5-methyl-1,3-phenylene)bis(9*H*-carbazole)

Chemical Formula: $C_{31}H_{22}N_2$

Exact Mass: 422.18

ME-MCP (2) Yield: 0.99g (59%).; **Appearance:** white solid.; 1H NMR (300 MHz, $CDCl_3$): δ_H = 8.08 (d, J = 7.7 Hz, 4H, Ph CH), 7.55 (s, 1H, Ph CH), 7.46 (s, 2H, Ph CH), 7.46 (d, 4H, Ph CH), 7.37 (td,

7.1, 1.2 Hz, 4H, Ph CH), 7.24 (td, 7.5, 1.0 Hz, 4H, Ph CH) and 2.53 (s, 3H, CH₃).; ¹³C NMR (400 MHz, CDCl₃): δ_C = 141.7, 140.7, 139.2, 126.6, 126.2, 123.6, 122.5, 120.5, 120.3, 109.8 and 21.7.; HRMS (TOF ES⁺) calculated for C₃₁H₂₂N₂⁺ [M+H]⁺ = 423.1861; found 423.1855.; IR (ATR) ν = 3057(CH), 2938 (CH₃), 1459 (CC), 1318 (CN) and 719 (CH). As this is a known compound the analysis was compared to literature analysis, and was found to be in agreement.⁴



3

TCP

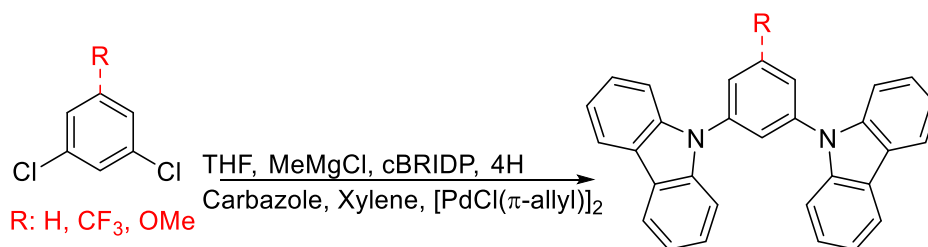
1,3,5-tri(9*H*-carbazol-9-yl)benzene

Chemical Formula: C₄₂H₂₇N₃

Exact Mass: 573.22

TCP (3) Yield: 0.61g (20%).; **Appearance:** white solid.; ¹H NMR (300 MHz, CDCl₃): δ_H = 8.10 (d, *J* = 7.6 Hz, 6H, Ph CH), 7.90 (s, 1H, Ph CH), 7.60 (d, *J* = 8.2 Hz, 6H, Ph CH), 7.41 (tD, *J* = 7.5 Hz, 1.2Hz, 6H, Ph CH) and 7.26 (td, *J* = 13.5 Hz, 0.9Hz, 6H, Ph CH).; ¹³C NMR (400 MHz, CDCl₃): δ_C = 141.7, 140.7, 139.2, 126.6, 126.2, 123.6, 122.5, 120.5, 120.3, 109.8 and 21.7.; HRMS (TOF LD⁺) calculated for C₄₂H₂₇N₃⁺ [M]⁺ = 573.2205; found 573.2205.; IR (ATR) ν = 3062 (CH), 1454 (CC), 1319 (CN) and 718 (CH). All the analyses were found to be in agreement with literature values.⁵

5.2 Synthesis of MCP derivatives via the Buchwald-Hartwig Reaction



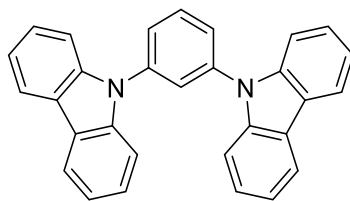
Scheme 4.2: MCP synthesis via the Buchwald-Hartwig reaction.

Note: All reactions performed at 0.5g scale (Aryl Halide).

Preparation of the catalyst solution: A 25 mL two-necked, round-bottom flask containing a Teflon stirring bar and anhydrous THF (5 mL) was evacuated and filled with argon (3 cycles). To the flask, $[\text{PdCl}(\pi\text{-allyl})]_2$ (1 mol%) and cBRIDP (4 mol%) were added and stirred under argon atmosphere.

A 50mL sealed, two-neck round-bottom flask containing a Teflon-coated magnetic stirring bar and equipped with dropping funnel was evacuated and filled with argon (3 cycles). Carbazole (2.3 eq.) and dry xylene were added to the flask and sealed using septum. The flask was then evacuated and refilled with argon (3 cycles). The reaction mixture was cooled to $\leq 5^\circ\text{C}$ using an ice bath, whilst being stirred vigorously. Subsequently, a solution of MeMgCl in THF (2.3 eq.) was added drop-wise to the mixture via a dropping funnel. The reaction temperature was maintained at $\leq 20^\circ\text{C}$, followed by addition of aryl halide (1 eq.). The aryl halide was added via a dropping funnel and, if solid, was dissolved in THF or xylene first. Subsequently, the catalyst solution was added via the dropping funnel after which the dropping funnel was washed using dehydrated THF (1 mL) and xylene (1 mL). The resulting mixture was stirred and refluxed at 80°C for 6 hours. After cooling the reaction mixture to room temperature, it was then poured into aqueous ammonium chloride solution and liquid-liquid extraction was performed using DCM (3 x 25 mL). The organic layer was dried using magnesium sulphate. The crude corresponding product was purified via column chromatography using hexane: ethyl acetate

(9:1), followed by recrystallization in MeOH. This process yielded corresponding MCP derivatives as white solid.



1

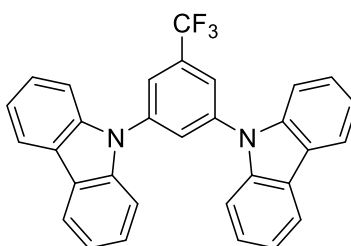
MCP

1,3-di(9*H*-carbazol-9-yl)benzene

Chemical Formula: C₃₀H₂₀N₂

Exact Mass: 408.16

MCP (1) Yield: 0.71g (85%).; **Appearance:** white solid.; **¹H NMR** (300 MHz, CDCl₃): δ_H = 8.09 (d, *J* = 7.6 Hz, 4H, Carb CH), 7.78 (m, 2H, Ph-CH), 7.64 (dd, *J* = 7.5, 2.0 Hz, 2H, *Ph*), 7.48 (d, *J* = 8.2 Hz, 4H, Carb CH), 7.38 (td, *J* = 7.2, 1.2 Hz, 4H, Ph CH) and 7.25 (td, *J* = 7.2, 1.2 Hz, 4H, Ph CH).; **¹³C NMR** (400 MHz, CDCl₃): δ_C = 140.6, 139.3, 131.2, 126.1, 125.8, 125.3, 123.6, 120.4, 120.3 and 109.7. As this is a known compound the **¹H NMR** and **¹³C NMR** were compared to literature values, which were found to be in agreement.¹



4

CF₃-MCP

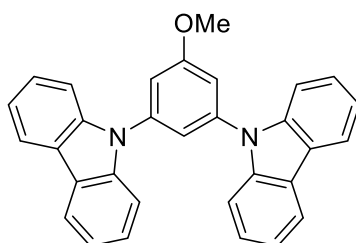
9,9'-(5-(trifluoromethyl)-1,3-phenylene)bis(9*H*-carbazole)

Chemical Formula: C₃₁H₁₉F₃N₂

Exact Mass: 476.15

CF₃-MCP (4) Yield: 0.78g (71%).; **Appearance:** white solid.; **¹H NMR** (300 MHz, CDCl₃): δ_H = 8.17 (d, *J* = 7.7 Hz, 4H, Ph CH), 8.04 (s, 1H, Ph CH), 7.98 (s, 2H, Ph CH), 7.53 (d, *J* = 8.0 Hz, 4H, Ph CH), 7.47 (td, *J* = 7.6 Hz, 1.2 Hz, 4H, Ph CH) and 7.35 (td, *J* = 7.4 Hz, 1.2Hz, 4H, Ph CH).; **¹³C NMR** (400 MHz, CDCl₃): δ_C = 140.4, 140.2, 128.1, 126.5, 123.9, 122.3, 122.3, 121.0, 120.7, 109.4 and

29.7.; **^{19}F NMR** (300 MHz, CDCl_3): $\delta_{\text{F}} = 62.63$.; **HRMS (TOF LD $^+$)** calculated for $\text{C}_{31}\text{H}_{19}\text{N}_2\text{F}_3^+$ $[\text{M}]^+$ = 476.1500; found 476.1497.; **Elemental analysis** calculated for $\text{C}_{31}\text{H}_{19}\text{N}_2\text{F}_3$ = C 78.14, H 4.02, F 11.96, N 5.88; found C 79.22, H 4.30, N 6.24.; **IR (ATR)** $\nu = 2971(\text{CH})$, $1465(\text{CC})$, $1357(\text{CN})$, $853(\text{CH})$ and $711(\text{CF})$.



5

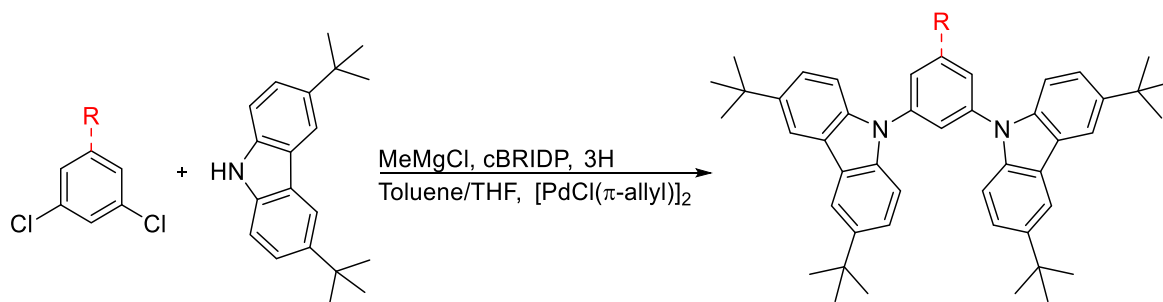
OME-MCP

9,9'-(5-methoxy-1,3-phenylene)bis(9H-carbazole)

Chemical Formula: $\text{C}_{31}\text{H}_{22}\text{N}_2\text{O}$

Exact Mass: 438.17

OME-MCP (5) Yield: 0.34g (50%).; **Appearance:** white solid.; **^1H NMR** (300 MHz, CDCl_3): $\delta_{\text{H}} = 8.15$ (dd, $J = 7.2$ Hz, 0.5 Hz, 4H, Ph CH), 7.58 (d, $J = 8.2$ Hz, 4H, Ph CH), 7.44 (td, $J = 6.8$ Hz, 1.5 Hz, 4H, Ph CH), 7.43 (d, $J = 9$ Hz, 1H, Ph CH), 7.31 (dt, $J = 7.5$ Hz, 1 Hz, 4H, Ph CH), 7.24 (d, $J = 1.8$ Hz, 2H, Ph CH) and 3.94 (s, 3H, OCH_3).; **^{13}C NMR** (400 MHz, CDCl_3): $\delta_{\text{C}} = 161.8$, 140.5 , 140.1 , 126.2 , 123.6 , 120.4 , 120.3 , 117.5 , 111.7 , 109.9 and 55.9 .; **HRMS (TOF ES $^+$)** calculated for $\text{C}_{31}\text{H}_{22}\text{N}_2^+$ $[\text{M}]^+$ + 439.1810; found 439.1803.; **Elemental analysis** calculated for $\text{C}_{31}\text{H}_{22}\text{N}_2\text{O}$ = C 84.91, H 5.06, N 6.39, O 3.65; found C 84.84, H 5.24, N 7.24.; **IR (ATR)** $\nu = 3057(\text{CH})$, $1470(\text{OMe})$, $1229(\text{CN})$ and $725(\text{CH})$.

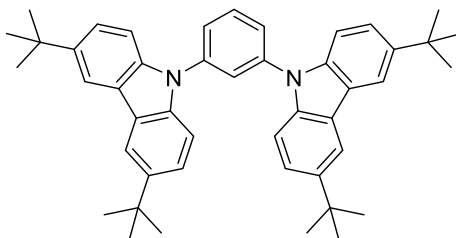


Scheme 4.3: Synthesis of T-MCP series via Buchwald-Hartwig reaction.

Note: All reactions performed at 0.5g scale (Aryl Halide).

Preparation of the catalyst solution: A 25 mL two-necked round-bottom flask containing a Teflon stirring bar and dry THF (5 mL), was evacuated and filled with argon (3 cycles). To the flask, $[\text{PdCl}(\pi\text{-allyl})]_2$ (1 mol%) and cBRIDP (4 mol%) were added and stirred under argon atmosphere.

A 50 mL sealed, two-neck round-bottom flask containing a Teflon-coated magnetic and stirring bar was evacuated and filled with argon (3 cycles). 3,6-Di-*tert*-butyl-9*H*-carbazole (2.1 eq.) and anhydrous toluene were added to the flask and sealed using septum. The flask was then evacuated and refilled with argon (3 cycles). The reaction mixture was cooled to $\leq 5^\circ\text{C}$ using an ice bath, whilst being stirred vigorously. Subsequently, solution of MeMgCl in THF (2.1 eq.) was added drop-wise to the mixture using a syringe through a septum. The reaction temperature was maintained at $\leq 20^\circ\text{C}$, followed by addition of aryl chloride (1 eq.). The aryl chloride was added using a syringe through a septum and, if solid, was dissolved in THF or toluene first. Subsequently, the catalyst solution was added using a syringe through a septum. The resulting mixture was stirred and refluxed at 90°C for 2 hours. After cooling the reaction mixture to room temperature, it was then poured into aqueous ammonium chloride solution and liquid-liquid extraction was performed using DCM (3 x 25 mL). The organic layer was dried using magnesium sulphate. The crude corresponding product was purified via column chromatography using hexane: ethyl acetate (9:1), followed by recrystallisation in DCM:MeOH (1:9). This process yielded **T-MCP** derivatives as a white solid.



6

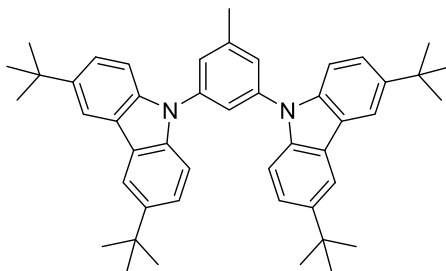
T-MCP

1,3-bis(3,6-di-*tert*-butyl-9*H*-carbazol-9-yl)benzene

Chemical Formula: C₄₆H₅₂N₂

Exact Mass: 632.41

T-MCP (6) Yield: 1.09g (87%).; **Appearance:** white solid.; **¹H NMR** (300 MHz, CDCl₃): δ_H = 8.17 (s, 4H), 7.80 (d, *J* = 9.4 Hz, 2H), 7.71 – 7.63 (m, 2H), 7.50 (s, 8H), 1.49 (s, 36H).; **¹³C NMR** (400 MHz, CDCl₃): δ_C = 143.3, 139.8, 139.1, 131.0, 125.0, 124.6, 123.9, 123.7, 116.4, 109.3, 34.9, 32.1.; **HRMS (TOF ES⁺)** calculated for C₄₆H₅₃N₂⁺ [M+H]⁺ 633.4204; found 633.4209.; **Elemental analysis** calculated for C₄₆H₅₂N₂ = C 87.29, H 8.28, N 4.43; found C 87.40, H 8.17, N 4.29.; **IR (ATR)** ν = 2942(CH), 1492(CC), 1251(CN) and 809(CH).



7

ME-T-MCP

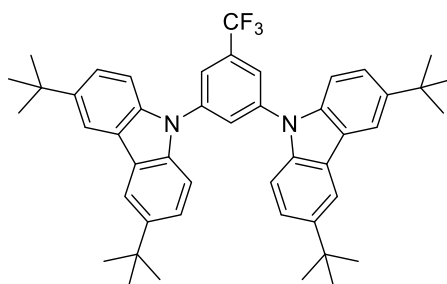
9,9'-(5-methyl-1,3-phenylene)bis(3,6-di-*tert*-butyl-9*H*-carbazole)

Chemical Formula: C₄₇H₅₄N₂

Exact Mass: 646.43

ME-T-MCP (7) Yield: 0.76g (79%).; **Appearance:** white solid.; **¹H NMR** (400 MHz, CDCl₃): δ_H = 8.16 (s, 4H), 7.60 (s, 1H), 7.50-7.45 (m, 10H), 2.56 (s, 3H), 1.47 (s, 36H).; **¹³C NMR** (400 MHz, CDCl₃): δ_C = 143.07, 141.27, 139.45, 139.01, 125.60, 123.70, 123.51, 121.57, 116.30, 109.26, 34.74, 32.01, 21.61.; **HRMS (TOF ES⁺)** calculated for C₄₇H₅₅N₂⁺ [M+H]⁺ 647.4366; found 647.4365.;

Elemental analysis calculated for $C_{47}H_{54}N_2$ = C 87.26, H 8.41, N 4.33; found C 87.06, H 8.27, N 4.21.; **IR (ATR)** ν = 2958 (CH), 1475(CC), 1293(CN) and 808 (CH).



8

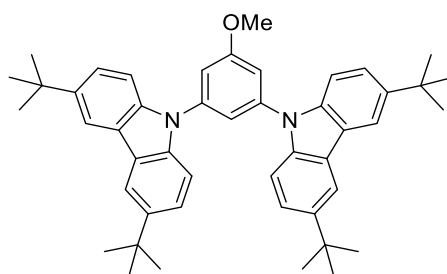
CF3-T-MCP

9,9'-(5-(trifluoromethyl)-1,3-phenylene)bis(3,6-di-*tert*-butyl-9*H*-carbazole)

Chemical Formula: $C_{47}H_{51}F_3N_2$

Exact Mass: 700.40

CF3-T-MCP (8) Yield: 0.35g (77%).; **Appearance:** white solid.; **1H NMR** (400 MHz, $CDCl_3$): δ_H = 8.16 (d, J = 7.5 Hz, 4H), 8.02 (s, 1H), 7.92 (d, J = 7.7Hz, 2H), 7.53-7.45 (m, 8H), 1.47 (s, 36H).; **^{13}C NMR** (400 MHz, $CDCl_3$): δ_C = 143.9, 140.6, 138.5, 133.9, 133.6, 127.0, 124.0, 123.9, 121.1, 116.5, 108.9, 34.8, 31.9.; **^{19}F NMR** (300 MHz, $CDCl_3$): δ_F = 62.7.; **HRMS (TOF ES $^+$)** calculated for $C_{47}H_{51}F_3N_2^+$ [M+H] $^+$ 701.4083; found 701.4078.; **Elemental analysis** calculated for $C_{47}H_{51}F_3N_2$ = C 80.54, H 7.33, F 8.13, N 4.00; found C 80.45, H 7.26, N 3.97.; **IR (ATR)** ν = 2956 (CH), 1485(CH), 1278(CC), 1140(CN) and 809(CH).



9

OMe-T-MCP

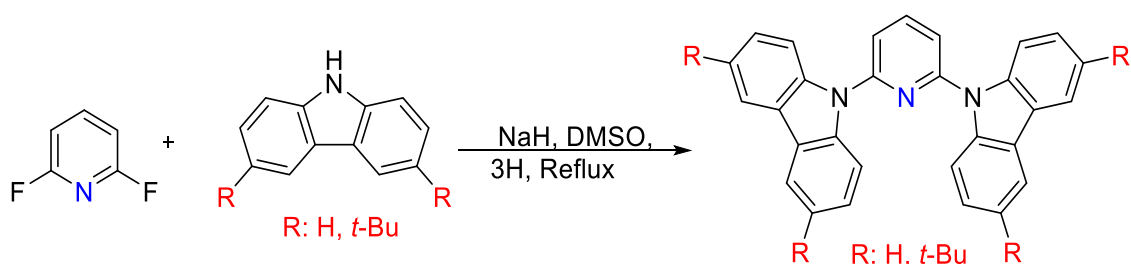
9,9'-(5-methoxy-1,3-phenylene)bis(3,6-di-*tert*-butyl-9*H*-carbazole)

Chemical Formula: $C_{47}H_{54}N_2O$

Exact Mass: 662.42

OME-T-MCP (9) Yield: 1.8g (69%).; **Appearance:** white solid.; **^1H NMR** (300 MHz, CDCl_3): δ_{H} = 8.22 (d, J = 7.5 Hz, 4H), 8.07 (s, 1H), 7.98 (d, J = 7.7Hz, 2H), 7.67-7.46 (m, 8H), 1.44 (s, 36H).; **^{13}C NMR** (400 MHz, CDCl_3): δ_{C} =161.6, 143.2, 140.4, 138.9, 123.8, 123.6, 116.7, 116.3, 110.7, 109.4, 103.2, 55.8, 34.8, 32.0; **HRMS (TOF ES $^+$)** calculated for $\text{C}_{47}\text{H}_{54}\text{N}_2\text{O}^+$ $[\text{M}+\text{Na}]^+$ 685.4143; found 685.4142.; **Elemental analysis** calculated for $\text{C}_{47}\text{H}_{54}\text{N}_2\text{O}$ = C 85.15, H 8.21, N 4.23, O 2.41; found C 84.92, H 8.2, N 4.27.; **IR (ATR)** ν = 2952(CH), 1475(OMe), 1261 (CN) and 815 (CH).

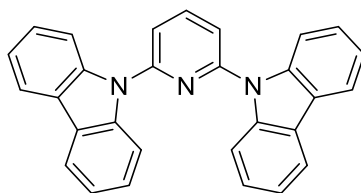
5.3 Synthesis of MCP Derivatives via Method 3



Scheme 4.4: MCP synthesis via Method 3.

Note: All reactions performed at 0.5g scale (Aryl Halide).

In a 25 mL round-bottom flask equipped with dropping funnel and Teflon stirrer bar, carbazole (2.4 eq.) was dissolved in DMSO (4mL) while stirring. Subsequently, NaH (3 eq.) in DMSO (4 mL) was added drop-wise while stirring. The resulting solution was left to stir for 30 minutes, after which, 2,6-difluoropyridine in DMSO (4 mL) was added drop-wise via a dropping funnel, followed by washing the dropping funnel with DMSO (3 mL). The light yellow reaction mixture was then heated at 160 °C for 1 hour, resulting in the formation of a pale pink solution. After cooling the reaction mixture to room temperature, it was poured into water (20 mL) forming a white precipitate, which was collected through filtration. The crude product was purified using recrystallisation in methanol, yielding a white solid.



10

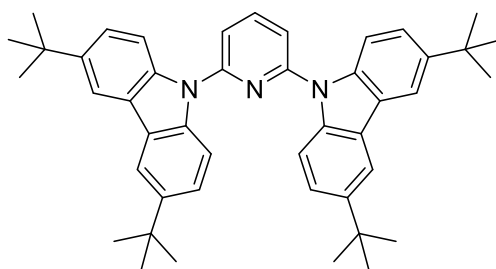
PY-MCP

2,6-di(9*H*-carbazol-9-yl)pyridine

Chemical Formula: C₂₉H₁₉N₃

Exact Mass: 409.16

PY-MCP (10) Yield: 0.96g (54%).; **Appearance:** white solid.; **¹H NMR** (300 MHz, CDCl₃): δ_H = 8.08 (m, 5H, 4 Ph CH & 1Py CH), 7.97 (d, *J* = 8.2 Hz, 4H, Ph CH), 7.59 (d, *J* = 7.9 Hz, 2H, Py CH), 7.36 (td, *J* = 7.3, 1.4 Hz, 4H, Ph CH) and 7.27 (td, *J* = 7.5 Hz, 1.0 Hz, 4H, Ph CH).; **¹³C NMR** (400 MHz, CDCl₃): δ_C = 151.5, 140.3, 139.5, 126.3, 124.5, 121.2, 120.1, 114.9 and 111.9.; **HRMS (TOF ES⁺)** calculated for C₃₁H₂₂N₂⁺ [M]⁺ 410.1657; found 410.1655.; **Elemental analysis** calculated for C₂₉H₁₉N₃ = C 85.06, H 4.68, N 10.26; found C 84.88, H 4.77, N 10.39.; **IR (ATR)** ν = 2952(CH), 1479 (C=C), 1260 (CN) and 817(CH). As this is a known compound the **¹H NMR** and **¹³C NMR** were compared to literature values, which were found to be in agreement.⁶



11

PY-T-MCP

2,6-bis(3,6-di-*tert*-butyl-9*H*-carbazol-9-yl)pyridine

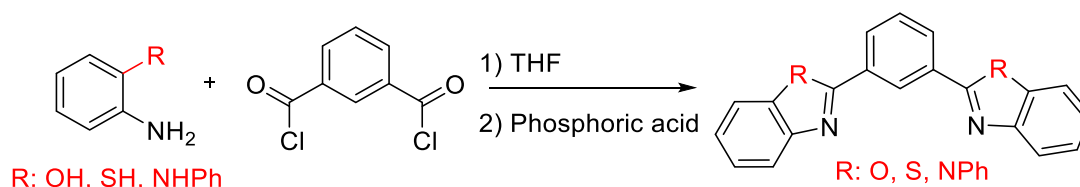
Chemical Formula: C₄₅H₅₁N₃

Exact Mass: 633.41

PY-T-MCP (11) Yield: 0.72g (66%).; **Appearance:** white solid.; **¹H NMR** (400 MHz, CDCl₃): δ_H = 8.13 (d, *J* = 1.9 Hz, 4H), 8.05 (t, *J* = 7.9 Hz, 1H), 7.97 (d, *J* = 8.7Hz, 2H), 7.56 (d, *J* = 7.9Hz, 2H), 7.45 (dd, *J* = 8.7Hz, 2.0 Hz, 4H) and 1.47 (s, 36H). **¹³C NMR** (400 MHz, CDCl₃): δ_C = 151.8, 144.1, 139.9, 137.9, 124.6, 123.9, 116.0, 113.5, 34.7 and 31.9.; **HRMS (TOF ES⁺)** calculated for

$C_{45}H_{52}N_3^+ [M]^+$ 634.4160; found 634.4161.; **Elemental analysis** calculated for $C_{45}H_{51}N_3$ = C 85.26, H 8.11, N 6.63; found C 85.35, H 8.09, N 6.46.; **IR (ATR)** ν = 2949(CH), 1452(CC), 1282 (CN) and 791(CH).

5.4 Synthesis of First Generation DPBI Derivatives



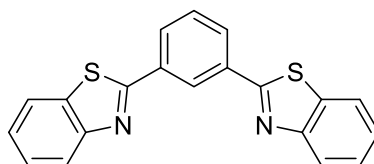
*Scheme 4.5: Hetero-X-azole synthesis via **Method 4**.*

Note: All reactions performed at 0.5g scale (Acid Chloride).

Step 1: In a 10 mL round-bottom flask at room temperature, aryl amine (2.2 eq.) was dissolved in THF (3 mL) by stirring, using a Teflon-coated magnetic stirrer bar. To the resulting brown solution the aryl acid chloride (1 eq.) was added drop-wise and stirred overnight. The resulting purple solution was poured into water (30 mL) causing precipitation. The solid was collected using vacuum filtration and dried over airflow. The filtered solid was taken through to Step 2.

Note: Step 1 performed under argon atmosphere for the synthesis of **DBT**.

Step 2: The resulting product from Step 1 was then placed in a 10 mL round-bottom flask, treated with *ortho*-phosphoric acid (7 mL) and refluxed at full power for 30 minutes. Subsequently, the reaction mixture was poured into water (50 mL) and neutralised using a base, causing precipitation. The crude product was suction filtered and dried over airflow. The corresponding product was purified via column chromatography using hexane:ethyl acetate (1:1) as the eluent, bearing a white solid.



12

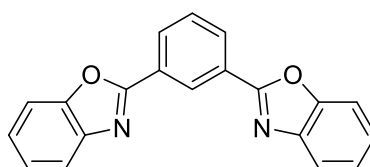
DBT

1,3-bis(benzo[d]thiazol-2-yl)benzene

Chemical Formula: $C_{20}H_{12}N_2S_2$

Exact Mass: 344.04

DBT (12) Yield: 0.39g (46%).; **Appearance:** white solid.; **1H NMR** (300 MHz, DMSO): δ_H = 8.85 (s, 1H, Ph CH), 8.27 (dd, J = 7.5 Hz, 1.8 Hz, 2H, Ph CH), 8.19 (m, J = 6.75 Hz, 4H, Ph CH), 7.80 (t, J = 7.5 Hz, 1H, Ph CH), 7.61 (dt, J = 7.5 Hz, 1.3 Hz, 2H, Ph CH) and 7.52 (dt, J = 7.5 Hz, 1.2 Hz, 2H, Ph CH).; **^{13}C NMR** (400 MHz, $CDCl_3$): δ_C = 166.2, 153.4, 134.5, 133.8, 130.7, 129.9, 126.8, 125.8, 124.7, 123.1 and 122.5.; **HRMS (TOF ES $^+$)** calculated for $C_{20}H_{12}N_2S_2^+$ [M+H] $^+$ 345.0520; found 345.0526. **IR (ATR)** ν = 3062(CH), 1453(CC), 1282(CN), 954(CH) and 711(CH). **1H NMR, ^{13}C NMR and HRMS** analyses were found to be in agreement with literature values.⁷



13

DBO

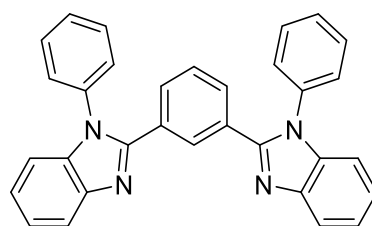
1,3-bis(benzo[d]oxazol-2-yl)benzene

Chemical Formula: $C_{20}H_{12}N_2O_2$

Exact Mass: 312.09

DBO (13) Yield: 0.36g (47%).; **Appearance:** white solid.; **1H NMR** (300 MHz, $CDCl_3$): δ_H = 9.18 (s, 1H, Ph CH), 8.75 (dd, J = 8 Hz, 1.7 Hz, 2H, Ph CH), 7.85 (dd, 6.3 Hz, 2.9 Hz, 4H, Ph CH), 7.74 (t, J = 8 Hz, 1H, Ph CH), 7.67 (dd, J = 6.3 Hz, 3.0 Hz, 1H, Ph CH) and 7.43 (m, 4H, Ph CH).; **^{13}C NMR** (400 MHz, $CDCl_3$): δ_C = 142.0, 130.2, 129.6, 128.1, 126.6, 125.5, 124.8, 120.2 and 110.7.; **HRMS (TOF ES $^+$)** calculated for $C_{20}H_{12}N_2S_2^+$ [M+H] $^+$ 313.0977; found 313.0981. **IR (ATR)** ν = 3064(CH),

1464(C=C), 1241(CO) and 716 (CH). ^1H NMR and HRMS analyses were found to be in agreement with literature values.⁸



14

DPBI

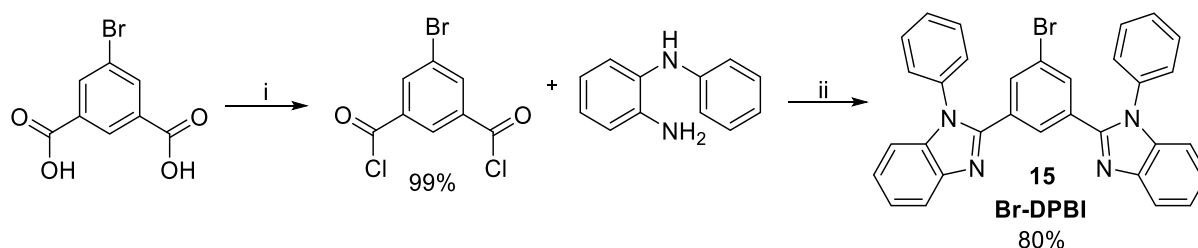
1,3-bis(1-phenyl-1H-benzo[d]imidazol-2-yl)benzene

Chemical Formula: $\text{C}_{32}\text{H}_{22}\text{N}_4$

Exact Mass: 462.18

DPBI (14) Yield: 0.68g (57%).; **Appearance:** white solid.; ^1H NMR (300 MHz, CDCl_3): δ_{H} = 7.88 (s, 1H, Ph CH), 7.79 (dd, J = 6 Hz, 1.4Hz, 2H, Ph CH), 7.55(m, 6H, Benzi CH), 7.46 (dd, J = 7.5 Hz, 1.7 Hz, 2H, Benzi CH), 7.35 (dd, J = 7.5, 1.5 Hz, 4H, N-Ph CH), 7.29 (dt, J = 5.25 Hz, 1.4 Hz, 4H, N-Ph CH), 7.28 (dd, J = 7 Hz, 1.4Hz, 1H, N-Ph CH) and 7.19 (dd, J = 7.5 Hz, 1.4 Hz, 2H, Ph CH). ; ^{13}C NMR (400 MHz, CDCl_3): δ_{C} = 151.4, 142.9, 137.4, 136.5, 130.5, 130.4, 130.3, 129.4, 128.8, 127.8, 124.0, 123.3, 119.9 and 110.96.; **HRMS (TOF ES⁺)** calculated for $\text{C}_{32}\text{H}_{22}\text{N}_4^+$ $[\text{M}+\text{H}]^+$ 463.1923; found 463.1917.; **Elemental analysis** calculated for $\text{C}_{32}\text{H}_{22}\text{N}_4$ = C 83.09, H 4.79, N 12.11; found C 83.32, H 4.74, N 11.92.; **IR (ATR)** ν = 3050 (CH), 1464(CC), 1290 (CN) and 722(CH).

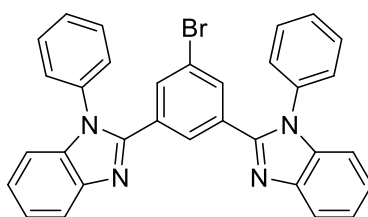
5.5 Synthesis of Second Generation DPBI Derivatives



Scheme 4.6: Synthesis of **Br-DPBi**. i) SOCl_2 (6eq.), reflux 3H; ii) **Method 4**: Step 1) Isophthaloyl dichloride (1eq.), N-phenylbenzene-1,2-diamine (2.2eq.) and THF; Step 2) o-phosphoric acid.

Note: Reactions performed at 0.5g scale (5-bromoisophthalic acid).

Step i: In a 50 mL round bottom flask, 5-bromoisophthalic acid (1 eq.) and SOCl_2 (6 eq.) were set up for reflux at 70°C . The reaction was stirred using a Teflon-coated magnetic stirrer bar. The reaction mixture was refluxed for 3 hours, after which the SOCl_2 was distilled off under reduced pressure, resulting in 5-bromoisophthaloyl dichloride. *Step ii (part 1)*: 5-bromoisophthaloyl dichloride (1 eq.), N-phenylbenzene-1,2-diamine (2.2 eq.) and THF (20 mL) were then placed in a 50 mL round-bottom flask equipped with a Teflon-coated magnetic stirrer bar. The resulting solution was left to stir overnight at room temperature. The resulting purple solution was then poured into water (50 mL) causing precipitation. The solid was collected using vacuum filtration and dried over airflow. *Step ii (part 2)*: The resulting product from part 1 was then placed in a 10 mL round-bottom flask, treated with *ortho*-phosphoric acid (7 mL) and refluxed at full power for 30 minutes. Subsequently, the reaction mixture was poured into water (50 mL) and neutralised using base, causing precipitation. The crude product was suction filtered and dried over airflow. The crude product was purified via column chromatography using toluene as the eluent, followed by recrystallization in toluene (and a few drops of THF just to encourage crystallisation), bearing a white solid.



15

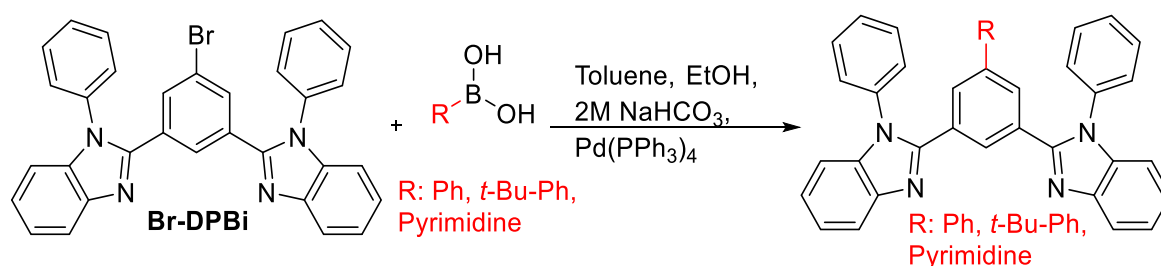
Br-DPBi

2,2'-(5-bromo-1,3-phenylene)bis(1-phenyl-1H-benzo[d]imidazole)

Chemical Formula: $\text{C}_{32}\text{H}_{21}\text{BrN}_4$

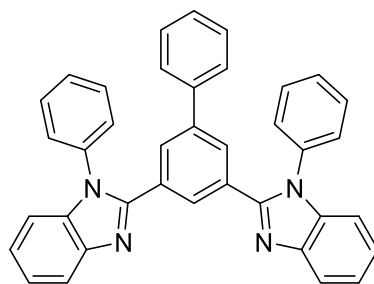
Exact Mass: 540.09

Br-DPBI (15) Yield: 2.31g(80%); **Appearance:** white solid.; $^1\text{H NMR}$ (300 MHz, DMSO- d_6): δ_{H} = 7.80 (dd, J = 7.5Hz and J =3Hz, 2H, Ph CH), 7.74(s, 1H, Ph CH), 7.60(m, 8H, Ph CH), 7.33(m, 8H, Ph CH) and 7.19(dd, J = 6Hz and J = 3Hz, 2H, Ph CH).; $^{13}\text{C NMR}$ (400 MHz, DMSO): δ_{C} = 149.0, 136.6, 135.2, 133.6, 130.7, 130.1, 127.9, 125.2, 124.6, 121.6, 118.9 and 111.7.; **HRMS (TOF ES $^+$)** calculated for $\text{C}_{32}\text{H}_{21}\text{BrN}_4^+$ $[\text{M}+\text{H}]^+$ 541.10228; found 541.1036.; **IR (ATR)** ν =2998 (CH), 1465(C=C) and 711 (CBr).



Scheme 4.7: Synthesis of DPBI derivatives via the Suzuki coupling reaction.

All reactions performed at 0.5g scale (**15**): A 50mL two-neck round-bottom flask equipped with a Teflon-coated magnetic stirring bar and a dropping funnel was evacuated and filled with argon (3 cycles). **Br-DPBI** (1 eq.), toluene (10mL), R-boronic acid (1.1 eq.), $\text{Pd}(\text{Ph}_3)_4$ (2 Mol%) and ethanol (5mL) were added to the flask. The flask was evacuated and filled with argon again. This was followed by the addition of 2M aqueous NaHCO_3 (10 eq.) drop-wise via a dropping funnel. The resulting mixture was stirred and refluxed at 100°C for 3 hours. After cooling the reaction mixture to room temperature, it was poured into water (20 mL) and extracted with DCM (3 x 25 mL). The organic layer was dried using magnesium sulphate and rotary evaporated. The crude solid was purified using column chromatography using hexane:ethyl Acetate (9:1). This then yielded corresponding product.



16

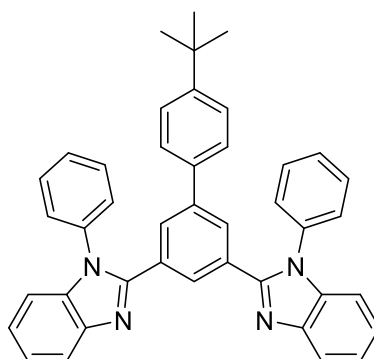
PH-DPBI

3,5-bis(1-phenyl-1*H*-benzo[*d*]imidazol-2-yl)-1,1'-biphenyl

Chemical Formula: C₃₈H₂₆N₄

Exact Mass: 538.22

PH-DPBI (16) Yield: 0.24g (48%).; **Appearance:** white solid.; **¹H NMR** (300 MHz, DMSO-*d*₆): δ_H = 8.11(s, 1H, Ph CH), 7.83 (dd, *J* = 7.5Hz and *J* = 3Hz, 2H, Ph CH), 7.63(m, 8H, Ph CH), 7.46(dd, *J* = 7.5Hz and *J* = 3Hz, 4H, Ph CH), 7.34(m, 8H, Ph CH), 7.23 (dd, *J* = 9Hz and 3Hz, 2H, Ph CH) and 7.04(dd, *J* = 6Hz and *J* = 3Hz, 2H, Ph CH).; **¹³C NMR** (400 MHz, DMSO-*d*₆): δ_C = 151.1, 142.9, 140.2, 139.0, 137.5, 136.8, 131.0, 130.7, 129.5, 129.4, 129.3, 128.6, 128.4, 128.1, 126.7, 124.1, 123.3, 120.0 and 110.9.; **HRMS (TOF ES⁺)** calculated for C₃₈H₂₆N₄⁺ [M+H]⁺ 539.2236; found 539.2236.; **Elemental analysis** calculated for C₃₈H₂₆N₄ = C 84.73, H 4.87, N 10.40; found C 84.57, H 4.75, N 10.22.; **IR (ATR)** ν = 3055 (CH), 1477(CC), 1293 (CN) and 724 (CH).



17

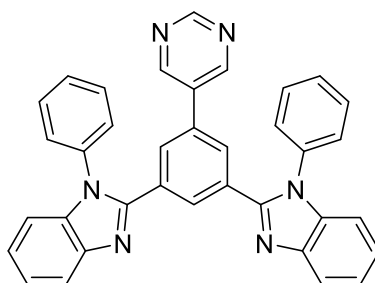
PHT-DPBI

2,2'-(4'-(*tert*-butyl))-1,1'-biphenyl-3,5-diylbis(1-phenyl-1*H*-benzo[*d*]imidazole)

Chemical Formula: C₄₂H₃₄N₄

Exact Mass: 594.28

PHT-DPBI (17) Yield: 0.28g (52%).; **Appearance:** white solid.; **^1H NMR** (300 MHz, DMSO- d_6): δ_{H} = 8.12(s, 1H, Ph CH), 7.83 (dd, J = 6Hz and J =3Hz, 2H, Ph CH), 7.65(m, 6H, Ph CH), 7.57(d, J = 1.6Hz, 2H, Ph CH), 7.47(d, J = 6, 4H, Ph CH), 7.35(m, 6H, Ph CH), 7.24 (dd, J = 9Hz and 3Hz, 2H, Ph CH), 6.94(d, J = 9Hz, 2H, Ph CH) and 1.28 (s, 9H, CH_3).; **^{13}C NMR** (400 MHz, DMSO- d_6): δ_{C} = 151.3, 151.1, 142.9, 139.9, 137.5, 136.8, 136.1, 131.0, 130.7, 129.5, 129.2, 128.2, 128.1, 126.4, 126.2, 124.1, 123.3, 120.0, 111.0, 34.7 and 31.4.; **HRMS (TOF ES $^+$)** calculated for $\text{C}_{42}\text{H}_{34}\text{N}_4$ $^+$ [M+H] $^+$ 595.2862; found 595.2869.; **Elemental analysis** calculated for $\text{C}_{42}\text{H}_{34}\text{N}_4$ = C 84.82, H 5.76, N 9.42; found C 84.68, H 5.59, N 9.30.; **IR (ATR)** ν =3373(Ar-CH), 2956 (CH_3), 1481 (CC), 1284 (CN) and 716 (CH).



18

PY-DPBI

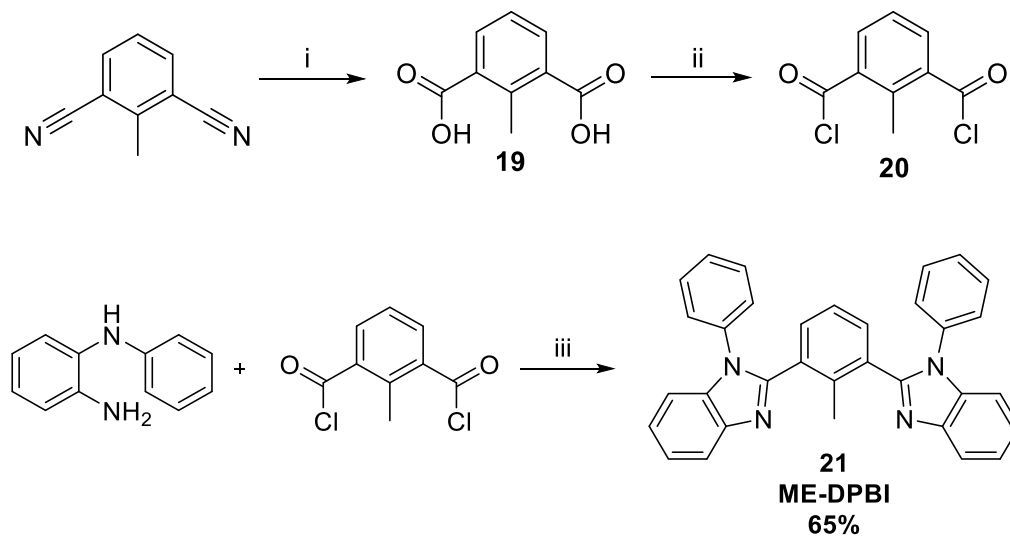
2,2'-(5-(pyrimidin-5-yl)-1,3-phenylene)bis(1-phenyl-1H-benzo[d]imidazole)

Chemical Formula: $\text{C}_{36}\text{H}_{24}\text{N}_6$

Exact Mass: 540.21

PY-DPBI (18) Yield: 0.13g (27%).; **Appearance:** white solid.; **^1H NMR** (300 MHz, DMSO- d_6): δ_{H} = 9.17(s, 1H, Py CH), 8.57(s, 1H, Py CH), 8.06(s, 1H, Ph CH), 7.83 (dd, J = 6Hz and 3Hz, 2H, Ph CH), 7.76 (d, J = 3Hz, 2H, Ph CH), 7.61(m, 7H, Ph CH), 7.44(dd, J = 9Hz and J = 3Hz, 4H, Ph CH), 7.34(m, 4H, Ph CH) and 7.24(d, 2H, Ph CH).; **^{13}C NMR** (400 MHz, DMSO- d_6): δ_{C} = 158.2, 154.8, 150.9, 142.9, 137.5, 136.5, 131.5, 130.7, 130.6, 129.6, 128.7, 128.2, 124.3, 123.5, 120.1, 111.1.; **HRMS (TOF ES $^+$)** calculated for $\text{C}_{36}\text{H}_{24}\text{N}_6$ $^+$ [M+H] $^+$ 541.2141; found 541.2144.; **Elemental analysis** calculated for $\text{C}_{36}\text{H}_{24}\text{N}_6$ = C 79.98, H 4.47, N 15.55; found C 79.80, H 4.31, N 15.53.; **IR (ATR)** ν =2982 (CH), 1396(CC), 1067 (CN) and 719(CH).

5.6 Synthesis of Third Generation DPBI Derivatives



Scheme 4.8: Synthesis of Me-DPBI. i) Ethylene glycol, 14M NaOH (aq); ii) SOCl_2 ; iii) **Method 4**.

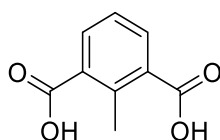
Step i: 2,6-dicyanotoluene (20 mmol) was dissolved in ethylene glycol (20 mL) and 14 M aqueous sodium hydroxide solution (7 mL, 0.10 mol) was then added to the solution. The mixture was refluxed and stirred overnight at 150 °C. Following reaction completion, the solution was cooled and neutralised using concentrated hydrochloric acid. The resulting solid was collected by filtration and then dried over air flow.

Step ii: 2-methylisophthalic acid (2.7 mmol) was dissolved in SOCl_2 (10 mL). The resulting solution was refluxed and stirred for 4 hours at 75 °C. The excess SOCl_2 was distilled off under reduced pressure, yielding a yellow solid.

Reactions performed at 0.5g scale (**20**).

Step iii (part 1): The resulting product from Step ii (1 eq.), N-phenylbenzene-1,2-diamine (2.2 eq.), and THF (20 mL) were then placed in a 50mL round-bottom flask equipped with a Teflon-coated magnetic stirrer bar. The resulting solution was left to stir overnight at room temperature. The resulting purple solution was then poured into water (50 mL), causing precipitation. The solid was collected using vacuum filtration and dried over airflow.

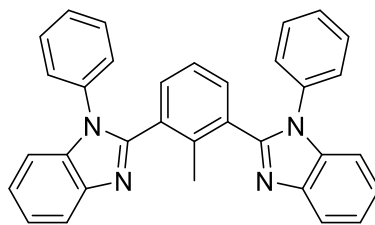
Step iii (part 2): The resulting product from Step iii (part 1) was then placed in a 10mL round-bottom flask, treated with *ortho*-phosphoric acid (7 mL) and refluxed at full power for 30mins. Subsequently, the reaction mixture was poured into water (50 mL) and neutralised using base, causing precipitation. The crude product was suction filtered and dried over airflow. The corresponding product was purified via column chromatography using hexane:ethyl acetate (1:1) as the eluent, followed by recrystallisation in toluene/hexane (2:2), bearing **ME-DPBI** as a white solid (80%).



19

2-methylisophthalic acid
Chemical Formula: C₉H₈O₄
Exact Mass: 180.04

2-Methylisophthalic acid (19) Yield: 3.59g (99%).; **Appearance:** white solid.; ¹H NMR (DMSO-d₆) δ_H: 13.14 (s, 2H, COOH), 7.81 (2H, d, J = 7.7 Hz, Ph CH), 7.36 (1H, t, J = 7.8 Hz, Ph CH), 2.59 (3H, s, CH₃).; ¹³C NMR (400 MHz, DMSO): δ_C = 169.6, 137.4, 134.2, 132.2, 126.1, 18.0.; IR (ATR) ν = 2895 (OH), 2594 (CH), 1682(CO), 1413 (CC), 1244 (CO) and 916(CH). The analysis was found to be in agreement with literature values.⁹



21

ME-DPBI

2,2'-(2-methyl-1,3-phenylene)bis(1-phenyl-1*H*-benzo[*d*]imidazole)

Chemical Formula: C₃₃H₂₄N₄

Exact Mass: 476.20

ME-DPBI (21) Yield: 0.152g(65%).; **Appearance:** white solid.; **¹H NMR** (300 MHz, DMSO-*d*₆): δ_H = 7.80 (d, *J* = 6.1 Hz, 2H, Ph CH), 7.47(d, *J* = 5.3 Hz, 6H, Ph CH), 7.37 (m, 4H, Ph CH), 7.31(m, 6H, Ph CH), 7.25 (m, 5H, Ph CH) and 7.16(t, *J* = 7.6 Hz, 2H, Ph CH).; **¹³C NMR** (400 MHz, DMSO): δ_C = 152.1, 143.0, 137.8, 136.0, 135.9, 132.6, 131.4, 130.1, 128.8, 127.2, 125.5, 123.8, 123.1, 119.9, 110.9 and 17.8.; **HRMS (TOF ES⁺)** calculated for C₃₃H₂₄N₄⁺ [M+H]⁺ 477.2079; found 477.2069.; **Elemental analysis** calculated for C₃₃H₂₄N₄ = C 83.17, H 5.08, N 11.76; found C 83.19, H 5.06, N 11.58.; **IR (ATR)** ν = 3050(CH), 1494(CC), 1374(CN) and 748 (CH).

5.7 Reference

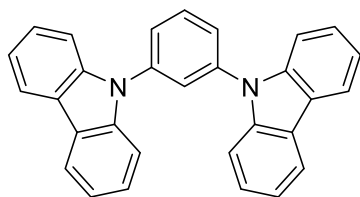
- 1 Gaussian 09, M. J. Frisch, G. W. Trucks, H. B. Schlegel, G. E. Scuseria, M. A. Robb, J. R. Cheeseman, G. Scalmani, V. Barone, G. A. Petersson, H. Nakatsuji, X. Li, M. Caricato, A. Marenich, J. Bloino, B. G. Janesko, R. Gomperts, B. Mennucci, H. P. Hratchian, J. V. Ortiz, A. F. Izmaylov, J. L. Sonnenberg, D. Williams-Young, F. Ding, F. Lipparini, F. Egidi, J. Goings, B. Peng, A. Petrone, T. Henderson, D. Ranasinghe, V. G. Zakrzewski, J. Gao, N. Rega, G. Zheng, W. Liang, M. Hada, M. Ehara, K. Toyota, R. Fukuda, J. Hasegawa, M. Ishida, T. Nakajima, Y. Honda, O. Kitao, H. Nakai, T. Vreven, K. Throssell, J. A. Montgomery, Jr., J. E. Peralta, F. Ogliaro, M. Bearpark, J. J. Heyd, E. Brothers, K. N. Kudin, V. N. Staroverov, T. Keith, R. Kobayashi, J. Normand, K. Raghavachari, A. Rendell, J. C. Burant, S. S. Iyengar, J. Tomasi, M. Cossi, J. M.

- Millam, M. Klene, C. Adamo, R. Cammi, J. W. Ochterski, R. L. Martin, K. Morokuma, O. Farkas, J. B. Foresman and D. J. Fox, *Gaussian Inc., Wallingford CT*, 2016.
- 2 P. J. Stephens, F. J. Devlin, C. F. Chabalowski and M. J. Frisch, *J. Phys. Chem.*, 1994, **98**, 11623.
- 3 T. Y. H. Lee, Q. Wang, J. U. Wallace and S. H. Chen, *J. Mater. Chem.*, 2012, **22**, 23175.
- 4 T. Kwon, M. K. Kim, J. Kwon, D. Shin, S. J. Park, C. Lee, J. Kim and J. Hong, *Chem. Mater.*, 2007, **19**, 3673.
- 5 K. Suzuki, Y. Hori and T. Kobayashi, *Adv. Synth. Catal.*, 2008, **350**, 652.
- 6 Y. Nakayama, N. Yokoyama, H. Nara, T. Kobayashi and M. Fujiwhara, *Adv. Synth. Catal.*, 2015, **357**, 2322.
- 7 B. Avitia, E. MacIntosh, S. Muhia and E. Kelson, *Tetrahedron Lett.*, 2011, **52**, 1631.
- 8 A. K.-W. Chan, E. S.-H. Lam, A. Y.-Y. Tam, D. P.-K. Tsang, W. H. Lam, M.-Y. Chan, W.-T. Wong and V. W.-W. Yam, *Chem. Eur. J.*, 2013, **19**, 13910.
- 9 L. Meca, I. Císařová, D. Drahoňovský and D. Dvřák, *Organometallics*, 2008, **27**, 1850.

6 Appendix i

6.1 Analytical Data of MCP Derivatives Synthesised via Ullmann Reaction

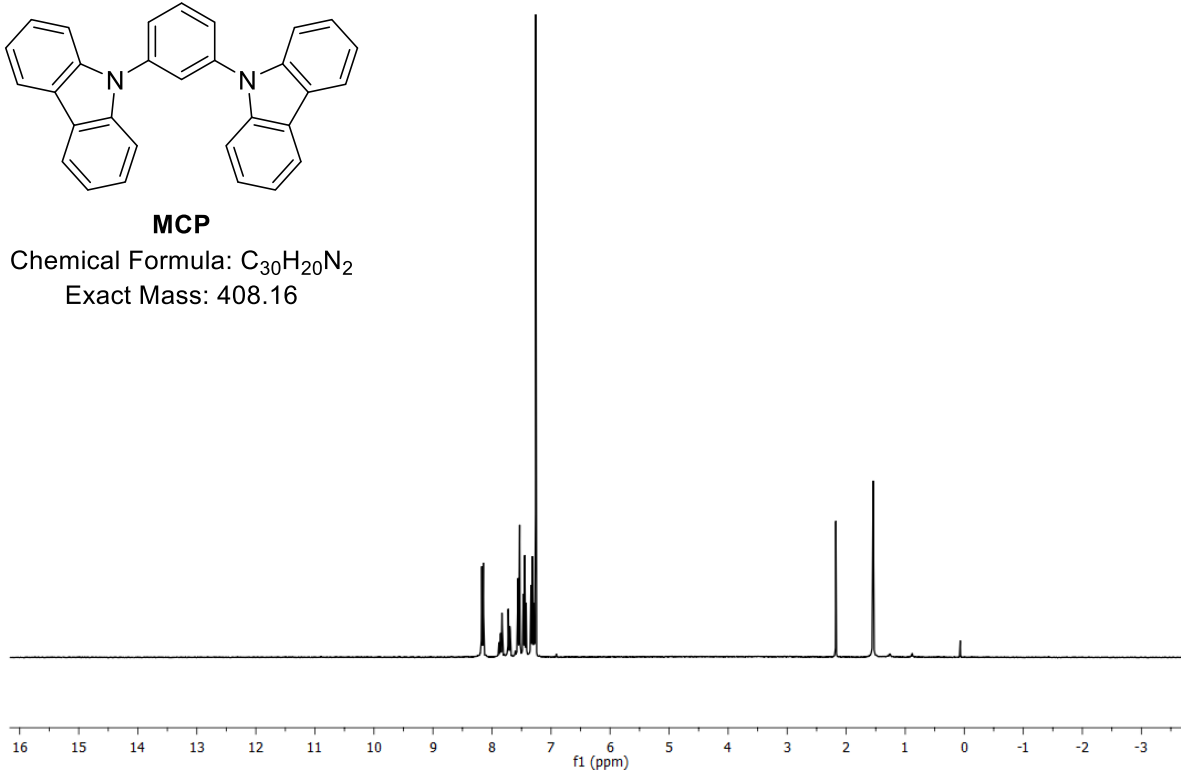
11-21-Baranoff-26



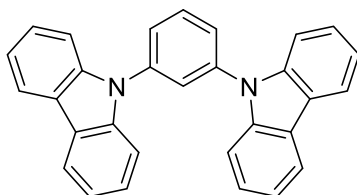
MCP

Chemical Formula: $C_{30}H_{20}N_2$

Exact Mass: 408.16



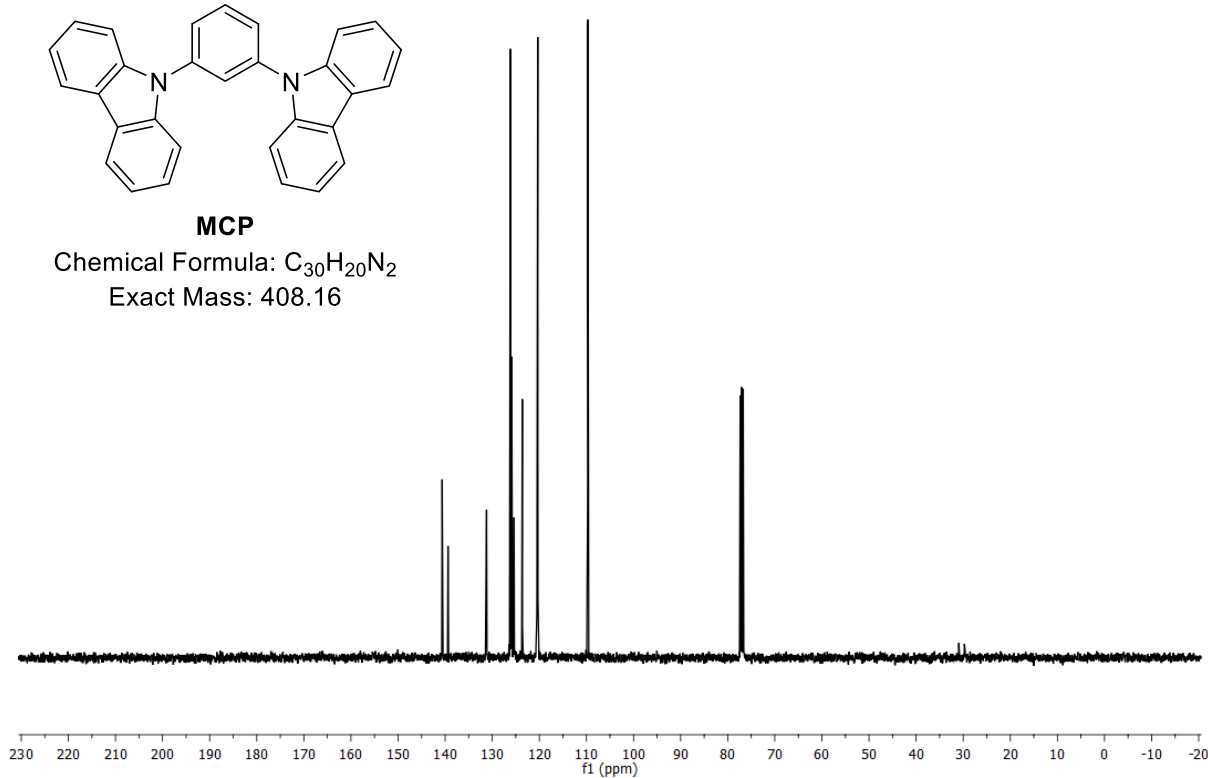
11-25-Baranoff-5



MCP

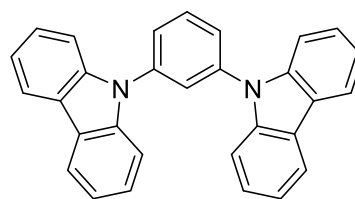
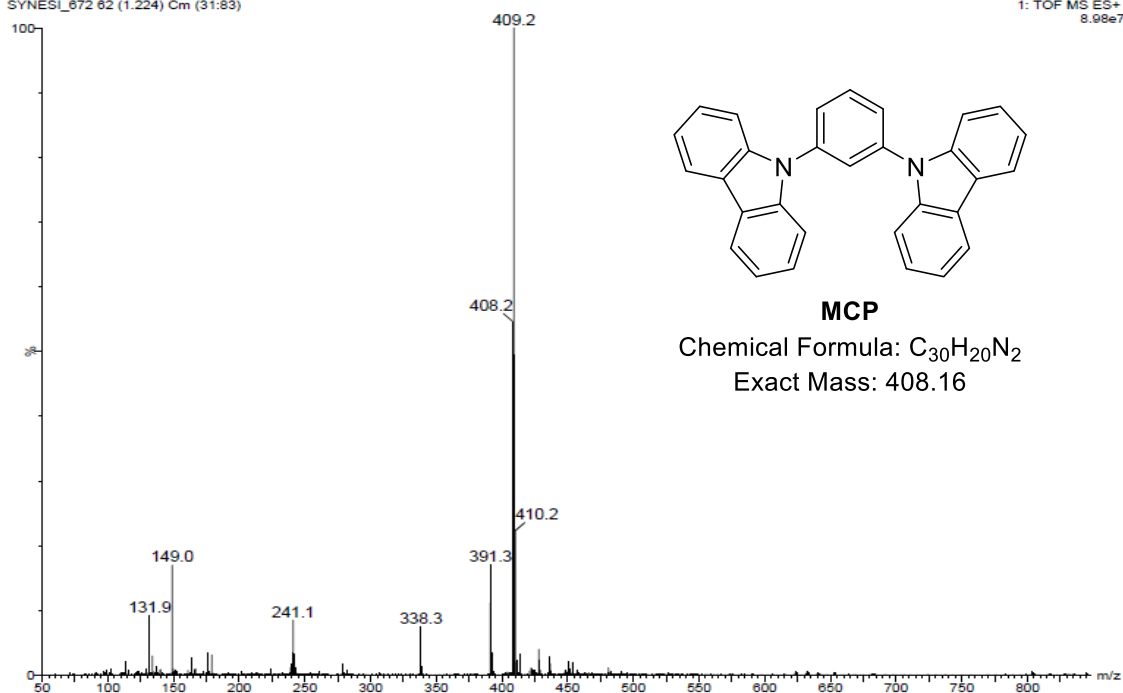
Chemical Formula: $C_{30}H_{20}N_2$

Exact Mass: 408.16



N.Sahotra NXs-15-re
SYNESI_672 62 (1.224) Cm (31:83)

1: TOF MS ES+
8.98e7

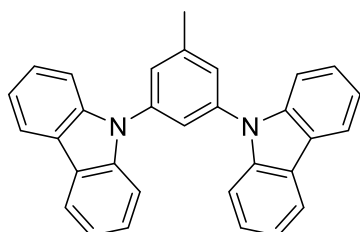


MCP

Chemical Formula: $C_{30}H_{20}N_2$

Exact Mass: 408.16

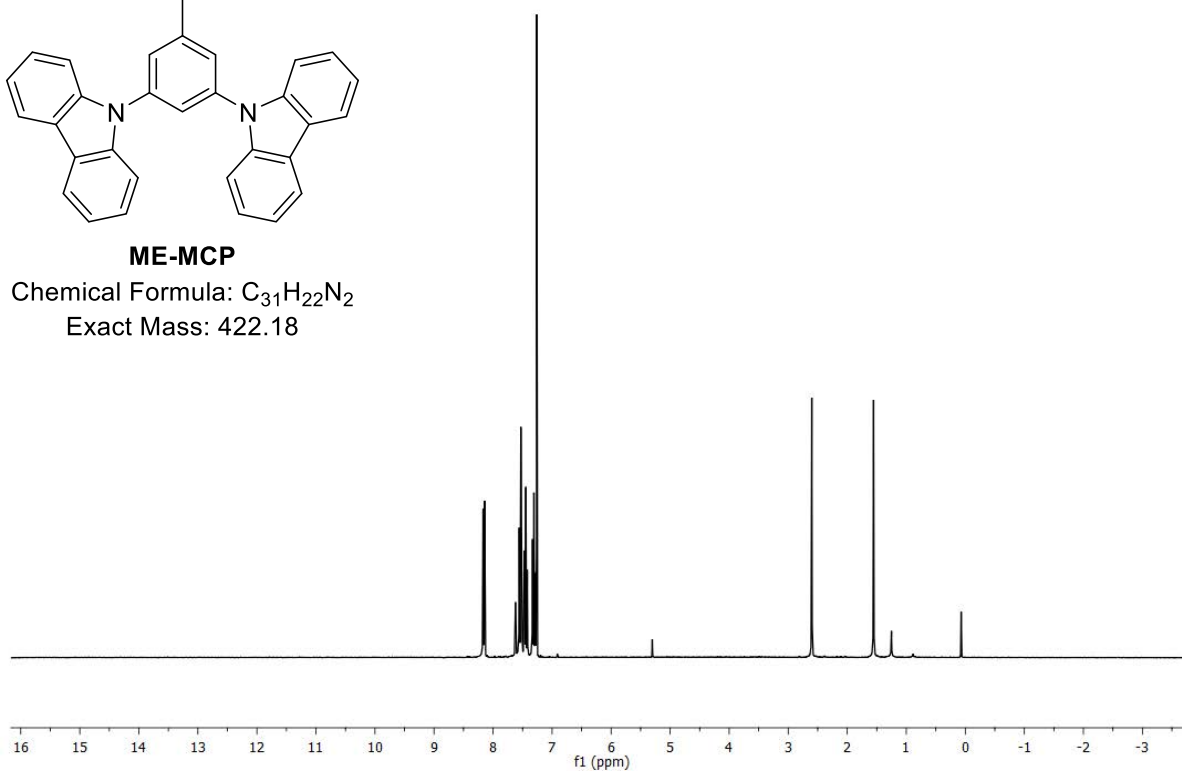
11-29-Baranoff-23



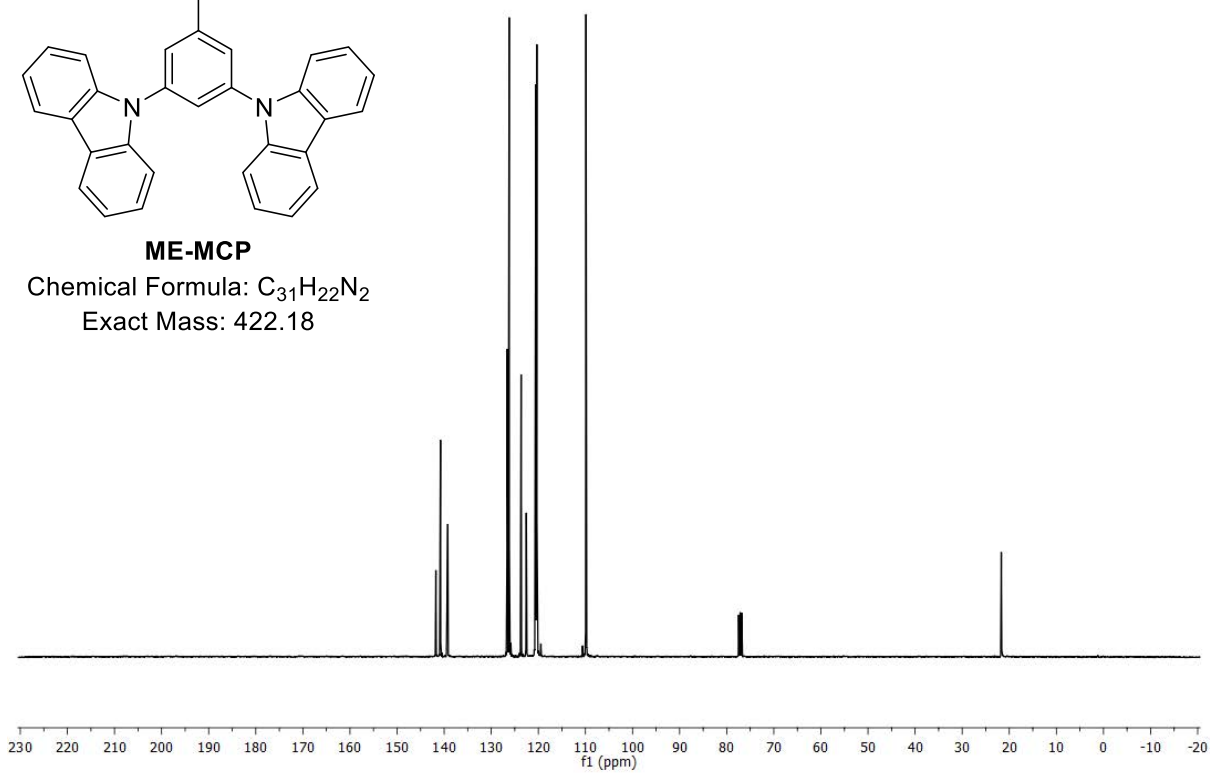
ME-MCP

Chemical Formula: $C_{31}H_{22}N_2$

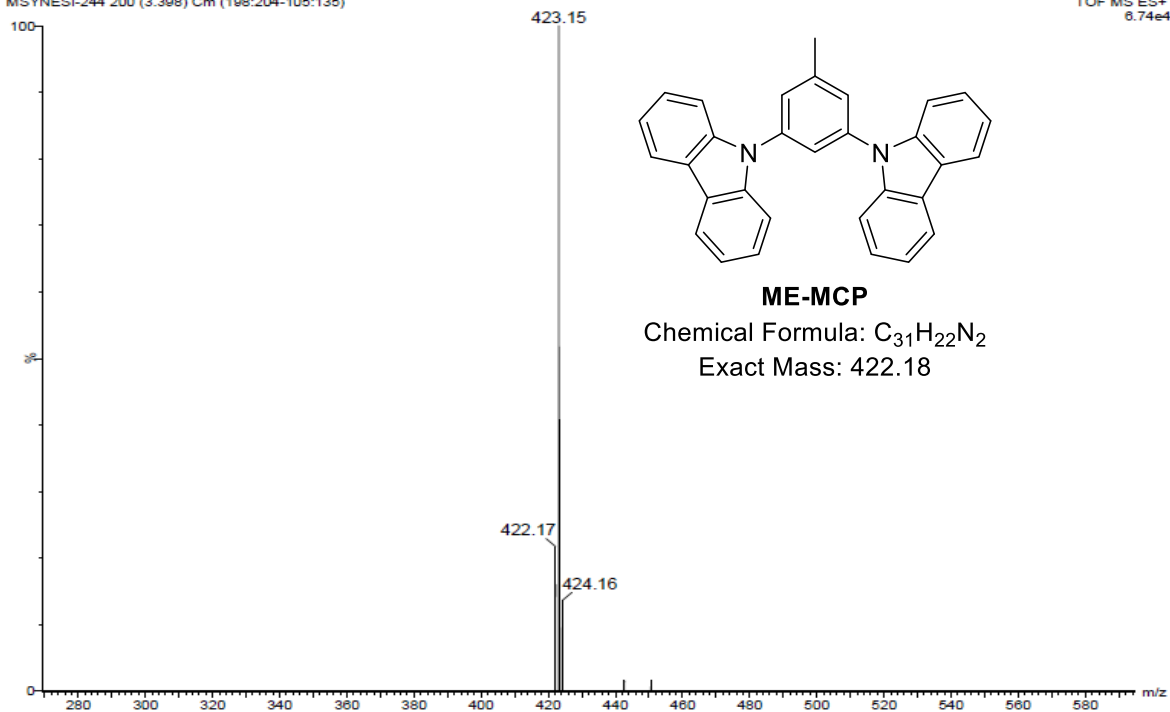
Exact Mass: 422.18



Chemical Formula: $C_{31}H_{22}N_2$
Exact Mass: 422.18



TOF MS ES+
6.74e4



Elemental Composition Report **N. Sahotra Nx5-16**

Single Mass Analysis

Tolerance = 5.0 PPM / DBE: min = -1.5, max = 1000.0

Element prediction: Off

Monoisotopic Mass, Even Electron Ions

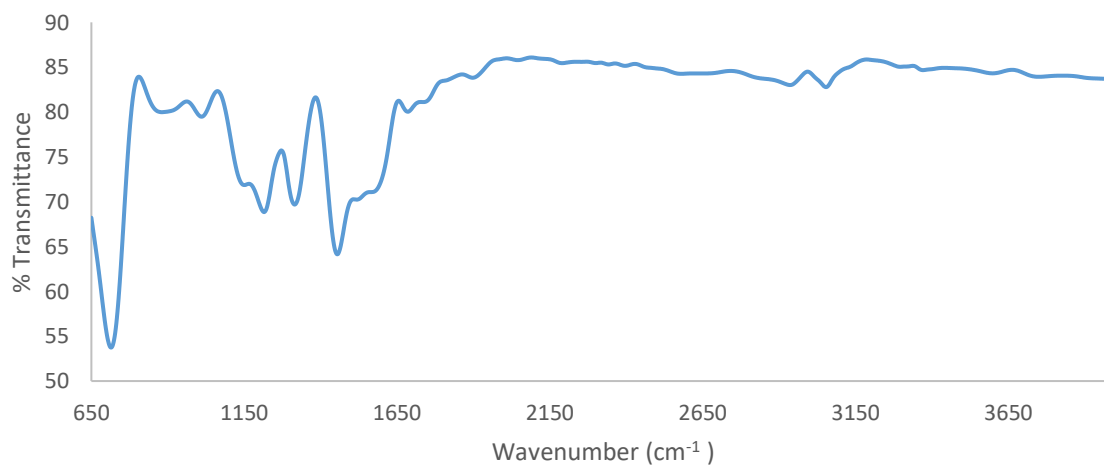
56 formula(e) evaluated with 1 results within limits (all results (up to 1000) for each mass)

Elements Used:

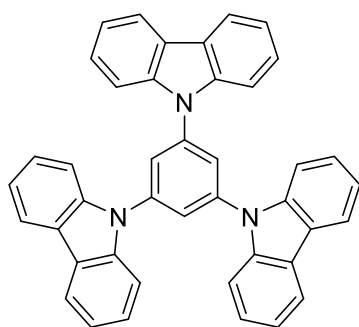
C: 0-100 H: 0-100 N: 1-10

Minimum:				-1.5	
Maximum:	5.0	5.0	1000.0		
Mass	Calc. Mass	mDa	PPM	DBE	Formula
423.1855	423.1861	-0.6	-1.4	21.5	C31 H23 N2

Infrared Spectrum of **ME-MCP**



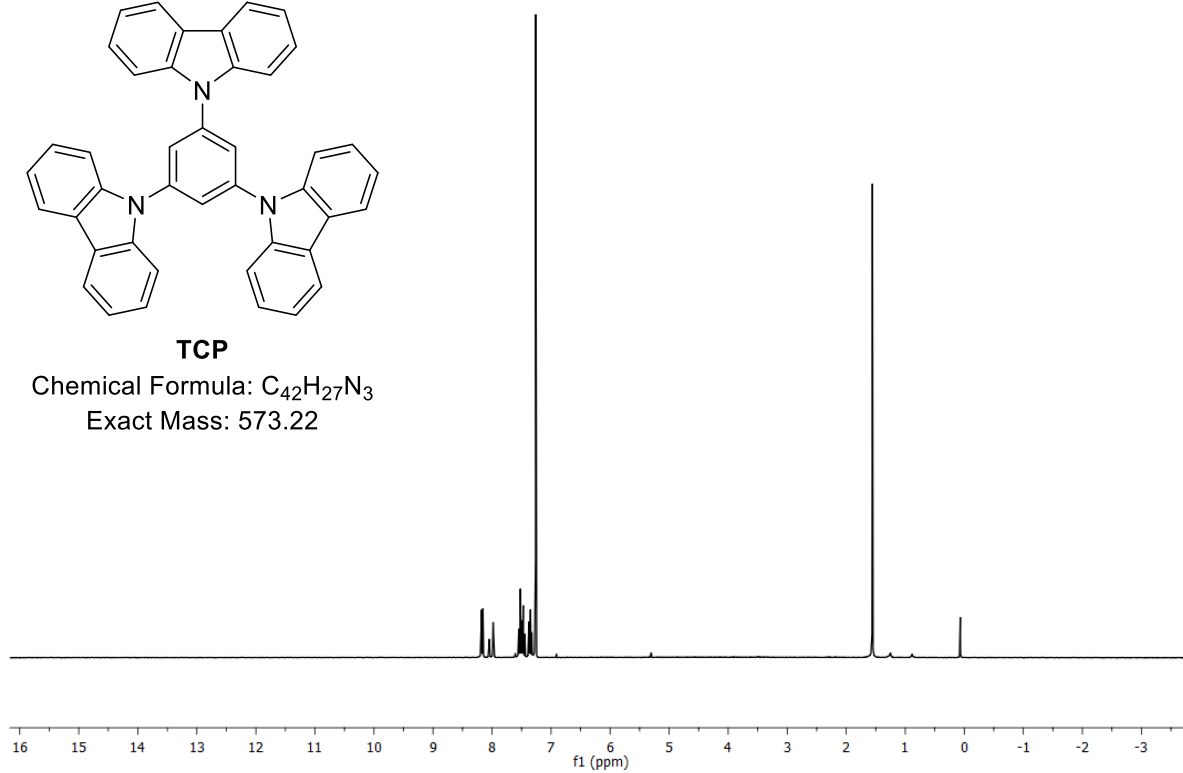
03-06-Baranoff-27



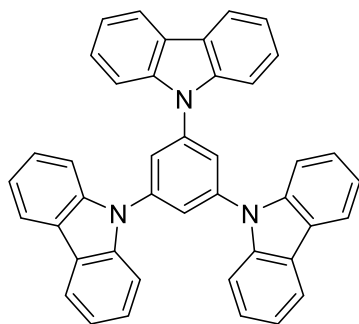
TCP

Chemical Formula: $C_{42}H_{27}N_3$

Exact Mass: 573.22



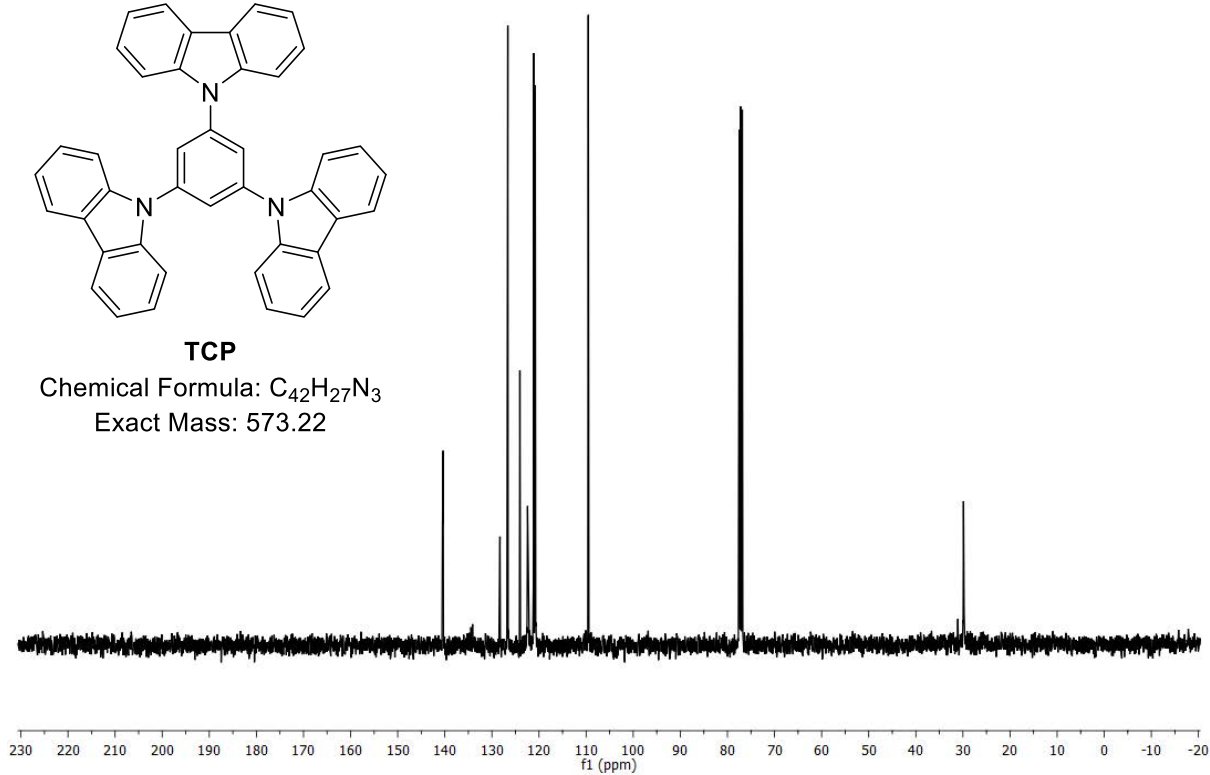
03-10-Baranoff-14

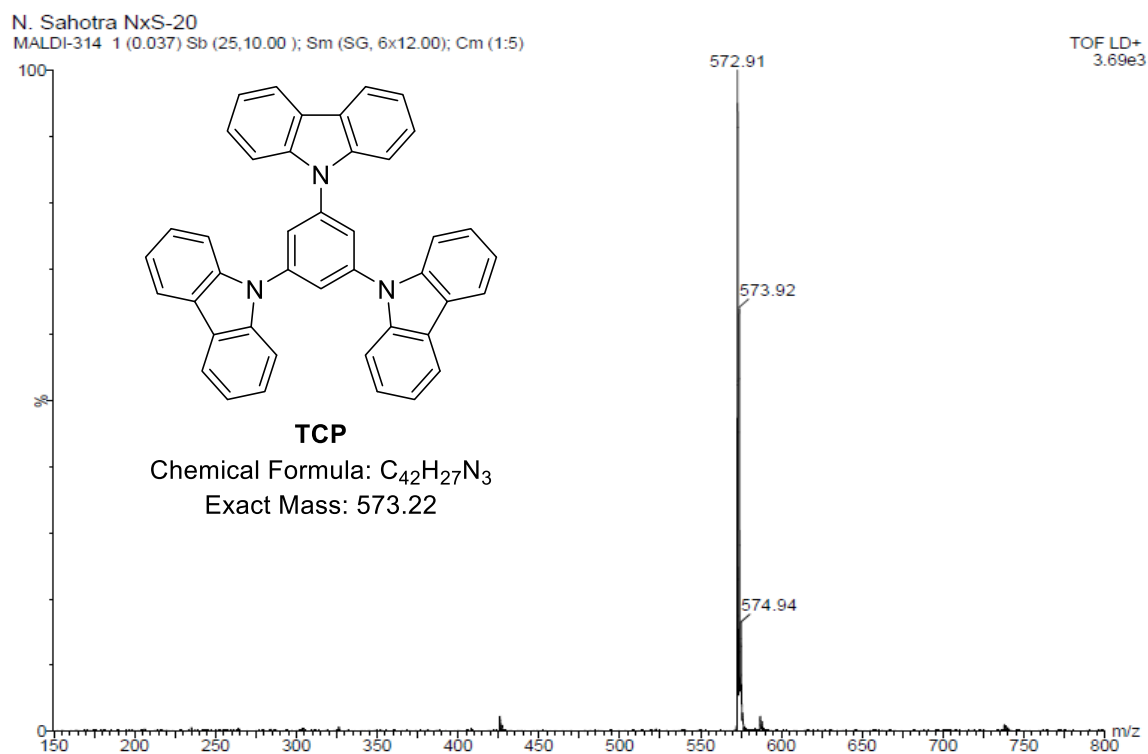


TCP

Chemical Formula: $C_{42}H_{27}N_3$

Exact Mass: 573.22





Elemental Composition Report N. Sahotra NxS-20

Single Mass Analysis

Tolerance = 10.0 PPM / DBE: min = -1.5, max = 50.0

Element prediction: Off

Monoisotopic Mass, Odd and Even Electron Ions

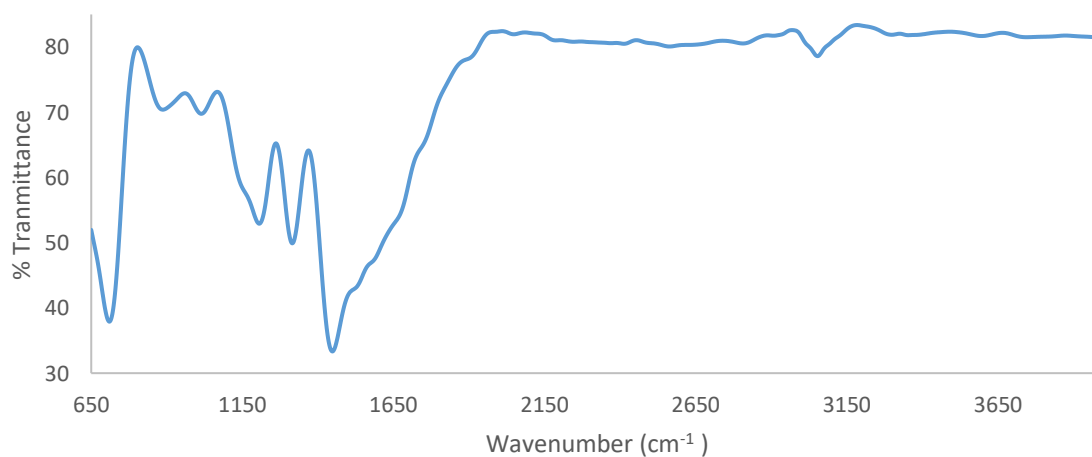
32 formula(e) evaluated with 1 results within limits (up to 50 best isotopic matches for each mass)

Elements Used:

C: 0-100 H: 0-100 N: 1-4

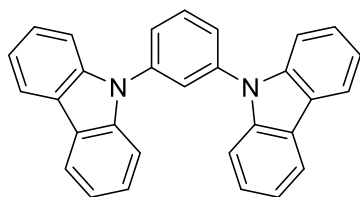
Minimum:				-1.5	
Maximum:		5.0	10.0	50.0	
Mass	Calc. Mass	mDa	PPM	DBE	Formula
573.2204	573.2205	-0.1	-0.2	31.0	C42 H27 N3

IR Spectrum of TCP



6.2 Analytical Data of MCP Derivatives Synthesised via Buchwald-Hartwig Reaction

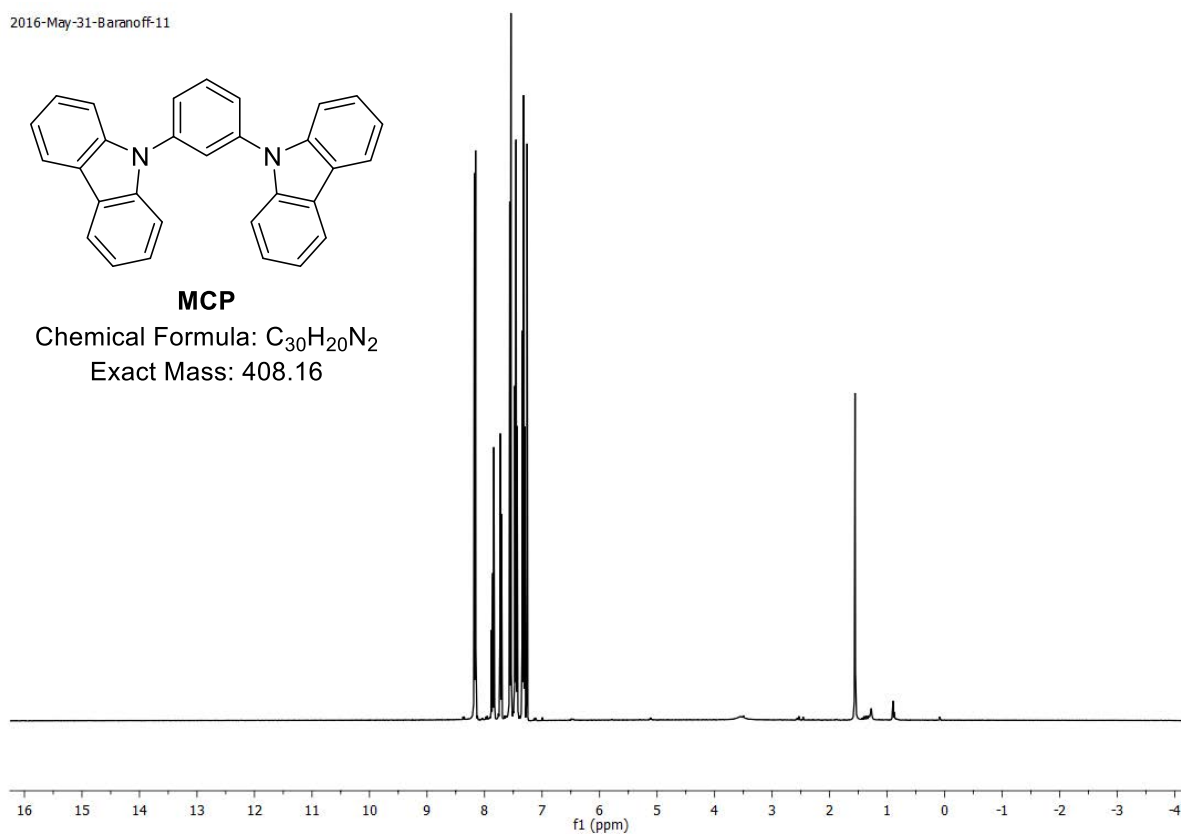
2016-May-31-Baranoff-11



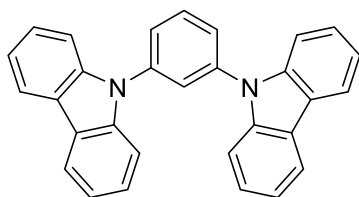
MCP

Chemical Formula: $C_{30}H_{20}N_2$

Exact Mass: 408.16



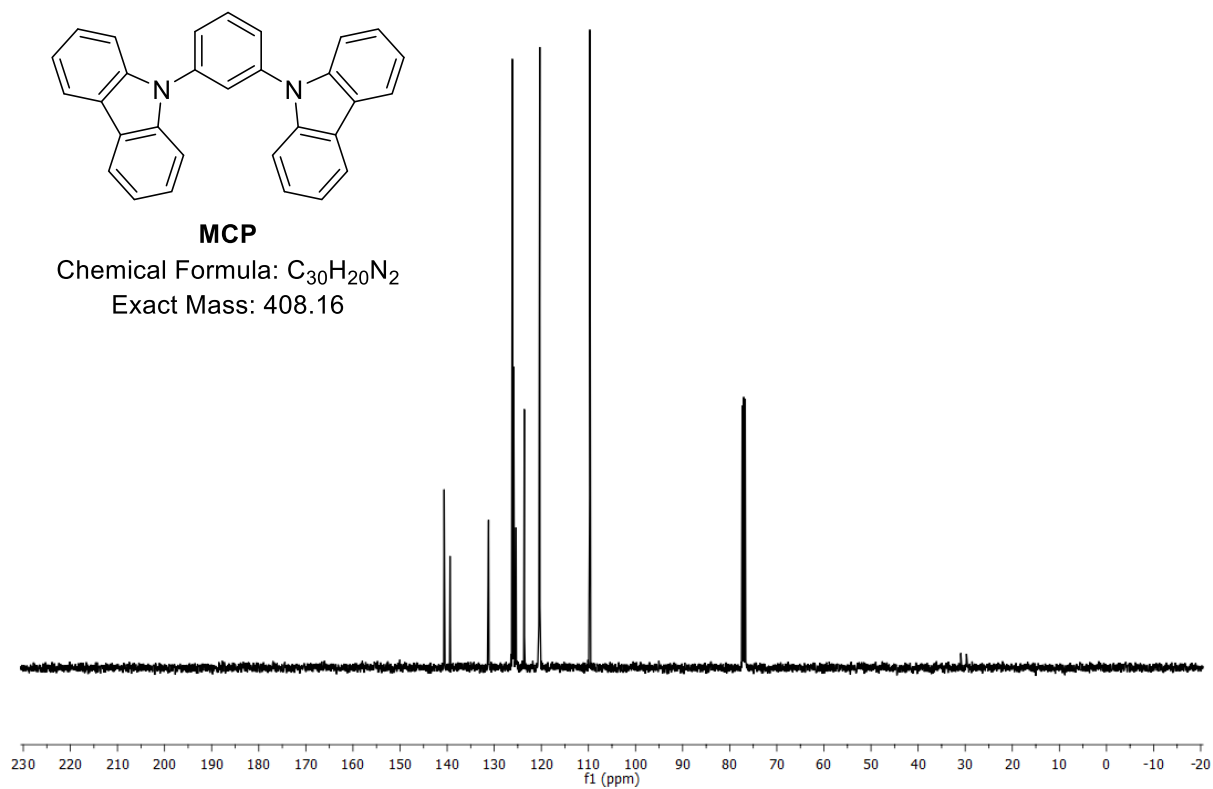
2016-May-31-Baranoff-11



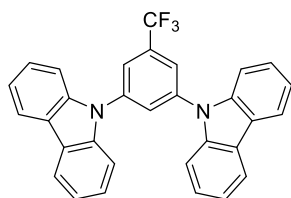
MCP

Chemical Formula: $C_{30}H_{20}N_2$

Exact Mass: 408.16



03-06-Baranoff-27

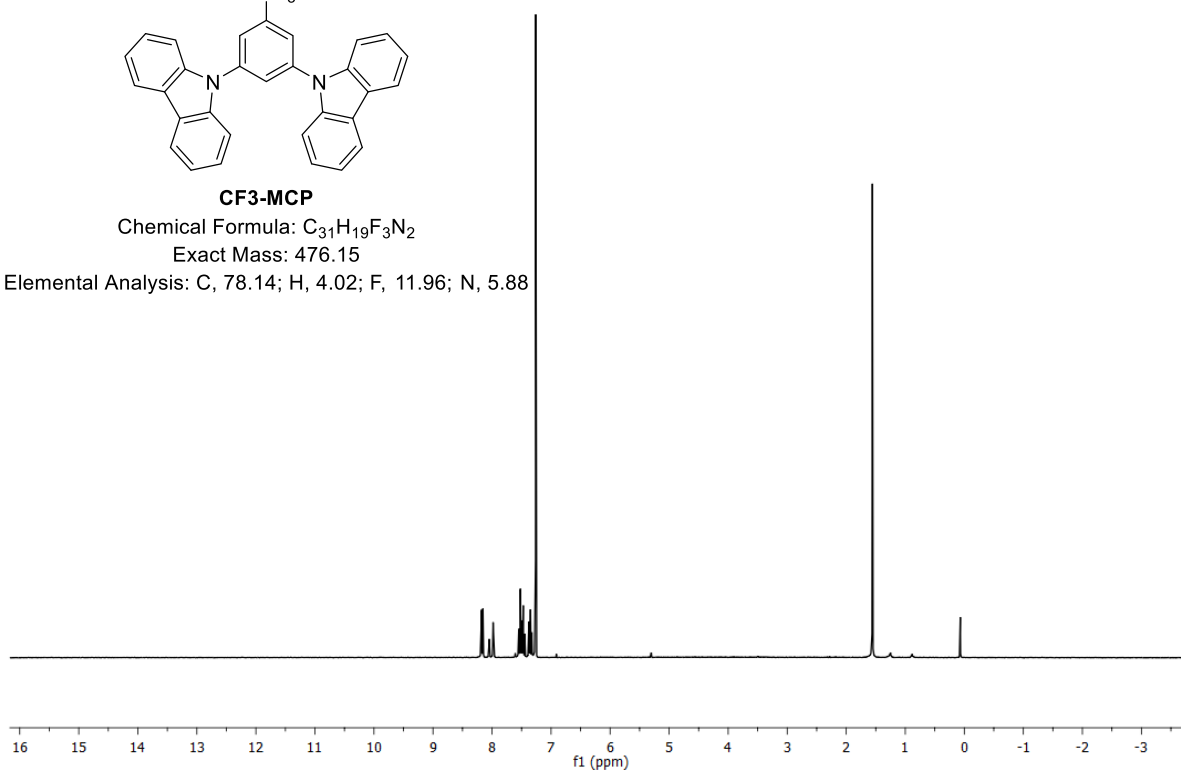


CF3-MCP

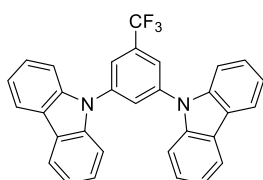
Chemical Formula: $C_{31}H_{19}F_3N_2$

Exact Mass: 476.15

Elemental Analysis: C, 78.14; H, 4.02; F, 11.96; N, 5.88



03-10-Baranoff-14

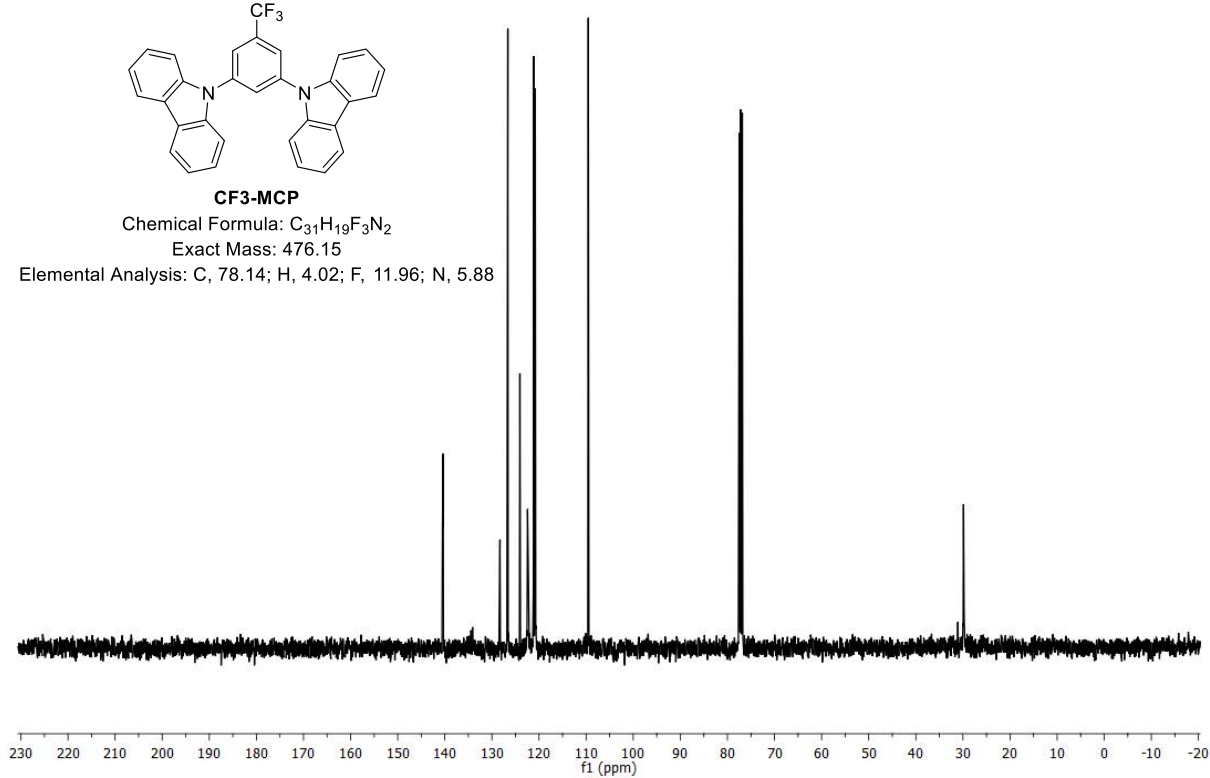


CF3-MCP

Chemical Formula: $C_{31}H_{19}F_3N_2$

Exact Mass: 476.15

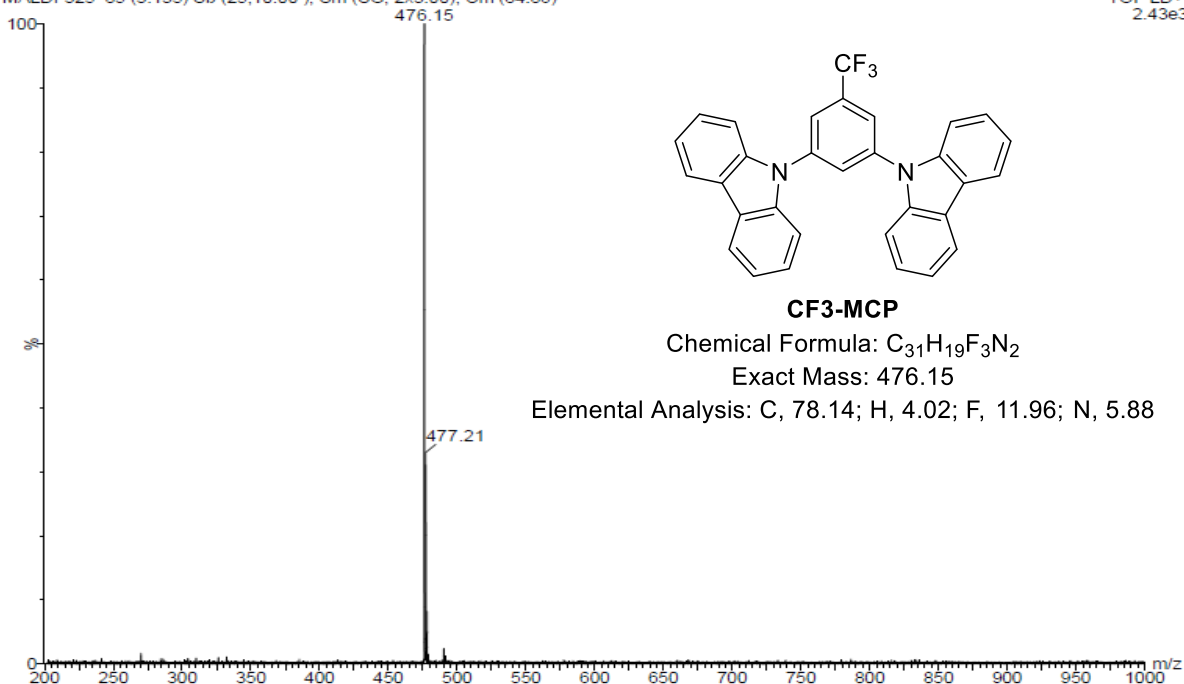
Elemental Analysis: C, 78.14; H, 4.02; F, 11.96; N, 5.88



N. Sahotra NxS-27

MALDI-325 85 (3.135) Sb (25,10.00); Sm (SG, 2x3.00); Cm (84:86)

TOF LD+
2.43e3



Elemental Composition Report N. Sahotra NxS - 27

Single Mass Analysis

Tolerance = 10.0 PPM / DBE: min = -1.5, max = 50.0

Element prediction: Off

Monoisotopic Mass, Odd and Even Electron Ions

111 formula(e) evaluated with 1 results within limits (up to 50 best isotopic matches for each mass)

Elements Used:

C: 0-100 H: 0-100 N: 1-4 F: 1-5

Minimum:				-1.5	
Maximum:		5.0	10.0	50.0	
Mass	Calc. Mass	mDa	PPM	DBE	Formula
476.1497	476.1500	-0.3	-0.6	22.0	C31 H19 N2 F3

Eager Xperience Summarize Results

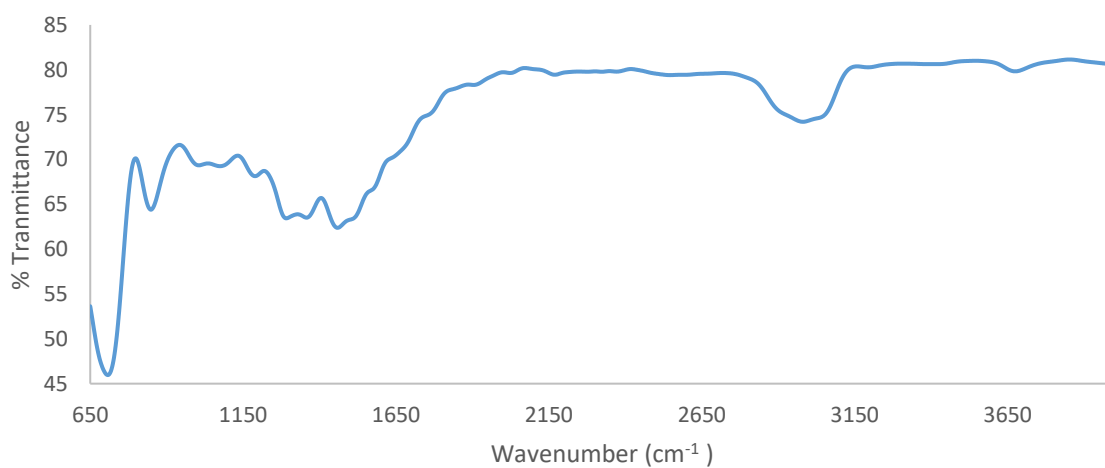
Date: 04/08/2015 @ 11:36:34

Method name: Nitrogen/Carbon/Hydrogen

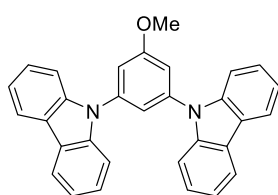
Method Filename: 16JULY2015.mth

Sample Name	Elemental %		
	Nitrogen	Carbon	Hydrogen
CF3-MCP	6.39	79.09	4.45
CF3-MCP	6.10	79.35	4.16
Average			
	6.24	79.22	4.30

IR Spectrum of CF3-MCP



04-24-Baranoff-45

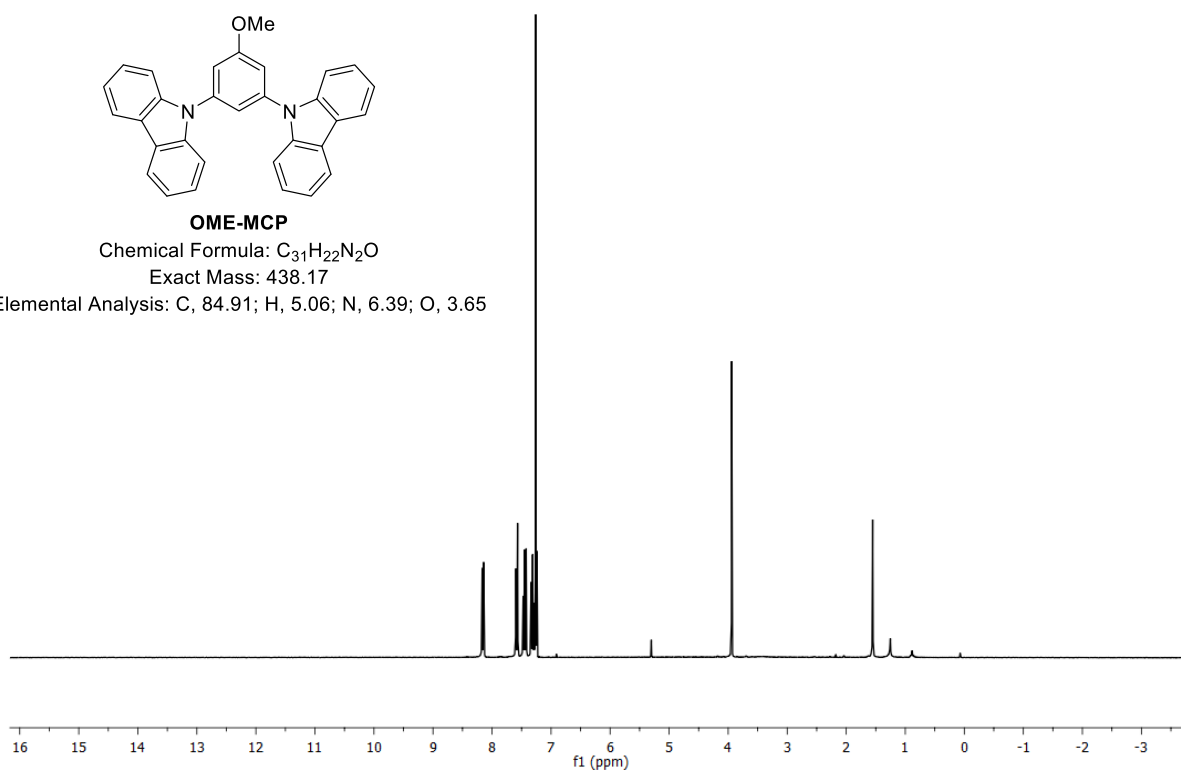


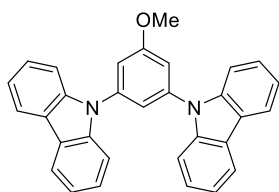
OME-MCP

Chemical Formula: $C_{31}H_{22}N_2O$

Exact Mass: 438.17

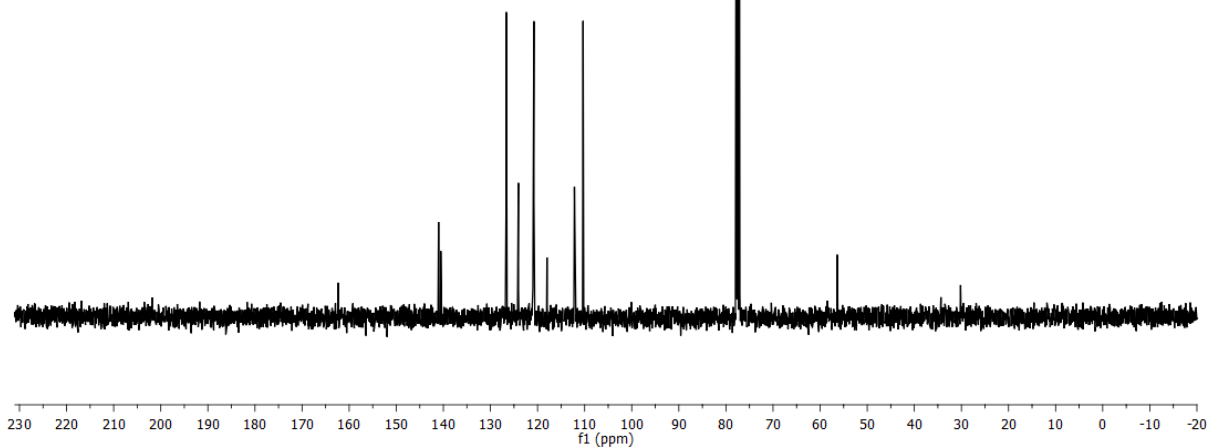
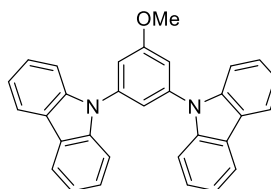
Elemental Analysis: C, 84.91; H, 5.06; N, 6.39; O, 3.65



**OME-MCP**Chemical Formula: $C_{31}H_{22}N_2O$

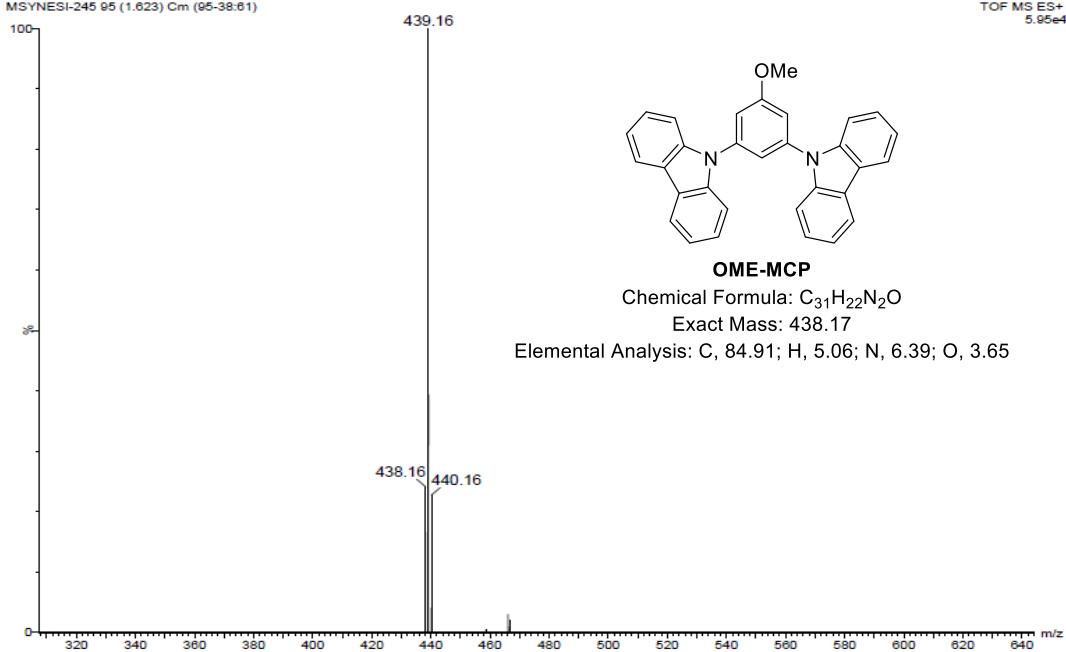
Exact Mass: 438.17

Elemental Analysis: C, 84.91; H, 5.06; N, 6.39; O, 3.65

N. Sahotra NxS-28
MSYNESI-245 95 (1.623) Cm (95-38.61)TOF MS ES+
5.95e4**OME-MCP**Chemical Formula: $C_{31}H_{22}N_2O$

Exact Mass: 438.17

Elemental Analysis: C, 84.91; H, 5.06; N, 6.39; O, 3.65



Elemental Composition Report **N. Sahotra NxS-28**

Single Mass Analysis

Tolerance = 5.0 PPM / DBE: min = -1.5, max = 1000.0

Element prediction: Off

Monoisotopic Mass, Even Electron Ions

260 formula(e) evaluated with 1 results within limits (all results (up to 1000) for each mass)

Elements Used:

C: 0-100 H: 0-100 N: 1-10 O: 1-5

Minimum: -1.5

Maximum: 5.0 5.0 1000.0

Mass	Calc. Mass	mDa	PPM	DBE	Formula
439.1803	439.1810	-0.7	-1.6	21.5	C31 H23 N2 O

Eager Xperience Summarize Results

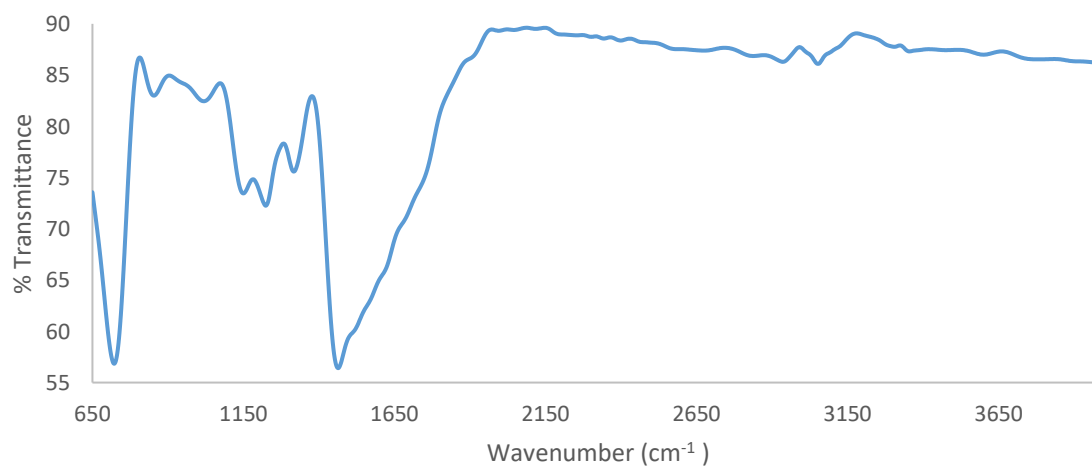
Date: 29/07/2015 @ 16:22:27

Method name: Nitrogen/Carbon/Hydrogen

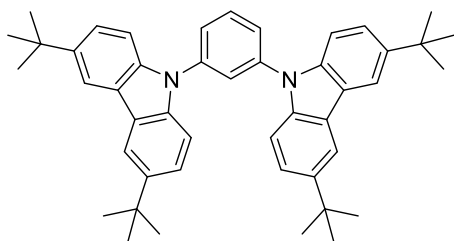
Method Filename: 16JULY2015.mth

Sample Name	Elemental %		
	Nitrogen	Carbon	Hydrogen
OME-MCP	7.32	84.79	5.23
OME-MCP	7.15	84.89	5.25
Average			
	7.24	84.84	5.24

IR Spectrum of **OME-MCP**



04-27-Baranoff-26

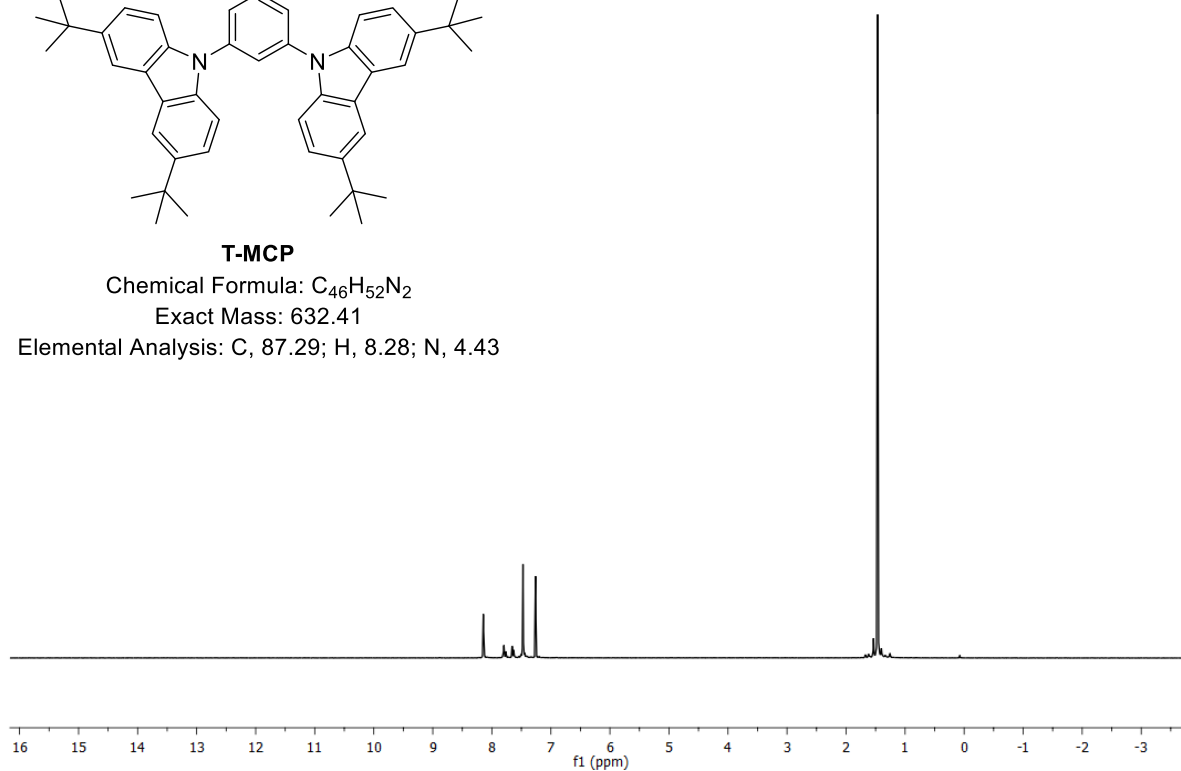


T-MCP

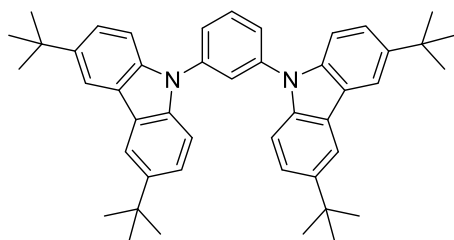
Chemical Formula: $C_{46}H_{52}N_2$

Exact Mass: 632.41

Elemental Analysis: C, 87.29; H, 8.28; N, 4.43



2017-Sep-14-Baranoff-10

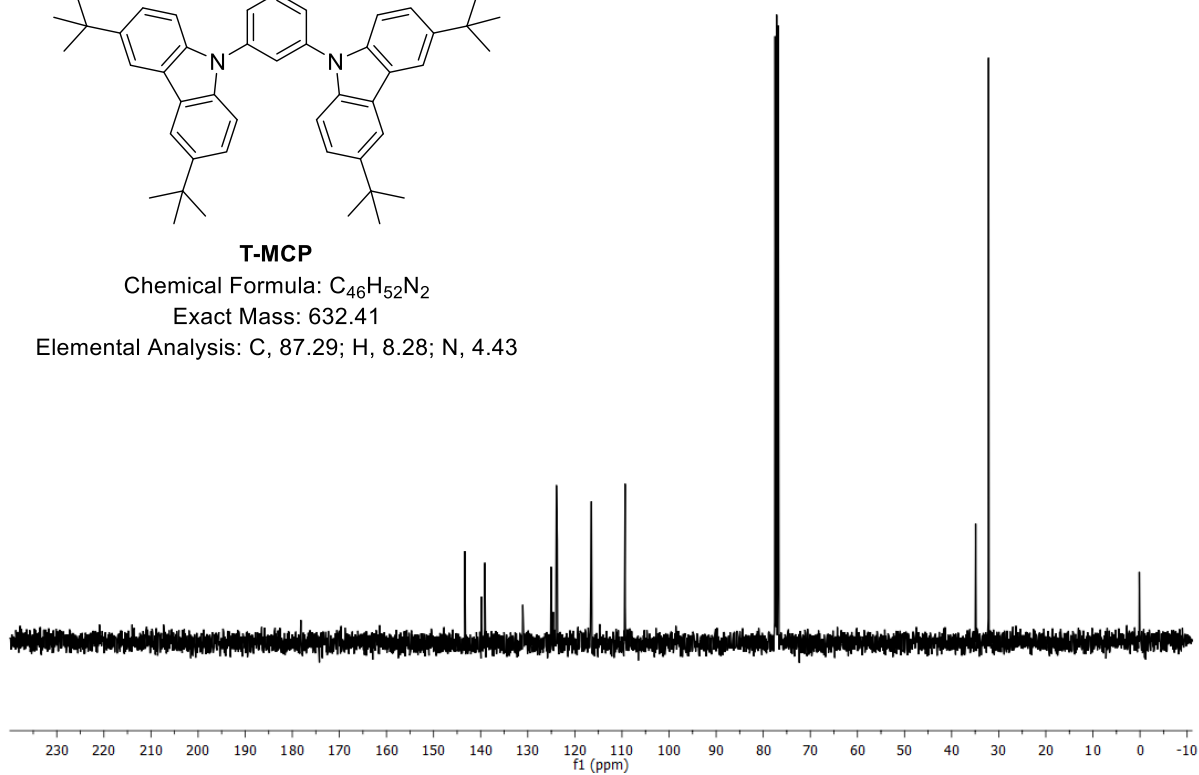


T-MCP

Chemical Formula: $C_{46}H_{52}N_2$

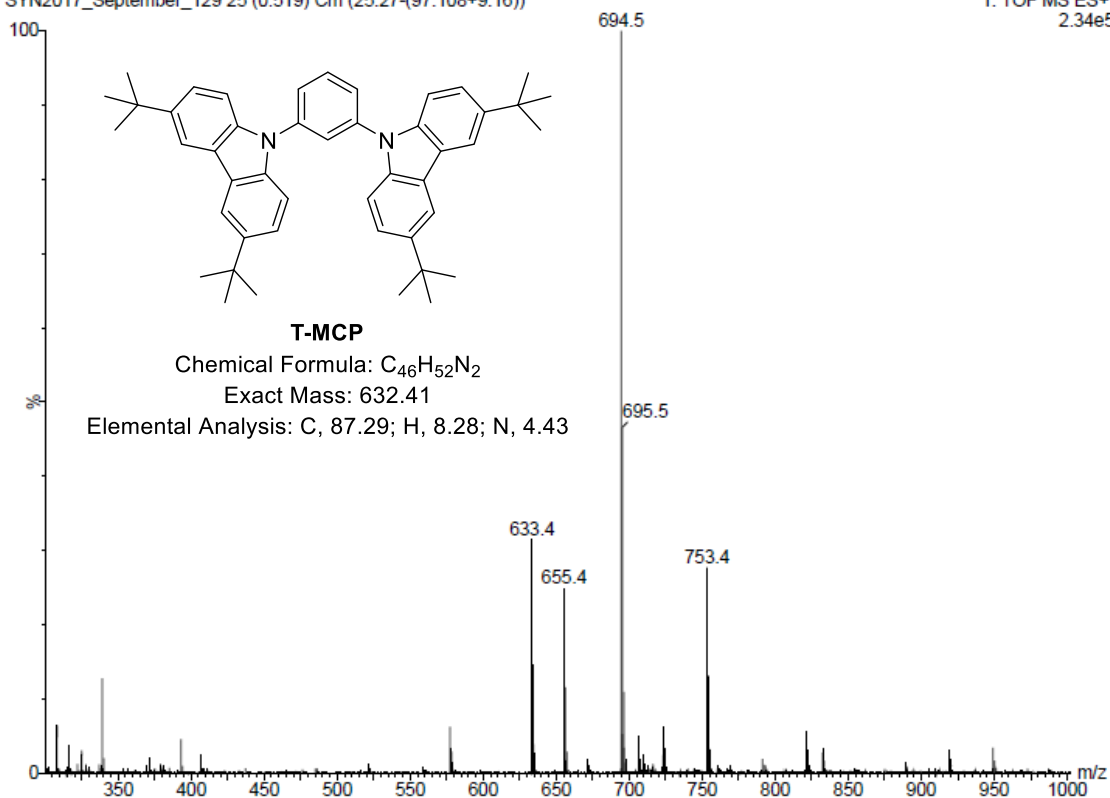
Exact Mass: 632.41

Elemental Analysis: C, 87.29; H, 8.28; N, 4.43



Nikhil Sahotra T-MCP
 SYN2017_September_129 25 (0.519) Cm (25:27-(97:108+9:16))

1: TOF MS ES+
 2.34e5



Elemental Composition Report Nikhil Sahotra T-MCP

Single Mass Analysis

Tolerance = 5.0 PPM / DBE: min = -1.5, max = 1000.0

Element prediction: Off

Monoisotopic Mass, Even Electron Ions

49 formula(e) evaluated with 1 results within limits (all results (up to 1000) for each mass)

Elements Used:

C: 0-100 H: 0-100 N: 0-5

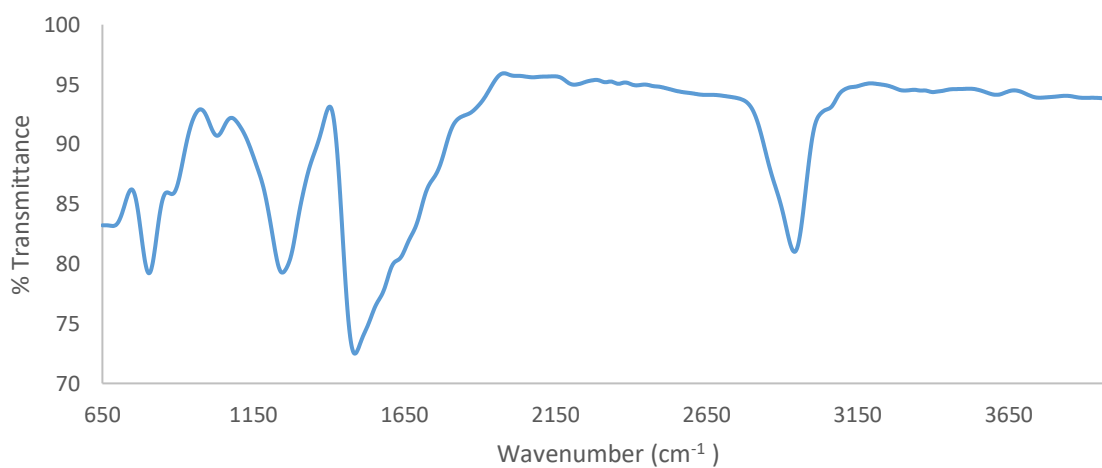
Minimum:			-1.5		
Maximum:	5.0	5.0	1000.0		
Mass	Calc. Mass	mDa	PPM	DBE	Formula
633.4204	633.4209	-0.5	-0.8	21.5	C46 H53 N2

Eager Xperience Summarize Results

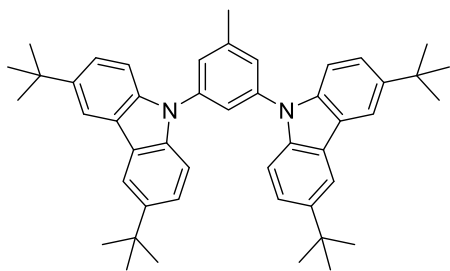
Date: 15/09/2017 @ 11:27:11
 Method name: Nitrogen/Carbon/Hydrogen
 Method Filename: 13September2017 retest 2.mth

Sample Name	Elemental %		
	Nitrogen	Carbon	Hydrogen
T-MCP	4.29	87.52	8.17
T-MCP	4.29	87.49	8.15
T-MCP	4.28	87.19	8.19
Average			
	4.29	87.40	8.17

IR Spectrum of T-MCP



2017-Mar-27-Baranoff-19

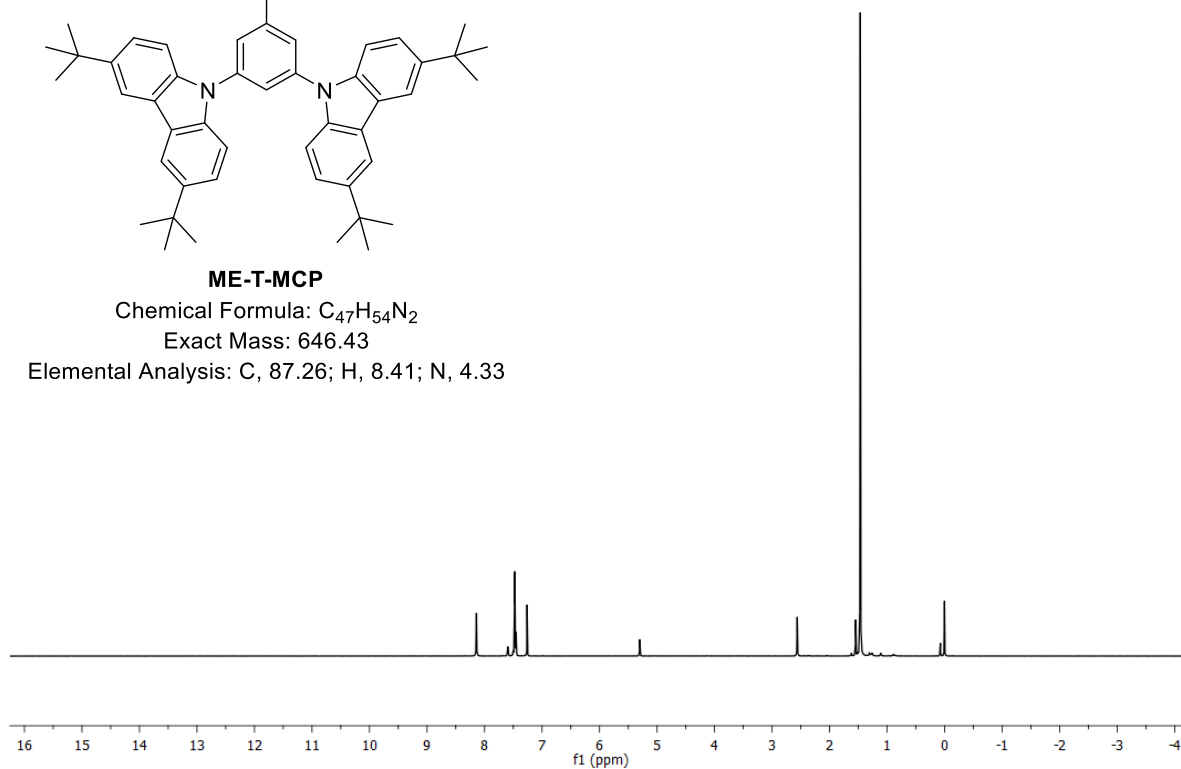


ME-T-MCP

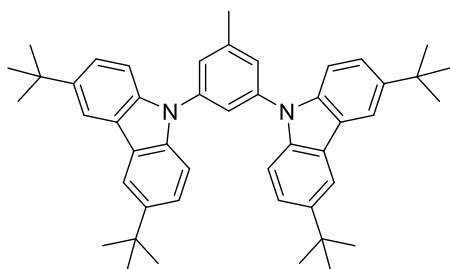
Chemical Formula: $C_{47}H_{54}N_2$

Exact Mass: 646.43

Elemental Analysis: C, 87.26; H, 8.41; N, 4.33



2017-Mar-27-Baranoff-19

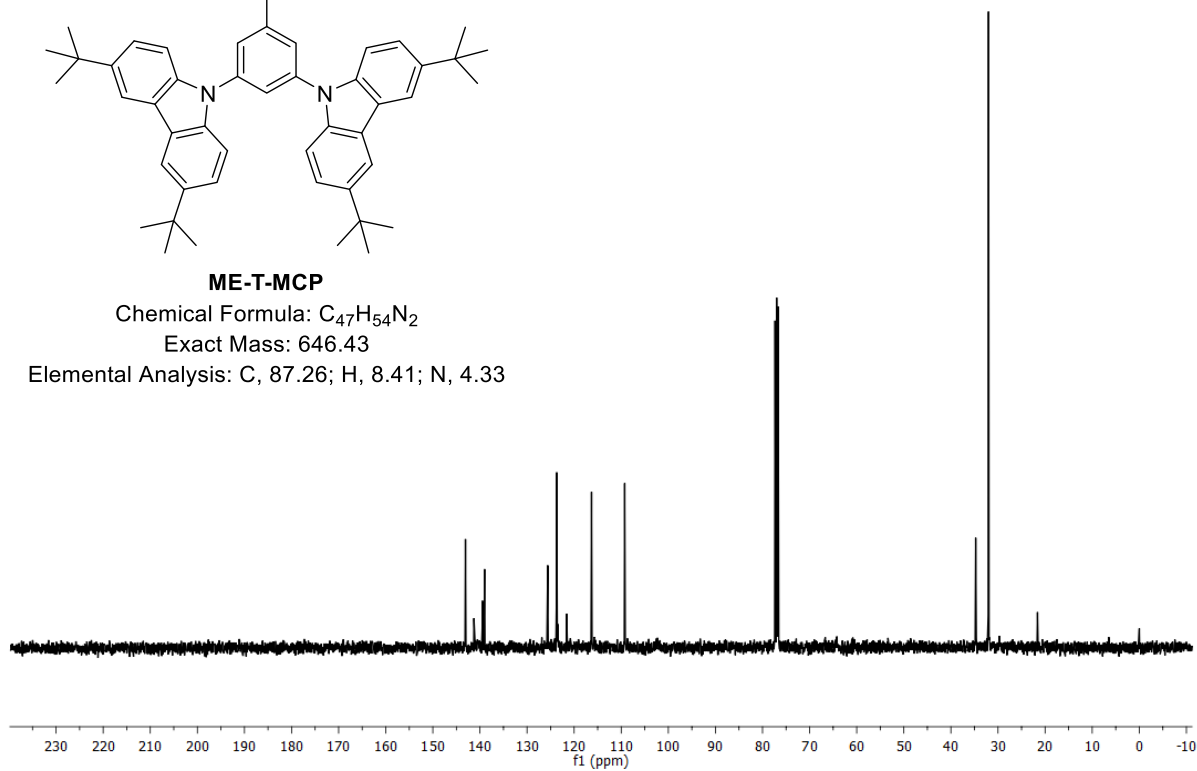


ME-T-MCP

Chemical Formula: $C_{47}H_{54}N_2$

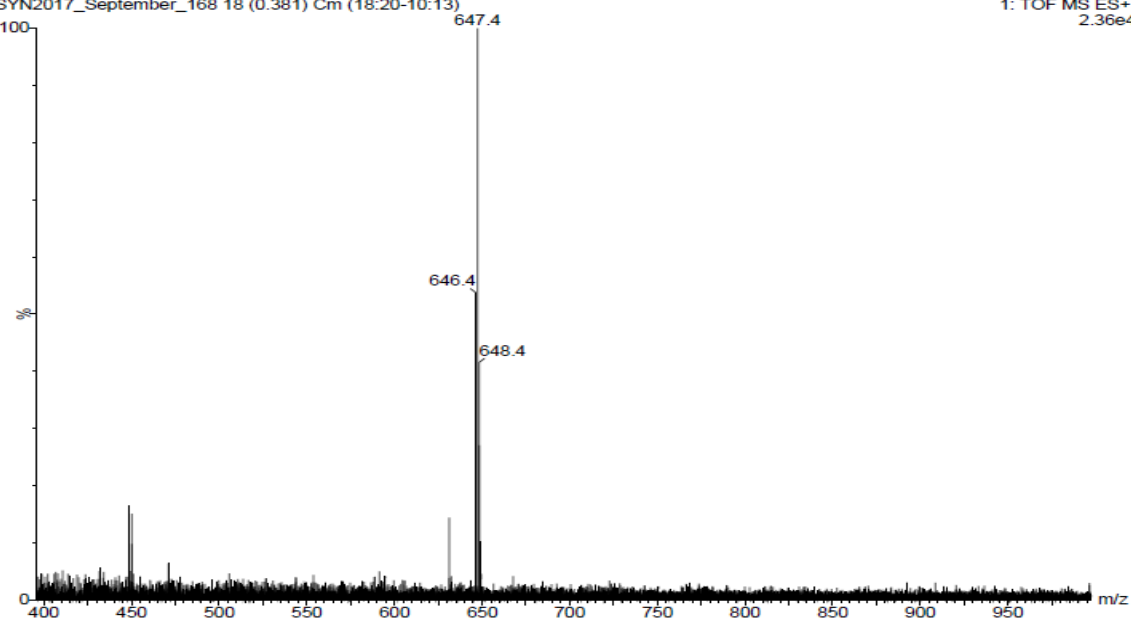
Exact Mass: 646.43

Elemental Analysis: C, 87.26; H, 8.41; N, 4.33



Nikhil Sahotra ME-T-MCP
 SYN2017_September_168 18 (0.381) Cm (18:20-10:13)

1: TOF MS ES+
 2.36e4



Elemental Composition Report Nikhil Sahotra ME-T-MCP

Single Mass Analysis

Tolerance = 5.0 PPM / DBE: min = -1.5, max = 1000.0

Element prediction: Off

Monoisotopic Mass, Even Electron Ions

50 formula(e) evaluated with 1 results within limits (all results (up to 1000) for each mass)

Elements Used:

C: 0-100 H: 0-100 N: 0-5

Minimum: -1.5

Maximum: 5.0 5.0 1000.0

Mass	Calc. Mass	mDa	PPM	DBE	Formula
647.4366	647.4365	0.1	0.2	21.5	C47 H55 N2

Eager Xperience Summarize Results

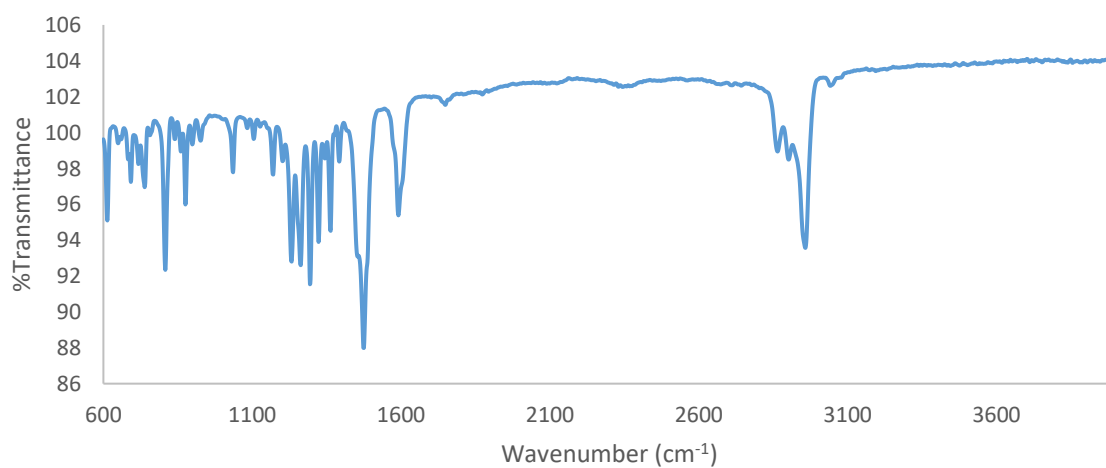
Date: 14/09/2017 @ 14:39:19

Method name: Nitrogen/Carbon/Hydrogen

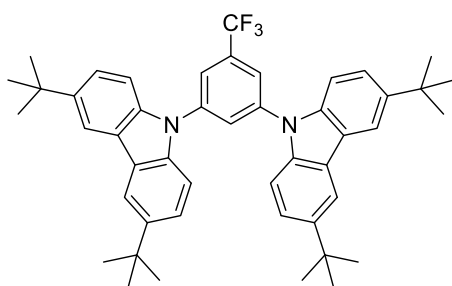
Method Filename: 13September2017 retest 2.mth

Sample Name	Elemental %		
	Nitrogen	Carbon	Hydrogen
ME-T-MCP	4.22	87.01	8.30
ME-T-MCP	4.20	87.10	8.24
	4.21	87.06	8.27

IR Spectrum of ME-T-MCP



2016-May-31-Baranoff-9

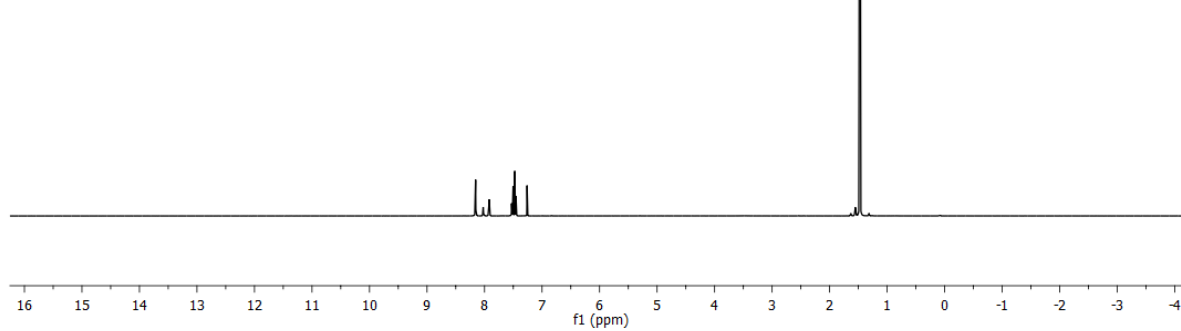


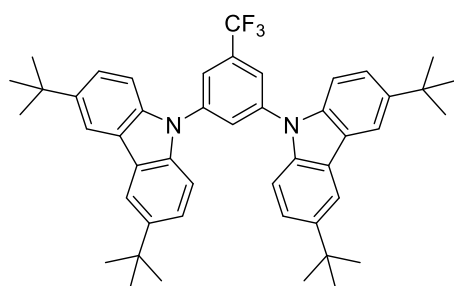
CF₃-T-MCP

Chemical Formula: C₄₇H₅₁F₃N₂

Exact Mass: 700.40

Elemental Analysis: C, 80.54; H, 7.33; F, 8.13; N, 4.00



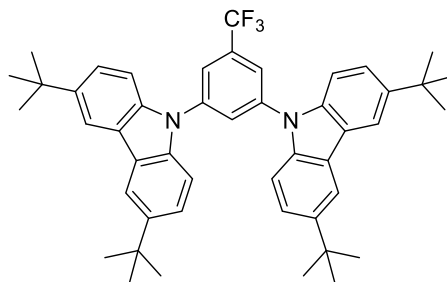
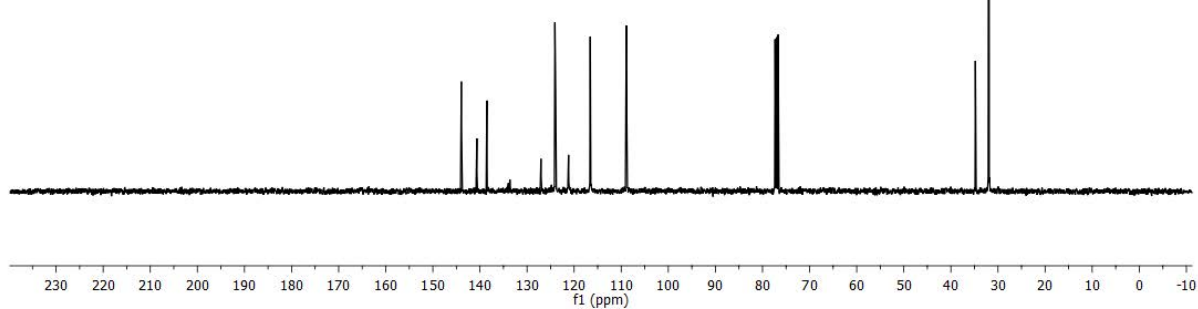


CF3-T-MCP

Chemical Formula: $C_{47}H_{51}F_3N_2$

Exact Mass: 700.40

Elemental Analysis: C, 80.54; H, 7.33; F, 8.13; N, 4.00

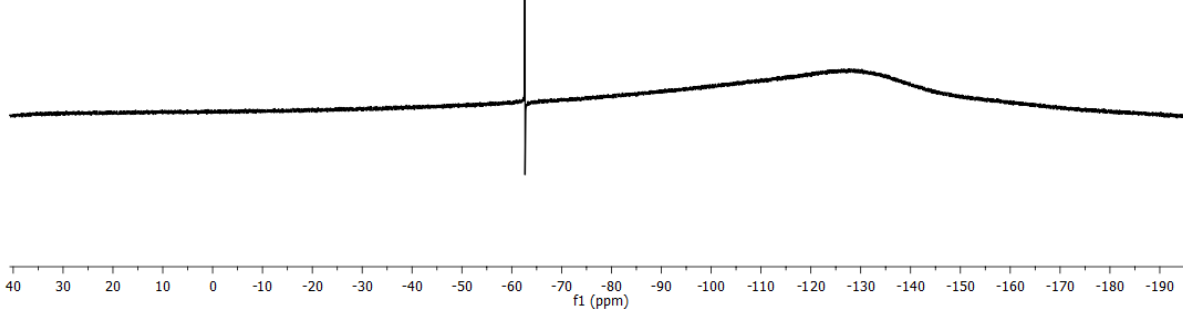


CF3-T-MCP

Chemical Formula: $C_{47}H_{51}F_3N_2$

Exact Mass: 700.40

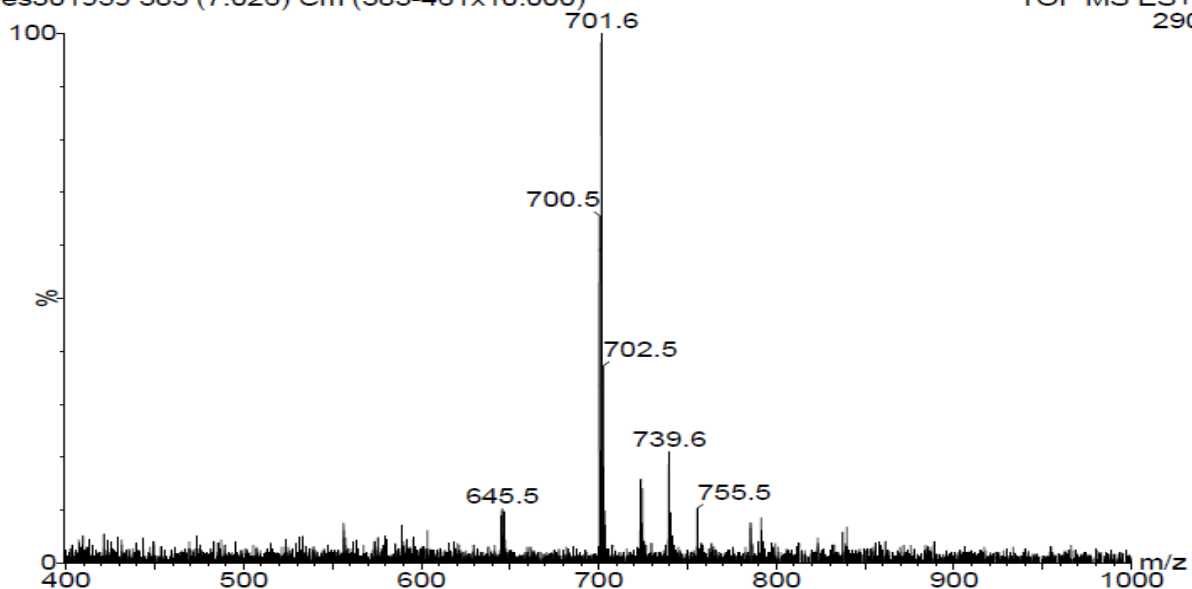
Elemental Analysis: C, 80.54; H, 7.33; F, 8.13; N, 4.00



Nikhil Sahotra NXS-75

es301959 383 (7.026) Cm (383-461x10.000)

TOF MS ES+
290



Elemental Composition Report Nikhil Sahotra CF3-T-MCP

Single Mass Analysis

Tolerance = 5.0 PPM / DBE: min = -1.5, max = 50.0

Element prediction: Off

Monoisotopic Mass, Even Electron Ions

252 formula(e) evaluated with 1 results within limits (up to 50 best isotopic matches for each mass)

Elements Used:

C: 0-200 H: 0-200 N: 1-5 F: 0-5

Minimum: -1.5

Maximum: 5.0 5.0 50.0

Mass	Calc. Mass	mDa	PPM	DBE	Formula
701.4080	701.4083	-0.3	-0.4	21.5	C47 H52 N2 F3

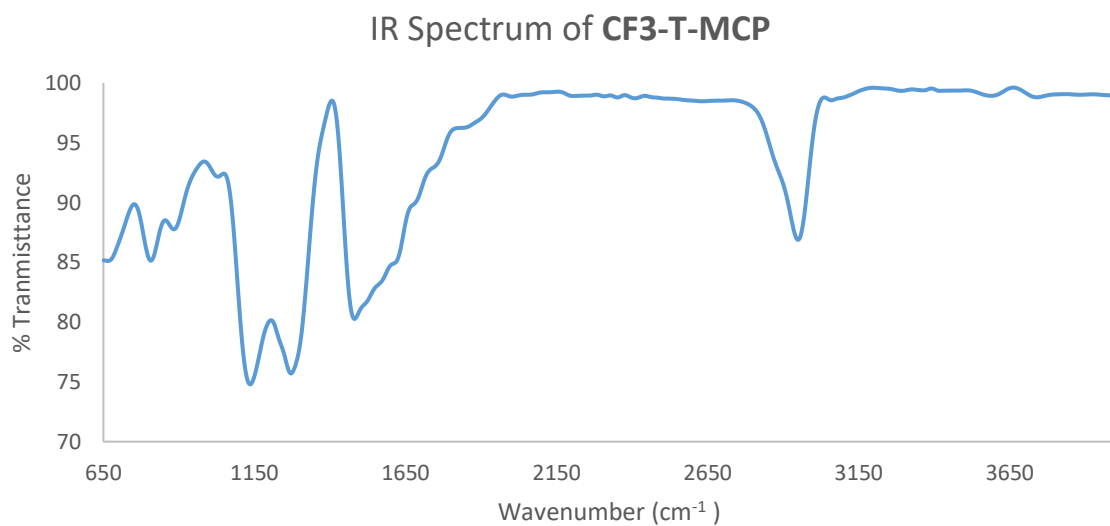
Eager Xperience Summarize Results

Date: 14/09/2017 @ 14:39:19

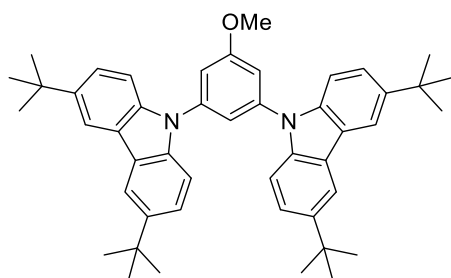
Method name: Nitrogen/Carbon/Hydrogen

Method Filename: 13September2017 retest 2.mth

Sample Name	Elemental %		
	Nitrogen	Carbon	Hydrogen
CF3-T-MCP	3.96	80.47	7.28
CF3-T-MCP	3.96	80.45	7.31
CF3-T-MCP	4	80.43	7.2
Average			
	3.97	80.45	7.26



02-17-Baranoff-21

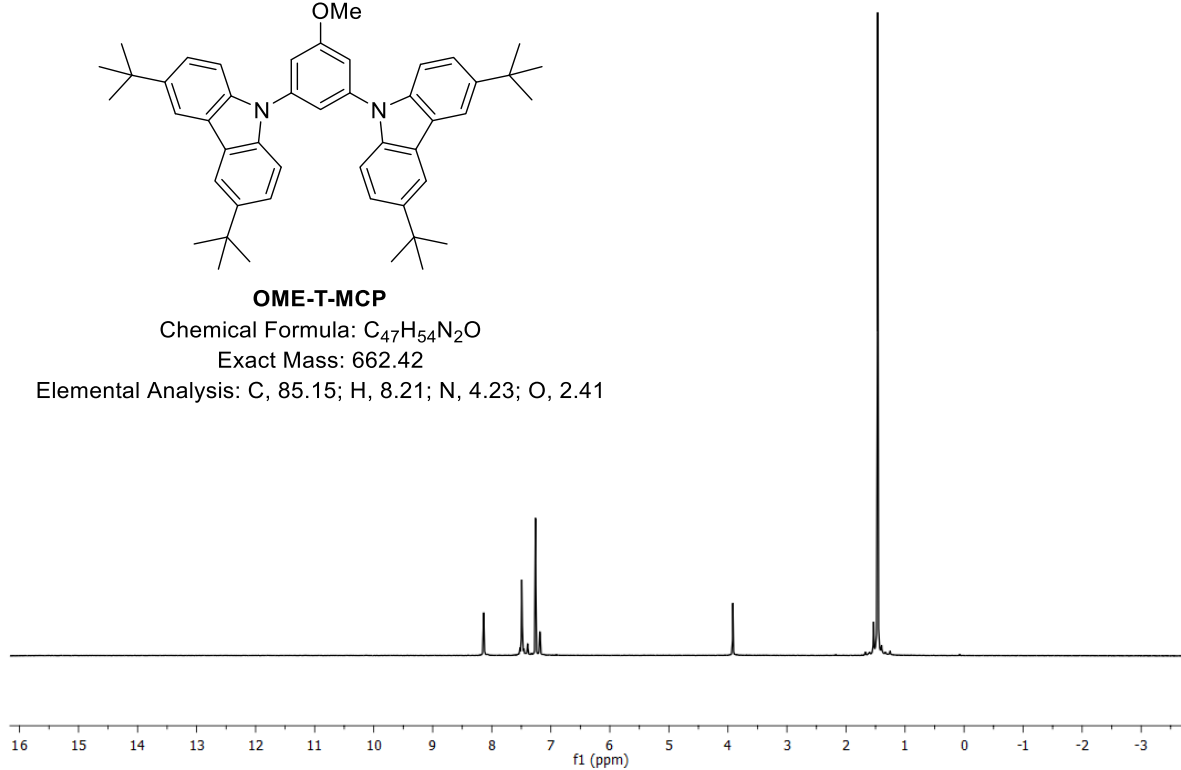


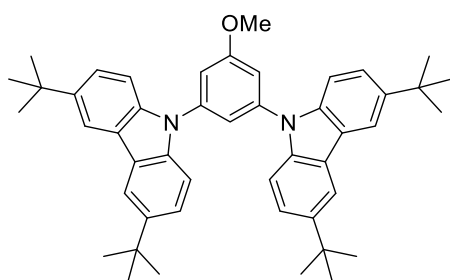
OME-T-MCP

Chemical Formula: C₄₇H₅₄N₂O

Exact Mass: 662.42

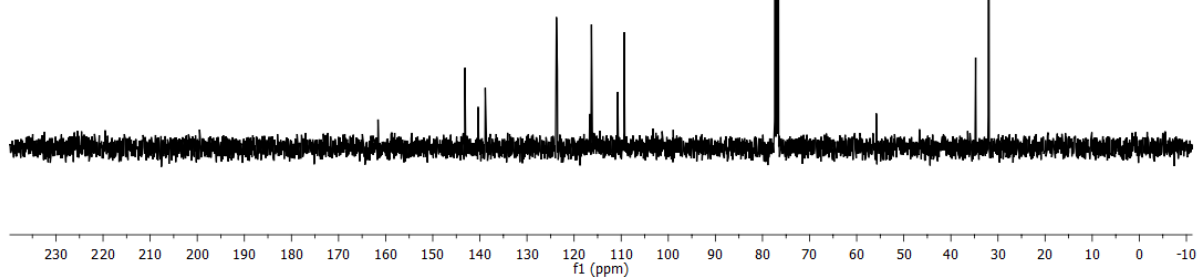
Elemental Analysis: C, 85.15; H, 8.21; N, 4.23; O, 2.41



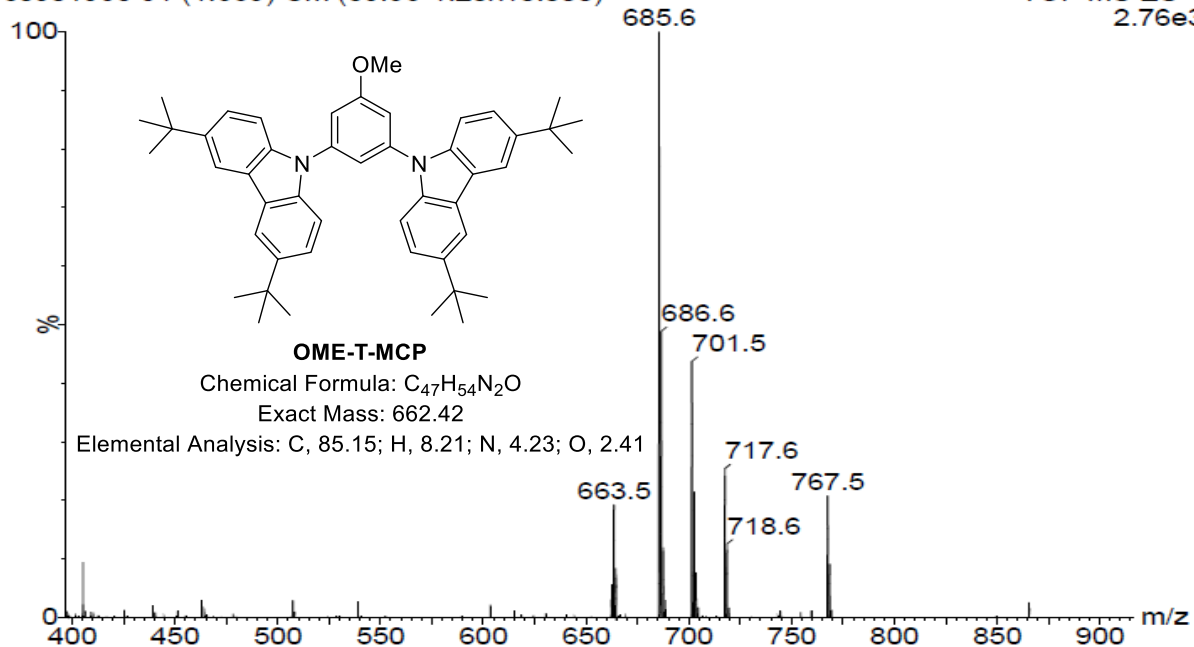
**OME-T-MCP**Chemical Formula: $C_{47}H_{54}N_2O$

Exact Mass: 662.42

Elemental Analysis: C, 85.15; H, 8.21; N, 4.23; O, 2.41

**Nikhil Sahotra NXS-78**

es301958 91 (1.669) Cm (89:96-1:20x10.000)

TOF MS ES+
2.76e3

Elemental Composition Report **Nikhil Sahotra OME-T-MCP**

Single Mass Analysis

Tolerance = 5.0 PPM / DBE: min = -1.5, max = 50.0

Element prediction: Off

Monoisotopic Mass, Even Electron Ions

297 formula(e) evaluated with 1 results within limits (up to 50 best isotopic matches for each mass)

Elements Used:

C: 0-200 H: 0-200 N: 0-5 O: 0-5

Minimum:				-1.5	
Maximum:	5.0	5.0	50.0		
Mass	Calc. Mass	mDa	PPM	DBE	Formula
663.4315	663.4314	0.1	0.2	21.5	C47 H55 N2 O

Eager Xperience Summarize Results

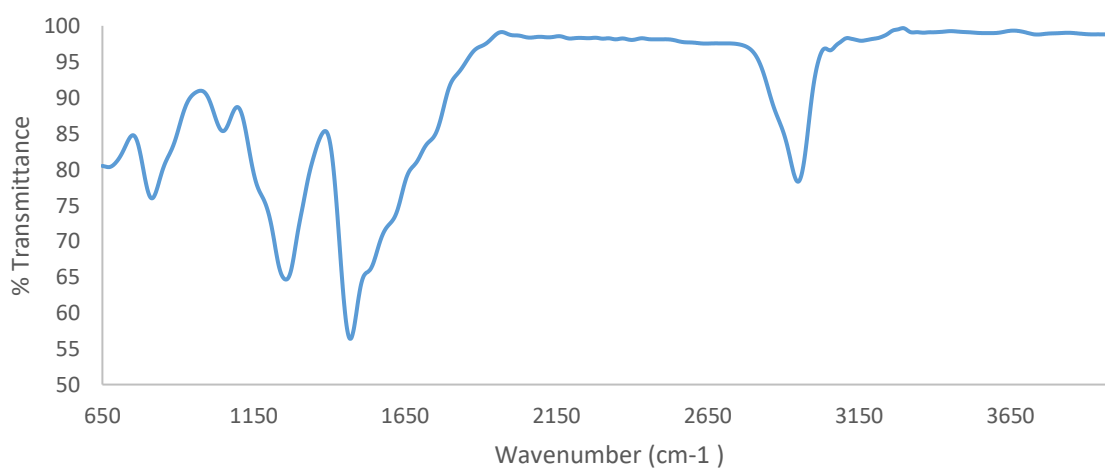
Date: 14/09/2017 @ 14:40:30

Method name: Nitrogen/Carbon/Hydrogen

Method Filename: 13September2017 retest 2.mth

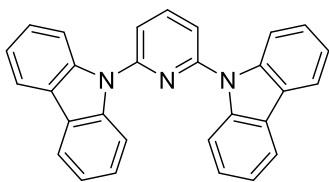
Sample Name	Elemental %		
	Nitrogen	Carbon	Hydrogen
OME-T-MCP	4.33	84.83	8.11
OME-T-MCP	4.22	85.01	8.29
Average			
	4.27	84.92	8.20

IR Spectrum of **OME-T-MCP**



6.3 Analytical data of MCP Derivatives Synthesised via Method 3

12-01-Baranoff-2

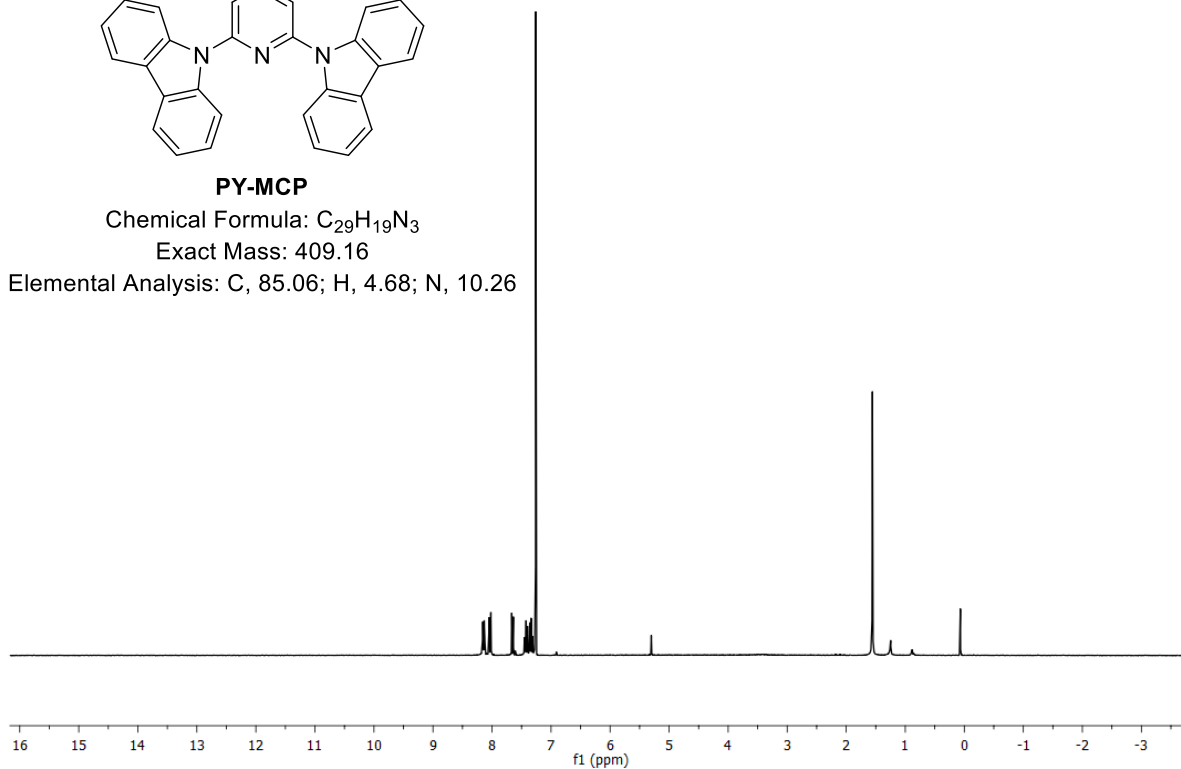


PY-MCP

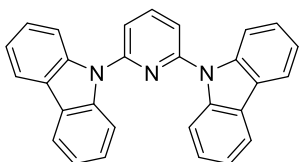
Chemical Formula: $C_{29}H_{19}N_3$

Exact Mass: 409.16

Elemental Analysis: C, 85.06; H, 4.68; N, 10.26



12-03-Baranoff-7

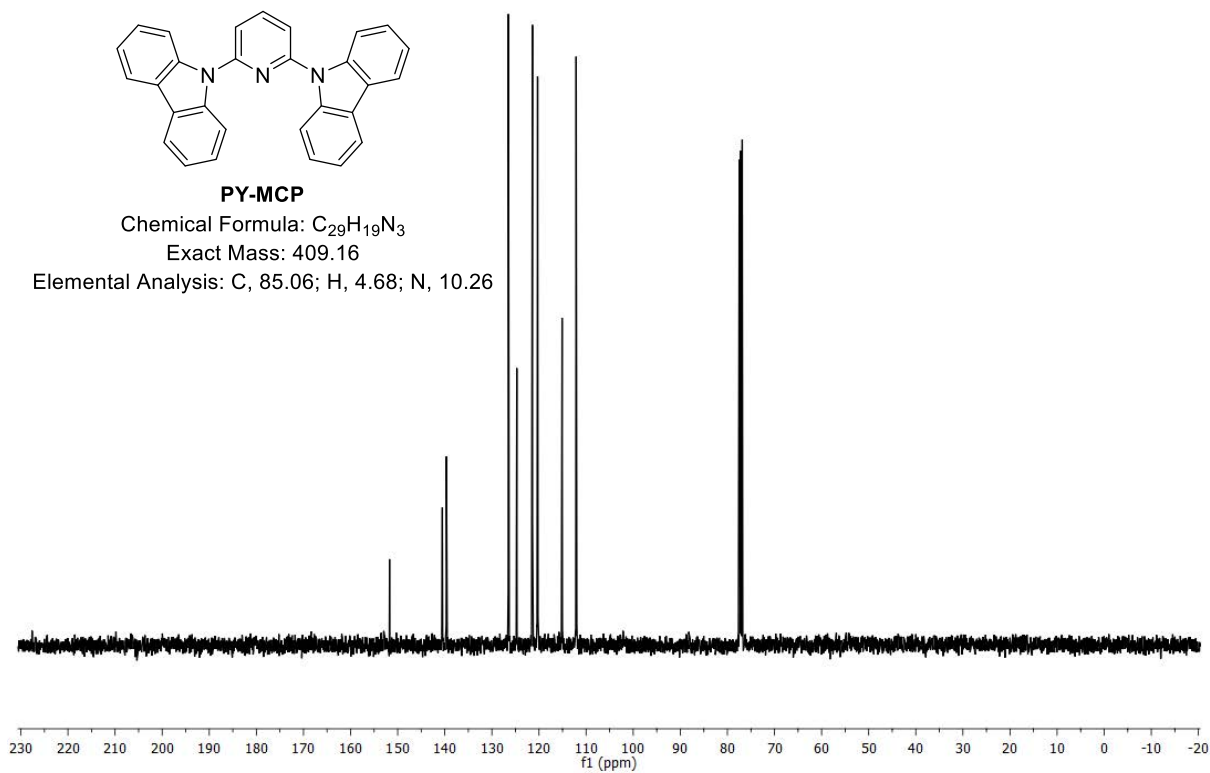


PY-MCP

Chemical Formula: $C_{29}H_{19}N_3$

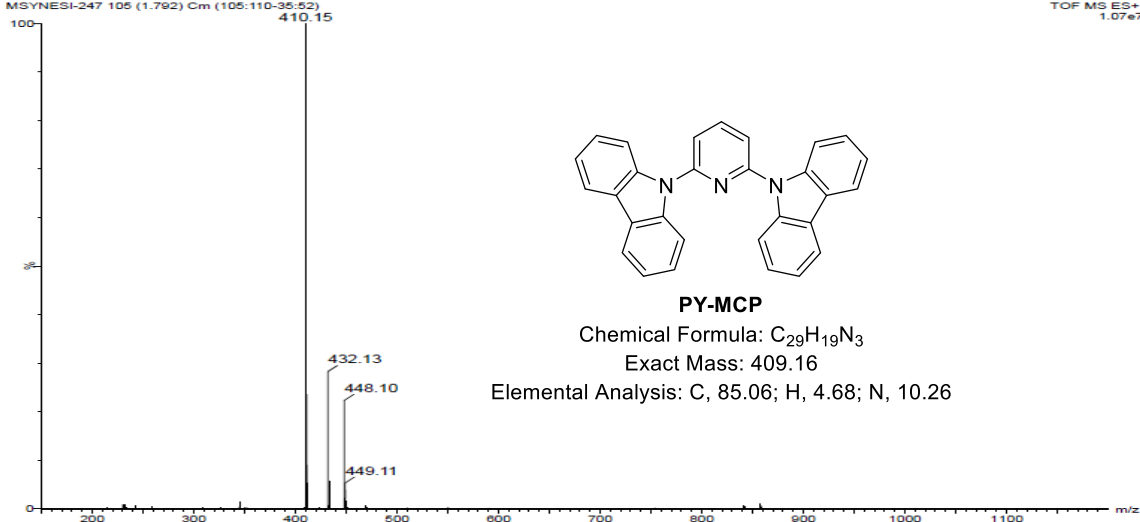
Exact Mass: 409.16

Elemental Analysis: C, 85.06; H, 4.68; N, 10.26



N. Sahotra NxS-19
MSYNESI-247 105 (1.792) Cm (105:110-35:52)

TOF MS ES+
1.07e7



Elemental Composition Report N. Sahotra NxS-19

Single Mass Analysis

Tolerance = 5.0 PPM / DBE: min = -1.5, max = 1000.0

Element prediction: Off

Monoisotopic Mass, Even Electron Ions

53 formula(e) evaluated with 1 results within limits (all results (up to 1000) for each mass)

Elements Used:

C: 0-100 H: 0-100 N: 1-10

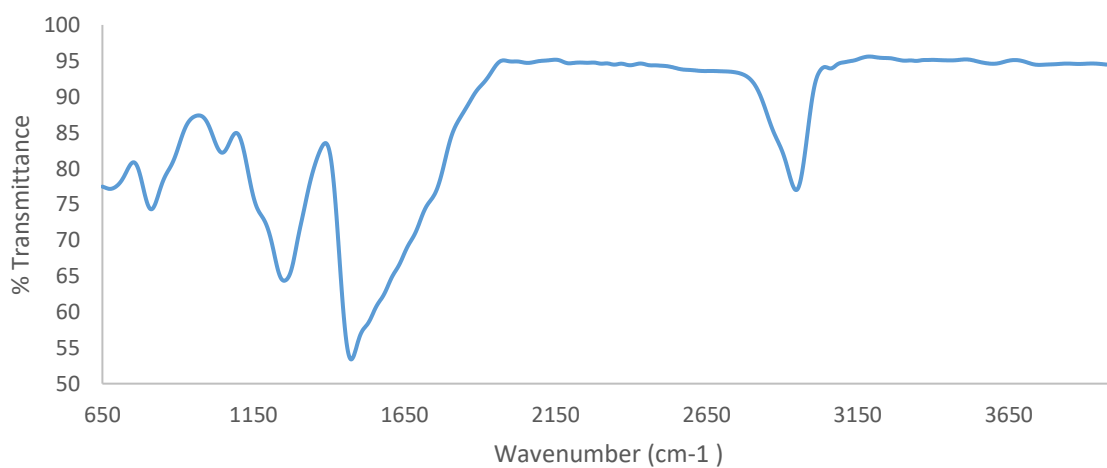
Minimum:				-1.5	
Maximum:	5.0	5.0	1000.0		
Mass	Calc. Mass	mDa	PPM	DBE	Formula
410.1655	410.1657	-0.2	-0.5	21.5	C ₂₉ H ₂₀ N ₃

Eager Xperience Summarize Results

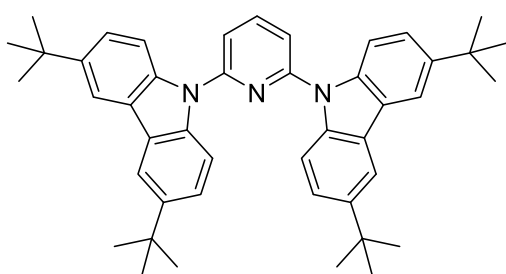
Date: 29/07/2015 @ 11:36:34
Method name: Nitrogen/Carbon/Hydrogen
Method Filename: 16JULY2015.mth

Sample Name	Elemental %		
	Nitrogen	Carbon	Hydrogen
PY-MCP	10.38	84.85	4.77
PY-MCP	10.40	84.9	4.76
Average			
	10.39	84.88	4.77

IR Spectrum of PY-MCP



2017-Sep-13-Baranoff-5

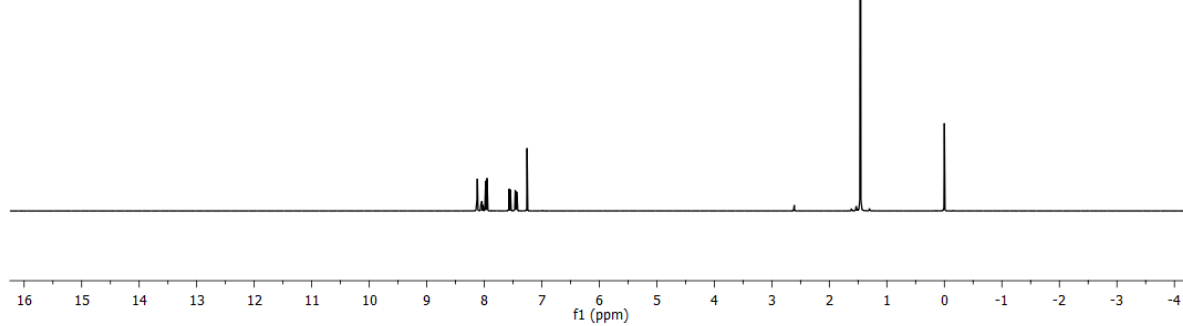


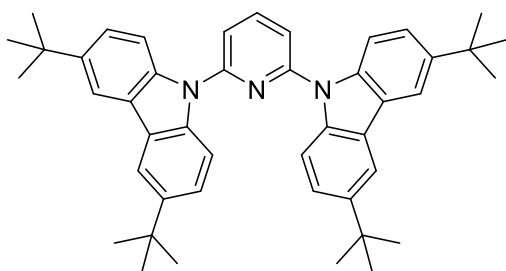
PY-T-MCP

Chemical Formula: $C_{45}H_{51}N_3$

Exact Mass: 633.41

Elemental Analysis: C, 85.26; H, 8.11; N, 6.63



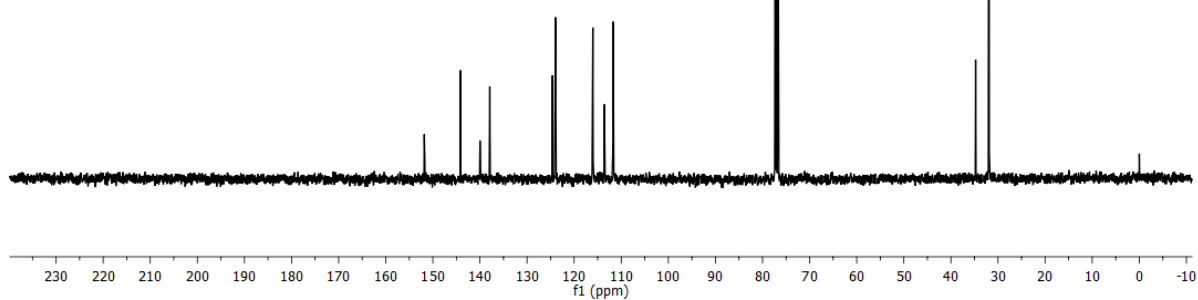


PY-T-MCP

Chemical Formula: $C_{45}H_{51}N_3$

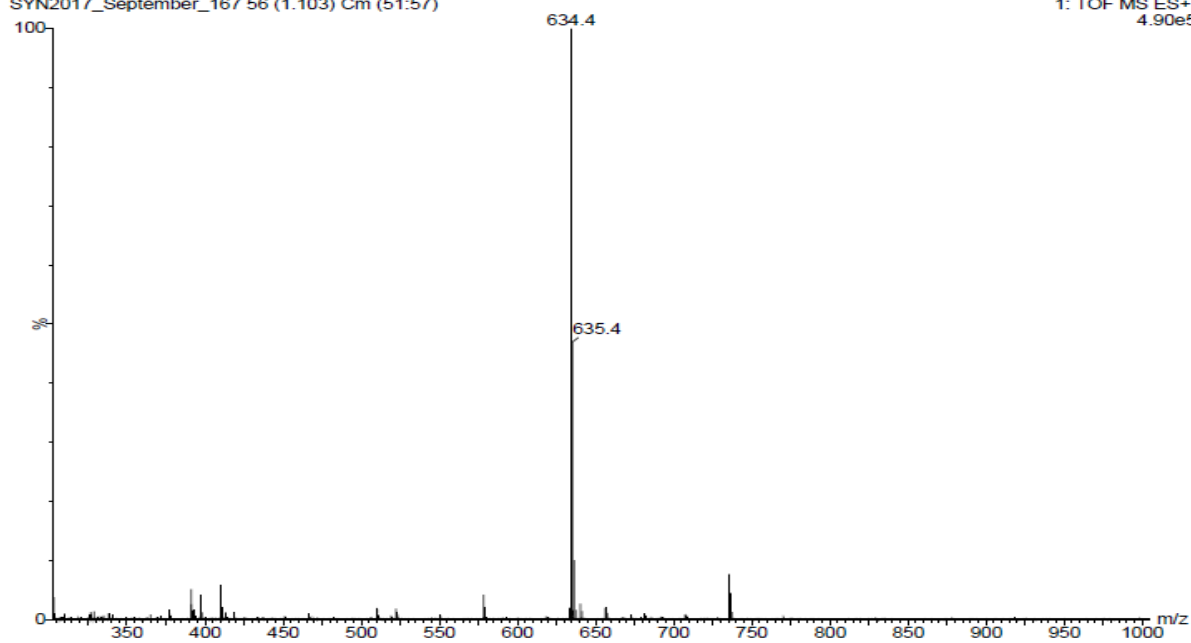
Exact Mass: 633.41

Elemental Analysis: C, 85.26; H, 8.11; N, 6.63



Nikhil Sahotra PY-T-MCP
SYN2017_September_167 56 (1.103) Cm (51:57)

1: TOF MS ES+
4.90e5



Elemental Composition Report **Nikhil Sahotra PY-T-MCP**

Single Mass Analysis

Tolerance = 5.0 PPM / DBE: min = -1.5, max = 1000.0

Element prediction: Off

Monoisotopic Mass, Even Electron Ions

48 formula(e) evaluated with 1 results within limits (all results (up to 1000) for each mass)

Elements Used:

C: 0-100 H: 0-100 N: 0-5

Minimum:				-1.5	
Maximum:	5.0	5.0	1000.0		
Mass	Calc. Mass	mDa	PPM	DBE	Formula
634.4160	634.4161	-0.1	-0.2	21.5	C45 H52 N3

Eager Xperience Summarize Results

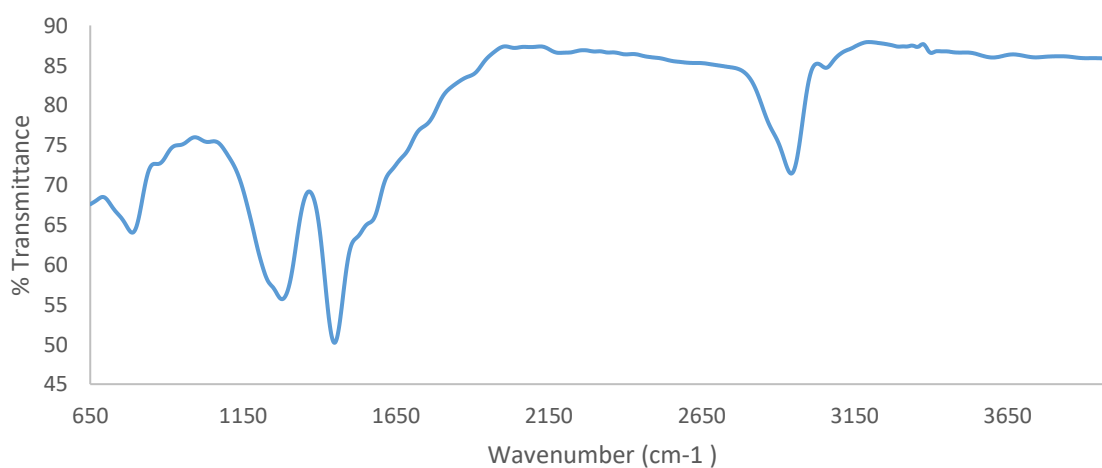
Date: 15/09/2017 @ 12:37:27

Method name: Nitrogen/Carbon/Hydrogen

Method Filename: 13September2017 retest 2.mth

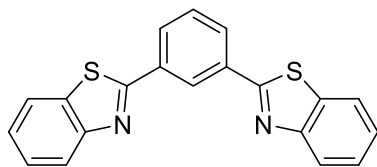
Sample Name	Elemental %		
	Nitrogen	Carbon	Hydrogen
PY-T-MCP	6.50	85.47	8.09
PY-T-MCP	6.43	85.22	8.08
Average			
	6.46	85.35	8.09

IR spectrum of **PY-T-MCP**



6.4 Analytical Data of First Generation TPBI Derivatives

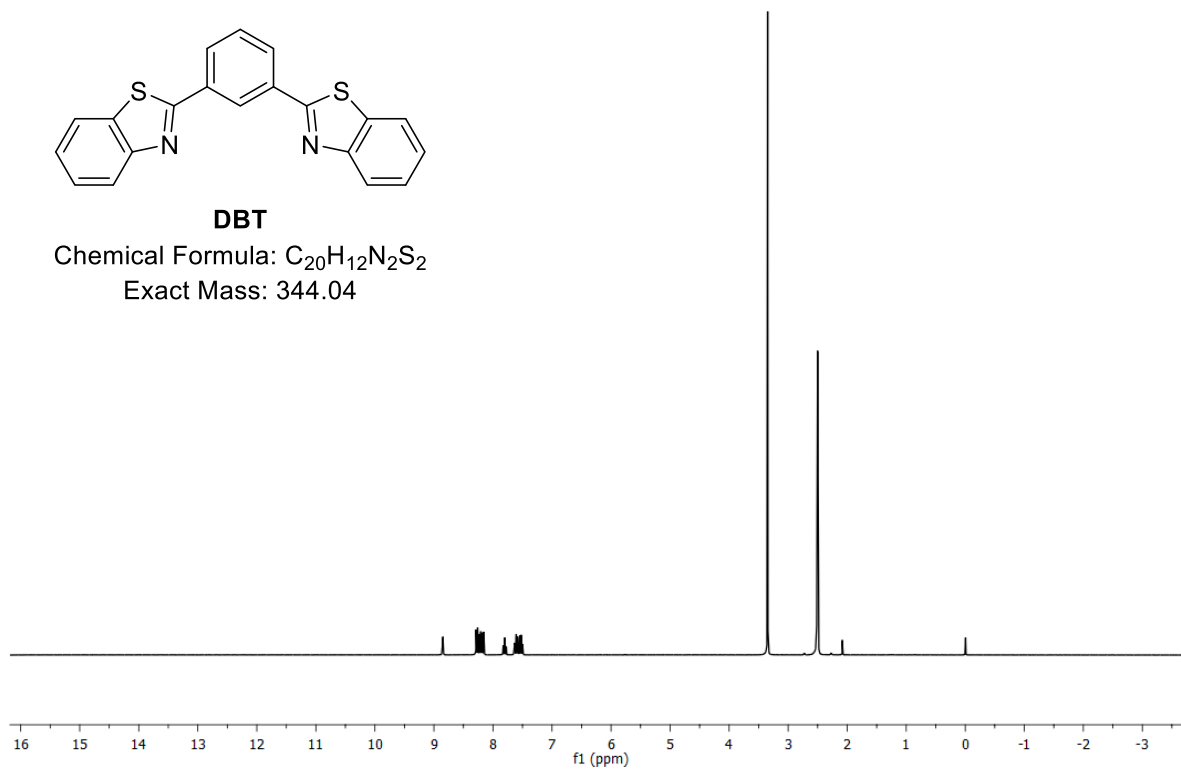
02-20-Baranoff-53



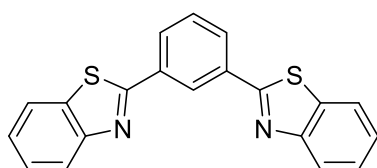
DBT

Chemical Formula: $C_{20}H_{12}N_2S_2$

Exact Mass: 344.04



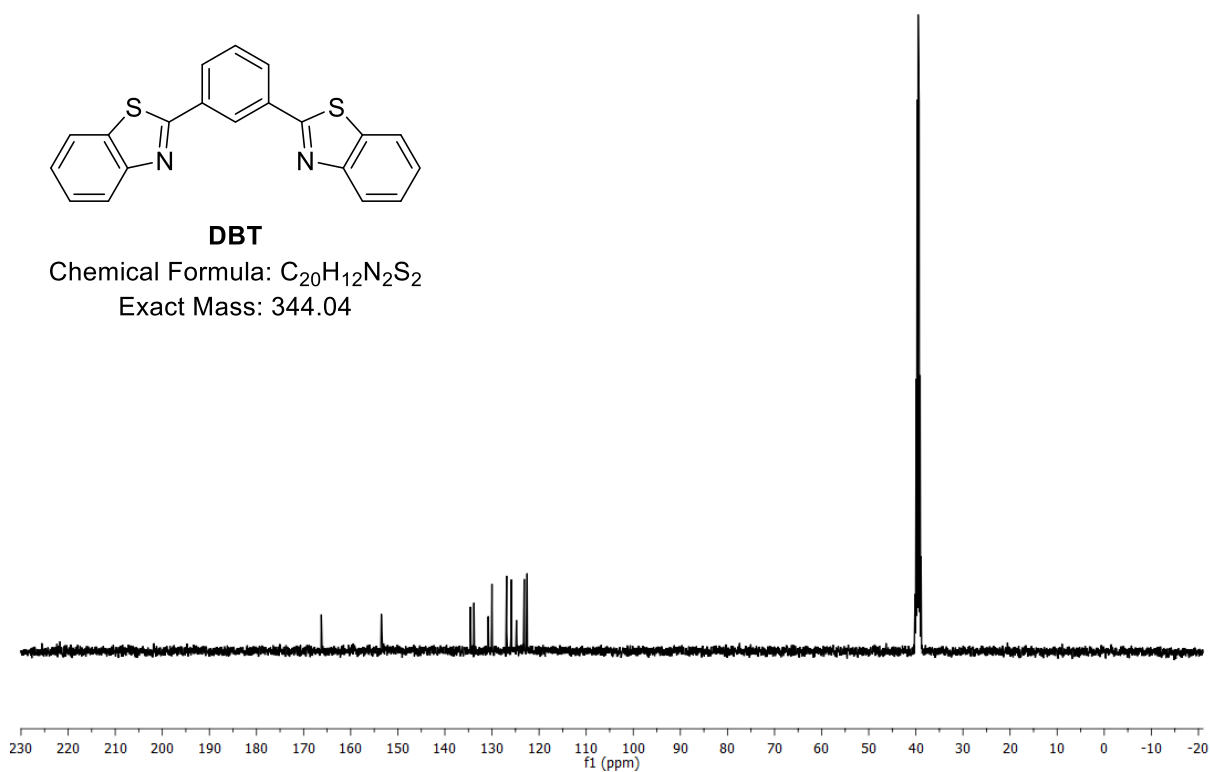
02-20-Baranoff-1



DBT

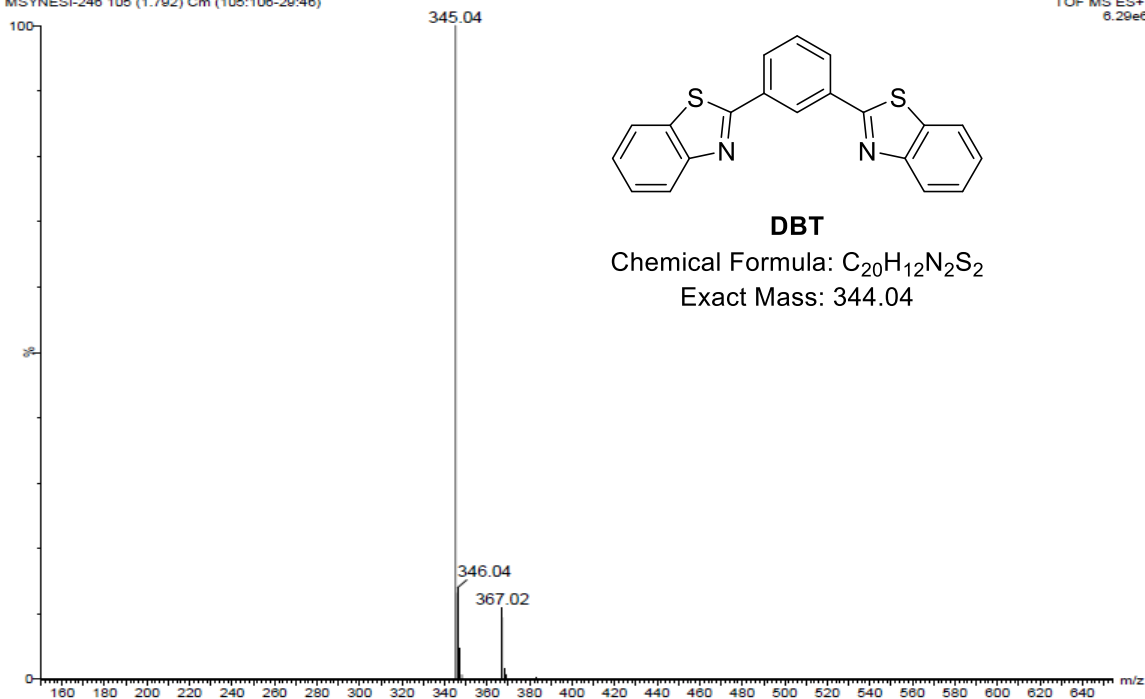
Chemical Formula: $C_{20}H_{12}N_2S_2$

Exact Mass: 344.04



N. Sahotra NxS-25
MSYNESI-246 105 (1.792) Cm (105:106-29:46)

TOF MS ES+
6.29e6



Elemental Composition Report N. Sahotra NxS-25

Single Mass Analysis

Tolerance = 5.0 PPM / DBE: min = -1.5, max = 1000.0

Element prediction: Off

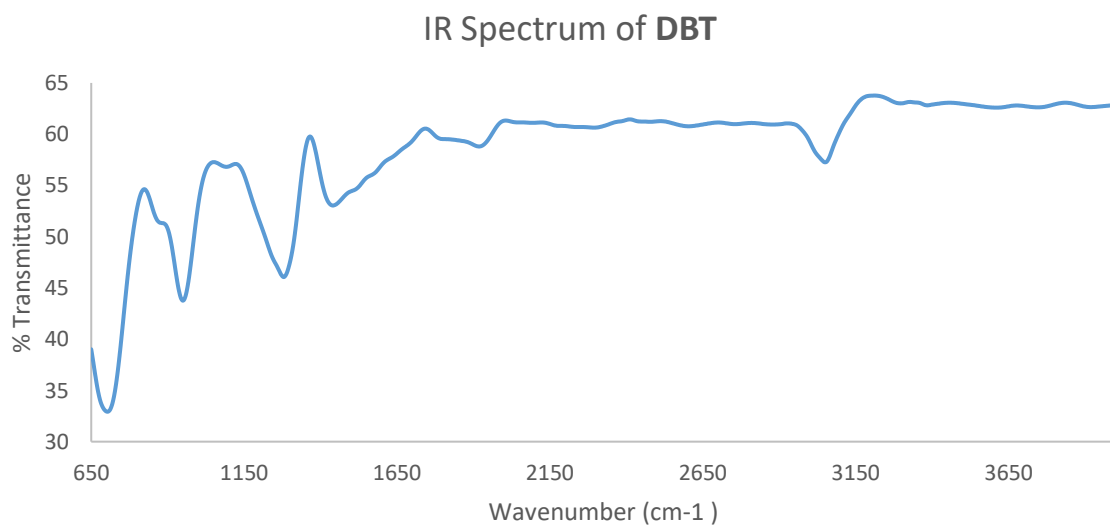
Monoisotopic Mass, Even Electron Ions

82 formula(e) evaluated with 1 results within limits (all results (up to 1000) for each mass)

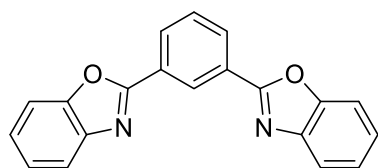
Elements Used:

C: 0-100 H: 0-100 N: 1-10 S: 1-2

Minimum:			-1.5		
Maximum:	5.0	5.0	1000.0		
Mass	Calc. Mass	mDa	PPM	DBE	Formula
345.0526	345.0520	0.6	1.7	15.5	C20 H13 N2 S2



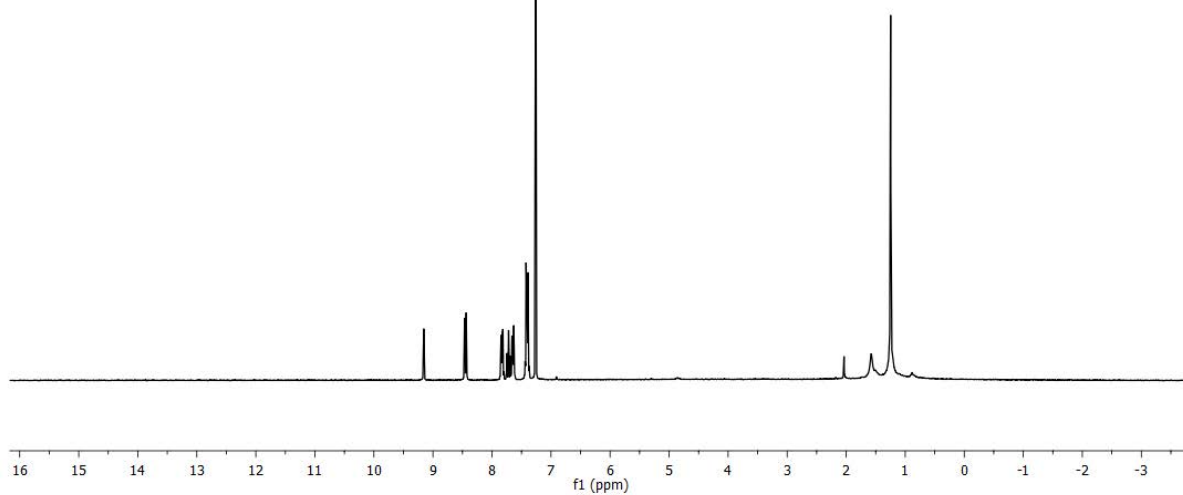
02-26-Baranoff-22

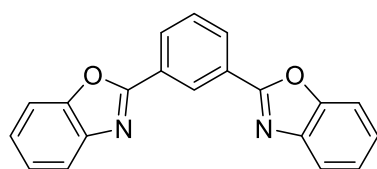


DBO

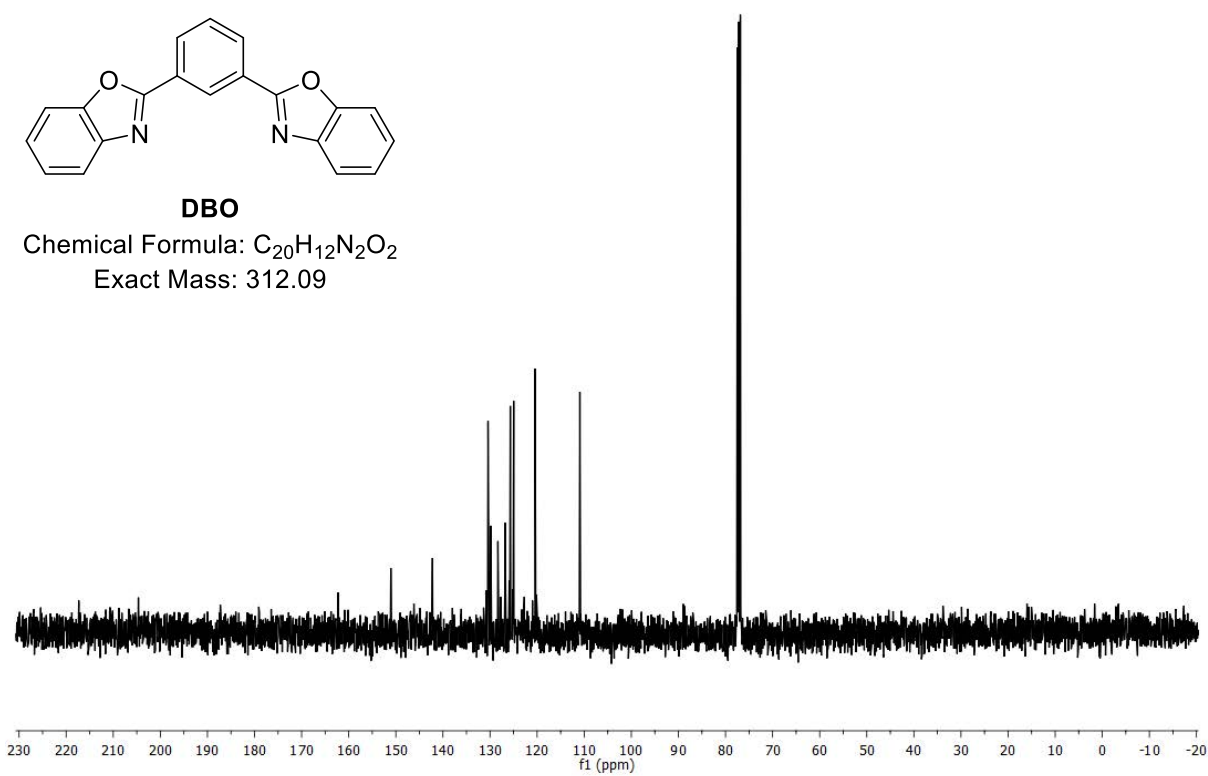
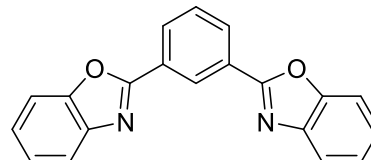
Chemical Formula: $C_{20}H_{12}N_2O_2$

Exact Mass: 312.09

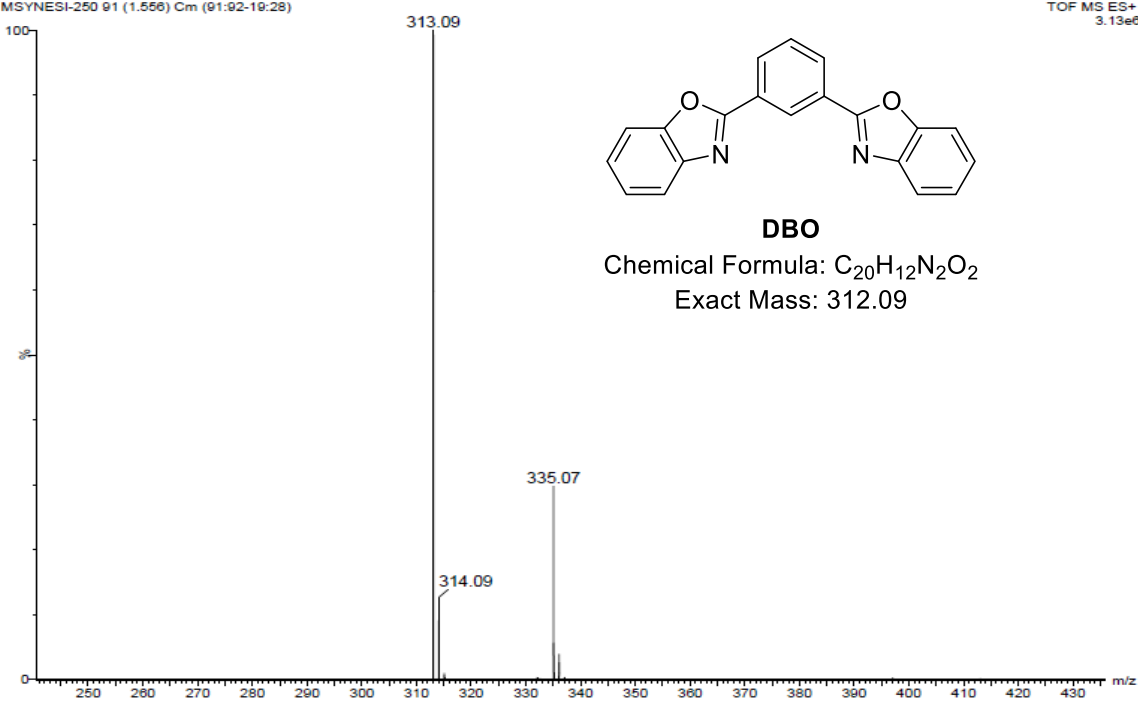


**DBO**Chemical Formula: $C_{20}H_{12}N_2O_2$

Exact Mass: 312.09

N. Sahotra NxS-26
MSYNESI-250 91 (1.556) Cm (91:92-19:28)TOF MS ES+
3.13e6**DBO**Chemical Formula: $C_{20}H_{12}N_2O_2$

Exact Mass: 312.09



Elemental Composition Report **N. Sahotra NxS-26**

Single Mass Analysis

Tolerance = 5.0 PPM / DBE: min = -1.5, max = 1000.0

Element prediction: Off

Monoisotopic Mass, Even Electron Ions

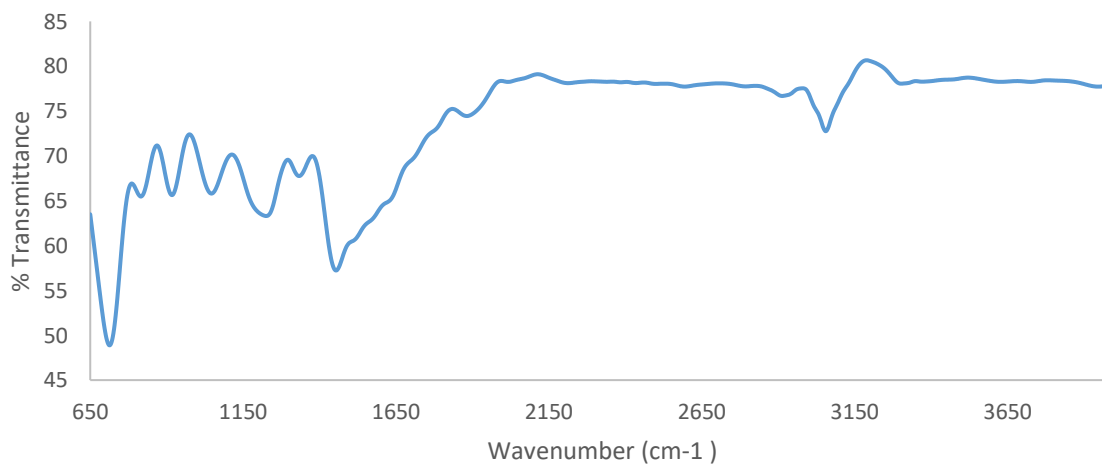
186 formula(e) evaluated with 1 results within limits (all results (up to 1000) for each mass)

Elements Used:

C: 0-100 H: 0-100 N: 1-10 O: 1-5

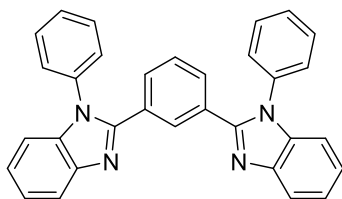
Minimum:			-1.5		
Maximum:	5.0	5.0	1000.0		
Mass	Calc. Mass	mDa	PPM	DBE	Formula
313.0981	313.0977	0.4	1.3	15.5	C20 H13 N2 O2

IR Spectrum of **DBO**



6.5 Analytical data of Second Generation TPBI Derivatives

02-20-Baranoff-52

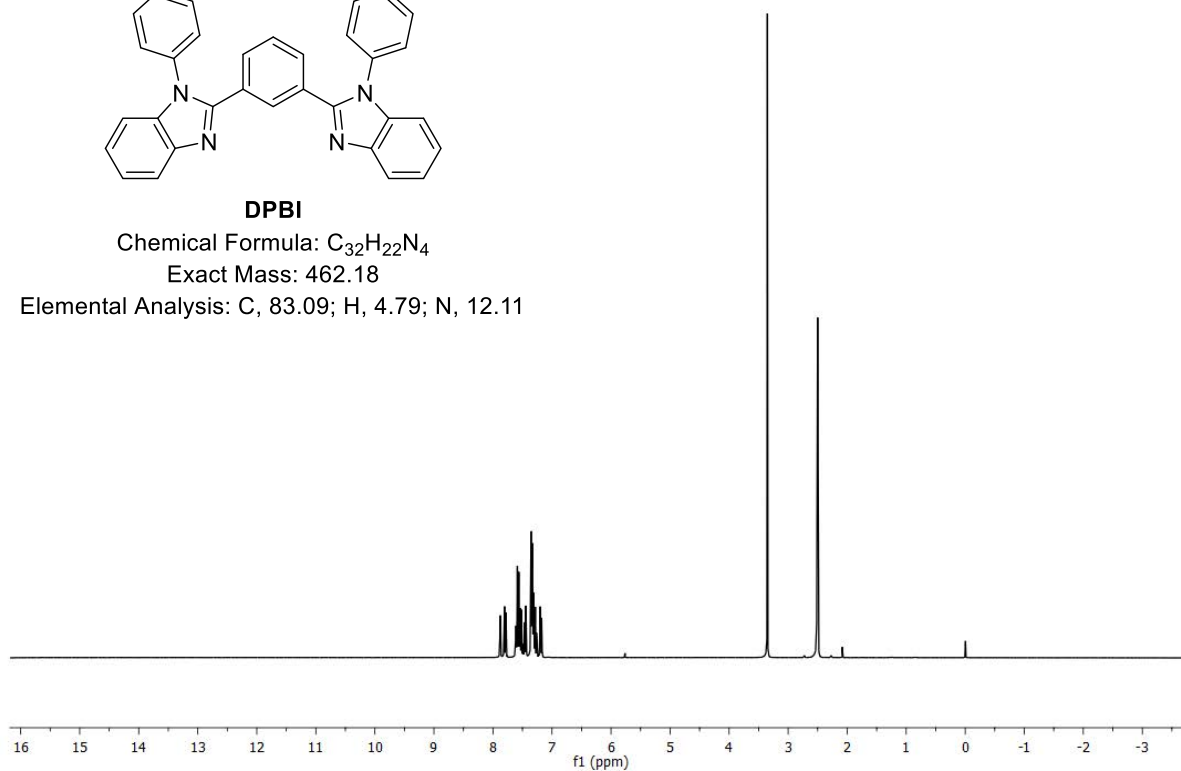


DPBI

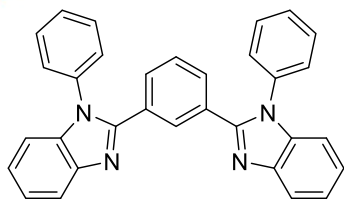
Chemical Formula: $C_{32}H_{22}N_4$

Exact Mass: 462.18

Elemental Analysis: C, 83.09; H, 4.79; N, 12.11



02-19-Baranoff-15

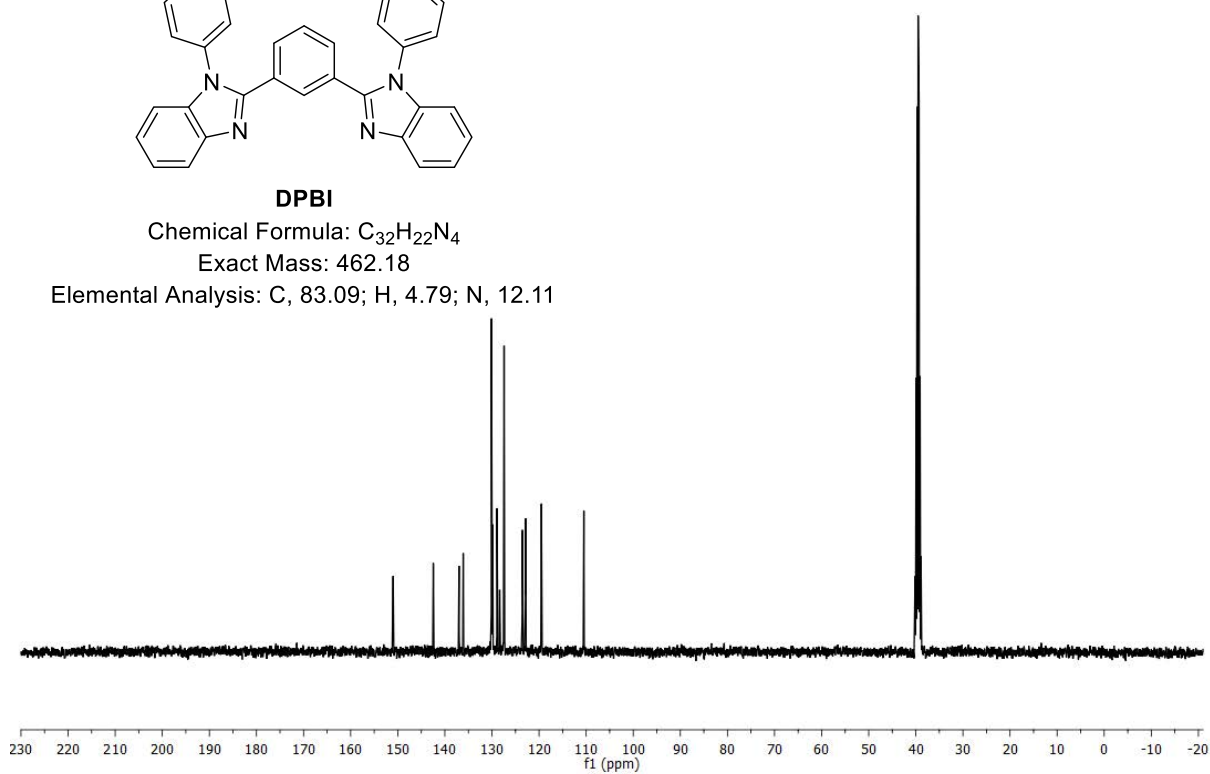


DPBI

Chemical Formula: $C_{32}H_{22}N_4$

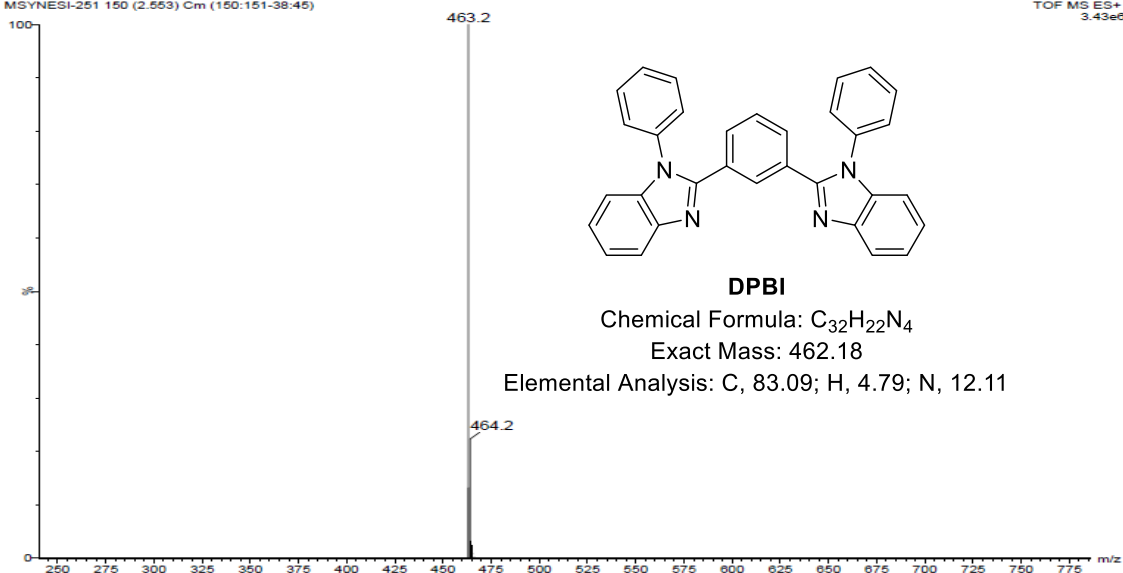
Exact Mass: 462.18

Elemental Analysis: C, 83.09; H, 4.79; N, 12.11



N. Sahotra NxS-23
MSYNESI-251 150 (2.553) Cm (150:151-38:45)

TOF MS ES+
3.43e6



Elemental Composition Report N. Sahotra NxS-23

Single Mass Analysis

Tolerance = 5.0 PPM / DBE: min = -1.5, max = 1000.0

Element prediction: Off

Monoisotopic Mass, Even Electron Ions

62 formula(e) evaluated with 1 results within limits (all results (up to 1000) for each mass)

Elements Used:

C: 0-100 H: 0-100 N: 1-10

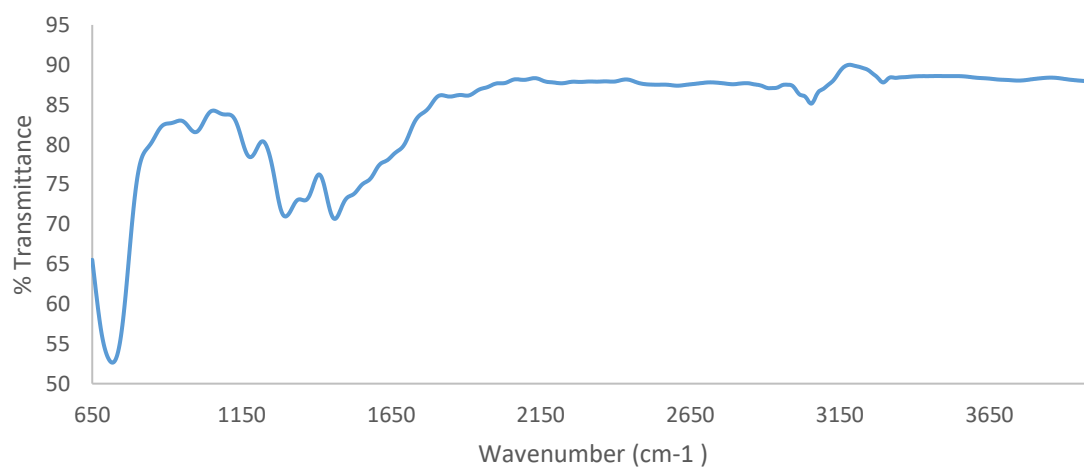
Minimum:				-1.5	
Maximum:	5.0	5.0	1000.0		
Mass	Calc. Mass	mDa	PPM	DBE	Formula
463.1917	463.1923	-0.6	-1.3	23.5	C32 H23 N4

Eager Xperience Summarize Results

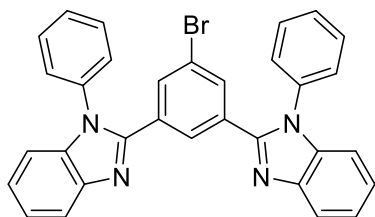
Date: 15/09/2017 @ 12:37:27
Method name: Nitrogen/Carbon/Hydrogen
Method Filename: 13September2017 retest 2.mth

Sample Name	Elemental %		
	Nitrogen	Carbon	Hydrogen
DPBI	12.00	83.72	4.75
DPBI	11.83	82.93	4.73
Average			
	11.92	83.32	4.74

IR Spectrum of DPBI



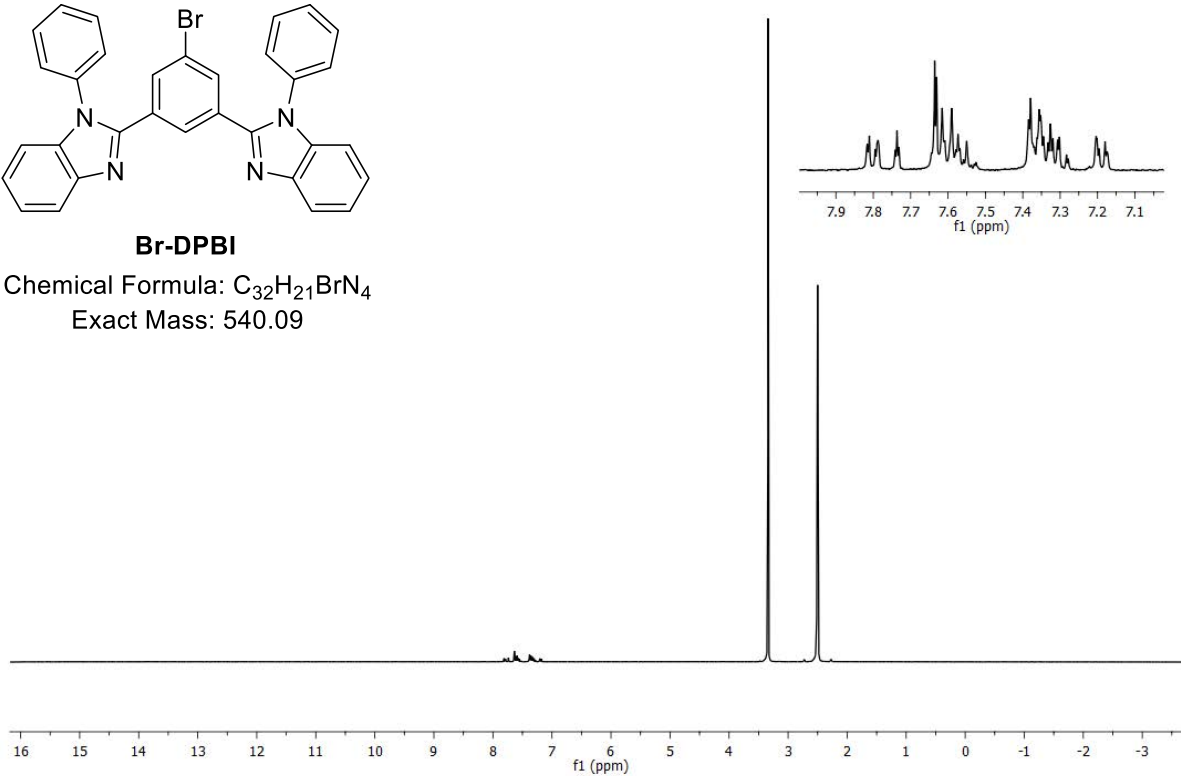
06-18-Baranoff-55

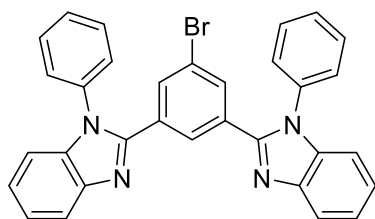


Br-DPBI

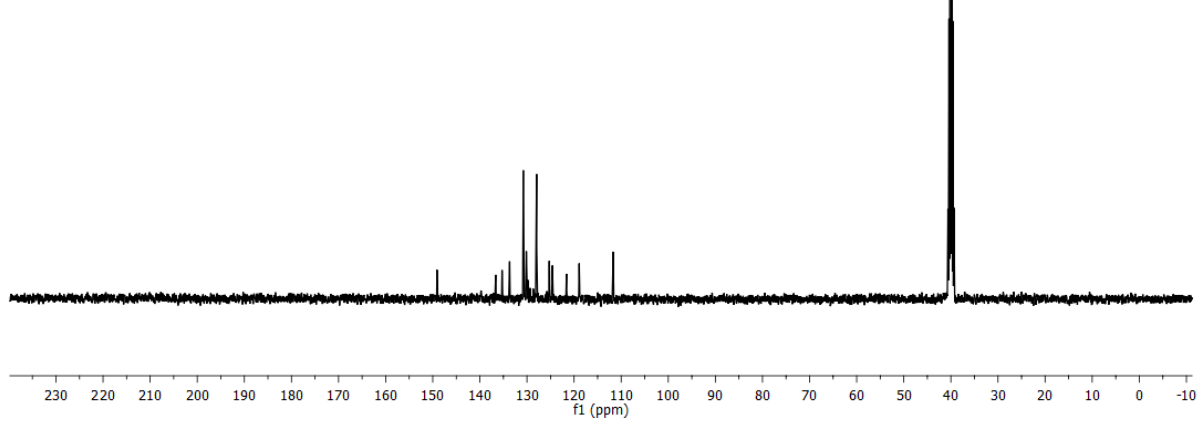
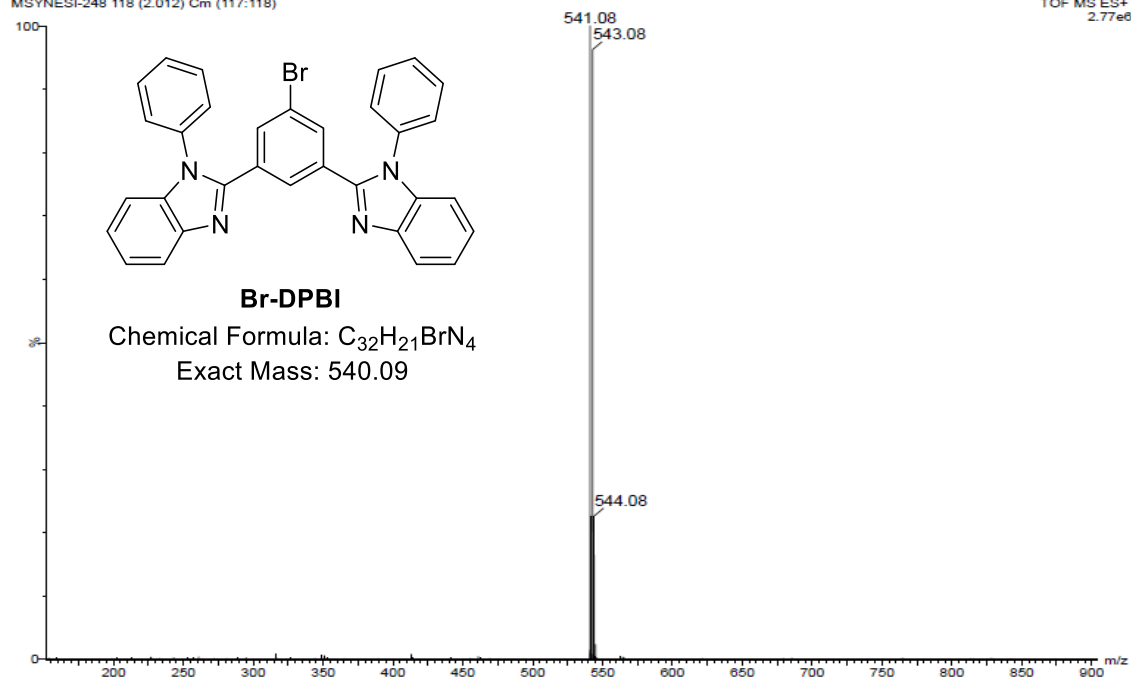
Chemical Formula: $C_{32}H_{21}BrN_4$

Exact Mass: 540.09



**Br-DPBI**Chemical Formula: $C_{32}H_{21}BrN_4$

Exact Mass: 540.09

N. Sahotra NxS-39
MSYNESI-248 118 (2.012) Cm (117:118)TOF MS ES+
2.77e6

Elemental Composition Report **N. Sahotra NxS-39**

Single Mass Analysis

Tolerance = 5.0 PPM / DBE: min = -1.5, max = 1000.0

Element prediction: Off

Monoisotopic Mass, Even Electron Ions

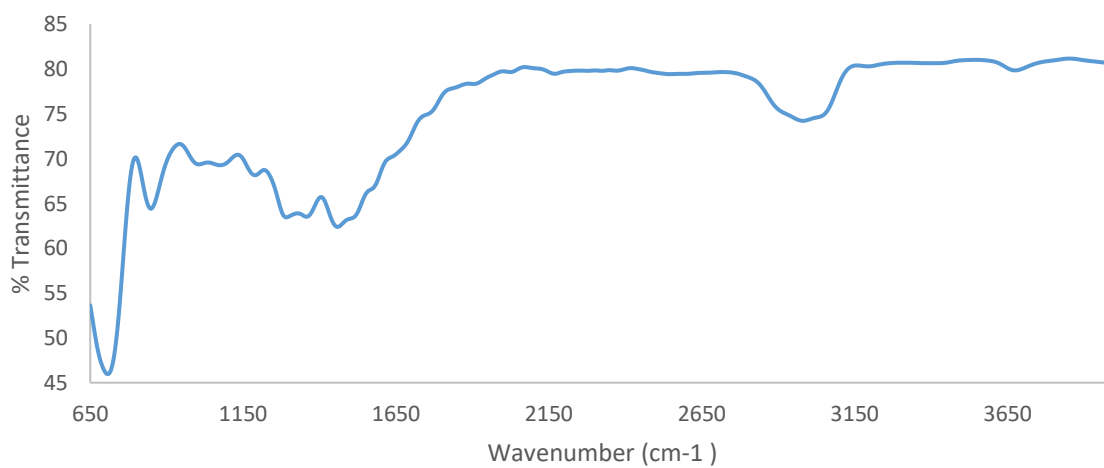
60 formula(e) evaluated with 1 results within limits (all results (up to 1000) for each mass)

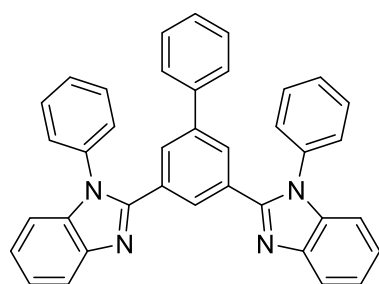
Elements Used:

C: 0-100 H: 0-100 N: 1-10 79Br: 1-1

Minimum:				-1.5	
Maximum:	5.0	5.0	1000.0		
Mass	Calc. Mass	mDa	PPM	DBE	Formula
541.1036	541.1028	0.8	1.5	23.5	C32 H22 N4 79Br

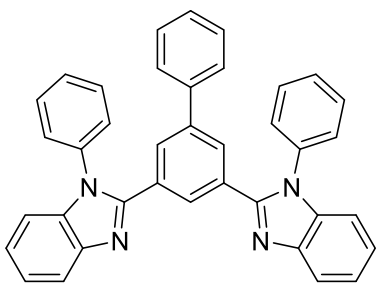
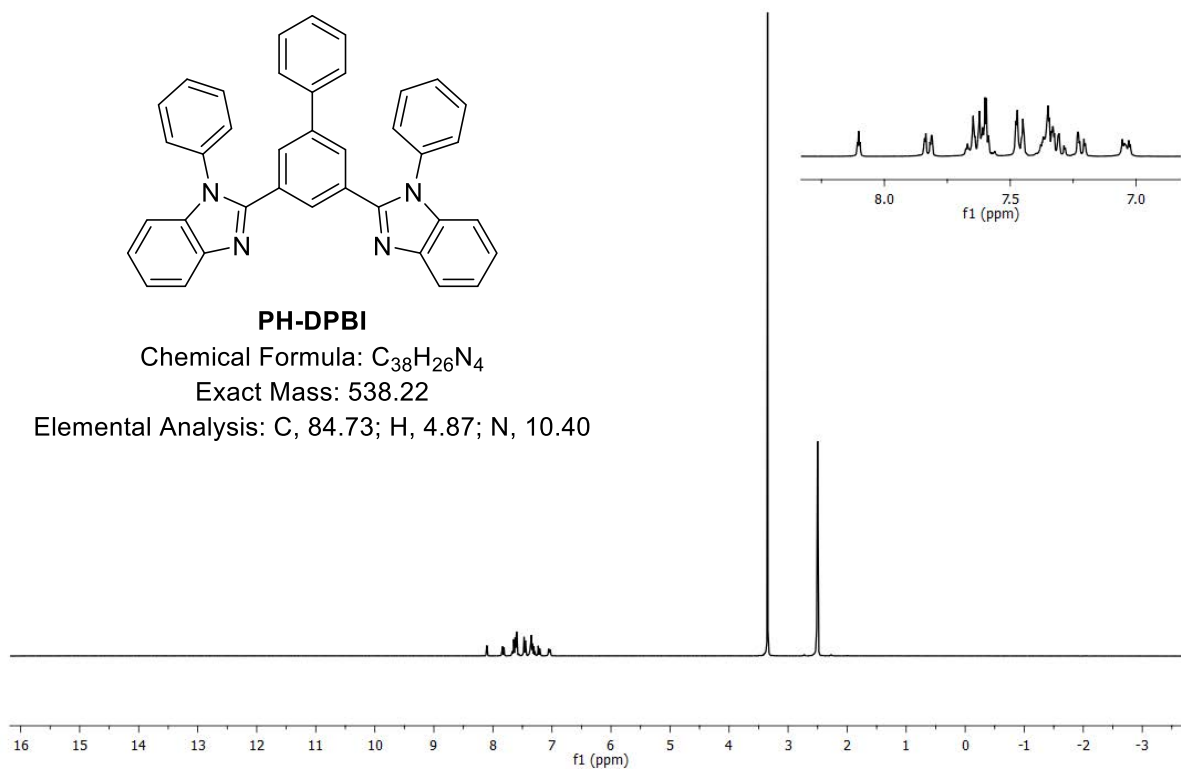
IR Spectrum of **Br-DPBI**



**PH-DPBI**Chemical Formula: $C_{38}H_{26}N_4$

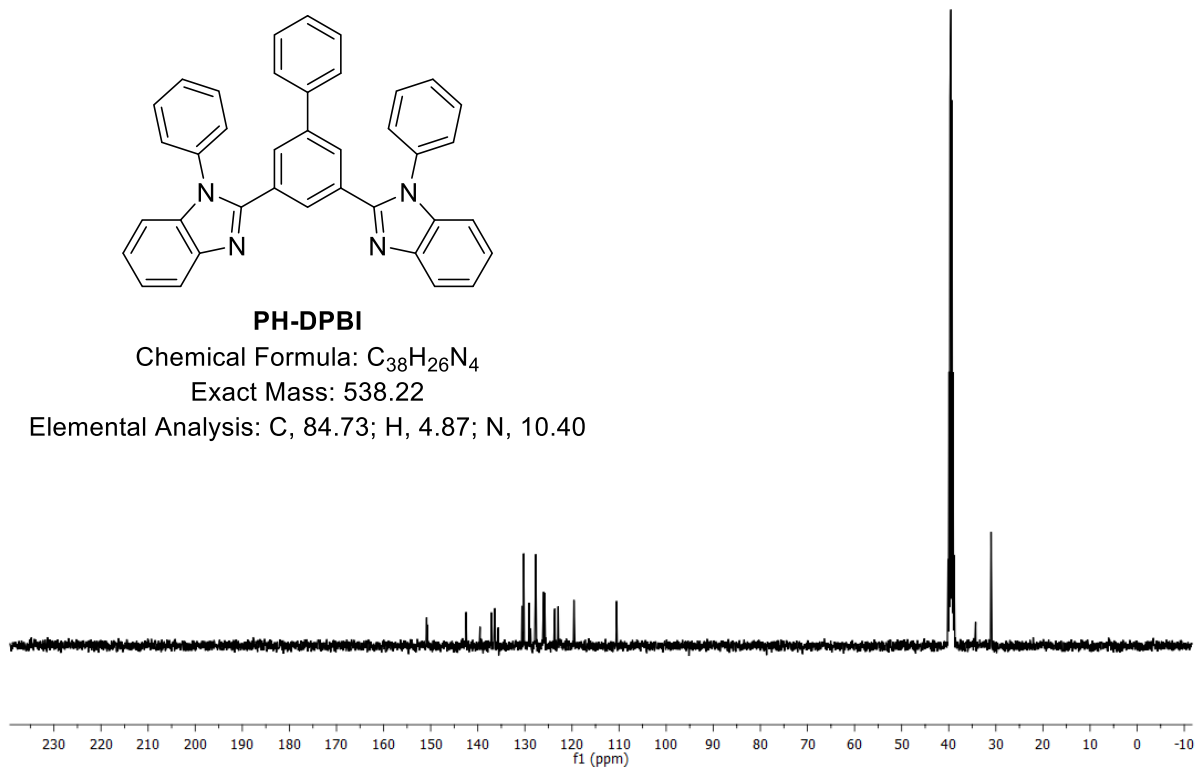
Exact Mass: 538.22

Elemental Analysis: C, 84.73; H, 4.87; N, 10.40

**PH-DPBI**Chemical Formula: $C_{38}H_{26}N_4$

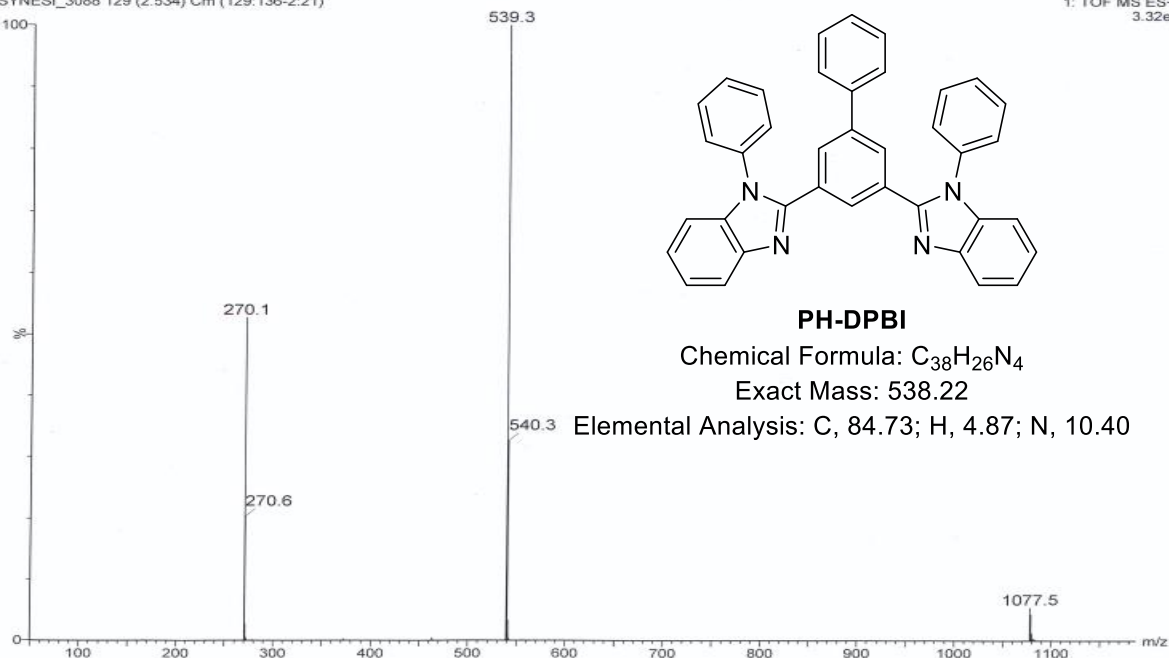
Exact Mass: 538.22

Elemental Analysis: C, 84.73; H, 4.87; N, 10.40



N. Sahotra NXS-40
SYNESI_3088 129 (2.534) Cm (129:136-2:21)

1: TOF MS ES+
3.32e7



Elemental Composition Report

Single Mass Analysis

Tolerance = 10.0 PPM / DBE: min = -1.5, max = 1000.0

Element prediction: Off

Number of isotope peaks used for I-FIT = 3

Monoisotopic Mass, Even Electron Ions

28 formula(e) evaluated with 1 results within limits (all results (up to 1000) for each mass)

Elements Used:

C: 0-100 H: 0-100 N: 4-4 79Br: 0-8

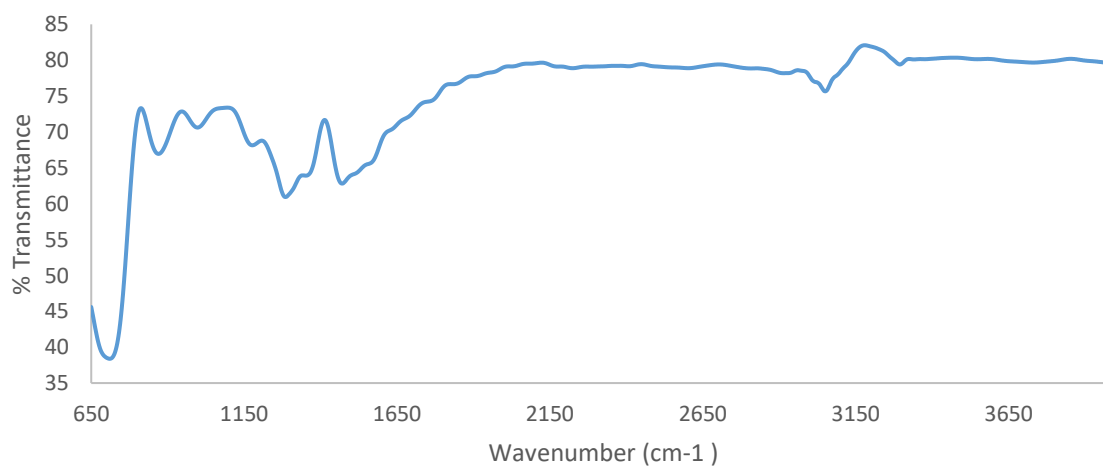
Minimum:			-1.5	
Maximum:	5.0	10.0	1000.0	
Mass	Calc. Mass	mDa	PPM	Formula
539.2236	539.2236	0.0	0.0	C38 H27 N4

Eager Xperience Summarize Results

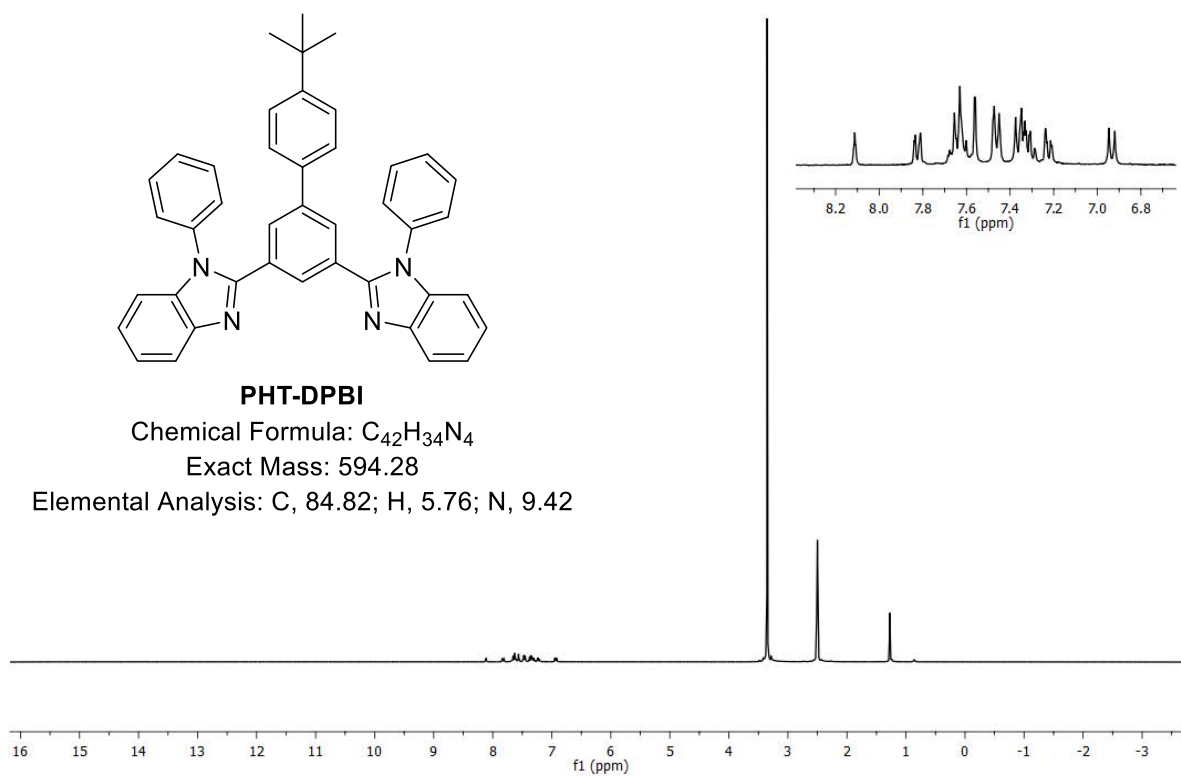
Date: 15/09/2017 @ 12:42:09
Method name: Nitrogen/Carbon/Hydrogen
Method Filename: 13September2017 retest 2.mth

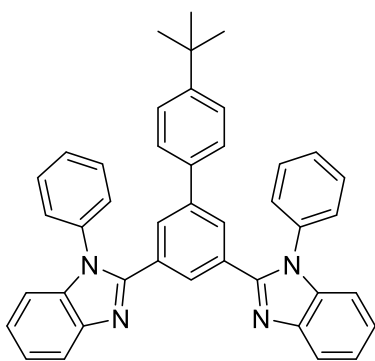
Sample Name	Elemental %		
	Nitrogen	Carbon	Hydrogen
PH-DPBI	10.12	84.54	4.74
PH-DPBI	10.32	84.60	4.75
Average			
	10.22	84.57	4.75

IR spectrum of **PH-DPBI**



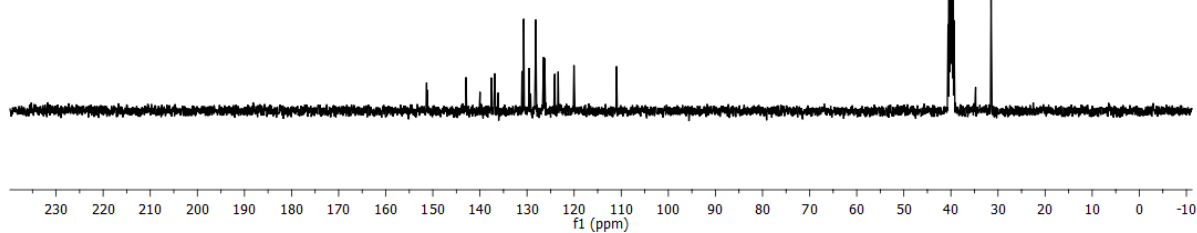
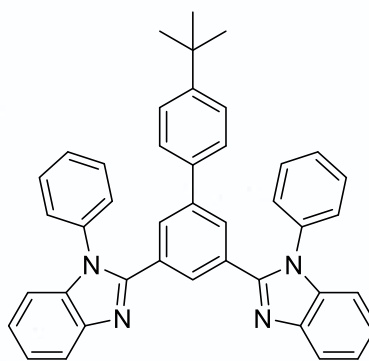
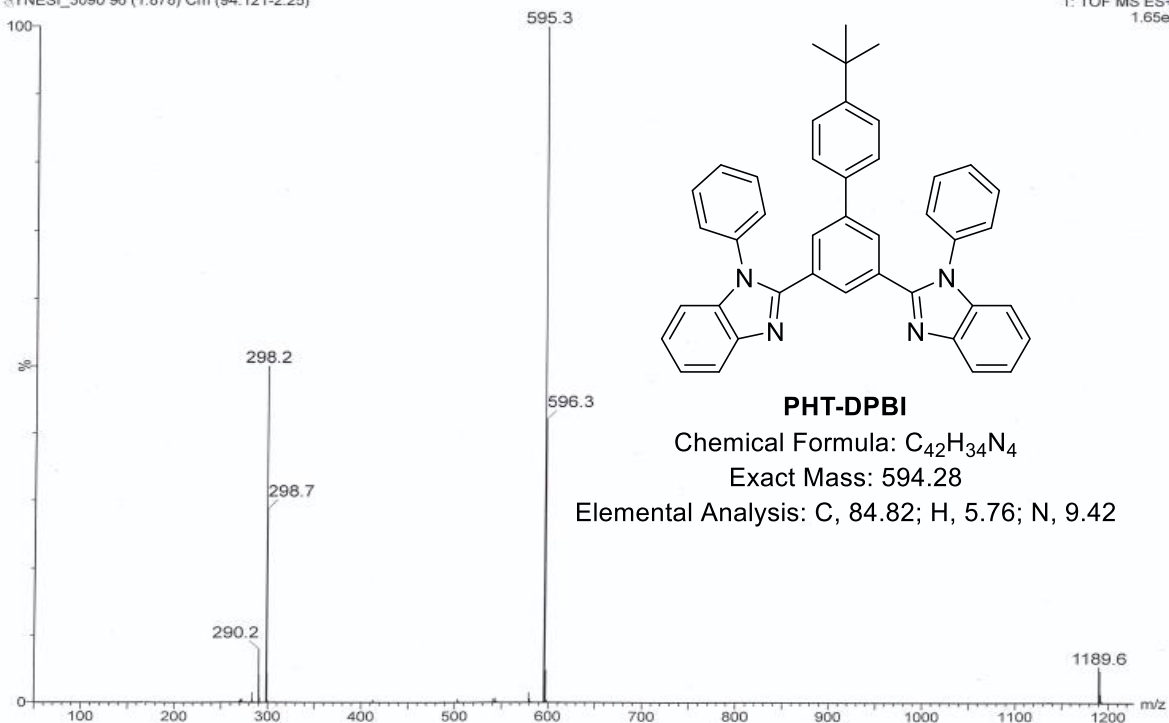
10-28-Baranoff-6



**PHT-DPBI**Chemical Formula: $C_{42}H_{34}N_4$

Exact Mass: 594.28

Elemental Analysis: C, 84.82; H, 5.76; N, 9.42

N.Sahotra NXS-42
SYNESI_3090 96 (1.878) Cm (94:121-2.25)1: TOF MS ES+
1.65e8**PHT-DPBI**Chemical Formula: $C_{42}H_{34}N_4$

Exact Mass: 594.28

Elemental Analysis: C, 84.82; H, 5.76; N, 9.42

Elemental Composition Report

Single Mass Analysis

Tolerance = 10.0 PPM / DBE: min = -1.5, max = 1000.0

Element prediction: Off

Number of isotope peaks used for I-FIT = 3

Monoisotopic Mass, Even Electron Ions

33 formula(e) evaluated with 1 results within limits (all results (up to 1000) for each mass)

Elements Used:

C: 0-100 H: 0-100 N: 4-4 79Br: 0-8

Minimum:				-1.5	
Maximum:	5.0	10.0	1000.0		
Mass	Calc. Mass	mDa	PPM	DBE	Formula
595.2869	595.2862	0.7	1.2	27.5	C42 H35 N4

Eager Xperience Summarize Results

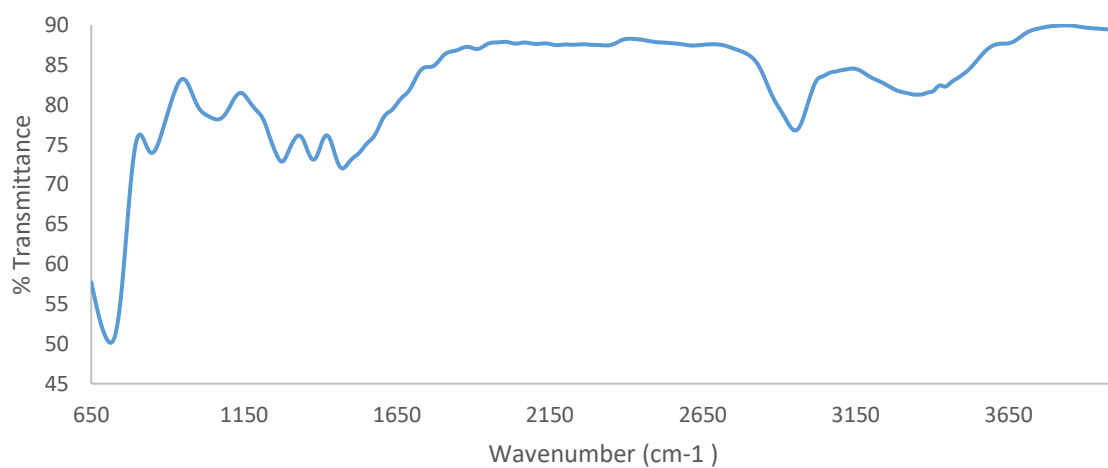
Date: 15/09/2017 @ 12:42:09

Method name: Nitrogen/Carbon/Hydrogen

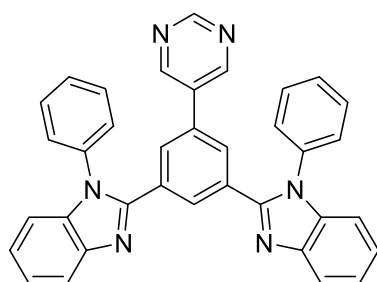
Method Filename: 13September2017 retest 2.mth

Sample Name	Elemental %		
	Nitrogen	Carbon	Hydrogen
PH-T-DPBI	9.24	84.70	5.56
PH-T-DPBI	9.36	84.65	5.62
Average			
	9.30	84.68	5.59

IR spectrum of PHT-DPBI



06-25-Baranoff-58



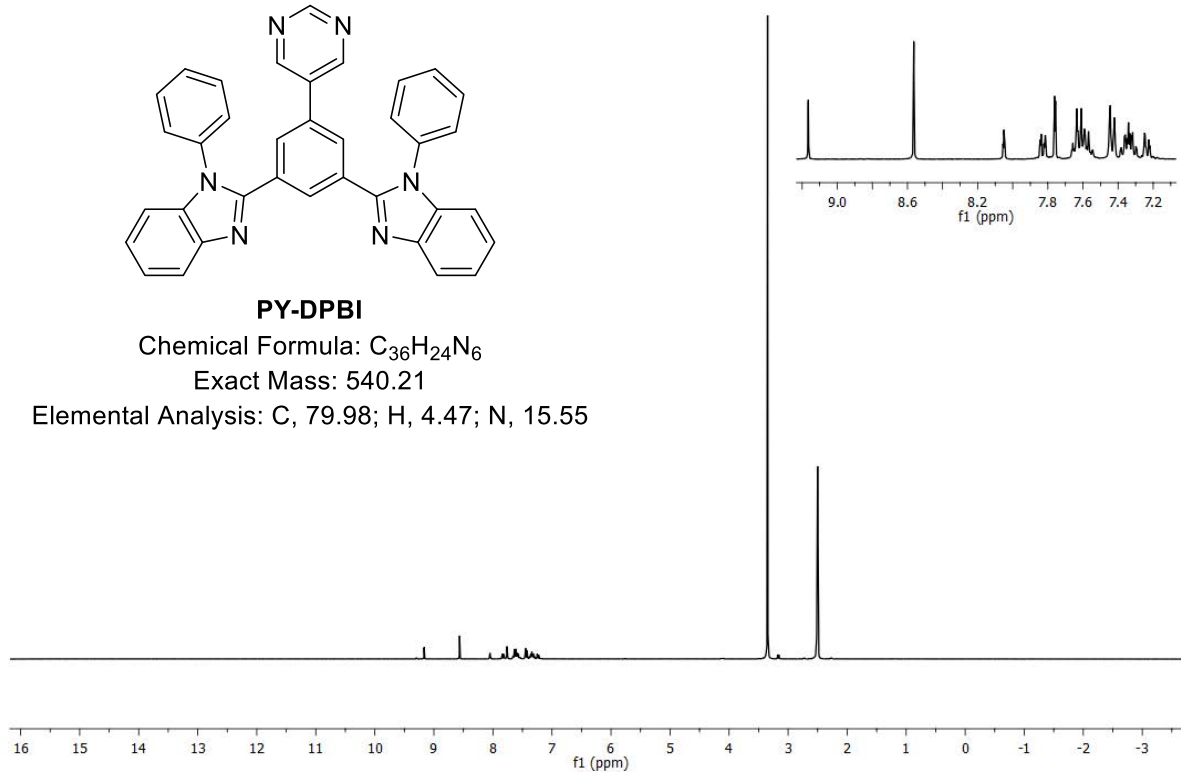
PY-DPBI

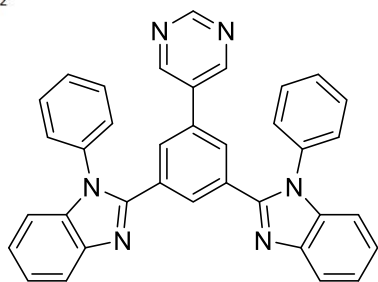
Chemical Formula: $C_{36}H_{24}N_6$

Exact Mass: 540.21

Elemental Analysis: C, 79.98; H, 4.47; N, 15.55

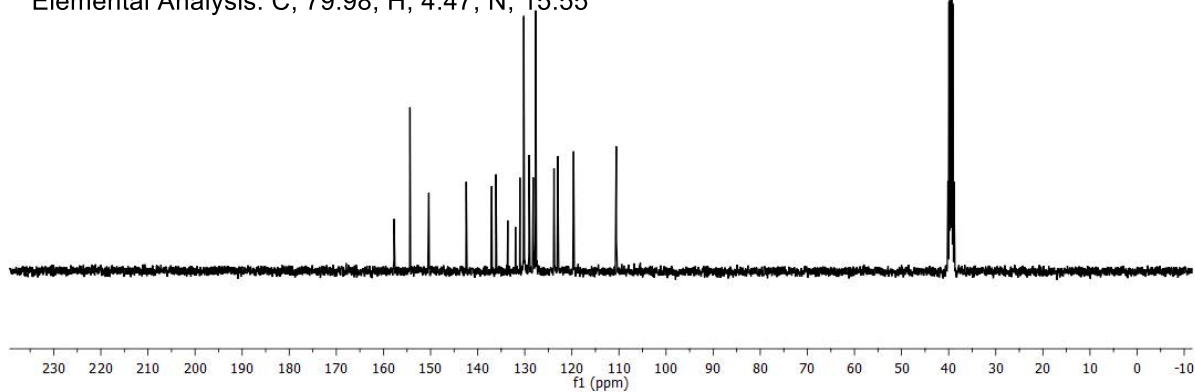
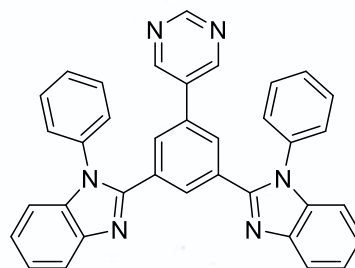
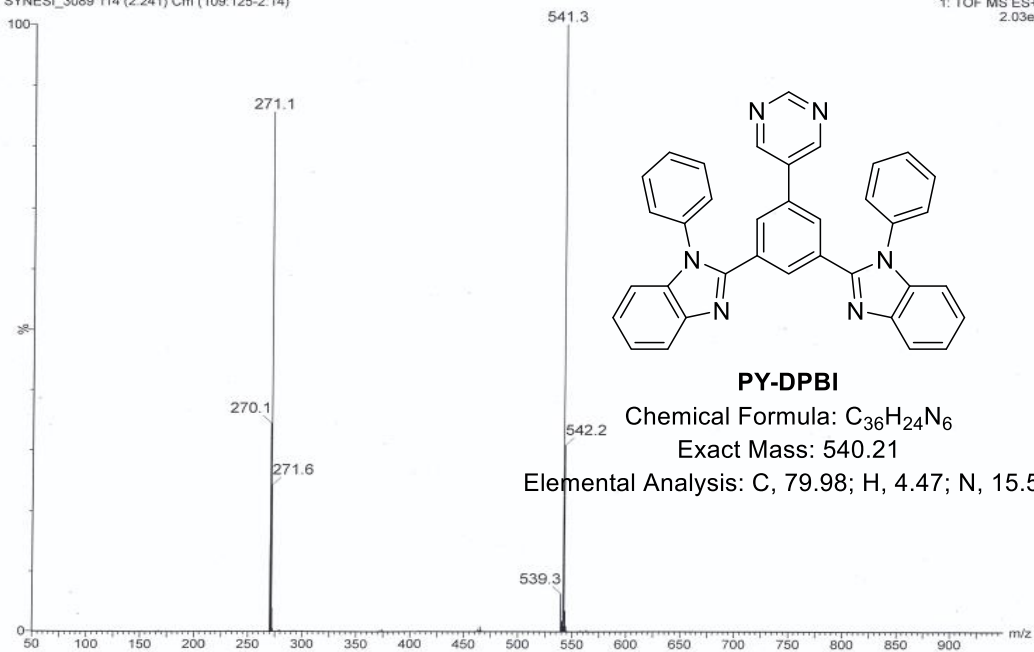
06-25-Baranoff-58



**PY-DPBI**Chemical Formula: $C_{36}H_{24}N_6$

Exact Mass: 540.21

Elemental Analysis: C, 79.98; H, 4.47; N, 15.55

N.Sahotra NXS-41
SYNESI_3089 114 (2.241) Cm (109:125-2:14)1: TOF MS ES+
2.03e7**PY-DPBI**Chemical Formula: $C_{36}H_{24}N_6$

Exact Mass: 540.21

Elemental Analysis: C, 79.98; H, 4.47; N, 15.55

Elemental Composition Report

Single Mass Analysis

Tolerance = 10.0 PPM / DBE: min = -1.5, max = 1000.0

Element prediction: Off

Number of isotope peaks used for i-FIT = 3

Monoisotopic Mass, Even Electron Ions

26 formula(e) evaluated with 1 results within limits (all results (up to 1000) for each mass)

Elements Used:

C: 0-100 H: 0-100 N: 6-6 79Br: 0-8

Minimum: -1.5

Maximum: 5.0 10.0 1000.0

Mass	Calc. Mass	mDa	PPM	DBE	Formula
541.2144	541.2141	0.3	0.6	27.5	C36 H25 N6

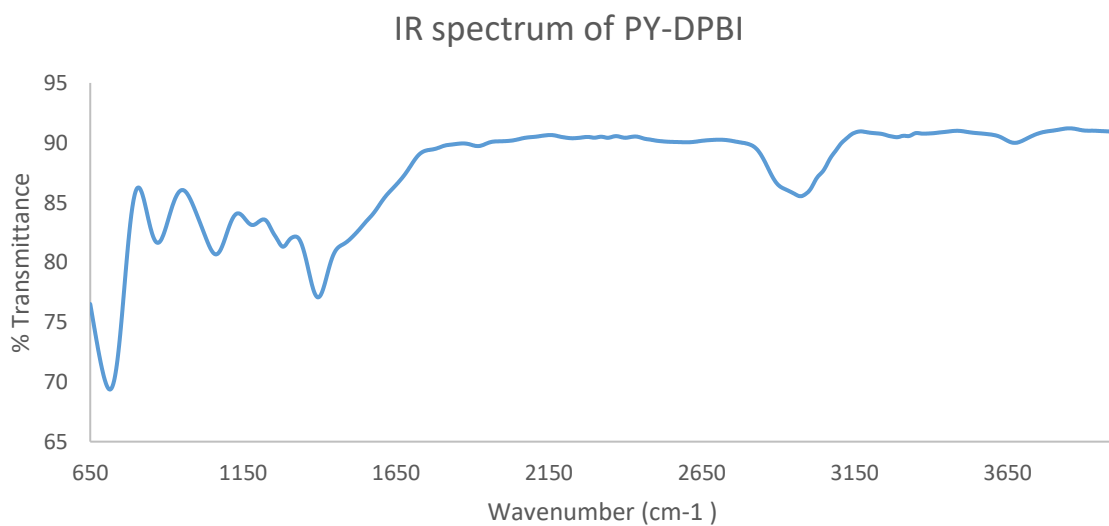
Eager Xperience Summarize Results

Date: 15/09/2017 @ 12:42:09

Method name: Nitrogen/Carbon/Hydrogen

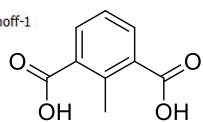
Method Filename: 13September2017 retest 2.mth

Sample Name	Elemental %		
	Nitrogen	Carbon	Hydrogen
PY-DPBI	15.63	79.84	4.25
PY-DPBI	15.43	79.75	4.37
Average			
	15.53	79.80	4.31

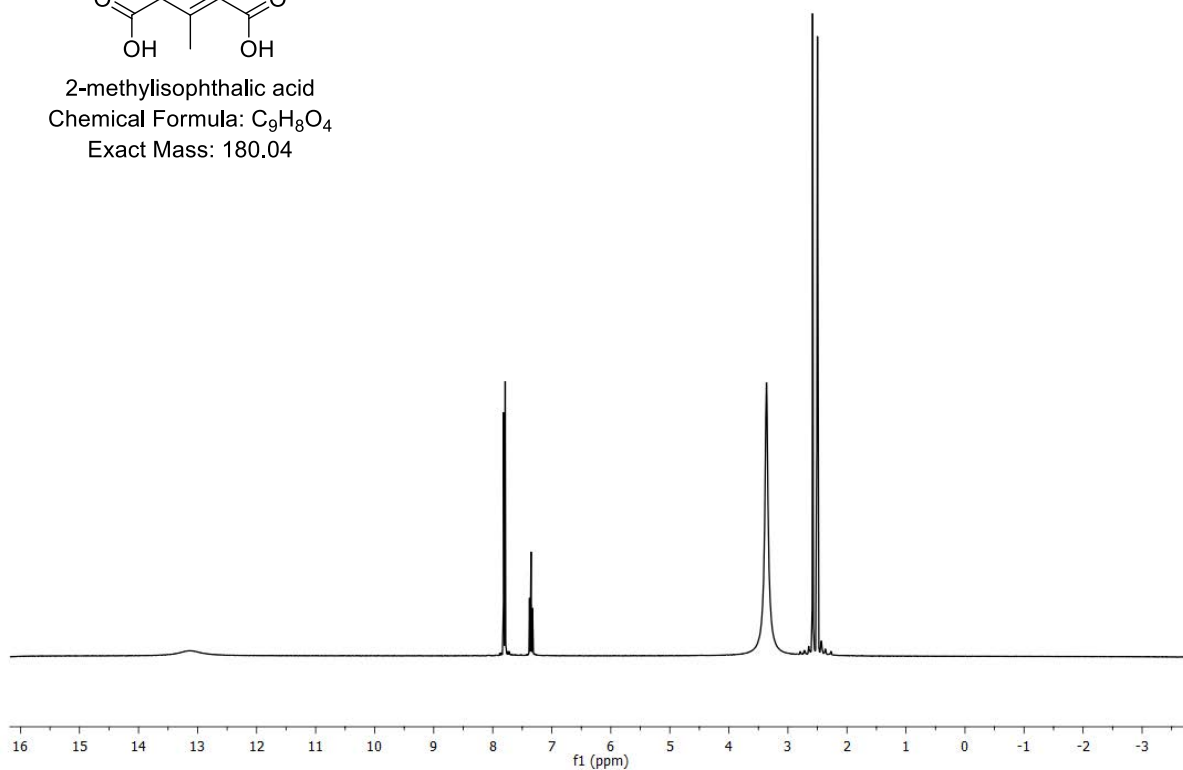


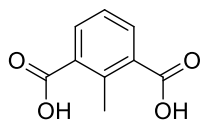
6.5 Analytical data of Third Generation TPBI Derivatives

12-05-Baranoff-1

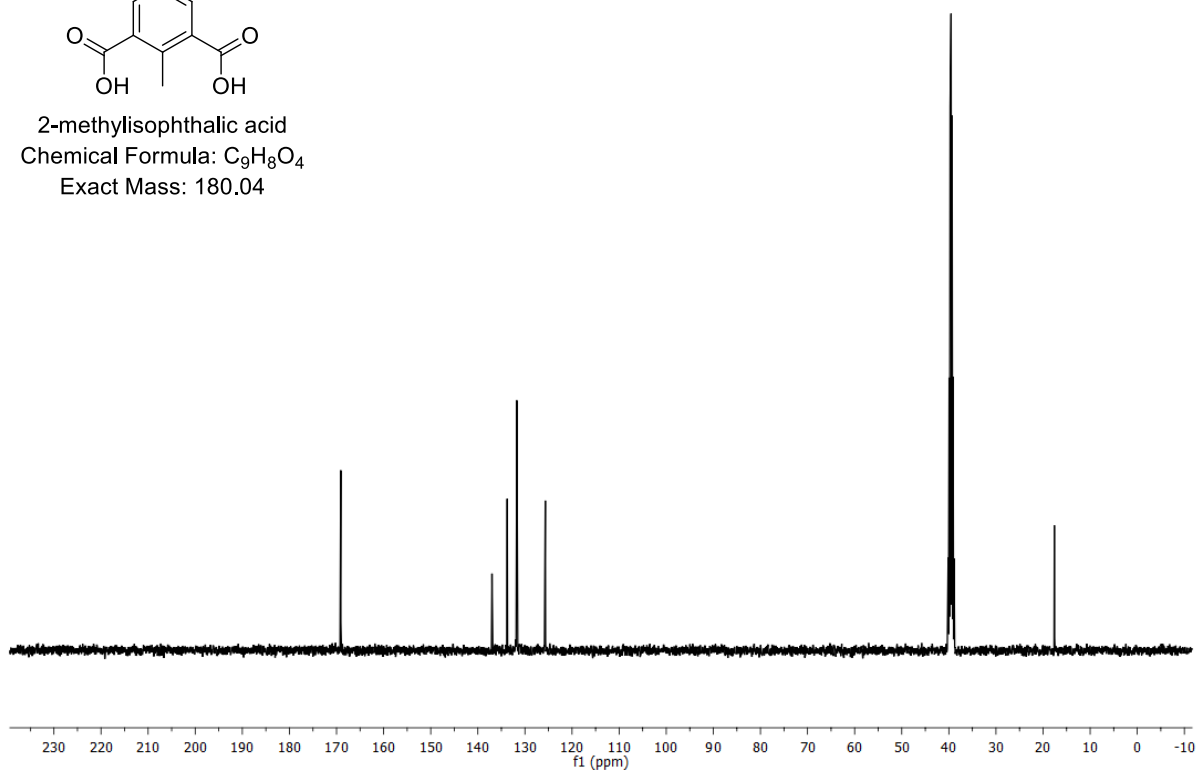


2-methylisophthalic acid
Chemical Formula: C₉H₈O₄
Exact Mass: 180.04

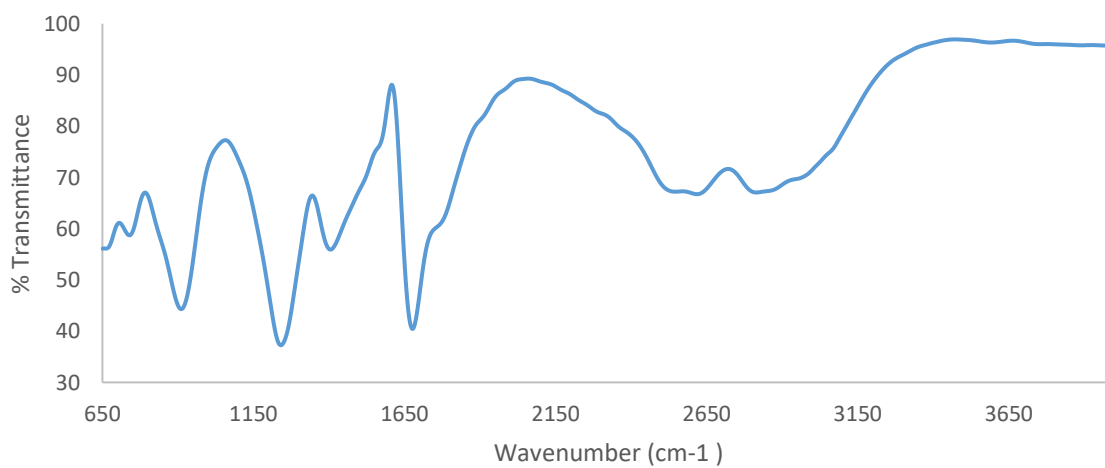




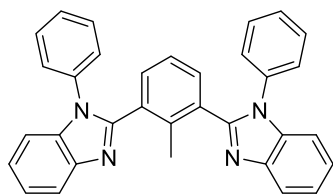
2-methylisophthalic acid
Chemical Formula: $C_9H_8O_4$
Exact Mass: 180.04



IR spectrum of 2-Methylisophthalic Acid



12-11-Baranoff-28

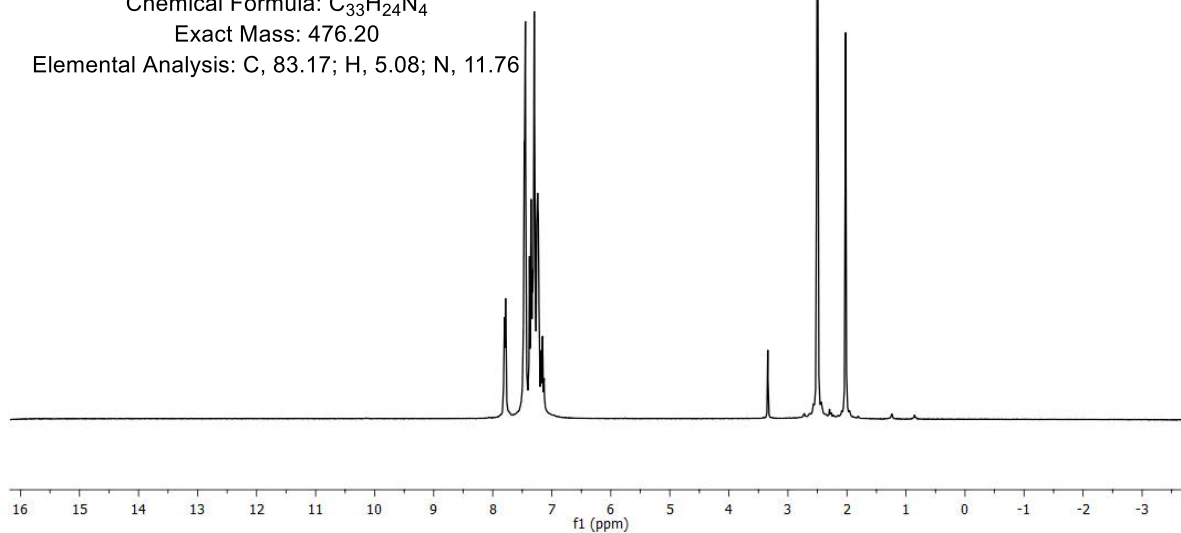


ME-DPBI

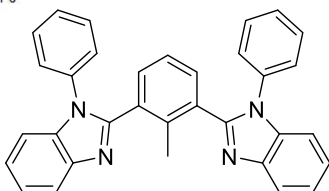
Chemical Formula: $C_{33}H_{24}N_4$

Exact Mass: 476.20

Elemental Analysis: C, 83.17; H, 5.08; N, 11.76



12-11-Baranoff-6

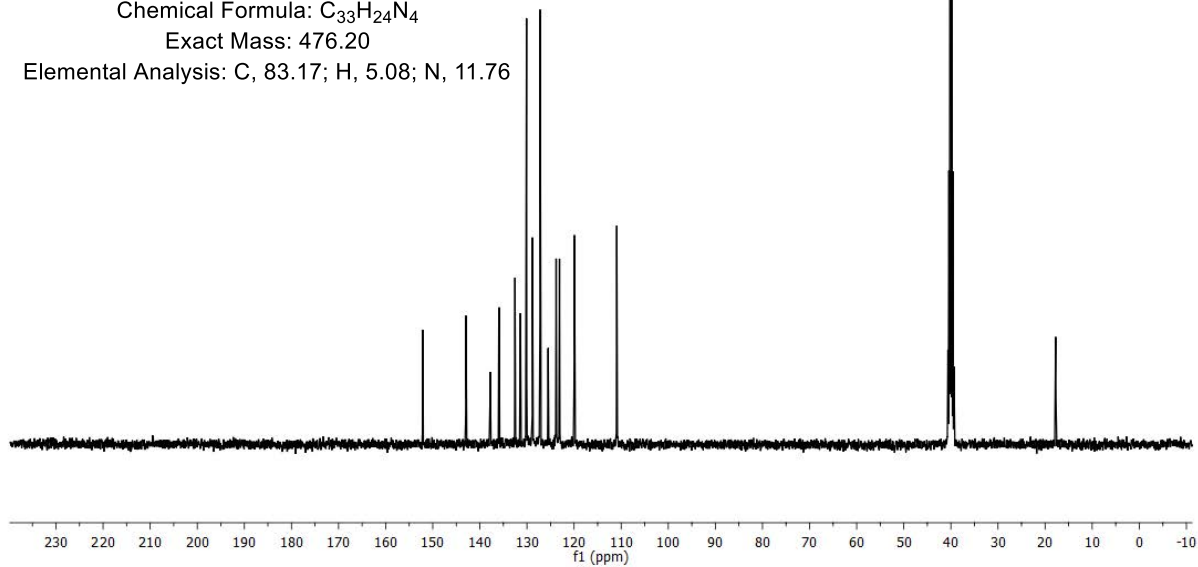


ME-DPBI

Chemical Formula: $C_{33}H_{24}N_4$

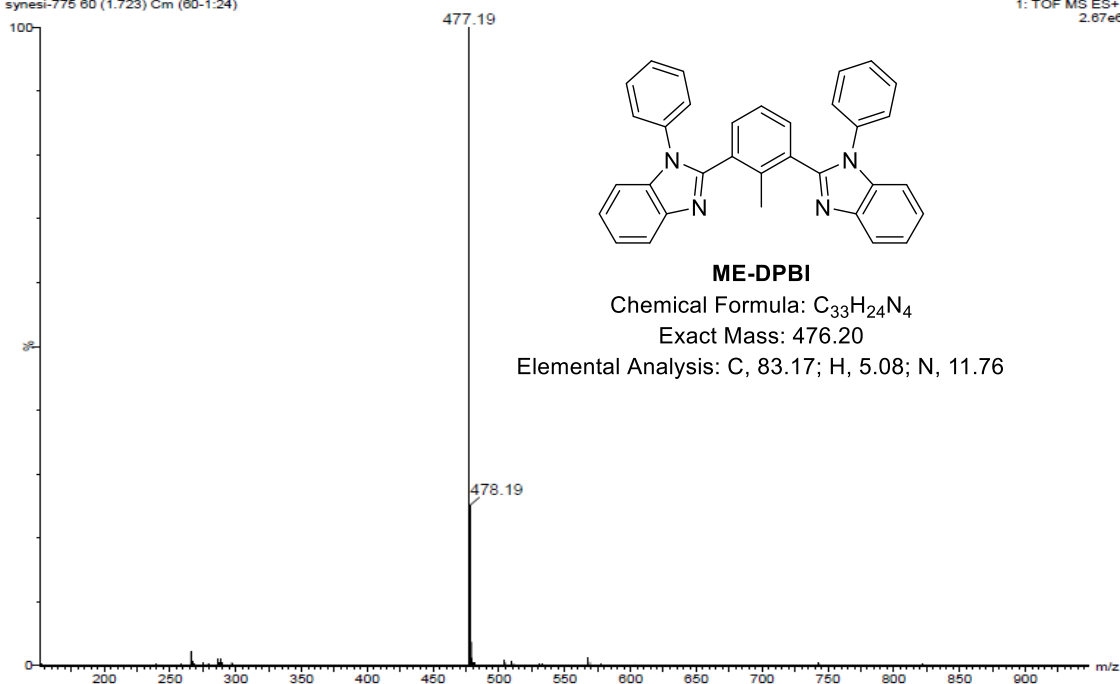
Exact Mass: 476.20

Elemental Analysis: C, 83.17; H, 5.08; N, 11.76



Nikhil Sahotra NXS-73-E
synesi-775 60 (1.723) Cm (60-1:24)

1: TOF MS ES+
2.67e6



Elemental Composition Report N. Sahotra NXS-73-E

Single Mass Analysis

Tolerance = 5.0 PPM / DBE: min = -1.5, max = 1000.0

Element prediction: Off

Monoisotopic Mass, Even Electron Ions

63 formula(e) evaluated with 1 results within limits (all results (up to 1000) for each mass)

Elements Used:

C: 0-100 H: 0-100 N: 1-10

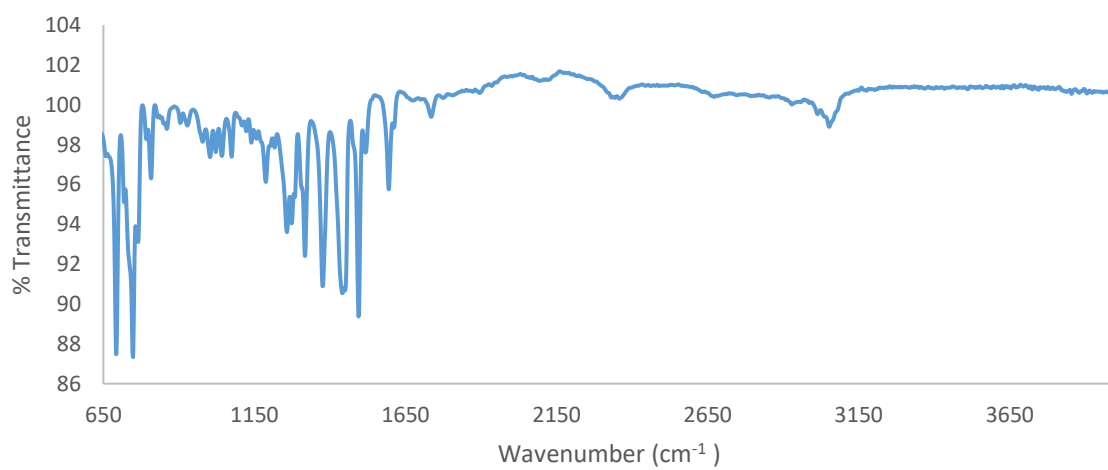
Minimum:					-1.5
Maximum:	5.0	5.0			1000.0
Mass	Calc. Mass	mDa	PPM	DBE	Formula
477.2069	477.2079	-1.0	-2.1	23.5	C33 H25 N4

Eager Xperience Summarize Results

Date: 15/09/2017 @ 12:42:09
Method name: Nitrogen/Carbon/Hydrogen
Method Filename: 13September2017 retest 2.mth

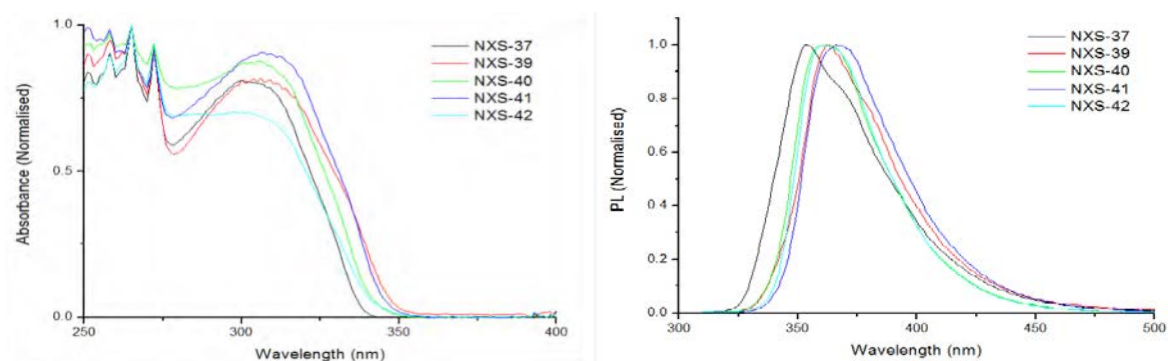
Sample Name	Elemental %		
	Nitrogen	Carbon	Hydrogen
ME-DPBI	11.56	83.09	5.07
ME-DPBI	11.59	83.28	5.05
Average			
	11.58	83.19	5.06

IR Spectrum of ME-DPBI

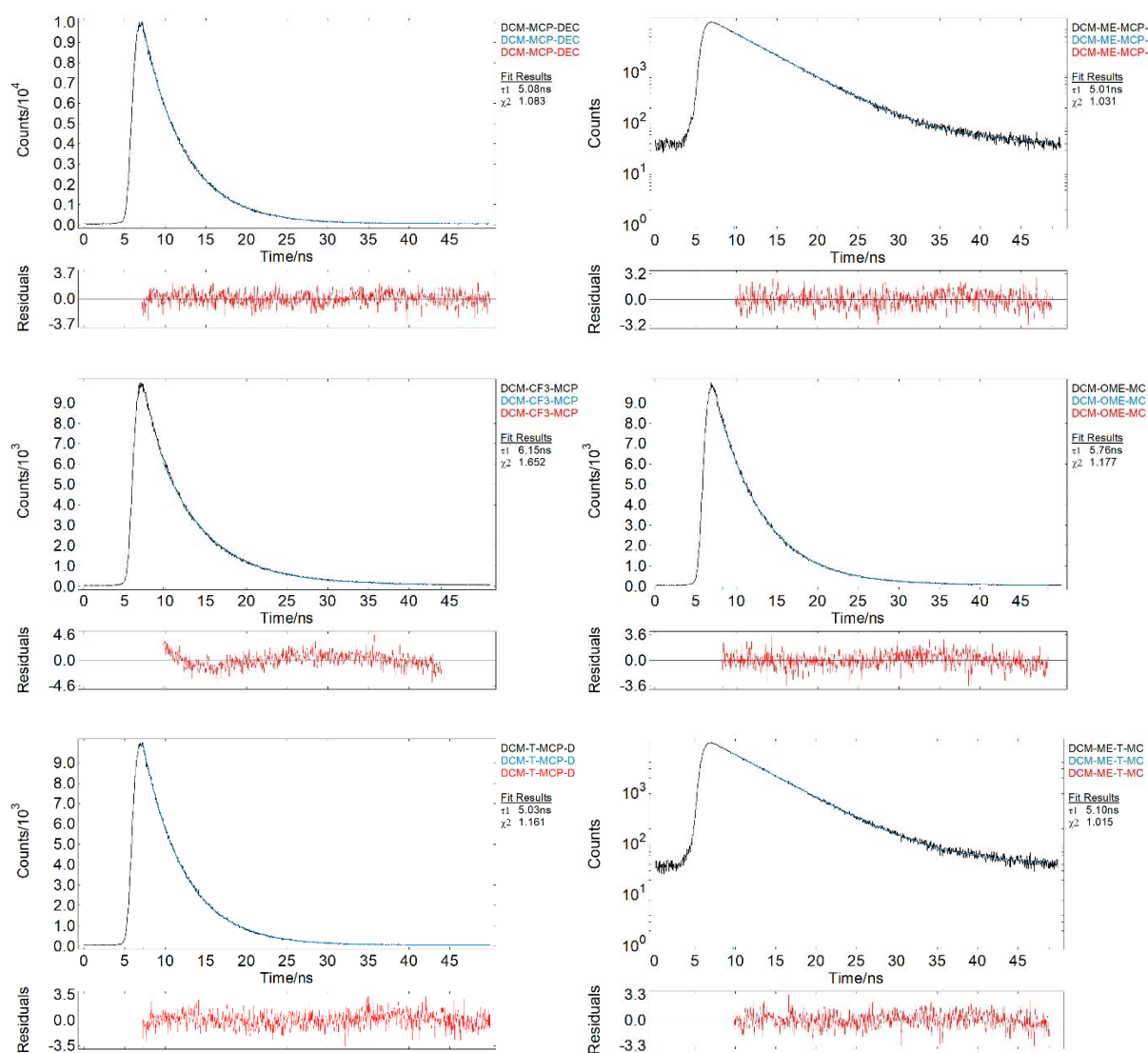


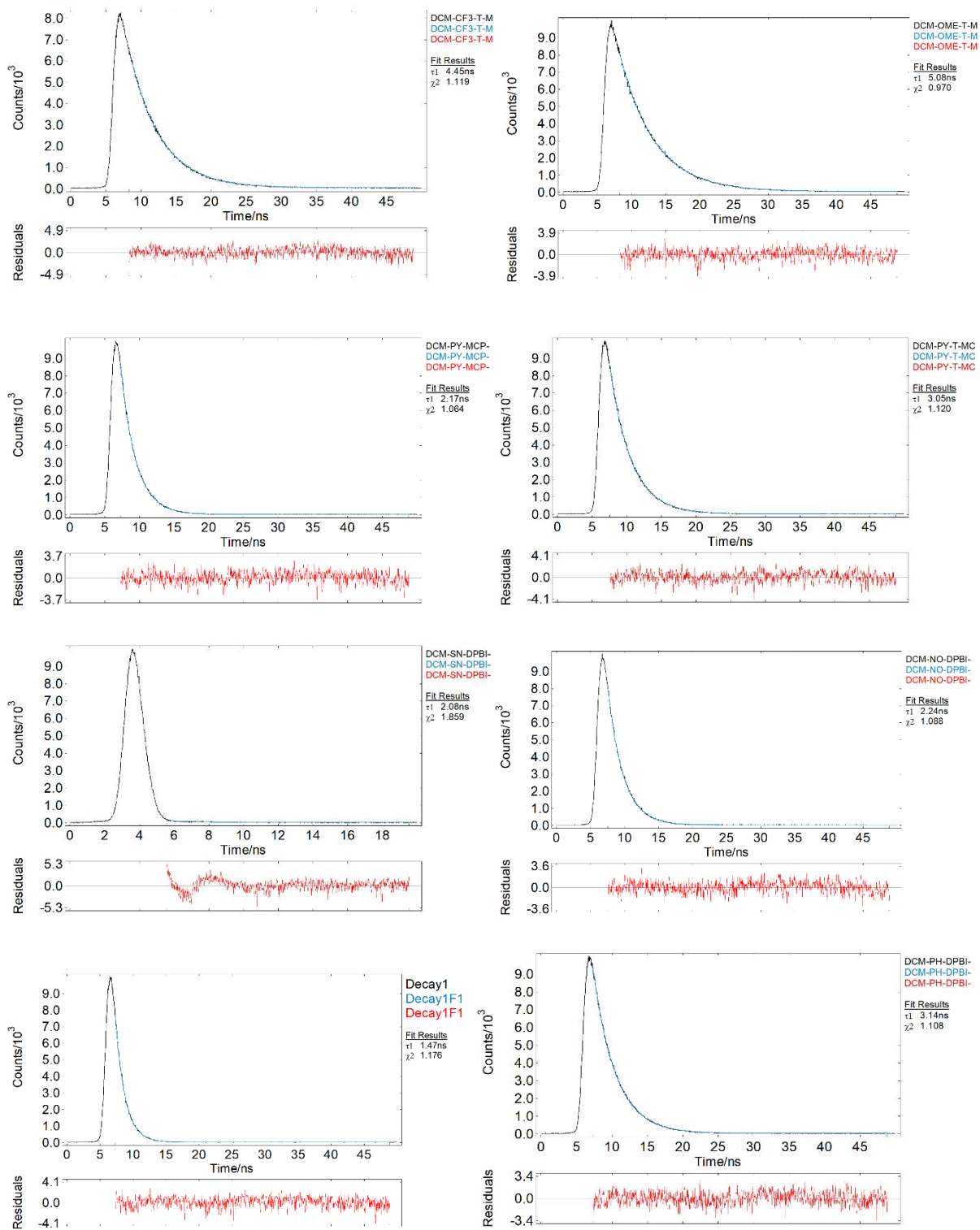
7 Appendix ii

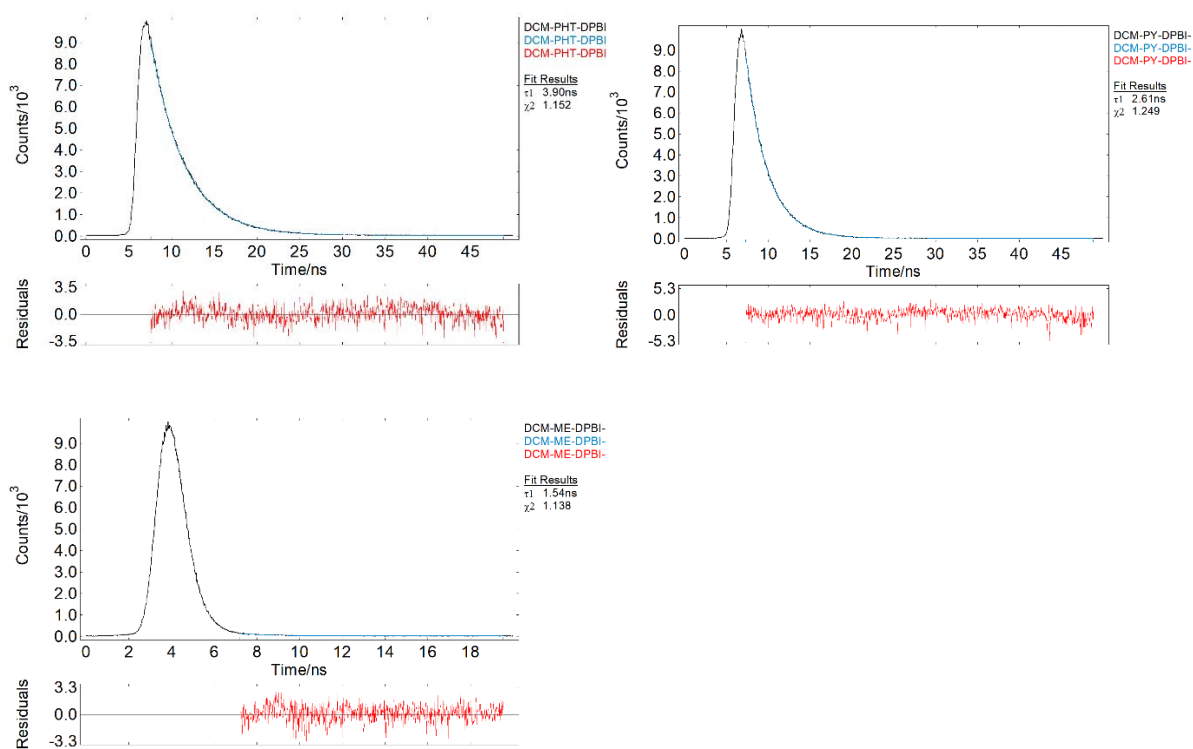
7.1 Photophysical Analysis of second generation TPBI



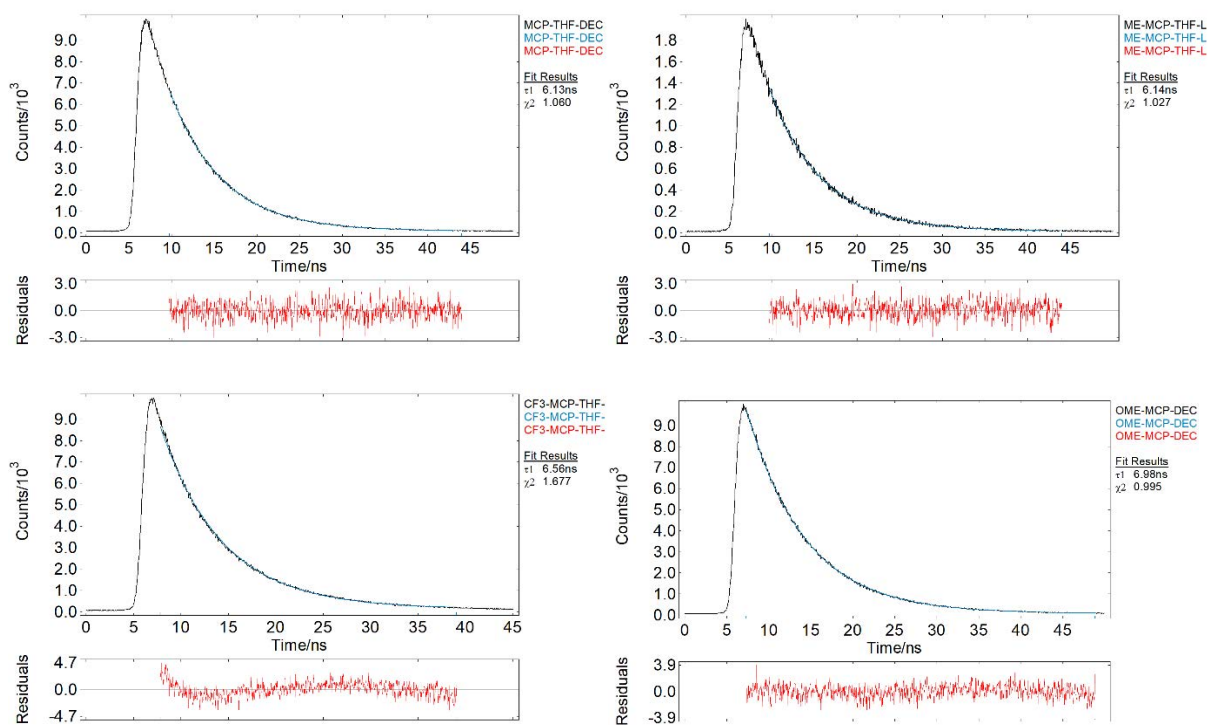
7.2 Fluorescence Lifetime Measurements in DCM

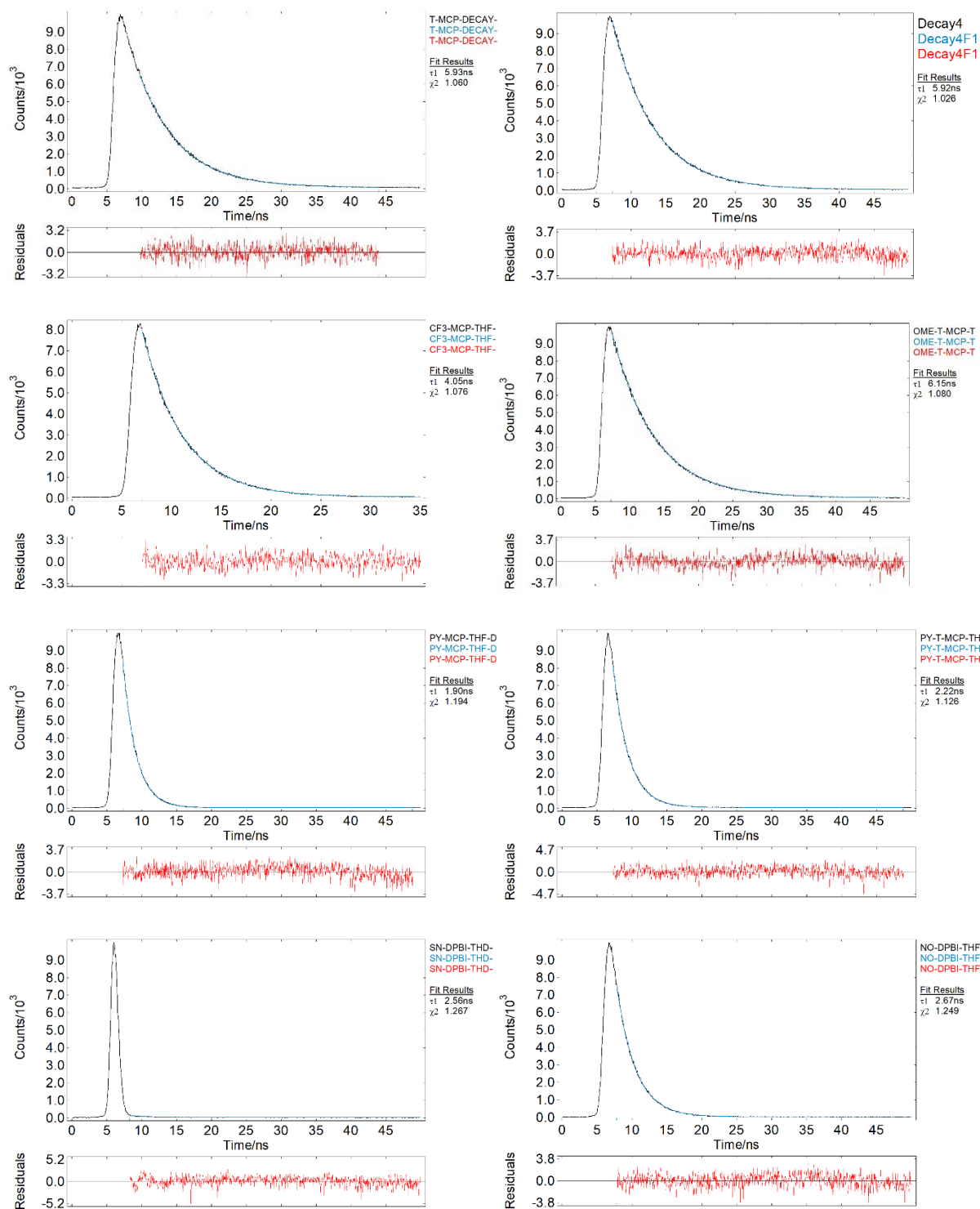


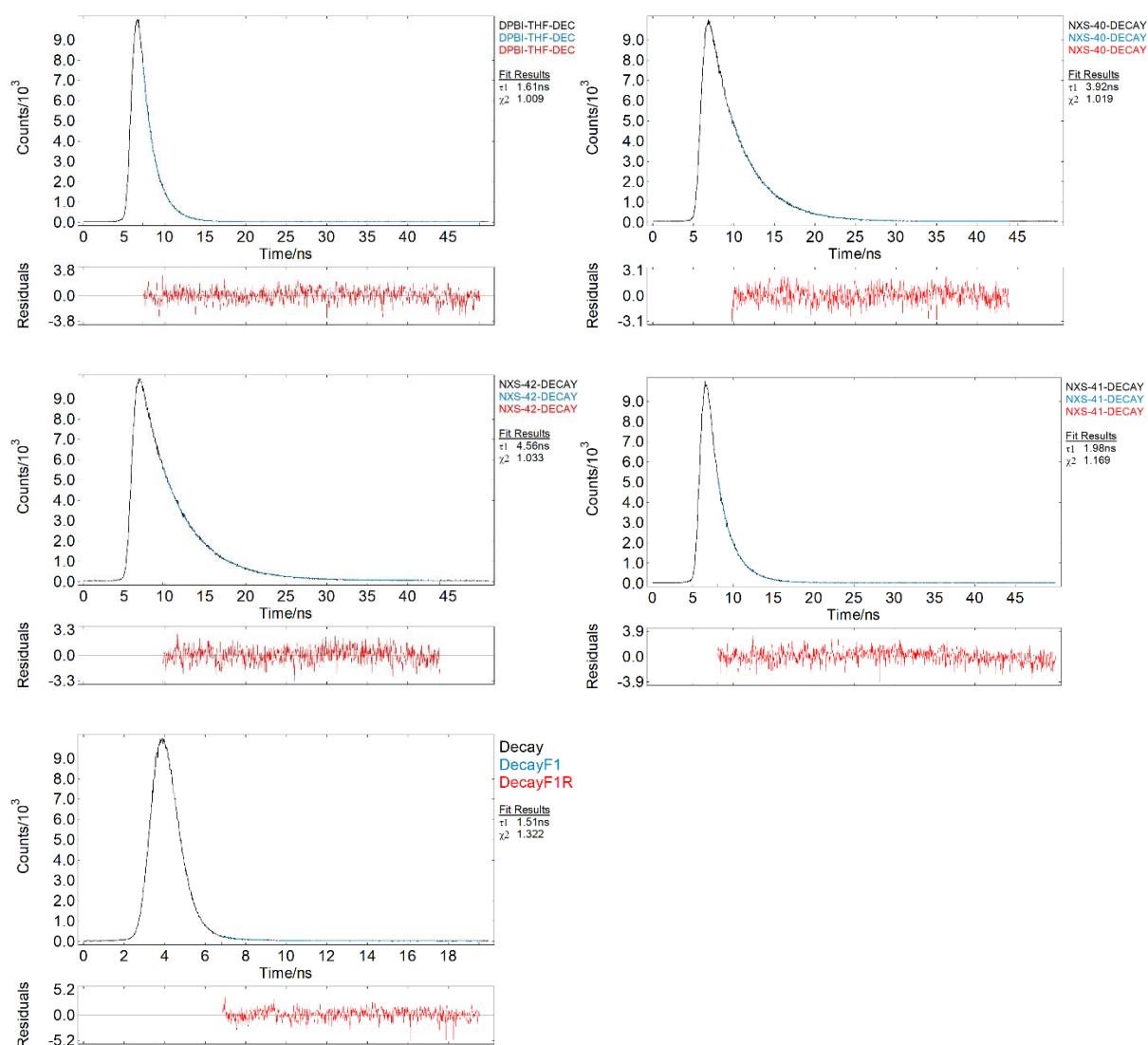




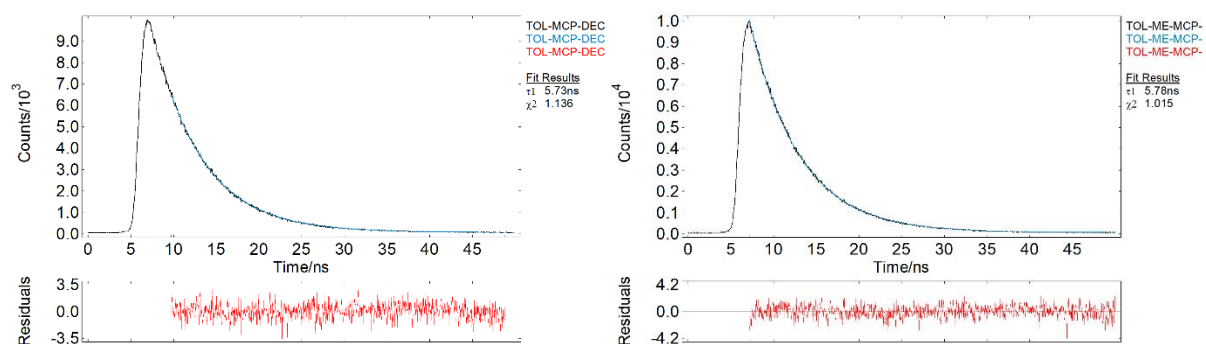
7.3 Fluorescence Lifetime Measurements in THF

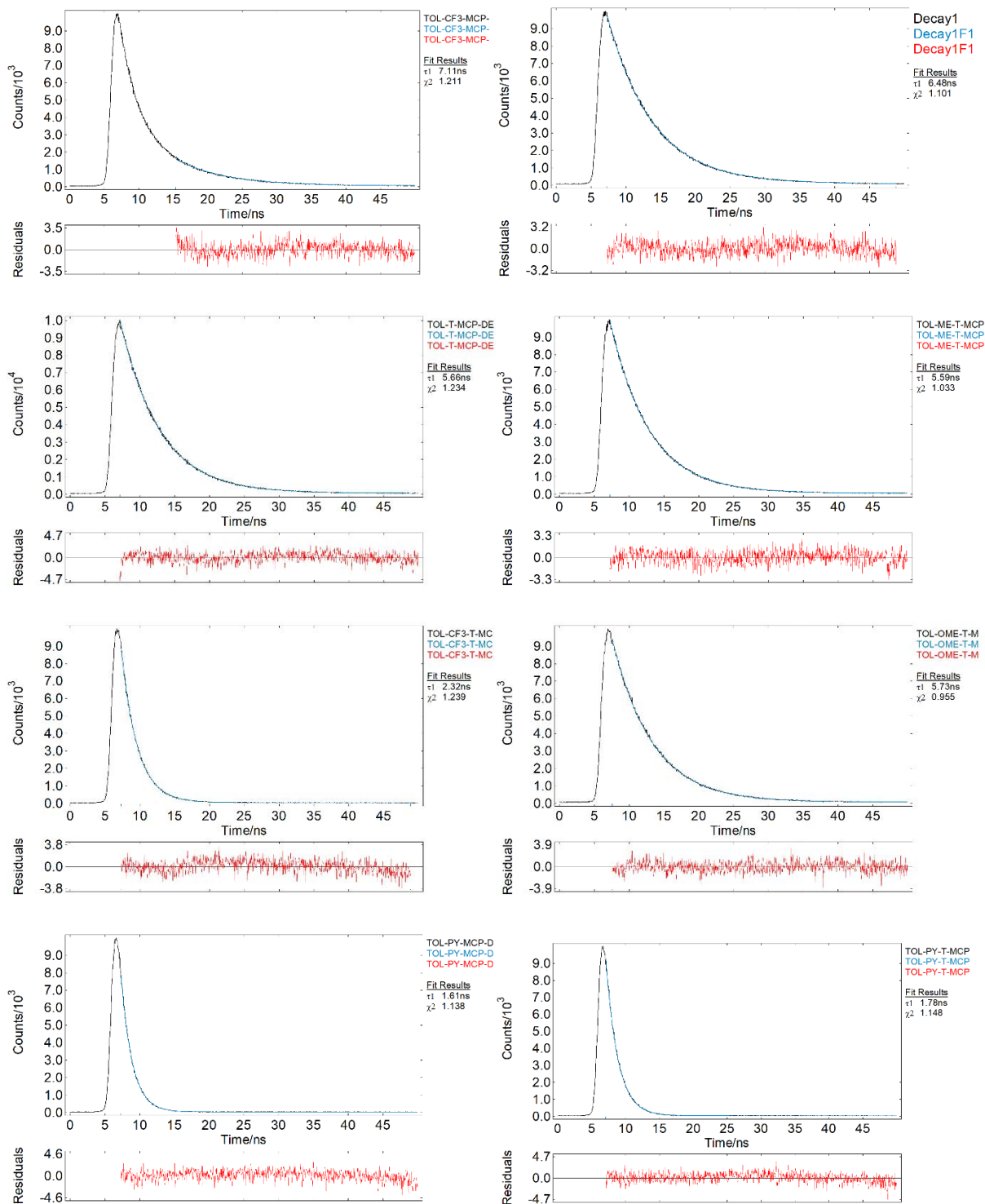


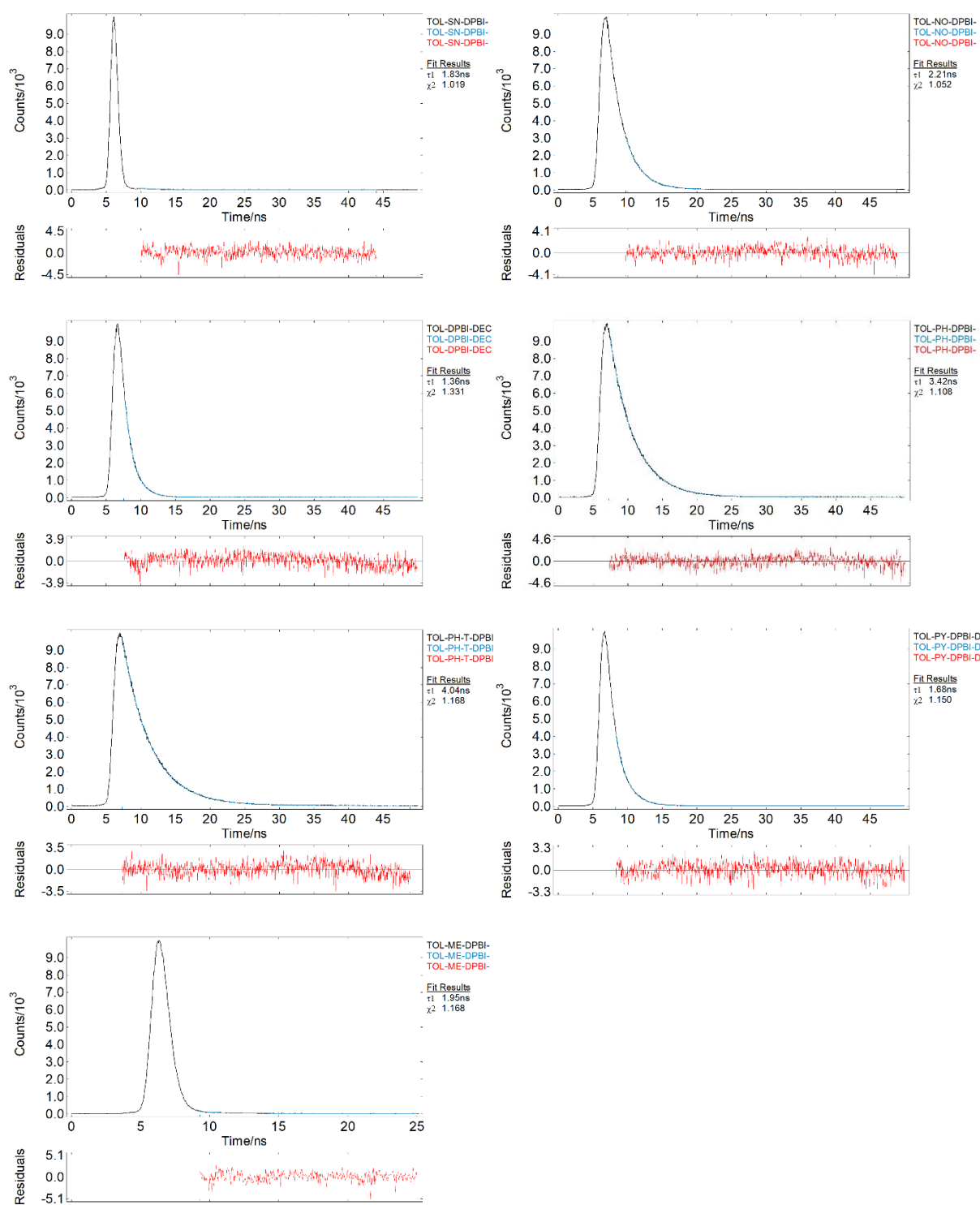




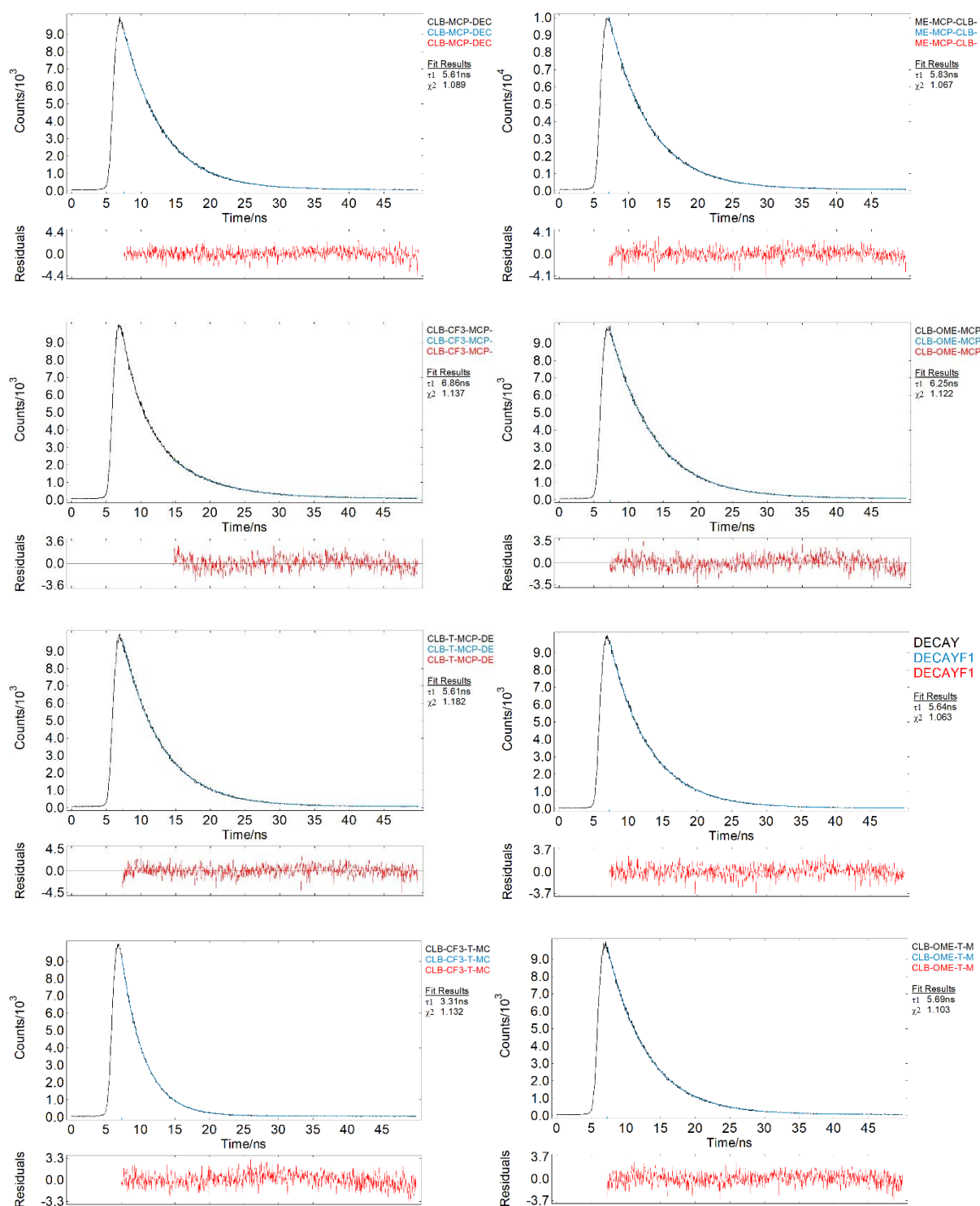
7.4 Fluorescence Lifetime Measurements in Toluene

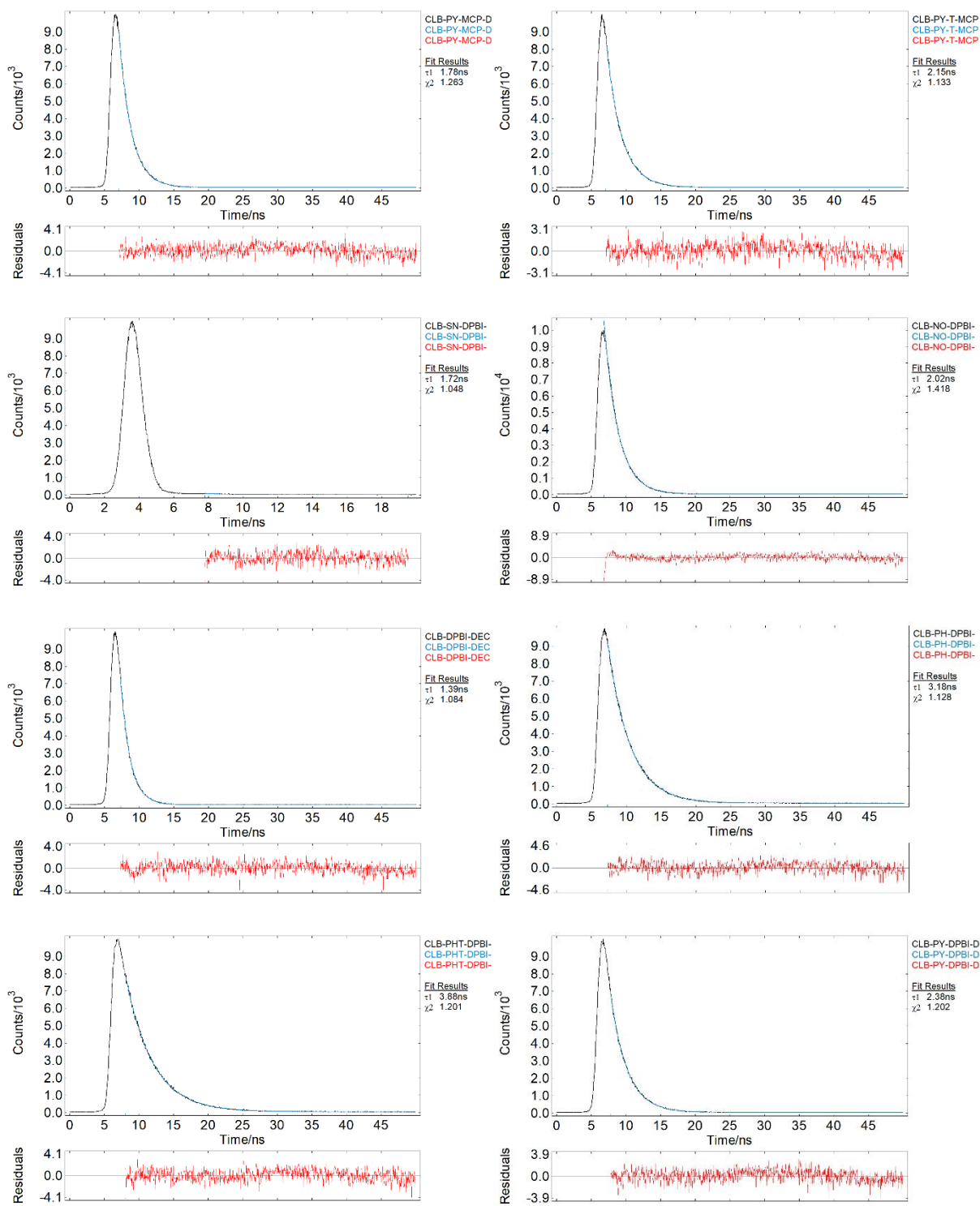


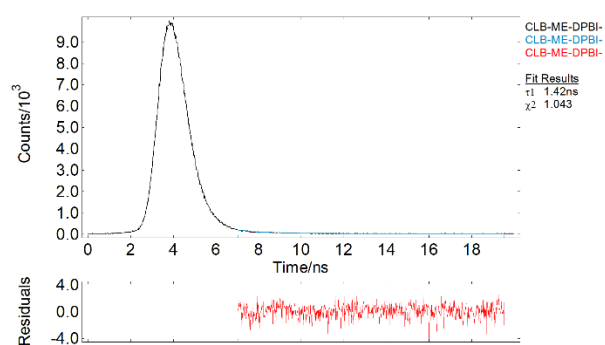




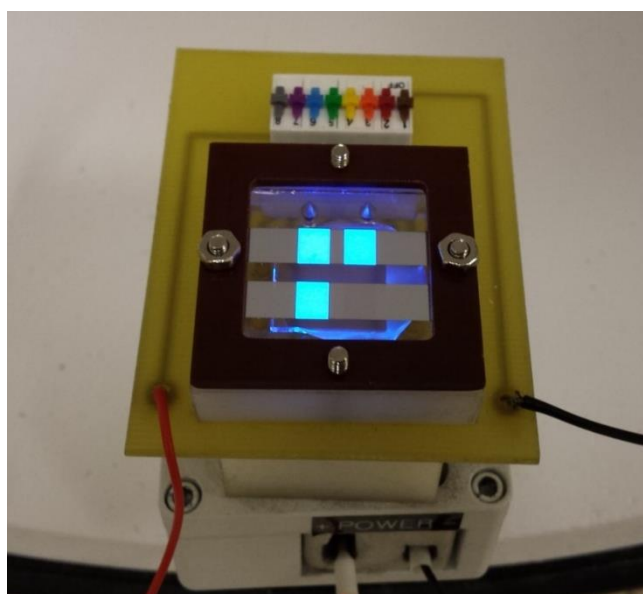
7.5 Fluorescence Lifetime Measurements in Chlorobenzene



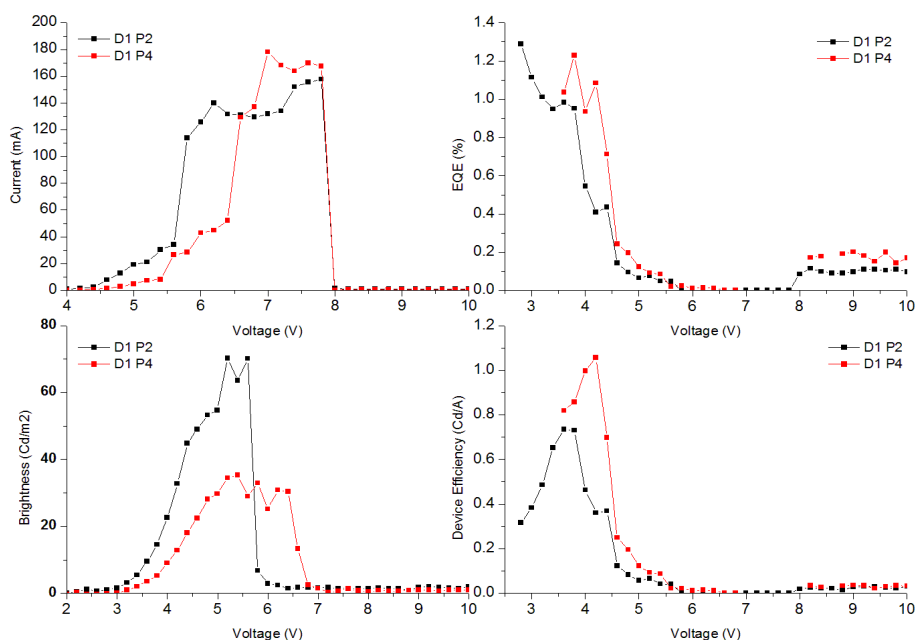




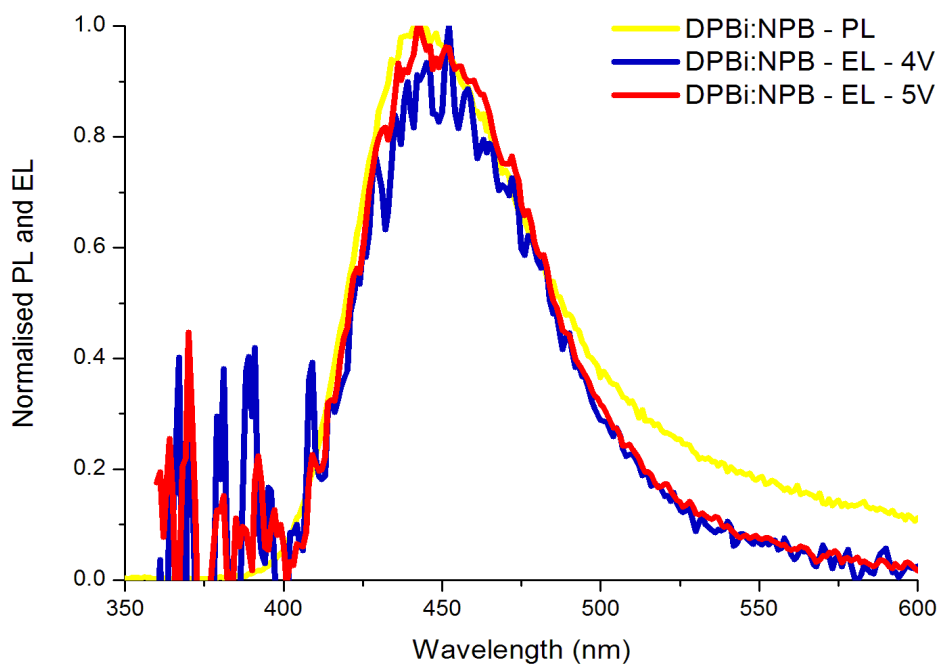
7.6 Solid state Analysis of Devices formulated using DPBI



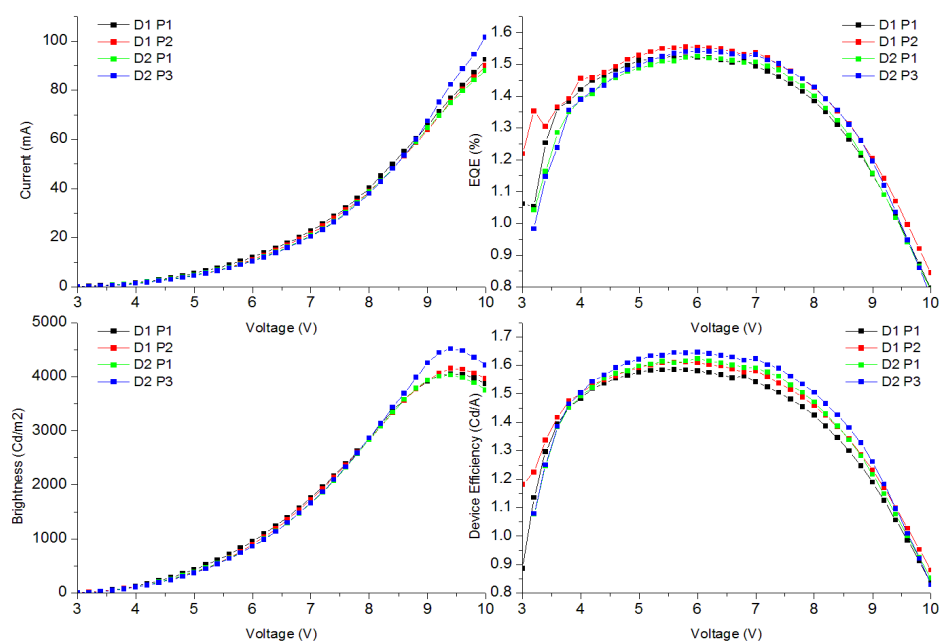
Device structure: ITO/TAPC (40nm)/DPBi:NPB (40nm)/TPBi (20nm)/BCP (20nm)
/LiF (1nm)/Al (70nm)



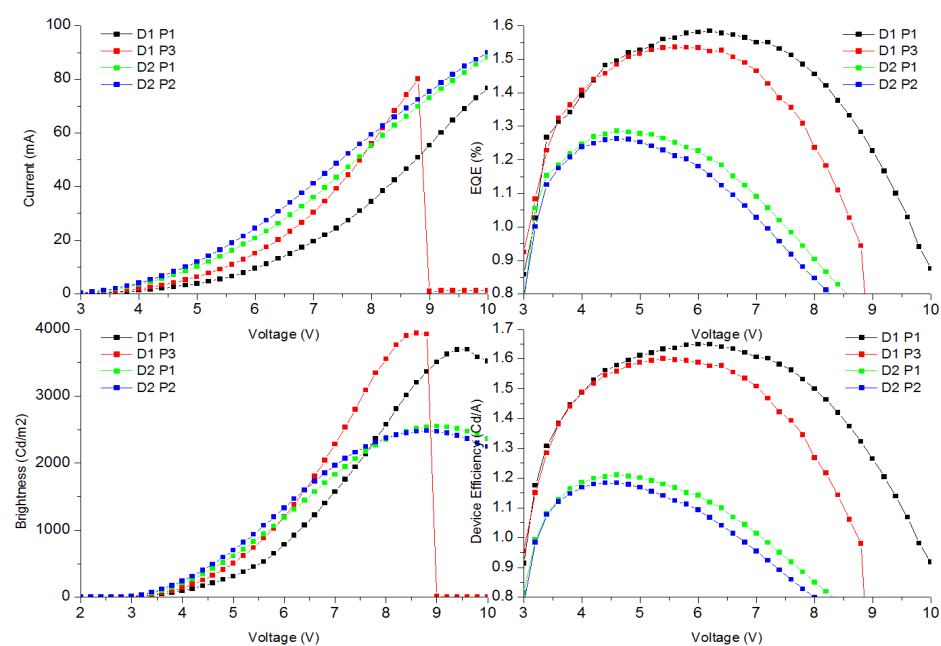
Device structure: ITO/TAPC (40nm)/DPBi:NPB (40nm)/TPBi (20nm)/BCP (20nm)
/LiF (1nm)/Al (70nm)



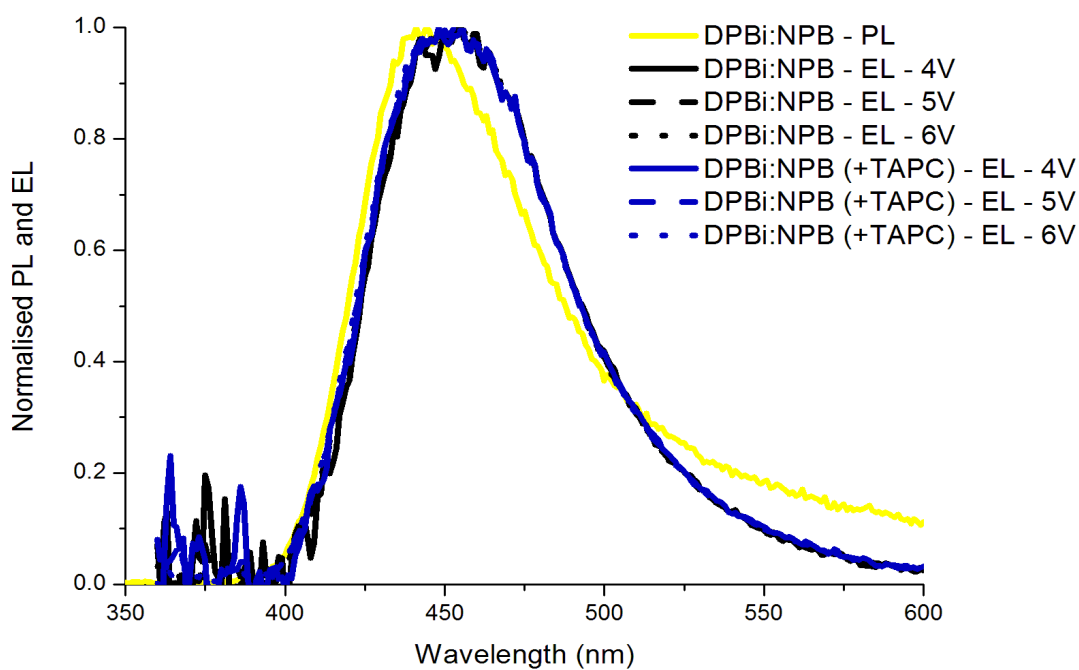
Device structure: ITO/TAPC (40nm)/DPBi:NPB (40nm)/TPBi (20nm)/BCP (20nm)
/LiF (1nm)/Al (70nm)



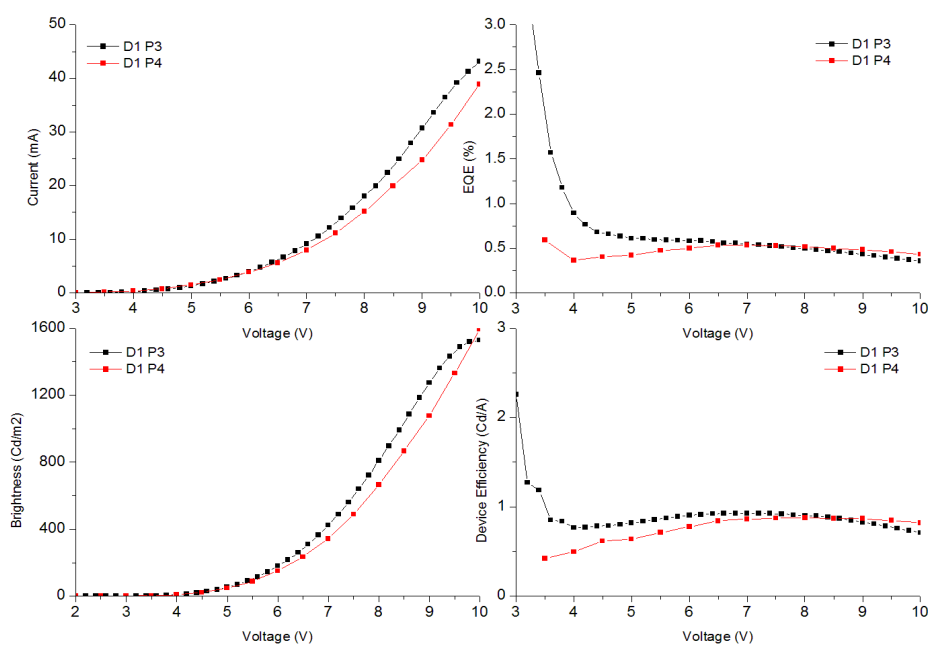
Device structure: ITO/NPB (30nm)/TAPC (10nm)/DPBi:NPB (30nm)/TPBi (60nm)
/LiF (1nm)/Al (70nm)



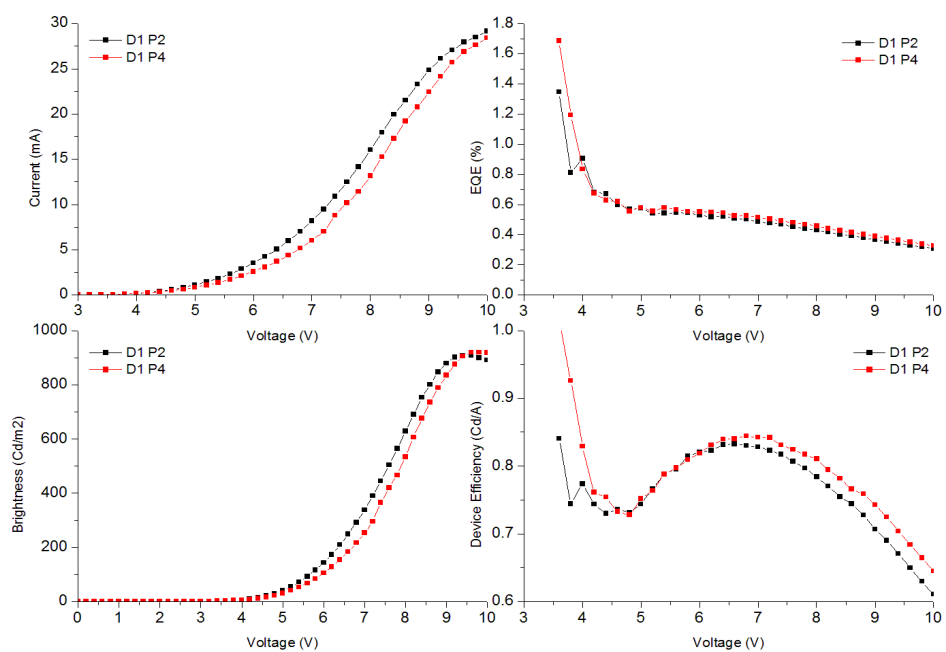
Device structure: ITO/NPB (30nm)/DPBi:NPB (30nm)/TPBi (60nm)
/LiF (1nm)/Al (70nm)



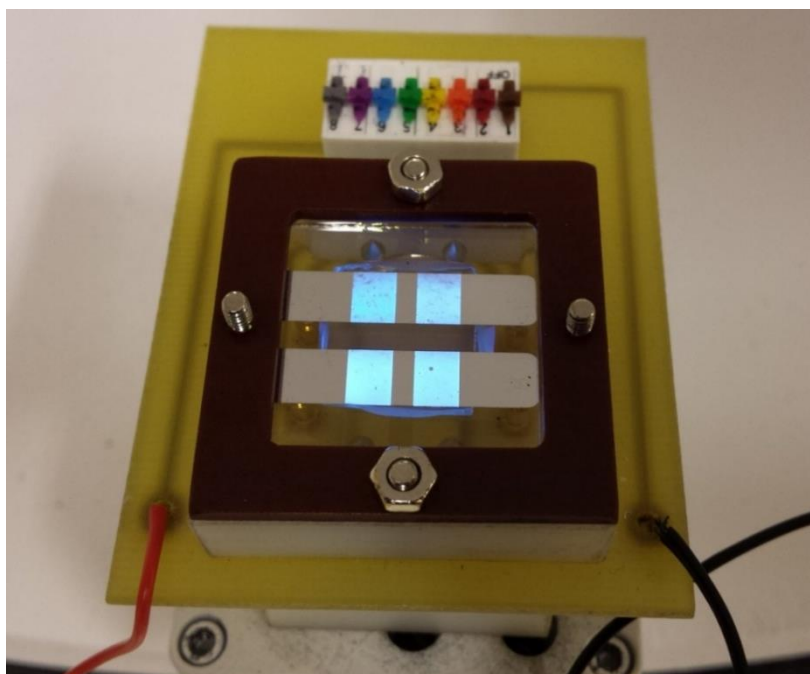
Device structure: ITO/NPB (30nm)/ \pm TAPC(10nm)/DPBi:NPB (30nm)/TPBi (60nm)/LiF (1nm)/Al (70nm)



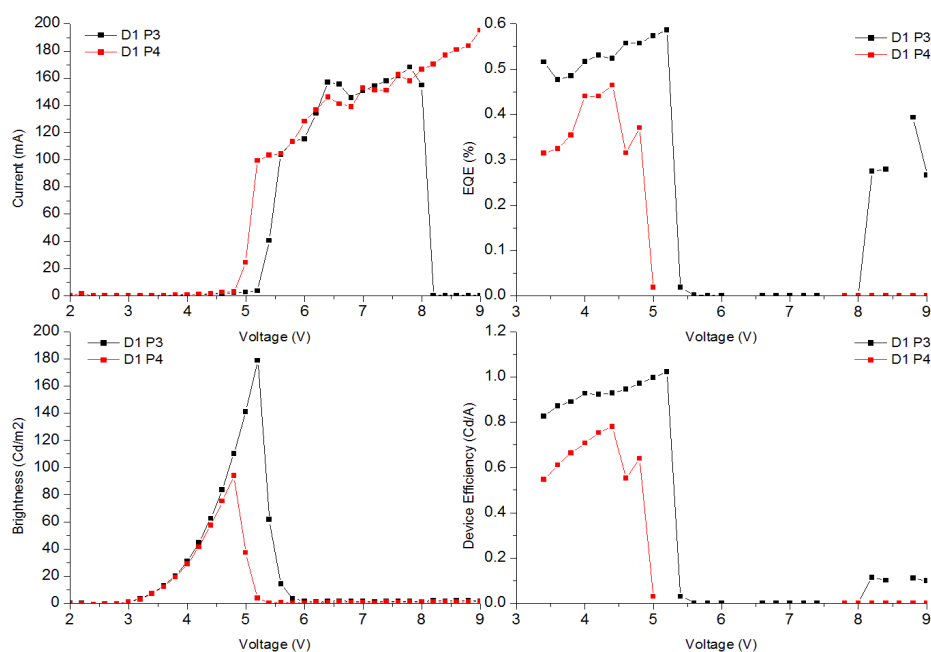
Device structure: ITO/NPB (40nm)/DPBi :TAPC (40nm)/TPBi (20nm)/BCP (20nm)
/LiF (1nm)/Al (80nm)



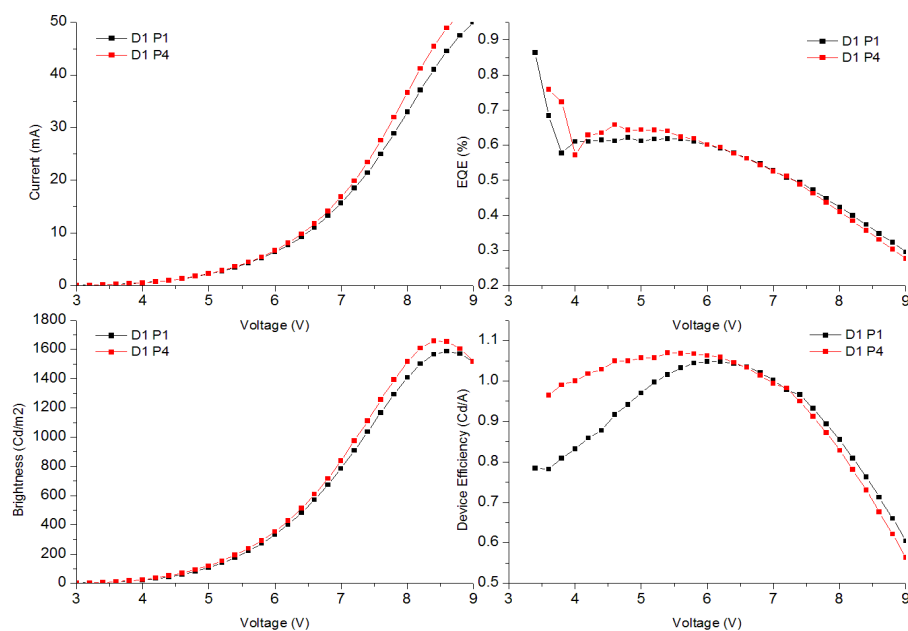
Device structure: ITO/NPB (40nm)/DPBi :TAPC (40nm)/TPBi (20nm)/BCP (20nm)
/LiF (1nm)/Al (80nm)



Device structure: ITO/NPB (30nm)/TAPC (10nm)/DPBi :TAPC (30nm)/TPBi (60nm)
/LiF (1nm)/Al (80nm)

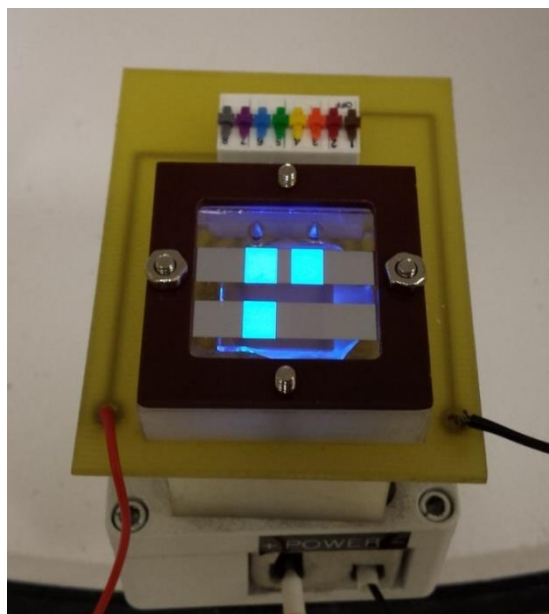


Device structure: ITO/NPB (30nm)/TAPC (10nm)/DPBi :TAPC (30nm)/TPBi (60nm)
/LiF (1nm)/Al (80nm)

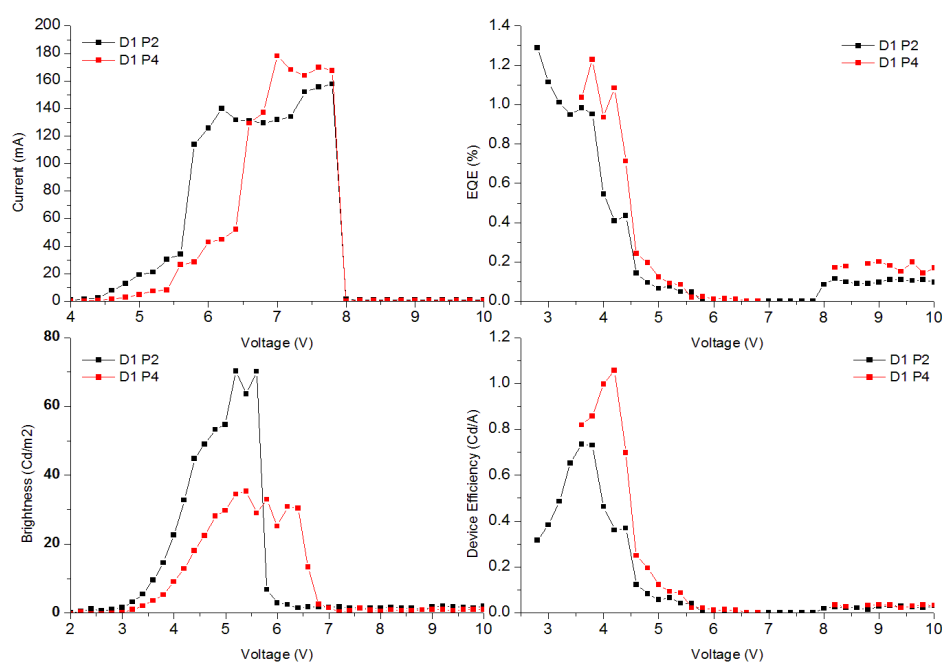


Device structure: ITO/NPB (30nm)/TAPC (10nm)/DPBi :TAPC (30nm)/TPBi (60nm)
/LiF (1nm)/Al (80nm)

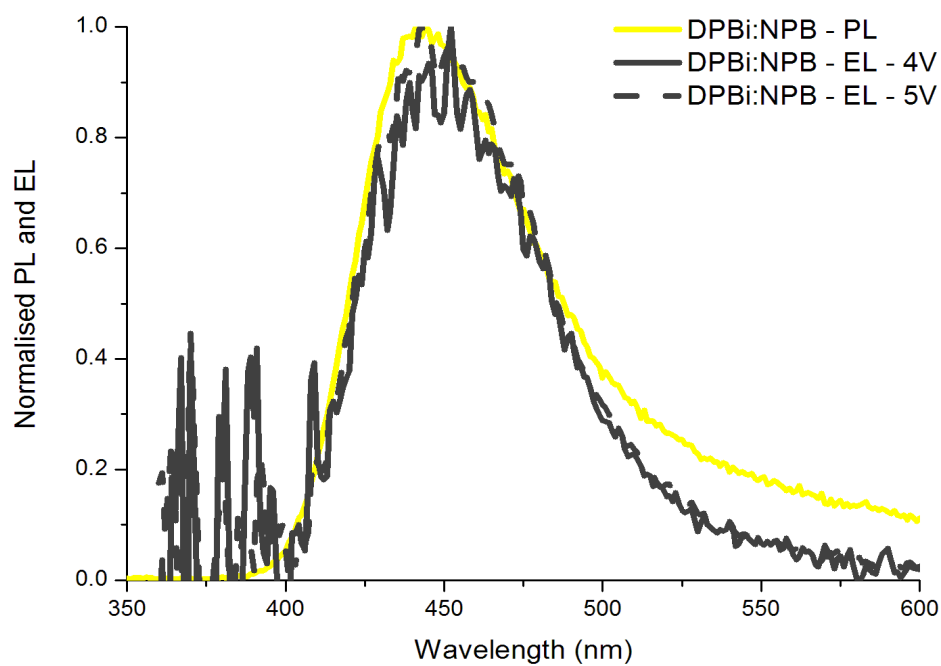
7.7 Solid state Analysis of Devices formulated using ME-DPBI



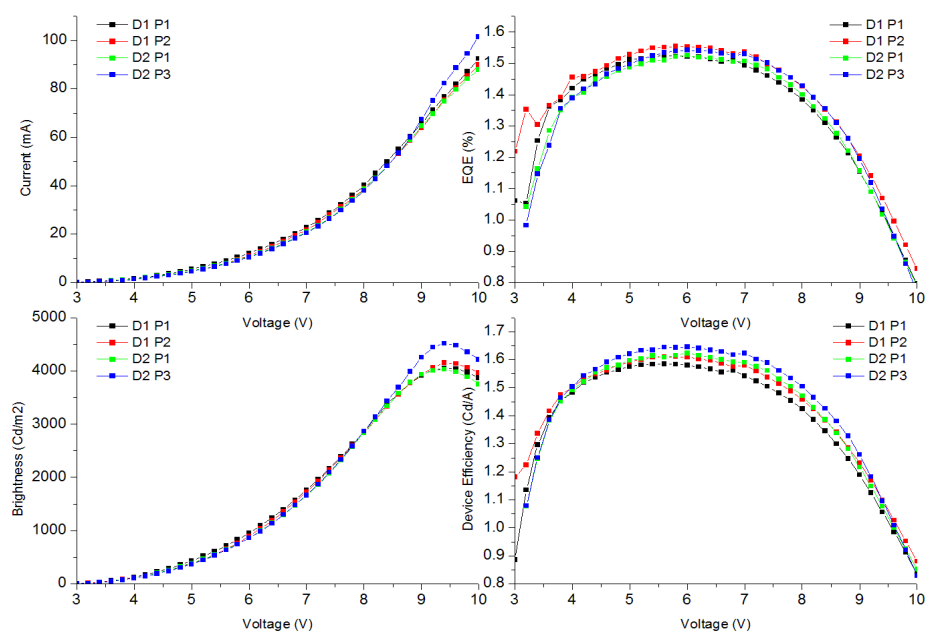
Device structure: ITO/TAPC (40nm)/m-DPBi:NPB (40nm)/TPBi (20nm)/BCP (20nm)
/LiF (1nm)/Al (70nm)



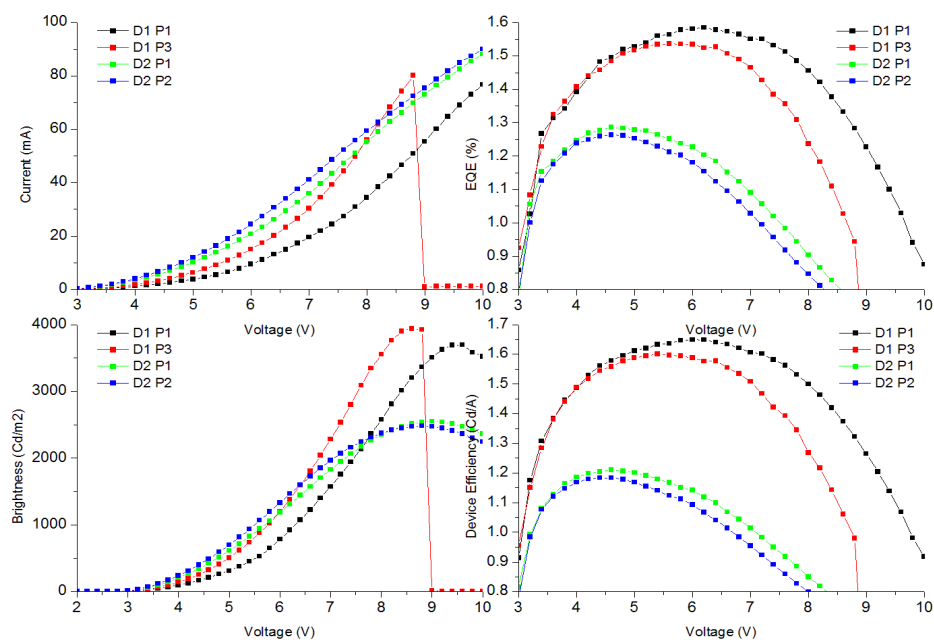
Device structure: ITO/TAPC (40nm)/m-DPBi:NPB (40nm)/TPBi (20nm)/BCP (20nm)
/LiF (1nm)/Al (70nm)



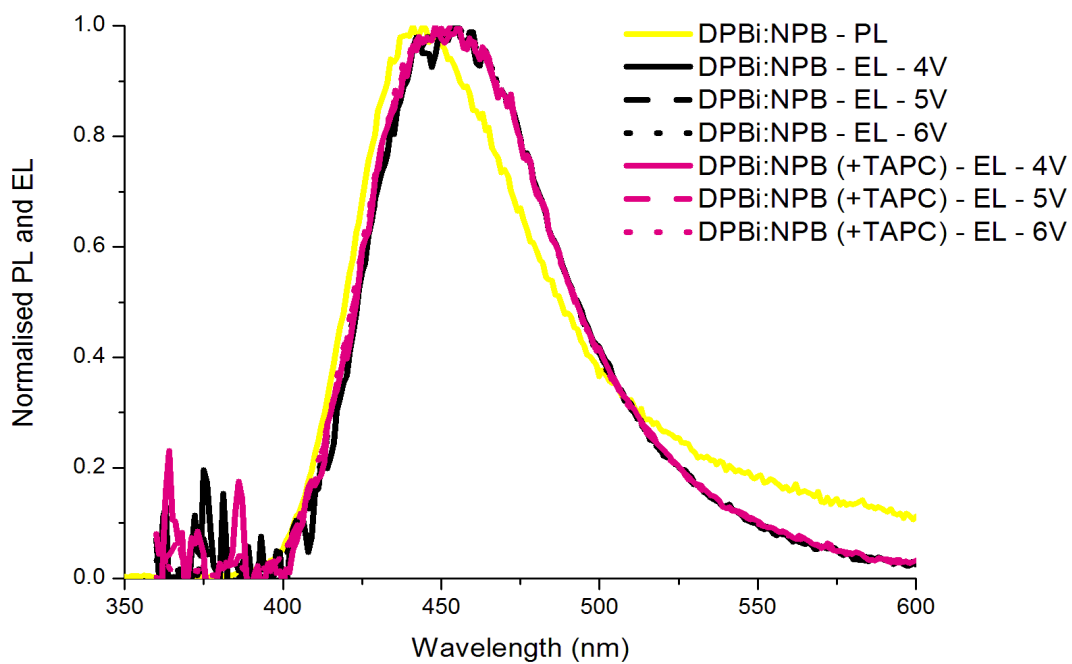
Device structure: ITO/TAPC (40nm)/m-DPBi:NPB (40nm)/TPBi (20nm)/BCP (20nm)
/LiF (1nm)/Al (70nm)



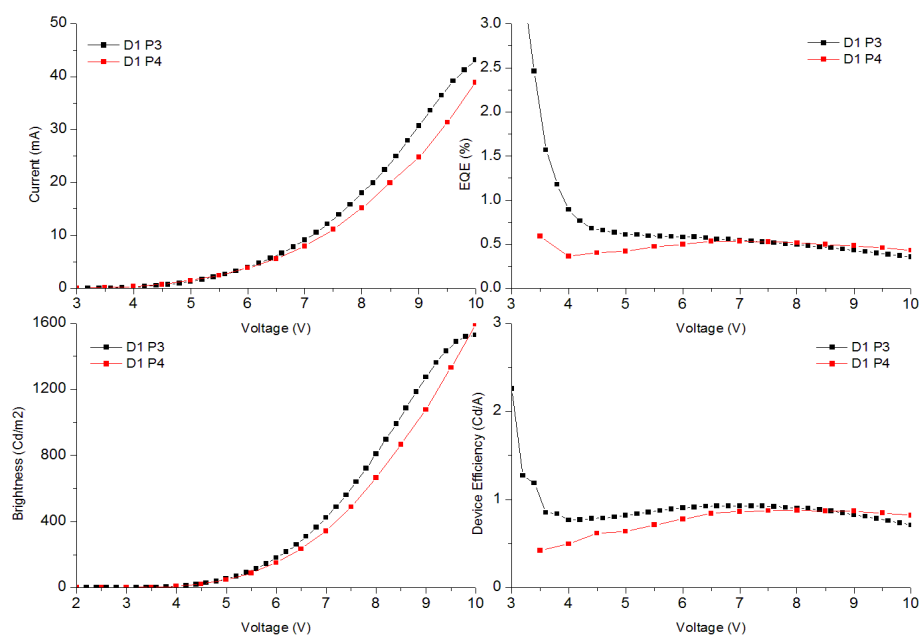
Device structure: ITO/NPB (30nm)/TAPC (10nm)/m-DPBi:NPB (30nm)/TPBi (60nm)
/LiF (1nm)/Al (70nm)



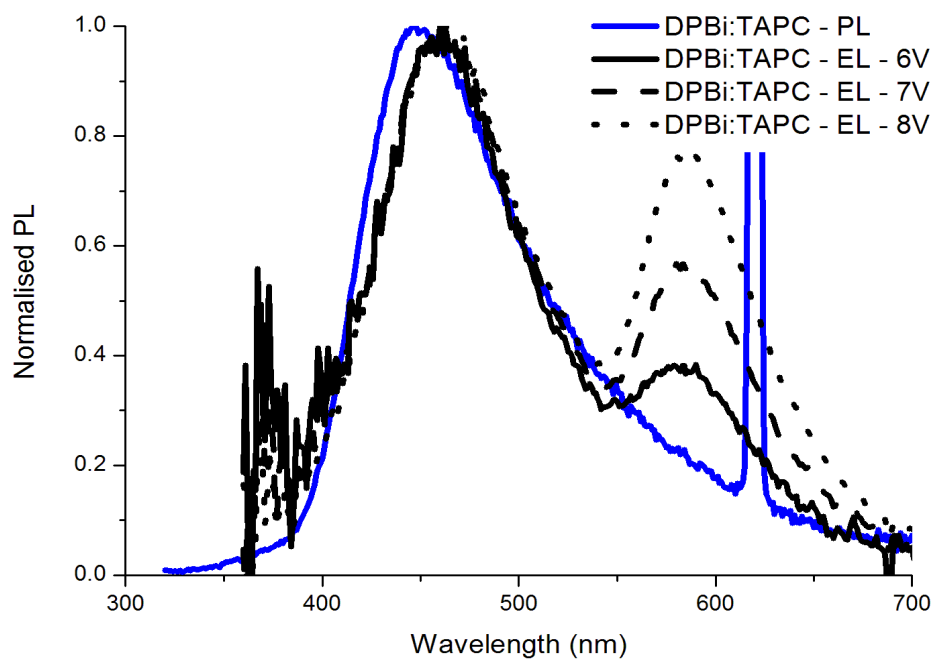
Device structure: ITO/NPB (30nm)/m-DPBi:NPB (30nm)/TPBi (60nm)
/LiF (1nm)/Al (70nm)



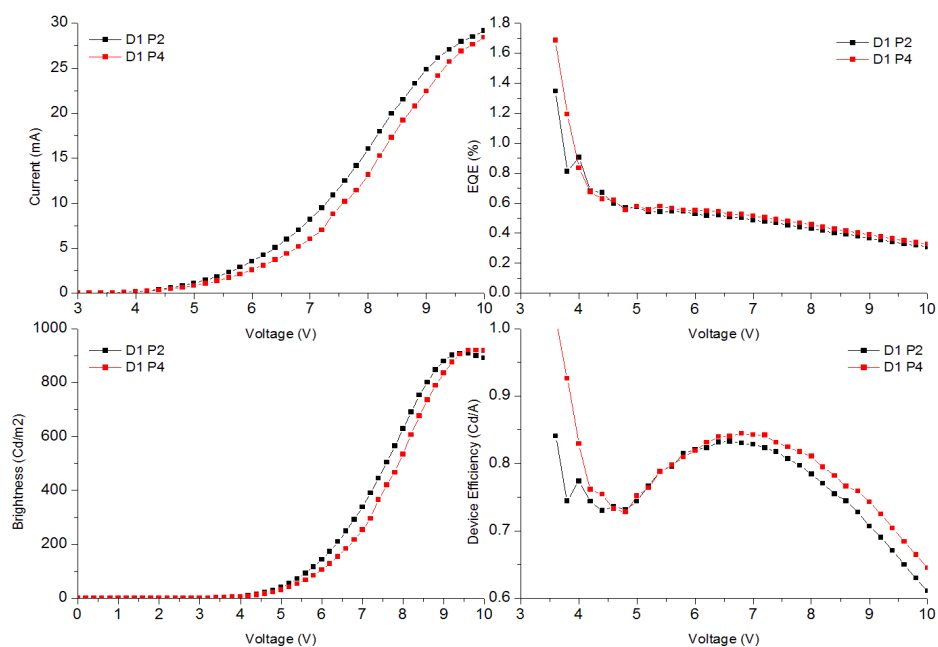
Device structure: ITO/NPB (30nm)/ \pm TAPC(10nm)/m-DPBi:NPB (30nm)/TPBi (60nm)
/LiF (1nm)/Al (70nm)



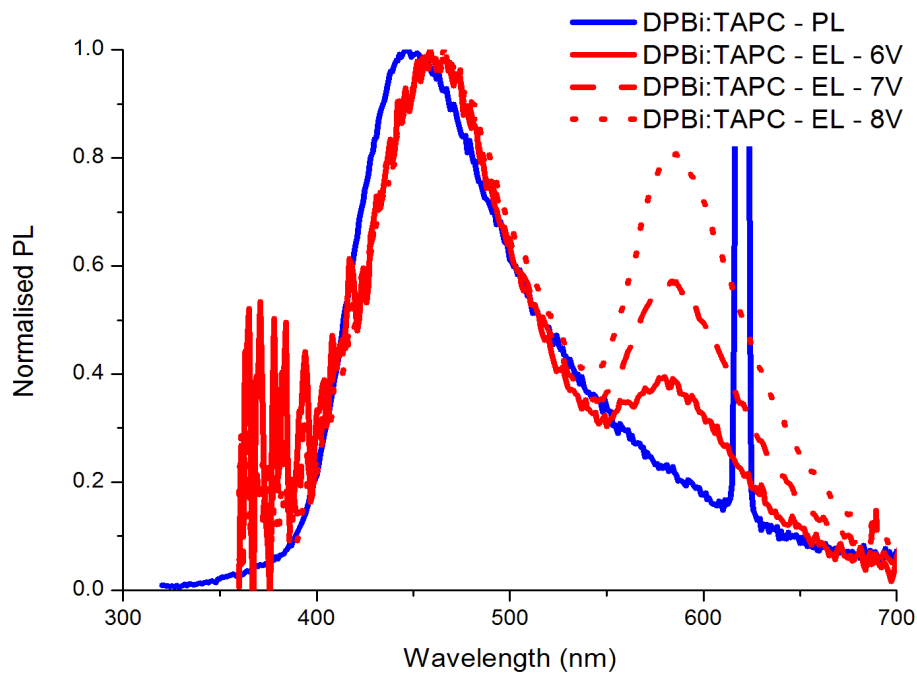
Device structure: ITO/NPB (40nm)/m-DPBi :TAPC (40nm)/TPBi (20nm)/BCP (20nm)
/LiF (1nm)/Al (80nm)



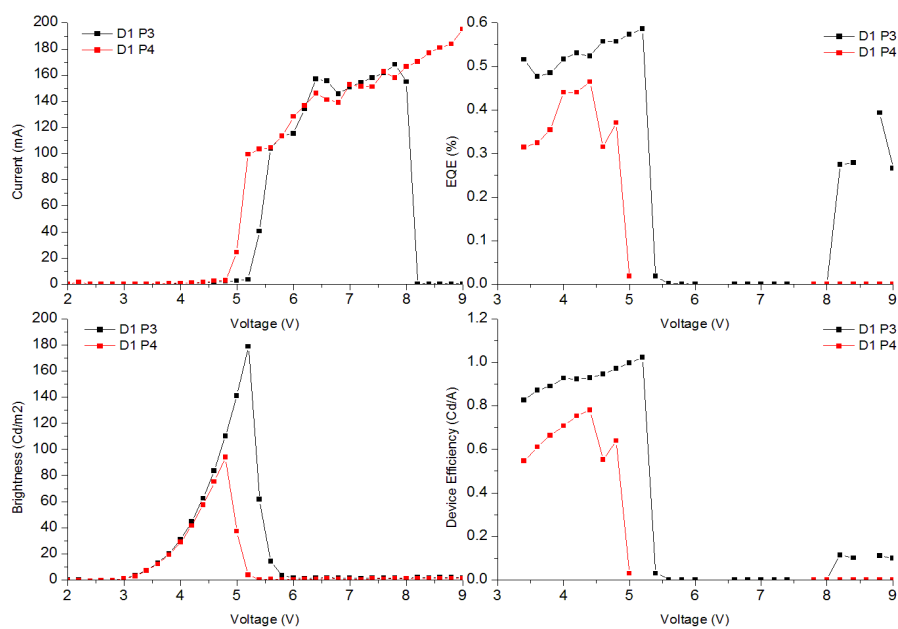
Device structure: ITO/NPB (40nm)/m-DPBi :TAPC (40nm)/TPBi (20nm)/BCP (20nm)
/LiF (1nm)/Al (80nm)



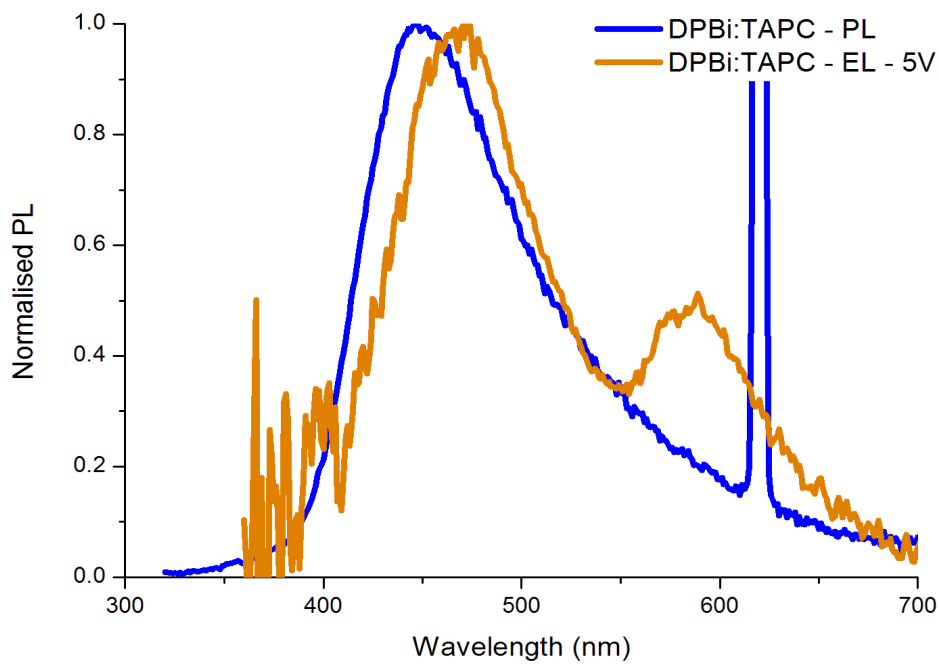
Device structure: ITO/NPB (40nm)/m-DPBi :TAPC (40nm)/TPBi (20nm)/BCP (20nm)
/LiF (1nm)/Al (80nm)



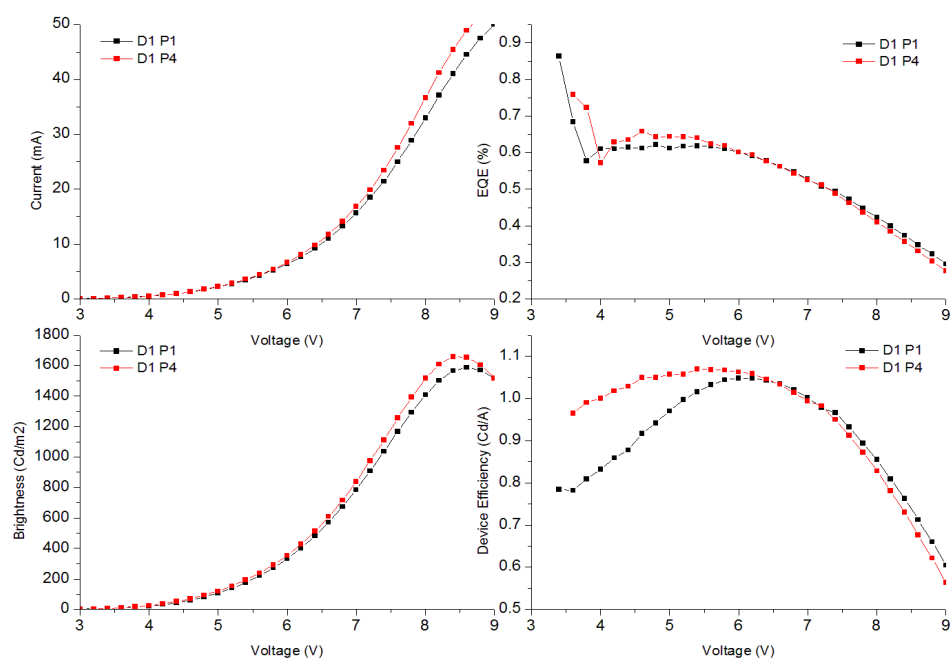
Device structure: ITO/NPB (40nm)/m-DPBi :TAPC (40nm)/TPBi (20nm)/BCP (20nm)
/LiF (1nm)/Al (80nm)



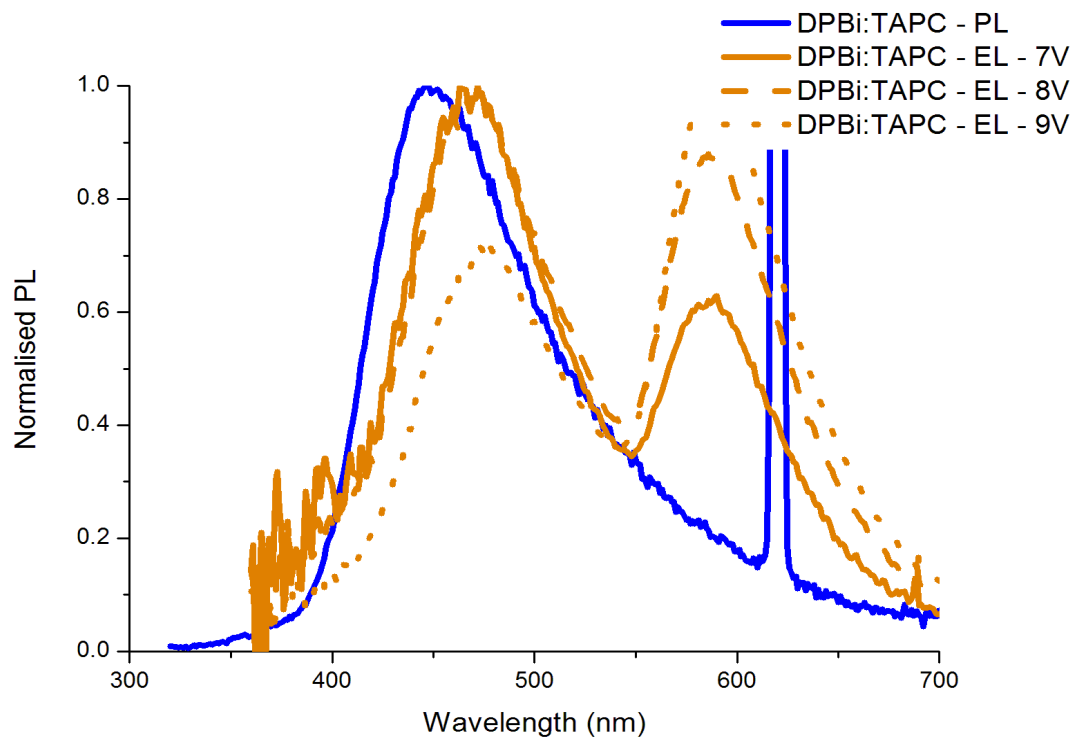
Device structure: ITO/NPB (30nm)/TAPC (10nm)/m-DPBi :TAPC (30nm)/TPBi (60nm)
/LiF (1nm)/Al (80nm)



Device structure: ITO/NPB (30nm)/TAPC (10nm)/m-DPBi :TAPC (30nm)/TPBi (60nm)
/LiF (1nm)/Al (80nm)



Device structure: ITO/NPB (30nm)/TAPC (10nm)/m-DPBi :TAPC (30nm)/TPBi (60nm)
/LiF (1nm)/Al (80nm)



Device structure: ITO/NPB (30nm)/TAPC (10nm)/m-DPBi :TAPC (30nm)/TPBi (60nm)
/LiF (1nm)/Al (80nm)